Title

Spectroscopy of Single Levitated Droplets: Unraveling Physical and Chemical Evolution of Atmospheric Aerosols

Permalink

https://escholarship.org/uc/item/9957t8ks

Author

Kim, Pyeongeun

Publication Date

2022

Peer reviewed|Thesis/dissertation

UNIVERSITY OF CALIFORNIA SAN DIEGO

Spectroscopy of Single Levitated Droplets: Unraveling Physical and Chemical Evolution of Atmospheric Aerosols

A dissertation submitted in partial satisfaction of the requirements
for the degree Doctor of Philosophy

in

Chemistry

by

Pyeongeun Kim

Committee in charge:

Professor Robert E. Continetti, Chair
Professor Vicki H. Grassian
Professor Judy Kim
Professor Jeffrey Severinghaus
Professor Jin Zhang

2022

The Dissertation of Pyeongeun Kim is approved, and it is acceptable in quality and form for publication on microfilm and electronically.

University of California San Diego

2022

DEDICATION

to Juyeon, my family, friends, and the ocean

EPIGRAPH

You’ve got to dig it to dig it, you dig?

Thelonious Monk

TABLE OF CONTENTS

LIST OF FIGURES

LIST OF TABLES

LIST OF SCHEMA

ACKNOWLEDGEMENTS

First and foremost, I must thank my wife, Juyeon Ham. Her encouragement and reassurance for me to pursue what I am curious about were essential for both the start and the end of my graduate school journey. My parents, Hyejin Yoon and Younghwan Kim, believed in me and provided limitless love and support from across the Pacific Ocean. I appreciate my brother Pyeongjin Kim takes good care of our family while I am overseas. I also thank my friends in Korea, for joyful memories growing up together and the warm welcome every time I visit, reminding me that I have had many places to call home.

For the last five years in San Diego, I spent majority of my time in the Continetti Lab, in the basement of Urey Hall. I cannot thank enough to my advisor, Bob Continetti, for the guidance and training from his experiences and skills as a scientist, while letting me explore the wondrous and infinite possibilities of physical chemistry. Still, I have a lot to learn from him. Of course, I want to thank past and present members of the Continetti lab. Their support and friendship have had a profound impact on me becoming a researcher who can design scientific experiments and answering why's of the world and finding a place I can feel like home (underground). In particular, I must thank Katherine Nadler for teaching me how to build and develop a custom scientific instrument, and Christian Boothby for continuing the quest of single droplet chemistry with much passion and curiosity. Additional thanks go to Eleanor Castracane and Austin Parsons for being wonderful labmates and more importantly, friends. Our memories in the lab struggling together and out somewhere having a beer will be cherished. I also thank Yanice Benitez, Katharine Lunny, Morgan Miller, and Jemma Gibbard for the guidance they provided as senior graduate students and a postdoc which shaped me as a scientist. I enjoyed interacting with newer members of the group – Sally Burke, Karl Hanold, and Zach Auvil – and

I will miss having day-to-day conversations with them. Joseph Taulane is greatly appreciated for helpful conversations and making our lives easier as a laboratory manager. I have had a privilege to work with such inspiring people, and I am happy that our paths have crossed in the basement.

Beyond the Continetti lab, I must thank Sifeng Gu, Satyam Khanal, and François Vermersch who are my housemates on Sandburg Avenue and best friends as well. During five years, my favorite activity was being out there (Tourmaline or 11th street of Del Mar) in the lineup with them and trying to catch some waves. They have been my immediate support group and I will never forget the time we shared in the beautiful San Diego. I am grateful that CAICE have supported my research throughout the years and have provided numerous opportunities to interact with fellow scientists from various backgrounds. I want to thank in particular but not limited to Vicki Grassian, Kim Prather, Paul DeMott, Gil Nathanson, Mark Johnson, and Wei Xiong for their encouragements and feedbacks. Lastly, I thank members of my doctoral committee: Judy Kim, Jin Zhang, and Jeff Severinghaus for helping this thesis to materialize.

CHAPTER SPECIFIC ACKNOWLEDGEMENTS

Chapter 3, in part, is a reprint of the material as it appears in Physical Chemistry Chemical Physics, 2019, Nadler, Katherine; Kim, Pyeongeun; Huang, Dao-Ling; Xiong, Wei; Continetti, Robert E. The dissertation author was the primary investigator and author of the work on citric acid in that manuscript and this chapter.

Chapter 4, in full, is a reprint of the material as it appears in Journal of Physical Chemistry B, 2020, Kim, Pyeongeun; Xiong, Wei; Continetti, Robert E. The dissertation author was the primary investigator and author of this paper.

Chapter 5, in full, is a reprint of the material as it appears in ACS Earth and Space Chemistry, 2021, Kim, Pyeongeun; Continetti, Robert E. The dissertation author was the primary investigator and author of this paper.

Chapter 6 contains unpublished material coauthored with Kim, Pyeongeun; Boothby, Christian; Grassian, Vicki H.; Continetti, Robert E. The dissertation author was the primary author of this chapter.

VITA

2012-2014	Republic of Korea Army
2017	Bachelor of Science, Yonsei University
2017-2018	Teaching Assistant, University of California San Diego
2017-2022	Research Assistant, University of California San Diego
2022	Doctor of Philosophy, University of California San Diego

PUBLICATIONS

“Water Diffusion Measurements of Single Charged Aerosols Using H_2O/D_2O Isotope Exchange and Raman Spectroscopy in an Electrodynamic Balance” Nadler, Katherine. A.; Kim, Pyeongeun; Huang, Dao-Ling; Xiong, Wei; Continetti, Robert E. *Physical Chemistry Chemical Physics* **2019**, *21* (27), 15062–15071.

“Evolution of Hydrogen-Bond Interactions within Single Levitated Metastable Aerosols Studied by in Situ Raman Spectroscopy” Kim, Pyeongeun; Xiong, Wei; Continetti, Robert E. *Journal of Physical Chemistry B* **2020**, *124* (42), 9385–9395.

“Accelerated Keto-Enol Tautomerization Kinetics of Malonic Acid in Aqueous Droplets” Kim, Pyeongeun; Continetti, Robert E. *ACS Earth and Space Chemistry* **2021**, *5* (9), 2212–2222.

“Photo-Induced Reactions of Nitrate by a Triplet-Triplet Energy Transfer Mechanism” Kim, Pyeongeun; Boothby, Christian; Grassian, Vicki H.; Continetti, Robert E. *Journal of Physical Chemistry Letters* **2022** (in preparation)

ABSTRACT OF THE DISSERTATION

Spectroscopy of Levitated Single Droplets:
Unraveling Physical and Chemical Properties of Atmospheric Aerosols

by

Pyeongeun Kim

Doctor of Philosophy in Chemistry

University of California San Diego, 2022

Professor Robert E. Continetti, Chair

Atmospheric aerosols are ubiquitous, and they have substantial impacts on climate and human health thus it is important to understand their physical and chemical transformation. However, physicochemical properties of aerosols are poorly understood due to the complexity of the system and difficulties in experiment. To accurately simulate the atmospheric aerosols in the laboratory environment, particle levitation and non-destructive probing are crucial to monitor the change in physicochemical properties in real-time without contact. An environment-controlled mobile electrodynamic balance (EDB) coupled with dual-beam laser spectroscopy setup was developed, achieving stable trapping of single droplet over a long period of time (~72 hours) and providing information on size, phase, and chemical composition of trapped droplet by Mie scattering imaging (MSI) and Raman spectroscopy.

The implementation of the custom-built EDB apparatus revealed new findings about the physical and chemical evolution of aerosol droplets. First, kinetic limitation of water diffusion was observed by the measurements of water diffusion coefficients in aqueous sucrose and aqueous citric acid droplets. The rates of water diffusion in single levitated droplets over a wide range of relative humidity (RH) were directly measured by H_2O/D_2O isotopic exchange. Although sucrose droplets show slower rate of water diffusion, the incomplete exchange of H_2O to D_2O was only observed for citric acid droplets. Second, the evolution of hydrogen bond interactions in sucrose and citric acid droplets versus RH was thoroughly investigated by 2D correlation analysis of Raman spectra. It was found that the hydrophilic functional groups govern the structures of hydrogen bond interactions with water, especially at lower RH conditions where the droplets experience metastable states. Next, the accelerated keto-enol tautomerization kinetics of malonic acid were quantized by spectroscopically monitoring the rate of C-H to C-D exchange at α-carbon. Lastly, reactions of nitrate anion (NO_3^-) by the 266 nm photoexcitation of sulfanilic acid were investigated in single acidic droplets. Absorption-emission analysis supported by computational calculations of excitation energies suggest that the triplet-triplet energy transfer from sulfanilic acid triggers the reactions of nitrate. The

experimental results and analysis presented in this thesis can improve the fundamental understanding of physical and chemical transformations of atmospheric aerosols.

CHAPTER 1: Introduction

1.1: Physical and Chemical Properties of Atmospheric Aerosols

Atmospheric aerosols are ubiquitous in nature. The size of aerosols suspended in air can vary from few nanometers (nm) to hundreds of micrometers (μm).[1] There are variety of sources that emit aerosols in the atmosphere such as breaking ocean waves,[2,3] volcanic eruptions,[4–6] dust storms,[7,8] fuel combustion, and respiratory activities.[9–11] When aerosols are directly emitted from the sources, they are called primary aerosols. Aerosols can also be formed by the nucleation of gas phase organic molecules with low volatility, which is often caused by photochemical reactions and oxidation with reactive atmospheric species.[12,13] In this case where aerosols are formed by series of chemical reactions of gaseous precursors, and they are called secondary aerosols. A detailed understanding of the physical and chemical transformations of atmospheric aerosols is critical to accurately estimate their impacts on climate and human health. The goal of this thesis is to obtain such better understandings by studying single electrodynamically-levitated aerosol particles in controlled environments with Raman spectroscopy.

Aerosols impact the temperature of the Earth by altering cloud albedo and radiative forcing.[14] Aerosol particles serve as condensation nuclei for the formation of cloud droplets and atmospheric ice particles.[15] Aerosols can directly affect the temperature of earth (direct effect). For example, collection of cloud droplets and ice particles can reflect sunlight, therefore they have a net cooling effect.[16] Soot particles, however, have a heating effect on the atmosphere because they can absorb sunlight effectively.[17] There are indirect effects of aerosols as well; microphysical properties of cloud aerosols influence precipitation such as rain, snow, and hail.[15] According to the report by intergovernmental panel on climate change (IPCC), the effect of anthropogenic aerosols on the radiative forcing of climate bears the largest uncertainty among other forcing agents, such as greenhouse gases, ozone, and surface albedo.[18]

In addition to the impact on the climate, aerosols have significant negative effects on public health. Epidemiological and toxicological studies have shown that ambient PM2.5 (particulate matter diameter < 2.5 µm) induces variety of adverse health effects such as cardiopulmonary disorders, initiation and progression of diabetes, and adverse birth outcomes.[19] In addition to poor outdoor air quality, it has been shown that indoor air pollution due to aerosols is also a significant threat to human health, especially in developing countries where biomass fuels are still used as an energy source.[20] Recently, a number of studies have shown the viability of pathogenic bacteria and viruses in the aerosol forms including SARS-CoV-2, which is the cause of global coronavirus pandemic started in 2020.[9–11,21,22]

Aerosols can undergo a variety of photochemical and oxidation reactions in the atmosphere, often referred toas aerosol aging, which in turn alters their physical and chemical properties related to the impacts on Earth's climate and human health discussed above.[23,24] Aging of aerosols occurs through reactions with oxidants in the atmosphere such as hydroxyl radicals (·OH), and through various of photo-induced reactions by solar UV radiation.[25–27] There is a strong correlation between the chemical composition of aerosols and important properties of aerosols related to climatic effects such as cloud condensation nuclei (CCN) activity and ice nucleation (IN) activity.[28–30] Oxidation of organic molecules in aerosols can change the hygroscopicity, viscosity, and rate of water diffusion by increasing the O:C ratio of the aerosols.[31–33] In addition, reactions of organic aerosols with solar UV radiation can lead to the generation of molecules with a large number of chromophores, altering the light-absorbing properties of aerosols.[14,34] Aging of atmospheric aerosol directly affects human health by forming amorphous coatings on the surface of aerosols, which enable long-range transport of carcinogens, such as polycyclic hydrocarbons.[35–37]

In terms of experimental methods for studying physical and chemical evolution of atmospheric aerosols, there are two distinctive approaches: ensemble-averaged studies of many particles, and single particle methods. For ensemble-averaged studies of aerosols, cloud chambers are used for measuring CCN and IN activities in terms of molecular composition of aerosols,[38–40] and flow tube reactors, often coupled with mass spectrometric analysis, are used to monitor the heterogeneous reactions of aerosols with reactive gases such as hydroxyl radical or ozone.[41–43] Aerosol samples from the cloud chamber or flow tube reactors are collected on the substrate for further chromatographic or spectroscopic analysis. The ensemble averaged method is useful, however, there are inherent limitations because the typical time needed for collection is relatively long (12 – 24 hours) and the samples can undergo modifications on substrate during storage and extraction.[44] To overcome these limitations, analytical instrumentations for single particle approach to the aerosol physics and chemistry have been developed. Techniques such as single particle mass spectrometers,[45,46] micro Raman spectroscopy,[47] optical tweezers,[48,49] and electrodynamic balances (EDBs)[50–53] provide complementary information about the physical and chemical characters of single aerosol particles or droplets of dynamic size ranges (nm to µm). In particular, single particle levitation techniques such as optical tweezers and EDBs have large benefits for accurately mimicking atmospheric aerosols because of the lack of surface contact, which can lead to the heterogeneous nucleation. Since aerosols in the atmosphere can reach high solute concentrations above the solubility limit, especially in dry conditions, the contactless levitation is essential for studying this metastable state of aerosol.[51,54,55] The coupling of single particle levitation technique and vibrational spectroscopy such as Raman spectroscopy has facilitated a more thorough understanding of physical and chemical properties of aerosols by providing valuable information about the functional groups and molecular interactions in a non-destructive manner. In the next two sections, an introduction of single particle levitation techniques and Raman spectroscopy will be given successively.

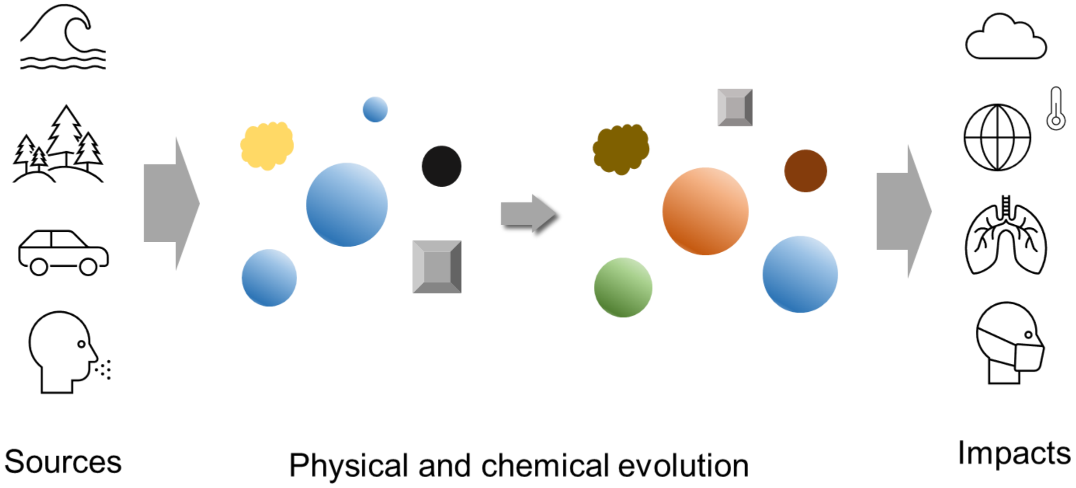

Figure 1.1: The physical and chemical evolution of atmospheric aerosols have substantial effects on the global climate and human health.

1.2: Single Particle Levitation Techniques

Levitation of small particles and droplets have drawn considerable attention of scientists in the past century.[56] It is interesting that three breakthrough experiments in the field of particle levitation led to three Nobel Prizes throughout the development of the technique.

Robert A. Millikan, a faculty at the University of Chicago designed an electrostatic balance, and measured the charge of the electron by analyzing the rate of falling charged oil droplets with and without the applied electric field.[57] The measured value of elemental electric charge from this experiment is about 0.6% different from the currently accepted value of 1.602×10^{-19} C. Millikan received the Nobel Prize in Physics in 1923. Electrostatic balances were used for the next decades for the study of levitated particles and droplets such as light scattering,[58] droplet evaporation,[59] photoionization,[60,61] and thermophoretic force measurements.[62,63]

In 1953, a major advance in particle levitation started at the University of Bonn, when the quadrupole ion trap mass spectrometer was developed by Wolfgang Paul.[64] This apparatus was used to filter the molecular ions by quadrupole AC field, but it was soon recognized that it could also stably trap charged particles. Paul's trap is also referred to as a quadrupole ion trap (QIT) or electrodynamic balance (EDB). Wolfgang Paul was awarded Nobel Prize in Physics in 1989. Wuerker *et al.* later adapted Paul's configuration of quadrupole trap and designed another version of the EDB using a four-electrode system with a bi-hyperbolic cross section.[65]

Lastly, trapping of a spherical particle or droplet can be achieved by using a highly focused laser beam and the optical gradient force exerted on the particle, and the instruments for this optical levitation technique are called optical tweezers. The principles of optical levitation by a single laser beam were established by Arthur Ashkin and by Roosen and Imbert.[66–68] Nobel Prize in

Physics were awarded to Ashkin in 2018 for the invention of the optical tweezer. Optical tweezers have wide range of applications such as aerosol studies, nanoengineering, quantum optics and biological research.[48,69] There are other techniques for particle levitation such as acoustic levitation and aerodynamic levitation.[70,71] In this thesis, however, the levitation of aerosol particles or droplets was achieved using an EDB.

EDBs have been widely used for the studies of atomic ions and aerosols. Davis and coworkers pioneered the research of aerosol physics and chemistry using EDB and light scattering properties.[72,73] The analysis of angular-dependent Mie scattering intensity profiles and parameters of trapping condition such as AC frequency and levitation voltage provided information about evaporation rate, size, mass, phase-separation, and chemical reactions in aerosol particles.[59,73–76] Reid *et al*. extensively studied the important physical properties of atmospheric aerosols such as density, concentration, and refractive index as a function of relative humidity (RH).[77–80] Chan and his group coupled an EDB with Raman spectroscopy to investigate hygroscopic properties and heterogeneous reactions of single aerosol particles.[81–86] Recently, EDBs were combined with mass-spectrometer thus simultaneously allowing optical and mass spectrometric analysis.[53,87,88] In the experiments described in later chapters single levitated particles inside the EDB were irradiated by a dual-beam laser with wavelengths of 266 nm and 532 nm. The 266 nm UV laser beam induces photoexcitation of organic photosensitizers in the droplet. Irradiation with the 532 nm laser probes chemical compositions by Raman spectroscopy and size and phase of the aerosol particle or droplet by Mie scattering imaging (MSI) in real-time.[50–52] The application of Raman spectroscopy to aerosol research will be discussed in the next section.

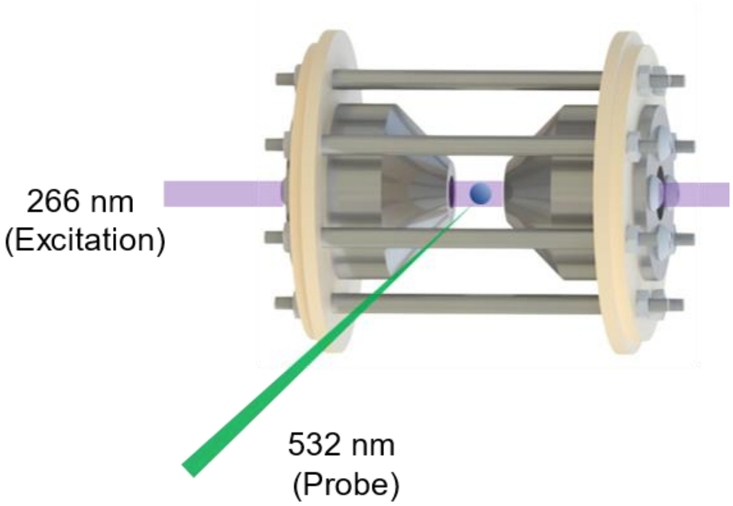

Figure 1.2: Schematic diagram of levitated droplet (blue sphere) in EDB with irradiation of 266 nm and 532 nm laser beams.

1.3: Raman Spectroscopy

To probe the physical and chemical properties of levitated aerosol particles or droplets, a non-destructive probing technique is necessary. Raman spectroscopy and Mie scattering imaging (MSI) are two laser-based techniques that utilize Stokes shifted and Rayleigh scattered light, respectively, from the levitated particle or droplet. In this section, a basic introduction of Raman spectroscopy will be given, and theoretical details will be described in Chapter 2.

Along with infrared (IR) absorption, Raman scattering is used to obtain information about the structure and properties of molecules from their vibrational transitions.[89] **Figure 1.3** depicts the fundamental differences between IR absorption and Raman scattering in terms of interaction between vibrational energy levels and incoming light. In short, IR absorption spectroscopy utilizes the linear phenomena of light absorption by vibrating dipoles, which is polarized chemical bonds in this case, according to the natural frequencies of the vibration. When the energy incoming photon is resonant with the energy difference between ground ($v = 0$) and first excited vibrational states ($v = 1$), the molecule absorbs the photon and is elevated in vibrational energy. For this absorption to take place, it is necessary for the vibrational motion to involve changes in dipole moment of the molecule. For example, the bending mode of CO_2 (linear O=C=C) is IR active but symmetric stretching mode is IR inactive because net change of dipole moment is zero for stretching motion. On the other hand, Raman scattering is a result of non-linear interaction of light and molecules, involving changes in polarization of electron clouds with respect to the molecular vibrations. For Raman scattering to occur, the changes in polarizability of the molecule at zero-point of given vibration needs to be non-zero. Therefore, in the example of CO2, bending mode is Raman inactive but symmetric stretching mode is Raman active. The interaction between incoming light and polarizability of the molecule promotes the molecule to the virtual state from ground vibrational state ($v = 0$) and rarely, relaxing to the first excited vibrational state ($v = 1$) as shown in **Figure 1.3**, as an example of Stokes-shifted Raman scattering.

The intensity of Raman scattering with respect to the vibrational frequency of the molecule can be described in spectrum with x-axis defined as Raman shift in wavenumber (cm^{-1}) as shown in **Figure 1.4**. Molecular vibrational motions such as libration (frustrated rotation), torsional, bending, rocking, wagging, symmetric, and asymmetric stretching can be detected by Raman spectroscopy with respect to the frequency of the specific vibration. Computational tools such as Gaussian09 software are often used to assign spectral peaks to the molecular vibrations through ab-initio or density functional theory (DFT) calculations.[90,91] For example, **Figure 1.4** shows the spectrum of an aqueous citric acid droplet revealing the C-H stretch peak near 2950 cm^{-1}, broad O-H stretch band centered near 3300 cm^{-1}, carbonyl stretch near 1700 cm^{-1}, CH_2 bending near 1400 cm^{-1}, and skeletal vibrations below 1000 cm^{-1}.

Raman spectroscopy has been a powerful tool for observing physical and chemical properties of atmospheric aerosols. The non-destructive nature of Raman scattering rules out the altering of physicochemical properties, which is often not the case for mass spectrometry or X-ray photoelectron spectroscopy. It also provides a real-time information about the sample which is important for monitoring the evolution of aerosol particles over time, making it especially useful for the single particle or droplet experiments. Raman spectroscopy has been widely used in the field of aerosol science, including but not limited to chemical characterization of single aerosol particles,[92,93] rate of water diffusion in model organic aerosols,[54,94] measuring aerosol pH,[48,95,96] hydrogen bond interactions,[47,97] and heterogeneous reactions.[82,83] The experimental setup used in the studies described in this thesis couples single particle levitation of charged aerosol in an EDB with laser Raman spectroscopy, and will be discussed in detail in Chapter 2.

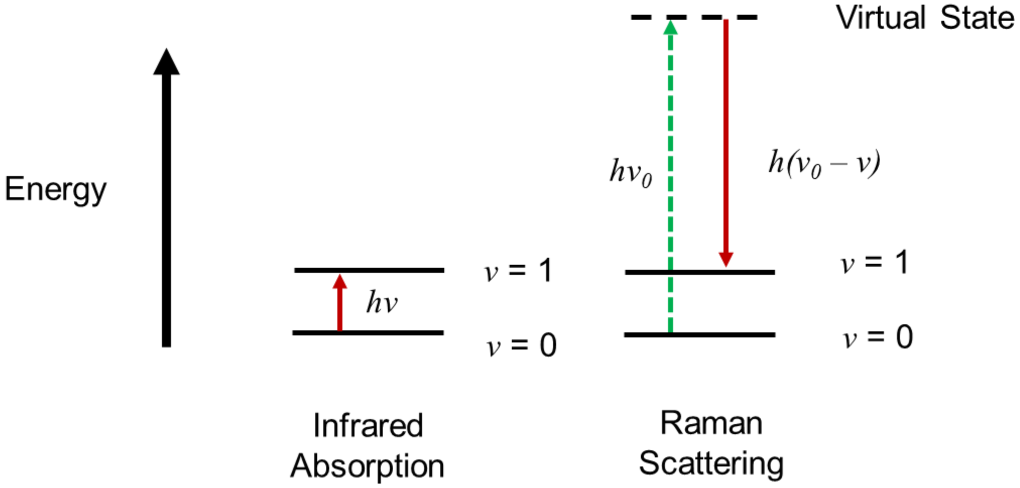

Figure 1.3: Energy-level diagram for IR absorption and Stokes Raman scattering for a vibrational transition between $v = 0$ and $v = 1$. On the left, a molecule absorbs a photon with energy of *hv* while on the right the scattered light lost energy of *hv*.

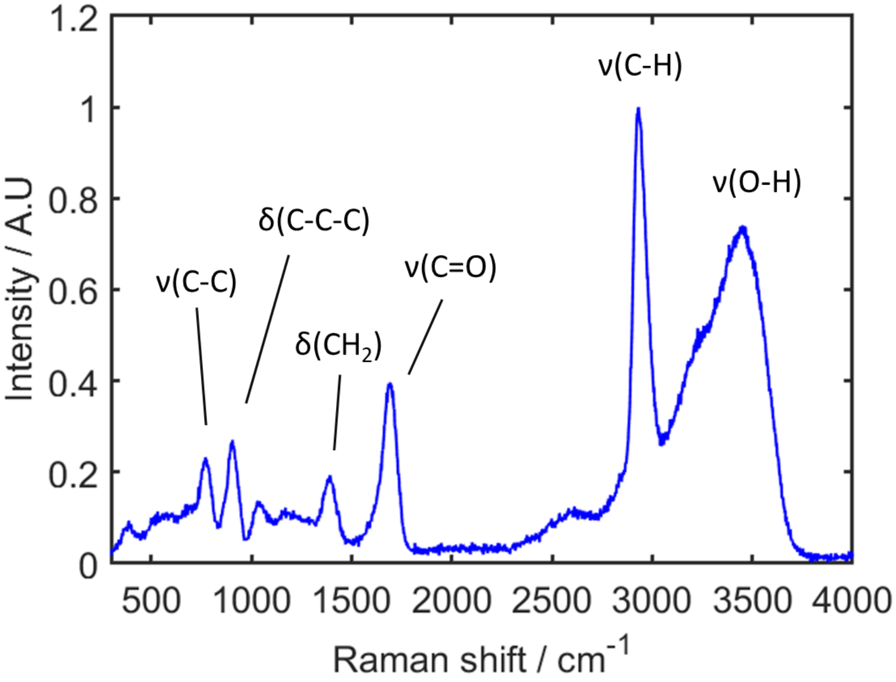

Figure 1.4: Raman spectrum of an aqueous citric acid droplet. Assignments to the characteristic Raman peaks are given in the spectrum. v and δ stands for stretching and bending of the atoms along the chemical bonds, respectively.

1.4: Structure of the Thesis

This introduction has provided the background for the understanding of physicochemical properties of atmospheric aerosols and their impact to the environment and health. In the second chapter the experimental apparatus for single particle levitation and spectroscopy are described, including methods of data acquisition and analysis. With experimental methods established, a water diffusion study of model organic aerosols (sucrose and citric acid) is presented in the third chapter. In particular, the observed kinetic limitation of water in citric acid droplets is discussed in detail. This study of water diffusion provided the motivation for the concept of the fourth chapter, examining the evolution of hydrogen bond interactions in sucrose and citric acid droplets. Following these investigations of physical properties of organic aerosols, studies of chemical reactions will be presented. In the fifth chapter, accelerated kinetics of keto-enol tautomerization in malonic acid droplets will be reported. Finally, photo-induced reactions of nitrate anions by sulfanilic acid will be discussed in the sixth chapter.

References

(1) Seinfeld, J. H.; Pandis, S. N. *Atmospheric Chemistry and Physics: From Air Pollution to Climate Change*; John Wiley & Sons, 2016.

(2) Bertram, T. H.; Cochran, R. E.; Grassian, V. H.; Stone, E. A. Sea Spray Aerosol Chemical Composition: Elemental and Molecular Mimics for Laboratory Studies of Heterogeneous and Multiphase Reactions. *Chem. Soc. Rev.* **2018**, *47* (7), 2374–2400.

(3) Quinn, P. K.; Collins, D. B.; Grassian, V. H.; Prather, K. A.; Bates, T. S. Chemistry and Related Properties of Freshly Emitted Sea Spray Aerosol. *Chem. Rev.* **2015**, *115* (10), 4383–4399.

(4) Guy, B.; Claire, G. Mount Pinatubo Aerosols, Chlorofluorocarbons, and Ozone Depletion. *Science* **1992**, *257* (5074), 1239–1242.

(5) Sawyer, G. M.; Salerno, G. G.; Le Blond, J. S.; Martin, R. S.; Spampinato, L.; Roberts, T. J.; Mather, T. A.; Witt, M. L. I.; Tsanev, V. I.; Oppenheimer, C. Gas and Aerosol Emissions from Villarrica Volcano, Chile. *J. Volcanol. Geotherm. Res.* **2011**, *203* (1), 62–75.

(6) Menard, G.; Moune, S.; Vlastélic, I.; Aguilera, F.; Valade, S.; Bontemps, M.; González, R. Gas and Aerosol Emissions from Lascar Volcano (Northern Chile): Insights into the Origin of Gases and Their Links with the Volcanic Activity. *J. Volcanol. Geotherm. Res.* **2014**, *287*, 51–67.

(7) Wang, Y.; Zhuang, G.; Sun, Y.; An, Z. Water-Soluble Part of the Aerosol in the Dust Storm Season—Evidence of the Mixing between Mineral and Pollution Aerosols. *Atmos. Environ.* **2005**, *39* (37), 7020–7029.

(8) Dey, S.; Tripathi, S. N.; Singh, R. P.; Holben, B. N. Influence of Dust Storms on the Aerosol Optical Properties over the Indo-Gangetic Basin. *J. Geophys. Res. Atmos.* **2004**, *109* (D20).

(9) Wang, C. C.; Prather, K. A.; Sznitman, J.; Jimenez, J. L.; Lakdawala, S. S.; Tufekci, Z.; Marr, L. C. Airborne Transmission of Respiratory Viruses. *Science* **2021**, *373* (6558).

(10) Knibbs, L. D.; Johnson, G. R.; Kidd, T. J.; Cheney, J.; Grimwood, K.; Kattenbelt, J. A.; O'Rourke, P. K.; Ramsay, K. A.; Sly, P. D.; Wainwright, C. E.; Wood, M. E.; Morawska, L.; Bell, S. C. Viability of Pseudomonas Aeruginosa in Cough Aerosols Generated by Persons with Cystic Fibrosis. *Thorax* **2014**, *69* (8), 740–745.

(11) Anderson, E. L.; Turnham, P.; Griffin, J. R.; Clarke, C. C. Consideration of the Aerosol Transmission for COVID-19 and Public Health. *Risk Anal.* **2020**, *40* (5), 902–907.

(12) Hallquist, M.; Wenger, J. C.; Baltensperger, U.; Rudich, Y.; Simpson, D.; Claeys, M.; Dommen, J.; Donahue, N. M.; George, C.; Goldstein, a. H.; Hamilton, J. F.; Herrmann,

H.; Hoffmann, T.; Iinuma, Y.; Jang, M.; Jenkin, M. E.; Jimenez, J. L.; Kiendler-Scharr, a.; Maenhaut, W.; McFiggans, G.; Mentel, T. F.; Monod, a.; Prévôt, a. S. H.; Seinfeld, J. H.; Surratt, J. D.; Szmigielski, R.; Wildt, J. The Formation, Properties and Impact of Secondary Organic Aerosol: Current and Emerging Issues. *Atmos. Chem. Phys.* **2009**, *9* (14), 5155–5236.

(13) Lim, Y. B.; Tan, Y.; Perri, M. J.; Seitzinger, S. P.; Turpin, B. J. Aqueous Chemistry and Its Role in Secondary Organic Aerosol (SOA) Formation. *Atmos. Chem. Phys.* **2010**, *10* (21), 10521–10539.

(14) Shrivastava, M.; Cappa, C. D.; Fan, J.; Goldstein, A. H.; Guenther, A. B.; Jimenez, J. L.; Kuang, C.; Laskin, A.; Martin, S. T.; Ng, N. L.; Petaja, T.; Pierce, J. R.; Rasch, P. J.; Roldin, P.; Seinfeld, J. H.; Shilling, J.; Smith, J. N.; Thornton, J. A.; Volkamer, R.; Wang, J.; Worsnop, D. R.; Zaveri, R. A.; Zelenyuk, A.; Zhang, Q. Recent Advances in Understanding Secondary Organic Aerosol: Implications for Global Climate Forcing. *Rev. Geophys.* **2017**, *55* (2), 509–559.

(15) Andreae, M. O.; Rosenfeld, D. Aerosol-Cloud-Precipitation Interactions. Part 1. The Nature and Sources of Cloud-Active Aerosols. *Earth-Science Rev.* **2008**, *89* (1–2), 13–41.

(16) DeMott, P. J.; Prenni, A. J.; Liu, X.; Kreidenweis, S. M.; Petters, M. D.; Twohy, C. H.; Richardson, M. S.; Eidhammer, T.; Rogers, D. C. Predicting Global Atmospheric Ice Nuclei Distributions and Their Impacts on Climate. *Proc. Natl. Acad. Sci.* **2010**, *107* (25), 11217–11222.

(17) Horvath, H. Atmospheric Light Absorption—A Review. *Atmos. Environ. Part A. Gen. Top.* **1993**, *27* (3), 293–317.

(18) IPCC. *Climate Change 2014 Part A: Global and Sectoral Aspects*; 2014.

(19) Feng, S.; Gao, D.; Liao, F.; Zhou, F.; Wang, X. The Health Effects of Ambient PM2.5 and Potential Mechanisms. *Ecotoxicol. Environ. Saf.* **2016**, *128*, 67–74.

(20) Mannucci, P. M.; Franchini, M. Health Effects of Ambient Air Pollution in Developing Countries. *Int. J. Environ. Res. Public Health* **2017**, *14* (9), 1–8.

(21) van Doremalen, N.; Bushmaker, T.; Morris, D. H.; Holbrook, M. G.; Gamble, A.; Williamson, B. N.; Tamin, A.; Harcourt, J. L.; Thornburg, N. J.; Gerber, S. I.; Lloyd-Smith, J. O.; de Wit, E.; Munster, V. J. Aerosol and Surface Stability of SARS-CoV-2 as Compared with SARS-CoV-1. *N. Engl. J. Med.* **2020**, *382* (16), 1564–1567.

(22) Prather, K. A.; Wang, C. C.; Schooley, R. T. Reducing Transmission of SARS-CoV-2. *Science* **2020**, *368* (6498), 1422–1424.

(23) Rudich, Y.; Donahue, N. M.; Mentel, T. F. Aging of Organic Aerosol: Bridging the Gap Between Laboratory and Field Studies. *Annu. Rev. Phys. Chem.* **2007**, *58* (1), 321–352.

(24) Shiraiwa, M.; Ammann, M.; Koop, T.; Poschl, U. Gas Uptake and Chemical Aging of

Semisolid Organic Aerosol Particles. *Proc. Natl. Acad. Sci.* **2011**, *108* (27), 11003–11008.

(25) Donahue, N. M.; Henry, K. M.; Mentel, T. F.; Kiendler-Scharr, A.; Spindler, C.; Bohn, B.; Brauers, T.; Dorn, H. P.; Fuchs, H.; Tillmann, R.; Wahner, A.; Saathoff, H.; Naumann, K. H.; Möhler, O.; Leisner, T.; Müller, L.; Reinnig, M. C.; Hoffmann, T.; Salo, K.; Hallquist, M.; Frosch, M.; Bilde, M.; Tritscher, T.; Barmet, P.; Praplan, A. P.; DeCarlo, P. F.; Dommen, J.; Prévôt, A. S. H.; Baltensperger, U. Aging of Biogenic Secondary Organic Aerosol via Gas-Phase OH Radical Reactions. *Proc. Natl. Acad. Sci. U. S. A.* **2012**, *109* (34), 13503–13508.

(26) Thomas, D. A.; Coggon, M. M.; Lignell, H.; Schilling, K. A.; Zhang, X.; Schwantes, R. H.; Flagan, R. C.; Seinfeld, J. H.; Beauchamp, J. L. Real-Time Studies of Iron Oxalate-Mediated Oxidation of Glycolaldehyde as a Model for Photochemical Aging of Aqueous Tropospheric Aerosols. *Environ. Sci. Technol.* **2016**, *50* (22), 12241–12249.

(27) Dalton, A. B.; Nizkorodov, S. A. Photochemical Degradation of 4-Nitrocatechol and 2,4-Dinitrophenol in a Sugar-Glass Secondary Organic Aerosol Surrogate. *Environ. Sci. Technol.* **2021**, *55* (21), 14586–14594.

(28) Wu, Z. J.; Poulain, L.; Henning, S.; Dieckmann, K.; Birmili, W.; Merkel, M.; van Pinxteren, D.; Spindler, G.; Müller, K.; Stratmann, F.; Herrmann, H.; Wiedensohler, A. Relating Particle Hygroscopicity and CCN Activity to Chemical Composition during the HCCT-2010 Field Campaign. *Atmos. Chem. Phys.* **2013**, *13* (16), 7983–7996.

(29) Furutani, H.; Dall'osto, M.; Roberts, G. C.; Prather, K. A. Assessment of the Relative Importance of Atmospheric Aging on CCN Activity Derived from Field Observations. *Atmos. Environ.* **2008**, *42* (13), 3130–3142.

(30) Wolf, M. J.; Goodell, M.; Dong, E.; Dove, L. A.; Zhang, C.; Franco, L. J.; Shen, C.; Rutkowski, E. G.; Narducci, D. N.; Mullen, S.; Babbin, A. R.; Cziczo, D. J. A Link between the Ice Nucleation Activity and the Biogeochemistry of Seawater. *Atmos. Chem. Phys.* **2020**, *20* (23), 15341–15356.

(31) Marshall, F. H.; Berkemeier, T.; Shiraiwa, M.; Nandy, L.; Ohm, P. B.; Dutcher, C. S.; Reid, J. P. Influence of Particle Viscosity on Mass Transfer and Heterogeneous Ozonolysis Kinetics in Aqueous-Sucrose-Maleic Acid Aerosol. *Phys. Chem. Chem. Phys.* **2018**, 17–20.

(32) Marshall, F. H.; Miles, R. E. H.; Song, Y. C.; Ohm, P. B.; Power, R. M.; Reid, J. P.; Dutcher, C. S. Diffusion and Reactivity in Ultraviscous Aerosol and the Correlation with Particle Viscosity. *Chem. Sci.* **2016**, *7* (2), 1298–1308.

(33) Virtanen, A.; Joutsensaari, J.; Koop, T.; Kannosto, J.; Yli-Pirilä, P.; Leskinen, J.; Mäkelä, J. M.; Holopainen, J. K.; Pöschl, U.; Kulmala, M.; Worsnop, D. R.; Laaksonen, A. An Amorphous Solid State of Biogenic Secondary Organic Aerosol Particles. *Nature* **2010**, *467* (7317), 824–827.

(34) Xie, M.; Chen, X.; Hays, M. D.; Lewandowski, M.; Offenberg, J.; Kleindienst, T. E.;

Holder, A. L. Light Absorption of Secondary Organic Aerosol: Composition and Contribution of Nitroaromatic Compounds. *Environ. Sci. Technol.* **2017**, *51* (20), 11607–11616.

(35) Berkemeier, T.; Steimer, S. S.; Krieger, U. K.; Peter, T.; Pöschl, U.; Ammann, M.; Shiraiwa, M. Ozone Uptake on Glassy, Semi-Solid and Liquid Organic Matter and the Role of Reactive Oxygen Intermediates in Atmospheric Aerosol Chemistry. *Phys. Chem. Chem. Phys.* **2016**, *18* (18), 12662–12674.

(36) Zhou, S.; Shiraiwa, M.; McWhinney, R. D.; Pöschl, U.; Abbatt, J. P. D. Kinetic Limitations in Gas-Particle Reactions Arising from Slow Diffusion in Secondary Organic Aerosol. *Faraday Discuss.* **2013**, *165*, 391–406.

(37) Shrivastava, M.; Lou, S.; Zelenyuk, A.; Easter, R. C.; Corley, R. A.; Thrall, B. D.; Rasch, P. J.; Fast, J. D.; Simonich, S. L. M.; Shen, H.; Tao, S. Global Long-Range Transport and Lung Cancer Risk from Polycyclic Aromatic Hydrocarbons Shielded by Coatings of Organic Aerosol. *Proc. Natl. Acad. Sci. U. S. A.* **2017**, *114* (6), 1246–1251.

(38) DeMott, P. J.; Rogers, D. C. Freezing Nucleation Rates of Dilute Solution Droplets Measured between −30° and −40°C in Laboratory Simulations of Natural Clouds. *J. Atmos. Sci.* **1990**, *47* (9), 1056–1064.

(39) DeMott, P. J. An Exploratory Study of Ice Nucleation by Soot Aerosols. *J. Appl. Meteorol. Climatol.* **1990**, *29* (10), 1072–1079.

(40) Ruehl, C. R.; James, D. F.; Wilson, K. R. Droplet Formation on Organic Aerosols. *Science* **2016**, *351* (6280), 1447.

(41) Chan, M. N.; Zhang, H.; Goldstein, A. H.; Wilson, K. R. Role of Water and Phase in the Heterogeneous Oxidation of Solid and Aqueous Succinic Acid Aerosol by Hydroxyl Radicals. *J. Phys. Chem. C* **2014**, *118* (50), 28978–28992.

(42) Ki Lam, H.; Xu, R.; Choczynski, J.; Davies, J. F.; Ham, D.; Song, M.; Zuend, A.; Li, W.; Steve Tse, Y. L.; Chan, M. N. Effects of Liquid-Liquid Phase Separation and Relative Humidity on the Heterogeneous Oh Oxidation of Inorganic-Organic Aerosols: Insights from Methylglutaric Acid and Ammonium Sulfate Particles. *Atmos. Chem. Phys.* **2021**, *21* (3), 2053–2066.

(43) Han, C.; Yang, W.; Wu, Q.; Yang, H.; Xue, X. Heterogeneous Photochemical Conversion of NO_2 to HONO on the Humic Acid Surface under Simulated Sunlight. *Environ. Sci. Technol.* **2016**, *50* (10), 5017–5023.

(44) Ault, A. P.; Axson, J. L. Atmospheric Aerosol Chemistry: Spectroscopic and Microscopic Advances. *Anal. Chem.* **2017**, *89* (1), 430–452.

(45) Pratt, K. A.; Prather, K. A. Mass Spectrometry of Atmospheric Aerosols—Recent Developments and Applications. Part II: On-Line Mass Spectrometry Techniques. *Mass Spectrom. Rev.* **2012**, *31* (1), 17–48.

(46) Pratt, K. A.; Prather, K. A. Mass Spectrometry of Atmospheric Aerosols—Recent Developments and Applications. Part I: Off-Line Mass Spectrometry Techniques. *Mass Spectrom. Rev.* **2012**, *31* (1), 1–16.

(47) Mael, L. E.; Peiker, G.; Busse, H. L.; Grassian, V. H. Temperature-Dependent Liquid Water Structure for Individual Micron-Sized, Supercooled Aqueous Droplets with Inclusions. *J. Phys. Chem. A* **2021**.

(48) Coddens, E. M.; Angle, K. J.; Grassian, V. H. Titration of Aerosol PH through Droplet Coalescence. *J. Phys. Chem. Lett.* **2019**, *10* (15), 4476–4483.

(49) Angle, K. J.; Neal, E. E.; Grassian, V. H. Enhanced Rates of Transition-Metal-Ion-Catalyzed Oxidation of S(IV) in Aqueous Aerosols: Insights into Sulfate Aerosol Formation in the Atmosphere. *Environ. Sci. Technol.* **2021**, *55* (15), 10291–10299.

(50) Nadler, K. A.; Kim, P.; Huang, D. L.; Xiong, W.; Continetti, R. E. Water Diffusion Measurements of Single Charged Aerosols Using H2O/D2O Isotope Exchange and Raman Spectroscopy in an Electrodynamic Balance. *Phys. Chem. Chem. Phys.* **2019**, *21* (27), 15062–15071.

(51) Kim, P.; Xiong, W.; Continetti, R. E. Evolution of Hydrogen-Bond Interactions within Single Levitated Metastable Aerosols Studied by in Situ Raman Spectroscopy. *J. Phys. Chem. B* **2020**, *124* (42), 9385–9395.

(52) Kim, P.; Continetti, R. E. Accelerated Keto-Enol Tautomerization Kinetics of Malonic Acid in Aqueous Droplets. *ACS Earth Sp. Chem.* **2021**, *5* (9), 2212–2222.

(53) Kohli, R. K.; Davies, J. F. Measuring the Chemical Evolution of Levitated Particles: A Study on the Evaporation of Multicomponent Organic Aerosol. *Anal. Chem.* **2021**, *93* (36), 12472–12479.

(54) Davies, J. F.; Wilson, K. R. Raman Spectroscopy of Isotopic Water Diffusion in Ultraviscous, Glassy, and Gel States in Aerosol by Use of Optical Tweezers. *Anal. Chem.* **2016**, *88* (4), 2361–2366.

(55) Lienhard, D. M.; Huisman, A. J.; Krieger, U. K.; Rudich, Y.; Marcolli, C.; Luo, B. P.; Bones, D. L.; Reid, J. P.; Lambe, A. T.; Canagaratna, M. R.; Davidovits, P.; Onasch, T. B.; Worsnop, D. R.; Steimer, S. S.; Koop, T.; Peter, T. Viscous Organic Aerosol Particles in the Upper Troposphere: Diffusivity-Controlled Water Uptake and Ice Nucleation? *Atmos. Chem. Phys.* **2015**, *15* (23), 13599–13613.

(56) Davis, E. J. A History of Single Aerosol Particle Levitation. *Aerosol Sci. Technol.* **1997**, *26* (3), 212–254.

(57) Millikan., R. A. On the Elementary Electrical Charge and the Avogadro Constant. *Phys. Rev.* **1913**, *2* (2), 109–143.

(58) Gucker, F. T.; Rowell, R. L. The Angular Variation of Light Scattered By Single Dioctyl

Phthalate Aerosol Droplets. *Discuss. Faraday Soc.* **1960**, No. 958.

(59) Davis, E. J.; Chorbajian, E. The Measurement of Evaporation Rates of Submicron Aerosol Droplets. *Ind. Eng. Chem. Fundam.* **1974**, *13* (3), 272–277.

(60) Pope, M. Electrostatic Determination of Photo-Ionization Potentials of Solids and Liquids. *J. Chem. Phys.* **1962**, *37* (5), 1001–1003.

(61) Pope, M. Surface Ionization Energies of Organic Compounds: Phthalocyanines. *J. Chem. Phys.* **1962**, *36* (10), 2810–2811.

(62) Saxton, R. L.; Ranz, W. E. Thermal Force on an Aerosol Particle in a Temperature Gradient. *J. Appl. Phys.* **1952**, *23*, 917.

(63) Jacobsen, S.; Brock, J. R. The Thermal Force on Spherical Sodium Chloride Aerosols. *J. Colloid Sci.* **1965**, *20* (6), 544–554.

(64) Paul, W.; Steinwedel, H. Notizen: Ein Neues Massenspektrometer Ohne Magnetfeld. *Zeitschrift für Naturforsch. A* **1953**, *8* (7), 448–450.

(65) Wuerker, R. F.; Shelton, H.; Langmuir, R. V. Electrodynamic Containment of Charged Particles. *J. Appl. Phys.* **1959**, *30* (3), 342–349.

(66) Ashkin, A. Acceleration and Trapping of Particles by Radiation Pressure. *Phys. Rev. Lett.* **1970**, *24* (4), 156–159.

(67) Roosen, G.; Imbert, C. Optical Levitation by Means of Two Horizontal Laser Beams: A Theoretical and Experimental Study. *Phys. Lett. A* **1976**, *59* (1), 6–8.

(68) A., A. Applications of Laser Radiation Pressure. *Science* **1980**, *210* (4474), 1081–1088.

(69) Moffitt, J. R.; Chemla, Y. R.; Smith, S. B.; Bustamante, C. Recent Advances in Optical Tweezers. *Annu. Rev. Biochem.* **2008**, *77* (August), 205–228.

(70) Crawford, E. A.; Esen, C.; Volmer, D. A. Real Time Monitoring of Containerless Microreactions in Acoustically Levitated Droplets via Ambient Ionization Mass Spectrometry. *Anal. Chem.* **2016**, *88* (17), 8396–8403.

(71) Avedisian, C. T. Experimental Study of High-Pressure Bubble Growth Within Multicomponent Liquid Droplets Levitated in a Flowing Stream of Another Immiscible Liquid. *Proc. R. Soc. London, Ser. A Math. Phys. Sci.* **1987**, *409* (1837), 271–285.

(72) Davis, E. J.; Ray, a. . Single Aerosol Particle Size and Mass Measurements Using an Electrodynamic Balance. *J. Colloid Interface Sci.* **1980**, *75* (2), 566–576.

(73) Davis, E. J.; Periasamy, R. Light-Scattering and Aerodynamic Size Measurements for Homogeneous and Inhomogeneous Microspherest. *Langmuir* **1985**, *1* (3), 373–379.

(74) Davis, E. J.; Ray, A. K. Single Aerosol Particle Size and Mass Measurements Using an

Electrodynamic Balance. *J. Colloid Interface Sci.* **1980**, *75* (2), 566–576.

(75) Ray, A. K.; Souyri, A.; Davis, E. J.; Allen, T. M. Precision of Light-Scattering Techniques for Measuring Optical-Parameters of Microspheres. *Appl. Opt.* **1991**, *30* (27), 3974–3983.

(76) Widmann, J. F.; Aardahl, C. L.; Davis, E. J. Microparticle Raman Spectroscopy. *TrAC - Trends Anal. Chem.* **1998**, *17* (6), 339–345.

(77) Davies, J. F.; Haddrell, A. E.; Reid, J. P. Time-Resolved Measurements of the Evaporation of Volatile Components from Single Aerosol Droplets. *Aerosol Sci. Technol.* **2012**, *46* (6), 666–677.

(78) Mason, B. J.; Cotterell, M. I.; Preston, T. C.; Orr-Ewing, A. J.; Reid, J. P. Direct Measurements of the Optical Cross Sections and Refractive Indices of Individual Volatile and Hygroscopic Aerosol Particles. *J. Phys. Chem. A* **2015**, *119* (22), 5701–5713.

(79) Preston, T. C.; Reid, J. P. Accurate and Efficient Determination of the Radius, Refractive Index, and Dispersion of Weakly Absorbing Spherical Particle Using Whispering Gallery Modes. *J. Opt. Soc. Am. B-Optical Phys.* **2013**, *30* (8), 2113–2122.

(80) Gregson, F. K. A.; Robinson, J. F.; Miles, R. E. H.; Royall, C. P.; Reid, J. P. Drying Kinetics of Salt Solution Droplets: Water Evaporation Rates and Crystallization. *J. Phys. Chem. B* **2019**, *123* (1), 266–276.

(81) Lee, A. K. Y.; Ling, T. Y.; Chan, C. K. Understanding Hygroscopic Growth and Phase Transformation of Aerosols Using Single Particle Raman Spectroscopy in an Electrodynamic Balance. *Faraday Discuss.* **2008**, *137* (852), 245–263.

(82) Lee, A. K. Y.; Chan, C. K. Single Particle Raman Spectroscopy for Investigating Atmospheric Heterogeneous Reactions of Organic Aerosols. *Atmos. Environ.* **2007**, *41*, 4611–4621.

(83) Lee, A. K. Y.; Chan, C. K. Heterogeneous Reactions of Linoleic Acid and Linolenic Acid Particles with Ozone: Reaction Pathways and Changes in Particle Mass, Hygroscopicity, and Morphology. *J. Phys. Chem. A* **2007**, *111* (28), 6285–6295.

(84) Peng, C.; Chan, M. N.; Chan, C. K. The Hygroscopic Properties of Dicarboxylic and Multifunctional Acids: Measurements and UNIFAC Predictions. *Environ. Sci. Technol.* **2001**, *35* (22), 4495–4501.

(85) Peng, C.; Chan, C. K.; Chow, A. H. L. Hygroscopic Study of Glucose, Citric Acid, and Sorbitol Using an Electrodynamic Balance: Comparison with UNIFAC Predictions. *Aerosol Sci. Technol.* **2001**, *35* (3), 753–758.

(86) Liang, Z.; Chu, Y.; Gen, M.; Chan, C. K. Single-Particle Raman Spectroscopy for Studying Physical and Chemical Processes of Atmospheric Particles. *Atmos. Chem. Phys.* **2022**, *22* (5), 3017–3044.

(87) Willis, M. D.; Rovelli, G.; Wilson, K. R. Combining Mass Spectrometry of Picoliter Samples with a Multicompartment Electrodynamic Trap for Probing the Chemistry of Droplet Arrays. *Anal. Chem.* **2020**, *92* (17), 11943–11952.

(88) Kohli, R. K.; Berkel, G. J. Van; Davies, J. F. An Open Port Sampling Interface for the Chemical Characterization of Levitated Microparticles. *Anal. Chem.* **2022**, *94* (8), 3441–3445.

(89) Lewis, I. R.; Edwards, H. Handbook of Raman Spectroscopy: From the Research Laboratory to the Process Line; Marcel Dekker: New York, NY, 2001.

(90) Frisch, M. J.; Trucks, G. W.; Schlegel, H. B.; Scuseria, G. E.; Robb, M. A.; Cheeseman, J. R.; Scalmani, G.; Barone, V.; Petersson, G. A.; Nakatsuji, H.; Li, X.; Caricato, M.; Marenich, A. V.; Bloino, J.; Janesko, B. G.; Gomperts, R.; Mennucci, B.; Hratch, D. J. Gaussian 09, Revision A.02. Gaussian, Inc.: Wallingford CT 2016.

(91) Brandán, S. A.; Bichara, L. C.; Lans, H. E.; Ferrer, E. G.; Gramajo, M. B. Vibrational Study and Force Field of the Citric Acid Dimer Based on the SQM Methodology. *Adv. Phys. Chem.* **2011**, *2011*, 347072.

(92) Fung, K. H.; Imre, D. G.; Tang, I. N. Detection Limits for Sulfates and Nitrates in Aerosol Particles by Raman Spectroscopy. *J. Aerosol Sci.* **1994**, *25* (3), 479–485.

(93) Kalume, A.; Beresnev, L. A.; Santarpia, J.; Pan, Y.-L. Detection and Characterization of Chemical Aerosol Using Laser-Trapping Single-Particle Raman Spectroscopy. *Appl. Opt.* **2017**, *56* (23), 6577.

(94) Price, H. C.; Murray, B. J.; Mattsson, J.; O'Sullivan, D.; Wilson, T. W.; Baustian, K. J.; Benning, L. G. Quantifying Water Diffusion in High-Viscosity and Glassy Aqueous Solutions Using a Raman Isotope Tracer Method. *Atmos. Chem. Phys.* **2014**, *14* (8), 3817–3830.

(95) Rindelaub, J. D.; Craig, R. L.; Nandy, L.; Bondy, A. L.; Dutcher, C. S.; Shepson, P. B.; Ault, A. P. Direct Measurement of PH in Individual Particles via Raman Microspectroscopy and Variation in Acidity with Relative Humidity. *J. Phys. Chem. A* **2016**, *120* (6), 911–917.

(96) Huang, Q.; Wei, H.; Marr, L. C.; Vikesland, P. J. Direct Quantification of the Effect of Ammonium on Aerosol Droplet PH. *Environ. Sci. Technol.* **2021**, *55* (1), 778–787.

(97) Suzuki, H.; Matsuzaki, Y.; Muraoka, A.; Tachikawa, M. Raman Spectroscopy of Optically Levitated Supercooled Water Droplet. *J. Chem. Phys.* **2012**, *136*, 234508.

CHAPTER 2: Experimental Methods

2.1: Introduction

In natural environments most aerosol particles and droplets are levitated in the air; therefore, to accurately investigate the physical and chemical properties of aerosols *in-situ*, levitation techniques and non-destructive probing are necessary. The single-particle approach to aerosol science has been developed and improved over the last 40 years to better understand the fate and environmental impacts of atmospheric aerosols.[1] Unlike analyzing ensembles of particles, as most field and laboratory studies, experiments on single particles can provide a detailed picture of physicochemical evolution without averaging different mixing states and sizes of the particles. Important physicochemical properties have been studied in terms of single-particle aerosol or droplet, *e.g.*, hygroscopicity,[2–4] phase state,[5,6] refractive index,[7,8] hydrogen bond interactions,[9,10] water diffusion,[11,12] pH,[13,14] and heterogeneous reactions.[15–17]

To further investigate the physics and chemistry of atmospheric aerosols at the single-particle level, an EDB equipped with environment-control features and dual-laser beam (266 and 532 nm) spectroscopy setup has been developed. A single charged particle or droplet can be levitated inside the trap for up to 3 days at controlled relative humidity (RH) and temperature for spectroscopic observation. The chemical composition of the droplet can be characterized by analyzing vibrational the vibrational spectrum through laser Raman spectroscopy by 532 nm probe beam, thus enabling real-time monitoring of chemical reactions in a single droplet. In addition, 266 nm irradiation can induce photochemical reactions in the droplets. The phase and size of the trapped particle were determined by Mie scattering imaging (MSI), which arises from the resonant interaction between incoming probe beam and the spherical particle. [18–20]

In this chapter, the theoretical principles of the EDB are described to provide detailed explanation of how a charged particle can be stably trapped in oscillating electric field. Then, the theoretical background for Raman spectroscopy is discussed from both classical and quantum mechanical perspectives. Lastly, fundamentals of MSI are examined in terms of the geometrical optics approximation. The theoretical development of each experimental technique is followed by a section showing practical applications and data acquisition procedures in the laboratory setting.

2.2: Electrodynamic Balance

2.2.1: Theory of Electrodynamic Levitation

The electrode geometry of EDB used for the experiments in this thesis is based on the open-electrode configuration by Schlemmer *et al.*,[21] as later characterized by Trevitt *et al.*[22,23] Electrodynamic levitation of charged particles or droplets is achieved by oscillating quadrupole electric fields. The geometric configurations of EDBs are designed to provide sinusoidally time varying forces to the droplet, where the strengths are proportional to the distance from a center.[24] In this special case, the electric potential of oscillating quadrupole field can be given in cylindrical coordinates as

$$\phi_{r,z} = \frac{\phi_0}{r_0^2}(r^2 - 2z^2) \tag{2.1}$$

where r_0 is a trap-specific geometric parameter, ϕ_0 is the AC driving potential applied to hyperbolic electrodes. Here, ϕ_0 can be given as

$$\phi_0(t) = U_0 + V_0 \sin(\Omega t) \tag{2.2}$$

where $\Omega = 2\pi f$ is the angular frequency in hertz (Hz), U_0 is the DC offset voltage applied, and V_0 is the voltage of the applied AC field.

Under this condition, Mathieu's differential equation can be used to describe the equations of motion of charged particles in electric field in terms of cylindrical coordinates.[1,21]

$$\frac{d^2u}{dx^2} + (a - 2q\cos 2x)u = 0 \tag{2.3}$$

In equation 2.3, u represents either z or r axis, and $x = \Omega t/2$ where Ω is angular frequency and t is time. The dimensionless constants (a and q) in equation 2.3 are referred to as stability parameters given as,

$$a_z = -2a_r = -\frac{8qU_0}{mz_0^2\Omega^2} \tag{2.4}$$

and

$$q_z = -2q_r = -\frac{4qV_0}{mz_0^2\Omega^2} \tag{2.5}$$

where q is the charge of the particle and m is the mass of the particle.[21,24]

Now, the equation of motion (equation 2.3) is solvable, and the solution can be expressed as an infinite series of harmonic functions, each proportional to exp $(\pm\beta_{r,z}\Omega/2t)$, where $\beta_{r,z}$ are functions of stability parameters $a_{r,z}$ and $q_{r,z}$.[24] When the voltage of the AC and offset DC fields are given, i.e., U_0 and V_0 are known, the two fundamental frequencies of orthogonal r and z components $\omega_{r,z} = \beta_{r,z}\Omega/2$ govern the motion of the particle. These two frequencies (ω_r and ω_z) are often referred to as secular frequencies of motion. By measuring the secular frequencies of motion, mass-to-charge ratio (*m/q*) of the oscillating particle can be determined. In the adiabatic limit, where the amplitude of micromotions is negligible compared to the amplitude of the secular motion, motion of the trapped particle can be described by an effective harmonic potential V_{eff} in *z*-direction.[21]

$$V_{eff} = \frac{1}{2}m\omega_z^2 z^2 \tag{2.6}$$

In this case, the relationship between $\omega_{r,z}$ and *m/q* can be given simply by using stability parameters ($q_{r,z}$),

$$\omega_z = \frac{|q_z|\,\Omega}{2\sqrt{2}} = \frac{\sqrt{2}V_0}{z_0^2\Omega}\left(\frac{m}{q}\right)^{-1} \tag{2.7}$$

and

$$\omega_z = 2\omega_r. \tag{2.8}$$

Using the relationships above, *m/q* can be expressed as equations 2.9 and 2.10.[21,23]

$$\frac{m}{q} = \frac{V_0}{\sqrt{2}\omega_r\Omega z_0^2} \tag{2.9}$$

$$\frac{m}{q} = \sqrt{2}\frac{V_0}{\omega_z\Omega z_0^2} \tag{2.10}$$

Therefore, *m/q* of the trapped particle can be obtained by measuring secular frequencies (ω_r or ω_z) of particle in oscillatory motion and knowing physical parameters (Ω, z_0, and V_0) of the quadrupole electric field.[21–26]

In case where the mass of the charged particles become sufficiently large, an external DC potential is required to compensate the gravitational force exerted on the particle. Here, the voltage of applied external DC (V_{DC}) can be used to determine *m/q* for the levitated particle.[27,28]

$$\frac{m}{q} = \frac{C_0 V_{DC}}{2 g z_0} \tag{2.11}$$

In equation 2.11, g is the acceleration of gravity, and C_0 is an empirical constant dependent on the specific geometry of the EDB. Comparing equation 2.11 with equations 2.9 and 2.10 shows that the *m/q* of the levitated particle can be determined without measuring the secular frequencies when the particle is heavy enough to require external DC potential.[29]

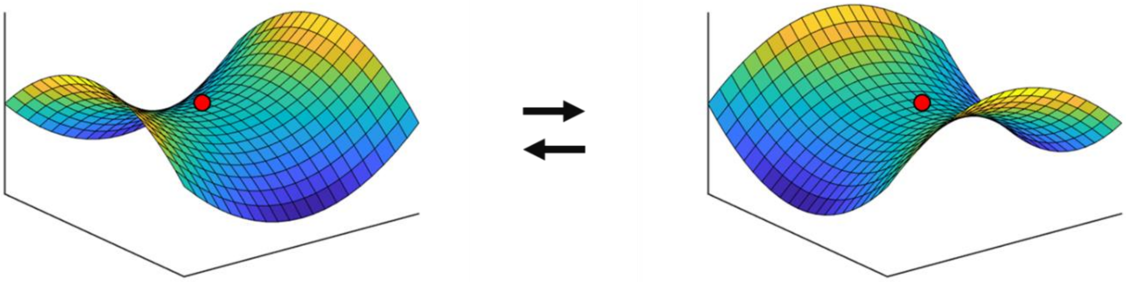

Figure 2.1: Graphical description of charged particle (red circle) trapped in the saddle point of oscillating quadrupole electric field.

2.2.2: Layout of the Electrodynamic Balance

Although the theoretical and experimental development of EDBs have been significantly advanced over the decades, none of them are available commercially today. Therefore, the EDB used in this thesis was built in-house and upgraded over the past five years to investigate various aspects of aerosol chemistry and physics.[30] As noted before, the geometry of the EDB used in this thesis is based on the open-electrode configuration by Schlemmer *et al.*[21] and Trevitt et al.[22,23]

Figure 2.2 shows the geometry of the EDB including all electrodes and the configuration of the charged droplet generator. For levitation of a charged droplet, two conical-shaped endcap electrodes carry the high-voltage (1.5 kV) AC potential. The sine wave with 2 V (rms) amplitude is generated by the Agilent Model 32210a waveform generator (synthesizer). This signal is then amplified to 10 V by a Krohn-Hite Model 7602M pre-amplifier, followed by high-voltage amplification to 1.5 kV by Matsusada AMS 1.5B20 HV amplifier. The synthesizer is connected to the data acquisition (DAQ) PC, enabling control of the frequency and amplitude of the initial sine wave. The connections for high-voltage AC potential generation are shown in **Figure 2.3**. The typical AC frequency range for droplet trapping is 60 to 180 Hz. In general, a lower AC frequency is required for larger droplets (higher mass), and higher frequency is needed for smaller droplets (as determined by equations 2.7 and 2.8). The endcap electrodes have a 1.5 mm cylindrical channel at the center, which enables a laser beam to pass through. This channel provides a pathway for calibration and alignment of the droplet when a 633 nm He-Ne laser is used, or for photoexcitation when the 266 nm output of the Nd:YAG laser is used.

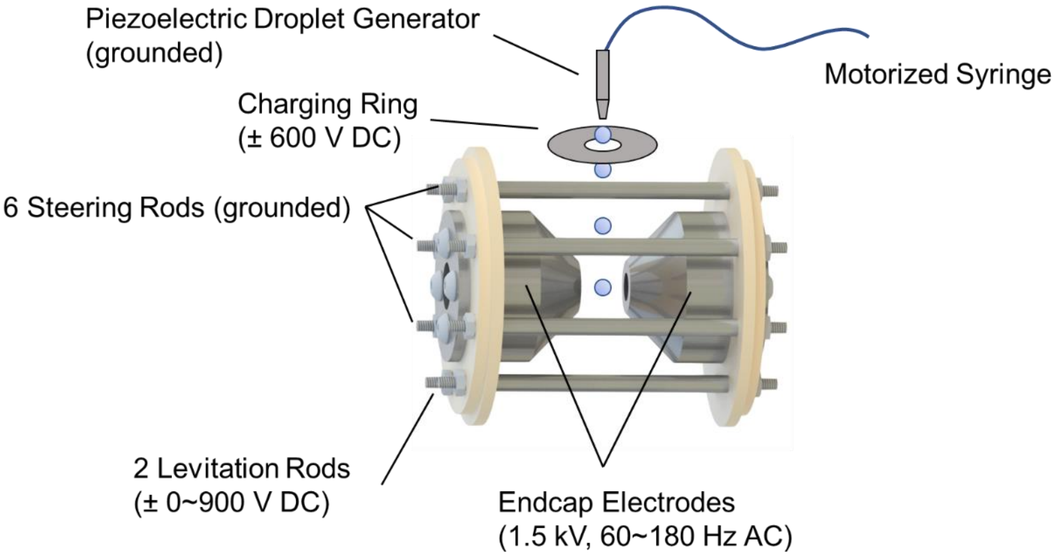

Figure 2.2: Schematic representation of the EDB with a charged droplet generator.

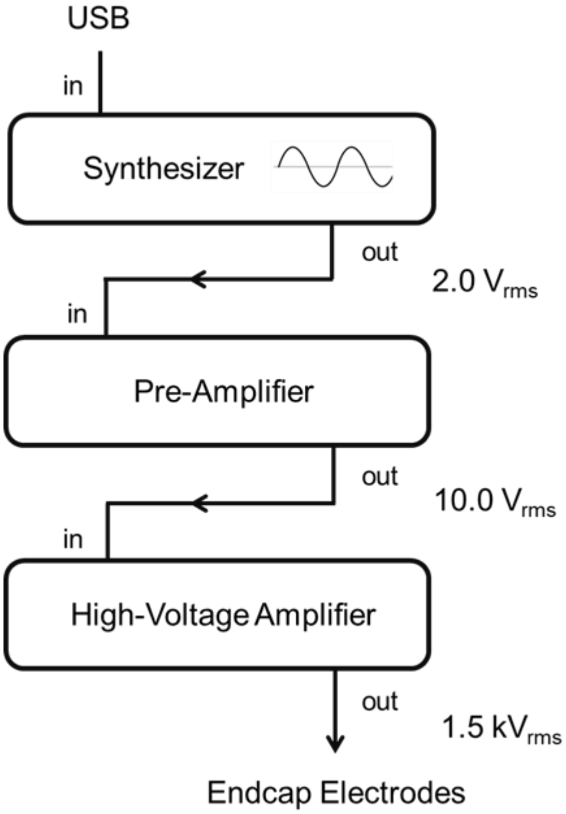

Figure 2.3: Electrical connections for high-voltage AC potentials applied to the endcap electrodes.

Additionally, there are eight rod electrodes mounted on the ceramic discs, surrounding the endcap electrodes. Six of the eight rod electrodes (steering rods) are electrically grounded and stabilize the alternating quadrupole electric field inside the trap. Two rod electrodes below the endcap electrodes provide compensation to the gravitational force applied to the charged droplet using a DC potential applied with the same polarity of the droplet charge. The DC potential for droplet levitation is provided by a SRS PS350 power supply, and the amplitude varies from 0 to ±900 V depending on the mass of the droplet.

Droplets introduced to the EDB are generated on-demand by the droplet generator module (Engineering Arts DE03) which controls the motorized syringe and piezoelectric dispense head with the tip. Overall layout for droplet generation is shown in **Figure 2.4.** The motorized syringe is equipped with a stepping motor and a 3-way valve which connects two of the three input/output ports. One of the ports is connected with the H_2O reservoir. All the tubes are filled with water from the reservoir. To generate droplets from the sample solution, a small volume of the solution (~20 μL) is aspirated into the dispense head with the diameter of 24, 40, or 67 μm diameter depending on the desired droplet size (bigger droplets with bigger diameter dispense head). A pulse signal is then sent from the computer to the piezoelectric drivers lined up along the dispense head to fire droplets into the trap. Typical conditions for droplet firing use a pulse frequency of 12.75 kHz and 10 inbursts per trigger, i.e., 10 droplets are generated on one-click.

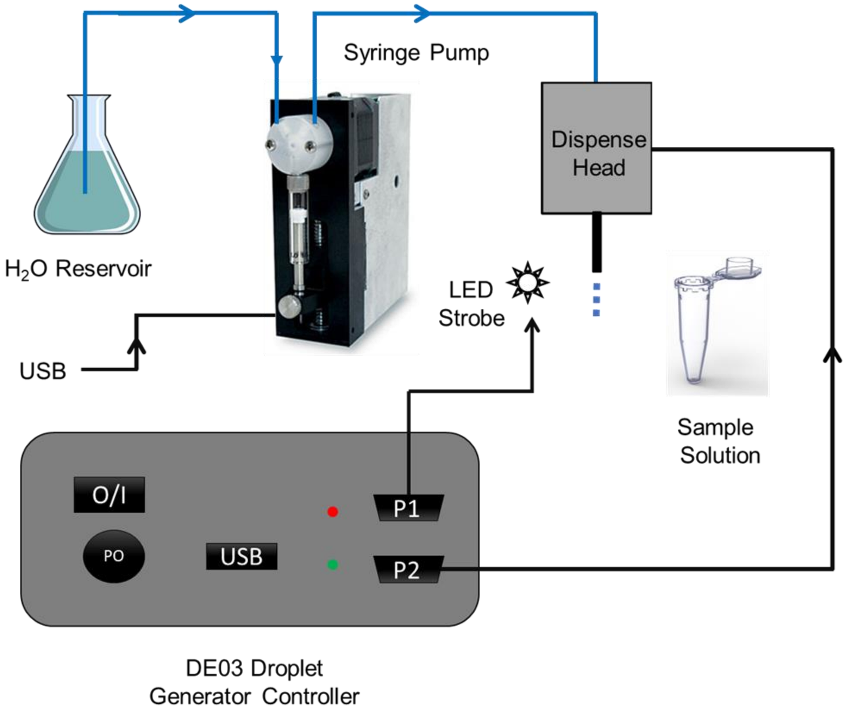

Figure 2.4: Droplet generator with motorized syringe and USB controller.

The metallic tip of piezoelectric droplet generator is grounded while a DC potential is applied to the inductive charging ring right below the tip using a SRS PS310 power supply. As droplets are generated from the tip, the electric field between charging ring and grounded tip induces an ionic imbalance in the solution, charging the droplets as they are shot through the tip.[20,31] Typical amplitude for inductive charging of droplets is ±600 V. It is important to set opposite polarities of DC potential on inductive charging ring and levitation rods to provide Coulombic repulsion between the charged droplet and levitation rods.

As the droplets are introduced into the EDB chamber, they equilibrate to the surrounding RH of the inner-chamber environment. The RH is controlled by using three digital mass flow controllers (MFCs, Alicat MC-500sccm) which mix dry nitrogen (N_2) with the humidified N_2 from the headspace of bubblers containing H_2O or D_2O. The layout for the humidity controller system is shown in **Figure 2.5**. MFCs are connected to the DAQ PC via USB and the mixing ratio of dry to humid N_2 as well as the total flow rate can be controlled using LabVIEW software. The H_2O/D_2O switching is achieved by three solenoid valves as shown in **Figure 2.5**. Valves 1 and 2 serve as an on-and-off switch for D_2O bubbler while valve 3 switches the coupling between H_2O and D_2O with exhaust and input channel to the EDB chamber. The three solenoid valves are connected to the DAQ PC by a relay system and controlled by the LabVIEW software as well. The relays in the circuit can be activated by the 5 V signal from the National Instrument USB-6008 multifunction I/O device.

The dry and humid mixed N_2 with desired RH is directed through copper tubing wrapped around and welded to a copper standoff in thermal contact with a Stirling cryocooler (Sunpower Cryotel CT) for a temperature-control capability. The RH and temperature inside the EDB are measured using a capacitive thin film polymer RH and temperature probe (Vaisala HMP110,

±1.5 % accuracy) placed into the Teflon channel approximately 25 mm above the trap where the airflow is passed directly over the sensor to the exhaust.

Once the droplets are fired, the AC frequency of the endcap electrodes and DC levitation voltage are adjusted to successfully trap a single droplet at the focus of the 532 nm laser. Typical trapping conditions for medium-sized (~50 µm diameter) droplets are 120 Hz for AC frequency and ±250 V for DC levitation. When the trapped droplet is located at the focus of 532 nm laser, light scattering from the droplet reaches a maximum intensity. The image of the droplet with light scattering from the laser is shown in **Figure 2.6**. An ethernet-interfaced CCD camera (Allied Vision Mako GigE) is used to stream the image of the droplet real-time to the DAQ PC. The computer-controlled motorized shutter is opened when the droplets are introduced into the trap and closed once the droplet is trapped stably, to isolate the environment of the trap from the laboratory.

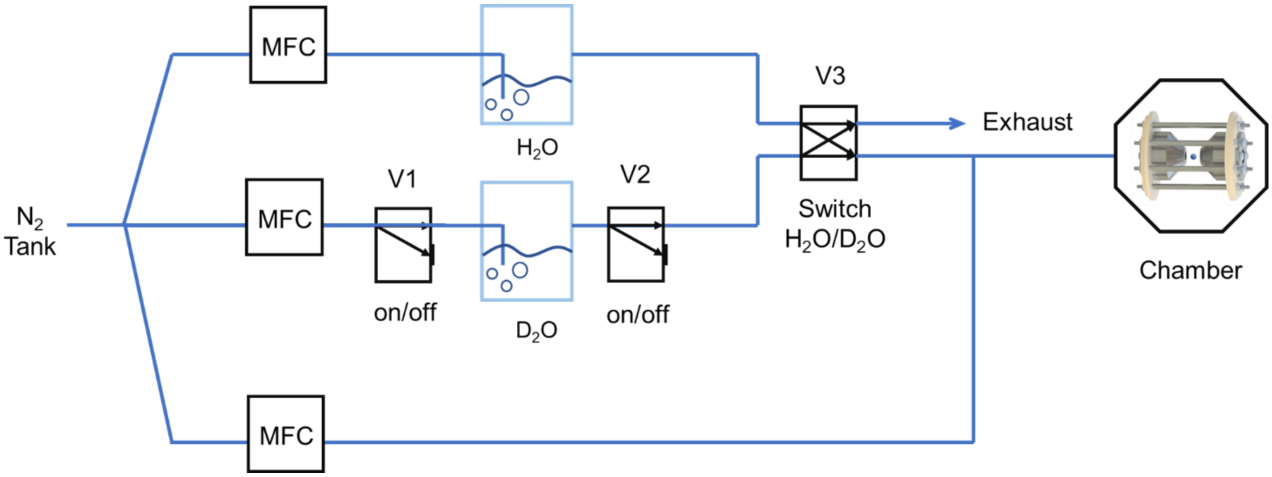

Figure 2.5: Layout for automated humidity and H_2O/D_2O control.

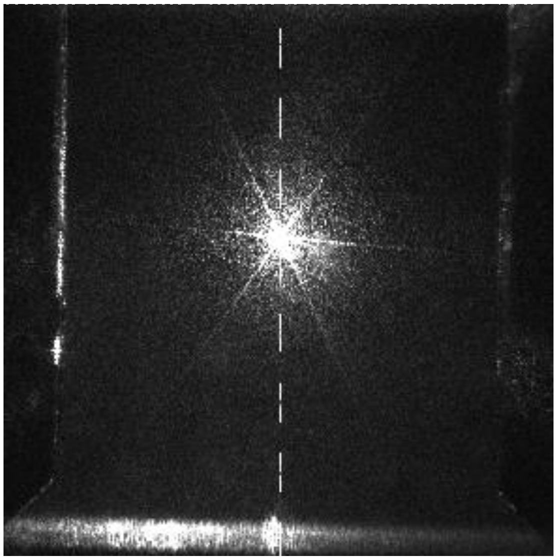

Figure 2.6: The real-time image of the trapped droplet located at the focus of 532 nm laser. The path of the laser is seen as a dashed line along the center of the image. The scattered light shows hexagonal diffraction spikes due to the shape of the camera aperture.[32] Two endcap electrodes can be seen on the left and right side of the image.

2.3: Aerosol Spectroscopy

2.3.1: Theory of Raman Spectroscopy

Raman scattering is a fundamental form of molecular spectroscopy.[33] Unlike elastic Rayleigh scattering, Raman scattering involves changes in energy in the process, due to the interaction between light-induced polarizability change and molecular motion. Raman scattered light can gain or lose the energy with respect to the incoming irradiation, and the amount of change in energy is related to the energy difference between the Raman-active vibronic states of the molecule.[34,35] In this thesis, vibrational Raman scattering caused by the change in the polarizability of the molecule with respect to its vibrational motion will be mainly discussed. The energy-level diagrams for Rayleigh and Raman scattering (Stokes and anti-Stokes shifted) are given in **Figure 2.7**.

To understand how the interaction between light (electromagnetic wave) and molecules produces Raman scattering, it is necessary to picture the dipole moment of the molecule with the external electric field. Using a Taylor's series expansion, the dipole moment of the molecule can be expanded in a power series in the applied electric field ($\vec{E}$),

$$\vec{\mu} = \vec{\mu}_0 + \alpha \cdot \vec{E} + \frac{1}{2}\beta : \vec{E}\vec{E} + \cdots \tag{2.12}$$

where $\vec{\mu}$ is the net dipole moment of the molecule, $\vec{\mu}_0$ is the permanent dipole moment, and the second and third terms describe induced dipole moments depend on polarizability (α) and hyperpolarizability (β). Raman scattering can be explained by the second (linear) term of the equation 2.12, where the polarizability α is involved. α is a second-rank tensor whose components $\rho\sigma$ terms are defined as equation 2.13.[35]

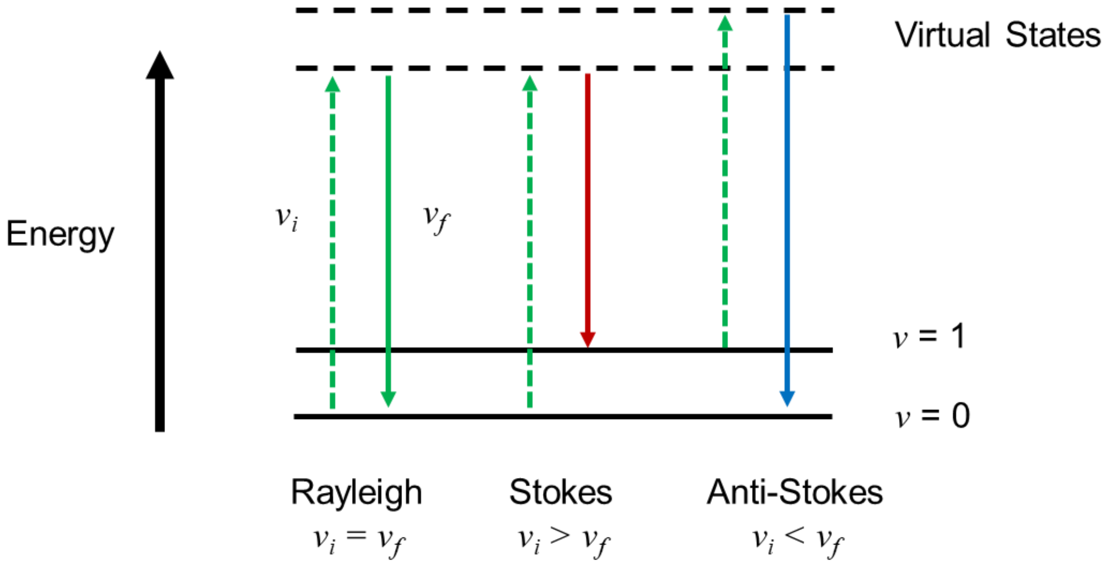

Figure 2.7: Energy-level diagram for Rayleigh (elastic) scattering and Raman scattering for vibrational transitions of a molecule from $v = 0$ to $v = 1$. The green dashed line represents excitation light with the energy $h\nu_i$. The resulting Raman scattering can be lower in energy (Stokes-shifted) or higher in energy (anti-Stokes shifted).

$$\alpha_{\rho\sigma} = \left(\frac{\partial \mu_\rho}{\partial E_\sigma}\right)_0 \tag{2.13}$$

The polarizability of an atom or molecule describes the response of the electron cloud to the influence of an external electric field. Therefore, large molecules with small permanent dipole moments are more polarizable than small molecules with large permanent dipole moments.[36,37]

In molecules, the ability of the external field to induce a dipole moment depends on the vibrational frequencies because chemical bonds have their own natural vibrations. Using the harmonic oscillator approximation, a molecular vibration can be viewed as a motion of a spring. Then, Hooke's law for restoring force (F) can be applied to the chemical bond,

$$F = -kx = -m\omega_0^2 x \tag{2.14}$$

where the force constant k is related to the mass and the harmonic frequency ω_0.[33,38] If a single electron along the bond axis is displaced by x by the external field E, the induced moment μ can be given as

$$\mu = -ex = \alpha E \tag{2.15}$$

using the second term of equation 2.12. When the restoring force (F) is balanced by the electric force $-eE$, the polarizability (α) can be expressed as a function of vibrational frequency.

$$\alpha = \frac{e^2}{m\omega_0^2} \tag{2.16}$$

Here, when the external electric field is a function of time,

$$E(t) = E_0 \exp[i(ky - \omega t)] \tag{2.17}$$

the equation of motion of a vibrating electron with external field can be given as

$$F = m\frac{d^2x}{dt^2} = -eE(t) - m\omega_0^2 x(t) - \Gamma\frac{dx}{dt} \tag{2.18}$$

In this equation the net force F has three contributions, the first term as an electric force, the second term as a restoring force, and the third term a frictional force. The constant Γ represents a dampening that slows down the oscillation.[35]

If the external field is polarized in the x direction and propagates in the y-direction, the displacement of the electron due to the field will be in x-direction. With this observation in mind, the solution for displacement x can be given as

$$x(t) = x_0 \exp[i(ky - \omega t)]. \tag{2.19}$$

Plugging equation 2.19 into equation 2.18 leads to equation 2.20

$$x(t) = \frac{-(e/m)E(t)}{\omega_0^2 - \omega^2 - i\omega/\tau} \tag{2.20}$$

where $\tau = m/\Gamma$ is the relaxation time for damping of the dipole oscillation. Expressing this result in terms of polarizability (α) and generalizing by total of N electrons divided into $f_j N$ groups having harmonic frequencies ω_j yield equation 2.21.

$$\alpha(\omega) = \frac{e^2}{m}\sum_j \frac{f_j}{\omega_j^2 - \omega^2 - i\omega/\tau} \tag{2.21}$$

This is the classical description of polarizability where the electron is interacting with the external time-dependent electric field. It is clear that the value of α becomes large when the frequency of external field (ω) is in resonance with one of the inherent vibrational frequencies of the molecule (ω_j). The derivation of equation 2.21 given here provides the groundwork for the theory behind relationship between the intensity of Raman scattering and molecular vibration.[35]

From a quantum mechanical point of view, the Kramers-Heisenberg-Dirac (KHD) equation can be used to describe the transition polarizability tensor $(\alpha_{\rho\sigma})_{if}$

$$(\alpha_{\rho\sigma})_{if} = \frac{1}{\hbar}\sum_{n}\left[\frac{\langle i|\mu_\sigma|n\rangle\langle n|\mu_\rho|f\rangle}{\omega + \omega_{nf} + i\Gamma_n} - \frac{\langle i|\mu_\rho|n\rangle\langle n|\mu_\sigma|f\rangle}{\omega - \omega_{ni} - i\Gamma_n}\right] \equiv \langle i|\hat{\alpha}_{\rho\sigma}|f\rangle \qquad (2.22)$$

where $\hbar$ is Planck's constant (h) divided by 2π, and the polarizability tensor with ρ and σ Cartesian directions is connecting vibrational states i and f.[34] Equation 2.21 has a similar physical interpretation with equation 2.20, *i.e.*, the transition polarizability becomes large when the frequency of incident light ω is close to that of a $i \rightarrow n$ transition ω_{ni}. The case when the value of ω is close to the value of ω_{ni} is referred as a resonance condition.[35,39]

The transition operator ($\hat{\alpha}_{\rho\sigma}$) for Raman scattering in a polyatomic non-linear molecule with N atoms is given as equation 2.23

$$\hat{\alpha}_{\rho\sigma} = \sum_{i=1}^{3N-6}\left(\frac{\partial\alpha_{\rho\sigma}}{\partial Q_i}\right)_0 Q_i \qquad (2.23)$$

where Q_i is the normal coordinate of i-th normal mode, and there are $3N - 6$ normal modes. For linear molecules, the total number of normal modes would be $3N - 5$. The subscript zero means the derivatives are evaluated at zero electric field. The Raman activity of a vibration depends on $(\partial\alpha/\partial Q)_0$, the change in polarizability during the vibrational motion, *i.e.*, $(\partial\alpha/\partial Q)_0$ of a molecular vibration mush have be non-zero value to be Raman-active.[33] **Figure 2.8** depicts two cases of polarizability versus normal coordinate during vibration. The slope of the graph at Q_0 must be non-zero to have Raman activity. For example, the slope at **Figure 2.8A** is zero, thus this vibration is Raman inactive, and the vibration in **Figure 2.8B** is Raman active because the slope has non-zero value. [33]

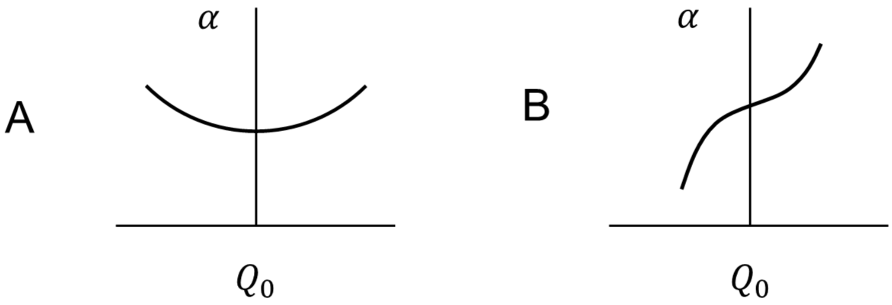

Figure 2.8: Polarizability versus normal coordinate for (A) Raman inactive and (B) Raman active normal modes.

When the energy of incident radiation has far less energy than the resonance condition (off-resonance limit), the expression for polarizability can be simplified as

$$(\alpha_{\rho\sigma})_{\mathrm{v}'\mathrm{v}''} = \frac{1}{\hbar}\sum_{n}\left[\frac{\left(\mu_{ge}^{0}\right)_{\rho}\left(\mu_{ge}^{(i)}\right)_{\sigma}\langle \mathrm{v}'|Q_i|\mathrm{v}''\rangle}{\omega_0 + \omega_{eg}} - \frac{\left(\mu_{ge}^{0}\right)_{\sigma}\left(\mu_{ge}^{(i)}\right)_{\rho}\langle \mathrm{v}'|Q_i|\mathrm{v}''\rangle}{\omega_0 - \omega_{eg}}\right]$$

$$\equiv \alpha_{\rho\sigma}^{(i)}\langle \mathrm{v}'|Q_i|\mathrm{v}''\rangle \tag{2.24}$$

where the transition dipole moment from the ground to excited electronic state according to Franck-Condon approximation is given as μ_{ge}^{0}, the derivative of transition dipole moment is defined as $\mu_{ge}^{(i)}$, and index of v represents vibrational quantum numbers. Since the eigenfunctions of harmonic oscillator form an orthogonal basis set,[40,41] $\langle \mathrm{v}'|Q_i|\mathrm{v}''\rangle$ vanishes unless $\mathrm{v}'' = \mathrm{v}' \pm 1$, thus giving the selection rule for Raman scattering ($\Delta\nu = \pm 1$). Finally, the matrix element of the normal coordinate contributing to the polarizability is for Stokes-shifted Raman scattering when $\mathrm{v}'' = \mathrm{v}' + 1$ and anti-Stokes when $\mathrm{v}'' = \mathrm{v}' - 1$ (**Figure 2.7**).[34,35]

In conclusion, Raman spectroscopy uses the inelastic scattered light which is shifted in frequency (energy) from the incident radiation by the vibrational energy that is gained or lost in the molecule. Therefore, measured Raman spectra provide information about the structure of molecules and the intermolecular interactions in Raman shift as a unit in wavenumber (cm^{-1}). This technique is non-destructive because the energy of irradiation – usually laser – is far lower than the energy of electronic excitation of small molecules of interest.[42] For these reasons, Raman spectroscopy can be considered as one of the ideal tools to probe physical and chemical properties of levitated aerosol particles or droplets in real-time.[9,11,43,44]

2.3.2: Mie Scattering Imaging

The phase and size of the trapped single particles or droplets can be measured from the angular scattering pattern of elastic scattering intensity. The interaction of light with spherical particles was described by Gustav Mie, and the theoretical treatment is referred to as Mie theory.[45] According to the Mie theory, the amplitude of an elastically scattered photon (*I*) is dependent on the scattering angle (*θ*) and the size parameter of the sphere defined as $x = 2\pi r/\lambda$ where r is the radius, m is the refractive index of the sphere, and λ is the wavelength of light (electromagnetic wave). This relationship can be expressed as equation 2.22.

$$I(x,m,\theta) = \sum_{n=1}^{N} \frac{2n+1}{n(n+1)} [a_n(x,m)\pi_n(\cos\theta) + b_n(x,m)\tau_n(\cos\theta)] \qquad (2.25)$$

Here, $a_n(x,m)$ and $b_n(x,m)$ are defined as scattering coefficients, and $\pi_n(\cos\theta)$ and $\tau_n(\cos\theta)$ are angular coefficients. Using a 2D CCD detector, light scattered from the spherical particle or droplet can be collected with 20 – 30° solid angle then information on size and refractive index can be obtained through Mie theory.

Mie theory is developed by applying Maxwell's equations to the sphere, and a somewhat rigorous calculation is needed to derive the planar wave equations (light) in spherical harmonics (particle).[46] However, when the size of the sphere is significantly larger than the wavelength of light, the geometric optics approximation can be made for simpler applications of Mie theory.[18] The geometric optics approximation treats the spherical particle as a spherical lens and the path of the incoming light can be describes in terms of partial reflection and refraction for each ray that interacts with the particle. Glantsching *et al*. showed the angular scattering intensity of water droplets with diameter 10 and 50 μm calculated using geometrical optics approximation agrees well with the Mie theory.[18] According to the geometrical optics approximation, the radius of the droplet can be determined by equation 2.23

$$r = \frac{\lambda}{\Delta\theta}\left(\cos\frac{\theta}{2} + \frac{n\sin\frac{\theta}{2}}{\sqrt{1 + n^2 - 2n\cos\frac{\theta}{2}}}\right)^{-1} \tag{2.26}$$

where $\Delta\theta$ (radian) is the spacing between light scattering pattern, θ is the median scattering angle, and n is the refractive index. Equation 2.23 can be applied to the determination of spherical droplet size by measuring $\Delta\theta$ from the image collected from CCD camera. This method of droplet-size measurement is referred to as Mie scattering imaging (MSI). An example of scattering image of the levitated droplet and processing is shown in **Figure 2.9**. The intensity values of the 2D image array are summed along the vertical axis of the image to produce the intensity spectrum as a function of scattering angle as shown in the plot below the scattering image in **Figure 2.9**. The intensity spectrum is then processed by a fast Fourier transform (FFT) to convert scattering angle-domain information into the frequency-domain. As a result of the FFT, frequency ($\Delta\theta$, degree^{-1}) of the scattering image can be obtained my locating the maximum magnitude of the frequency-domain plot (right-hand side of **Figure 2.9**). The computational processing of the geometric optics approximation with FFT is less demanding than the Mie theory calculations, enabling real-time size determination of a trapped droplet when refractive index (n) of the droplet is known. The geometrical optics approximation of Mie theory and MSI has been used in various aerosol studies, such as measuring evaporation rate of volatile components,[47] size determination of small particles,[19] vapor pressures of organic-inorganic mixture droplets,[48] and hygroscopicity of organic aerosols.[4]

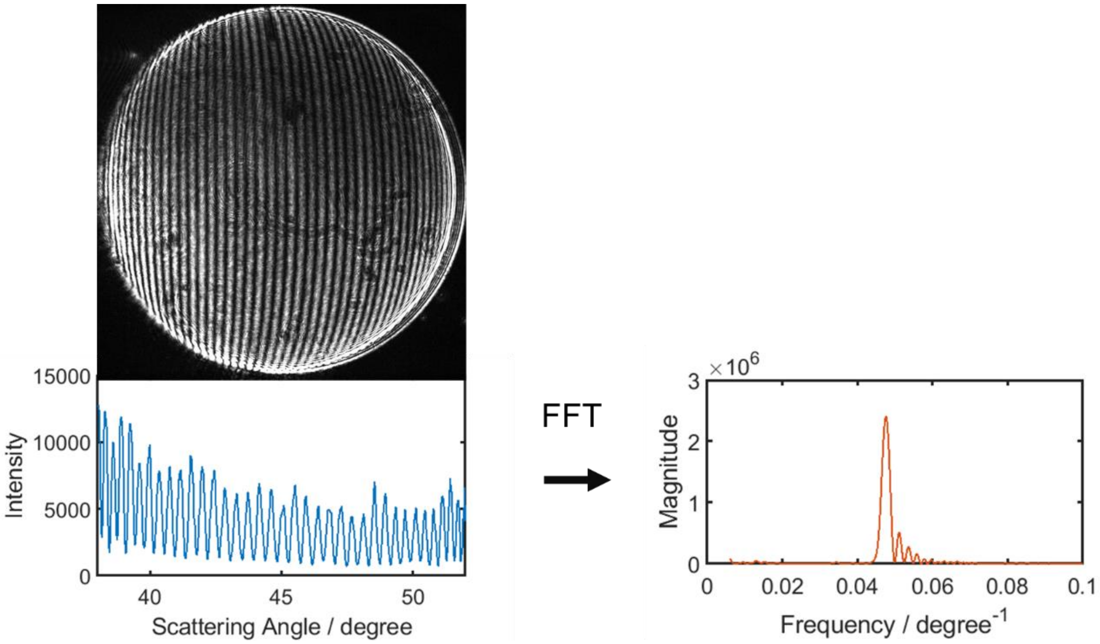

Figure 2.9: Mie scattering imaging (MSI) of a levitated droplet.

2.3.3: Laser and Spectrometer Setup

The environmental-controlled EDB is equipped with a dual-beam laser spectrometer setup that enables in-situ monitoring of droplet size by MSI, chemical compositions as well as intermolecular interactions by Raman spectroscopy, and studies of single-droplet photochemistry using the 266 nm laser. The layout of EDB with laser paths and optics are shown in **Figure 2.10**. The 266 and 532 nm output (4th and 2nd harmonic) of pulsed Nd:YAG laser (RPMC Wedge XF, 3.5 µs pulse width, 80kHz repetition rate) irradiate the levitated droplet perpendicular to each other. The laser produces both output wavelengths simultaneously, and a motorized filter flip (Thorlabs MFF 101) mounted with 266 nm long-pass filter (Semrock RazorEdge U-grade) is used as a switch for 266 nm output. When UV irradiation is not required, the 266 nm output is filtered out and only 532 nm output is directed to the trap. A harmonic beamsplitter (Thorlabs HBSY134) is located past the motorized filter flip, where the 266 nm beam is reflected, and the 532 nm beam is transmitted. After the harmonic beamsplitter, the 532 nm beam is directed to the trap by Nd:YAG mirror (NB1-K13) and 532 nm dichroic beamsplitter (Semrock RazorEdge). The dichroic beamsplitter serves as a mirror for 532 nm beam, thus the path of the beam is aligned to the droplet by adjusting the Nd:YAG mirror and the beamsplitter. The 532 nm beam is then focused on the levitated droplet by a focusing lens (Thorlabs LA1590 0.5" F = 25.0 mm) attached to the stainless-steel trap housing.

The droplet irradiated by the 532 nm laser produces elastic (Mie) and inelastic (Stokes-shifted Raman) scattering, and both signals contain valuable information. The Mie scattering image is collimated by a lens attached to the trap housing, then collected by a CCD camera (Allied

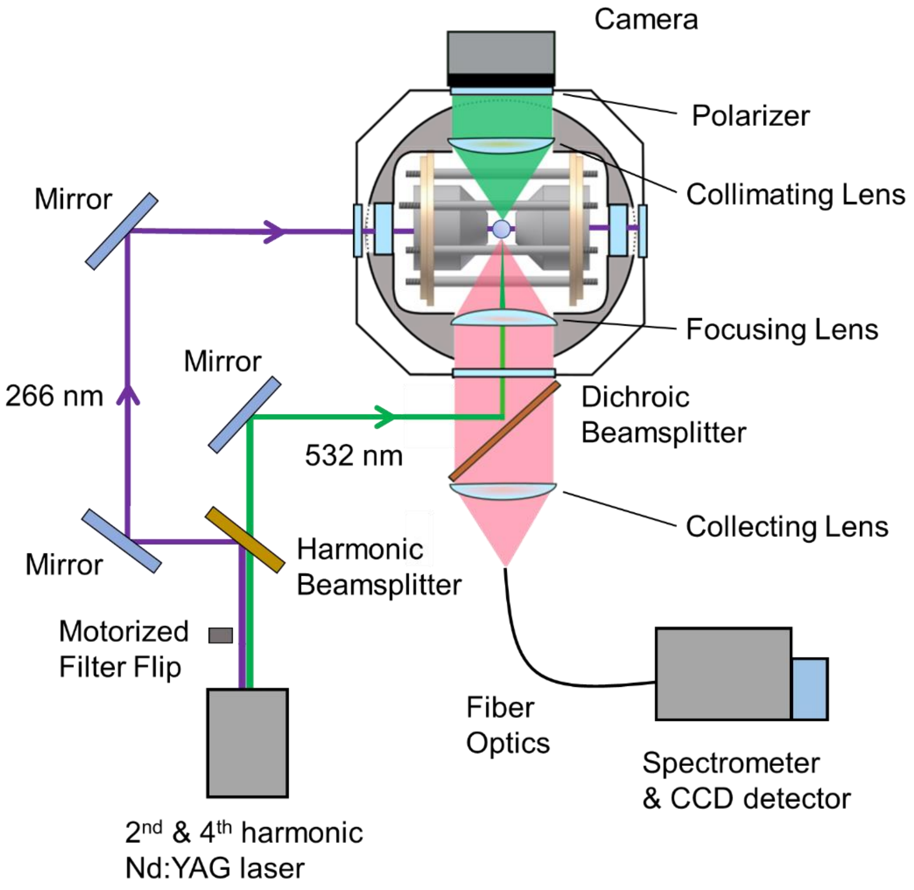

Figure 2.10: The EDB with Raman spectroscopy and MSI setup.

Vision Mako GigE) equipped with a polarizer which enhances the definition of the image. The collection angle for Mie scattering is 135° with respect to the laser path (45° forward) and the solid angle is 16.3°. An example of the image collected by the CCD is shown in **Figure 2.9**. Because the regular pattern is observed only when the droplet is perfectly spherical, information about the phase can be achieved from the shape of the pattern. For example, when the droplet undergoes efflorescence, the Mie scattering image no longer shows a regular fringe pattern, instead a noisy laser-speckled signal is observed. When the droplet is in the liquid phase, *i.e.*, spherical shape, the size of the droplet can be measured by MSI described in **Figure 2.9** and equation 2.23. This method of FFT processing the image can achieve an accuracy of ± 100 nm for droplets.[4]

The back-scattered Raman signal is collimated by the focusing lens attached to the trap housing, focused by a F = 100 mm plano-convex lens (Thorlabs LA1251-A), and collected to the multimode optical fiber (Thorlabs BFL105LS02 round-to-linear, ϕ105 μm). The optical fiber is connected to the f/4.1 spectrometer (Horiba iHR 320) with a fiber adapter (Horiba 220F). The spectrometer is equipped with a turret with three diffraction gratings (600 g/mm & 500 nm blazed, 1200 g/mm & 500 nm blazed, and 1200 g/mm holographic). 600 g/mm grating was used for most of the measurements because it can cover the whole Raman spectral range from 300 cm^{-1} to 4000 cm^{-1}. The spectrum is collected by the TE-cooled, back-illuminated CCD detector (Horiba SynapsePlus BIUV) with 2048 x 512 pixels. The exposure time for Raman spectral measurements was 10 – 30 s, depending on the desired signal-to-noise ratio (S/N). Raman spectra of bulk samples (solution or solids) can be measured by inserting an NMR tube filled with sample into the trap. The calibration of the Raman spectrum was made by using four sharp Raman peaks of solid naphthalene (Raman shift: 513.8, 763.8, 1382.2, and 3056.4 cm^{-1}) as shown in **Figure 2.11**. These four peaks were used as reference points, and a linear regression was made between the corresponding pixel numbers and wavelength of the peaks converted from wavenumbers.

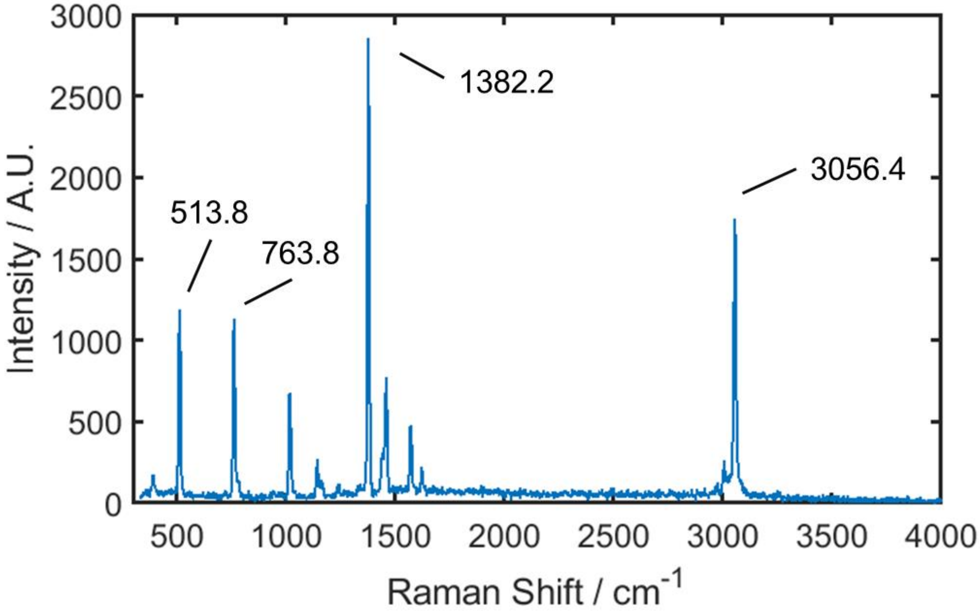

Figure 2.11: Raman spectrum of solid naphthalene used for CCD calibration.

Photochemistry of droplets with UV-absorbing molecules can be triggered using the 266 nm beam of the Nd:YAG laser. When the motorized filter is lifted, the 266 nm output is reflected by the harmonic beamsplitter and directed to the trap by two laser-line mirrors (NB1-K04) perpendicular to the 532 nm output. The path of the laser is fine adjusted to pass through the holes of the endcap electrodes, so that the droplet is located within the path of the 266 nm beam (**Figure 2.10**). The same path is used for calibration of the position of the levitated droplet and alignment of 532 nm laser with the droplet. For the alignment, 633 nm He-Ne laser (Uniphase Helium-Neon Gas Laser) with two broadband mirrors (Thorlabs BB1-E02) are used. The optimum position of the droplet is determined at where the 633 nm scattering signal measured from the spectrometer is maximum. After the position of the droplet is fixed, the path of 532 nm beam is adjusted for maximum illumination which can be observed from the real-time image collected by the Camera (**Figure 2.6**). Because there is only a single path available passing through two endcap electrodes, mirrors need to be altered according to the desired application (broadband mirror & 633 nm for alignment or laser line mirror & 266 nm for photochemistry).

To summarize, in order to investigate the physical and chemical transformations of aerosols, the single particle levitation technique (EDB) is coupled with spectroscopic capabilities in the work described in this thesis. Droplets of sample solutions can be charged using an piezolelectric droplet generator in conjunction with an inductive charging ring, then introduced into the trap and stabilized by adjusting the AC frequency and amplitude and DC levitation trapping voltages. Once a single droplet is trapped, the 532 nm beam can be used to probe the phase, size, and chemical composition in real-time. The 266 nm beam can further induce photochemical reactions in the droplet in the presence of UV-absorbing molecules. In the following chapters, the applications of the EDB system to studies of physical properties (water diffusion and hydrogen bond interactions) as well as chemical reactions (keto-enol tautomerization and photosensitized reactions of nitrate) of single levitated droplets will be discussed.

References

(1) Davis, E. J. A History of Single Aerosol Particle Levitation. *Aerosol Sci. Technol.* **1997**, *26* (3), 212–254.

(2) Peng, C.; Chan, C. K.; Chow, A. H. L. Hygroscopic Study of Glucose, Citric Acid, and Sorbitol Using an Electrodynamic Balance: Comparison with UNIFAC Predictions. *Aerosol Sci. Technol.* **2001**, *35* (3), 753–758.

(3) Lee, A. K. Y.; Ling, T. Y.; Chan, C. K. Understanding Hygroscopic Growth and Phase Transformation of Aerosols Using Single Particle Raman Spectroscopy in an Electrodynamic Balance. *Faraday Discuss.* **2008**, *137* (852), 245–263.

(4) Marsh, A.; Miles, R. E. H.; Rovelli, G.; Cowling, A. G.; Nandy, L.; Dutcher, C. S.; Reid, J. P. Influence of Organic Compound Functionality on Aerosol Hygroscopicity: Dicarboxylic Acids, Alkyl-Substituents, Sugars and Amino Acids. *Atmos. Chem. Phys.* **2017**, *17* (9), 5583–5599.

(5) Richards, D. S.; Trobaugh, K. L.; Hajek-Herrera, J.; Price, C. L.; Sheldon, C. S.; Davies, J. F.; Davis, R. D. Ion-Molecule Interactions Enable Unexpected Phase Transitions in Organic-Inorganic Aerosol. *Sci. Adv.* **2020**, *6* (47), 1–12.

(6) Huynh, E.; Olinger, A.; Woolley, D.; Kohli, R. K.; Choczynski, J. M.; Davies, J. F.; Lin, K.; Marr, L. C.; Davis, R. D. Evidence for a Semisolid Phase State of Aerosols and Droplets Relevant to the Airborne and Surface Survival of Pathogens. *Proc. Natl. Acad. Sci. U. S. A.* **2022**, *119* (4).

(7) Preston, T. C.; Reid, J. P. Accurate and Efficient Determination of the Radius, Refractive Index, and Dispersion of Weakly Absorbing Spherical Particle Using Whispering Gallery Modes. *J. Opt. Soc. Am. B-Optical Phys.* **2013**, *30* (8), 2113–2122.

(8) Mason, B. J.; Cotterell, M. I.; Preston, T. C.; Orr-Ewing, A. J.; Reid, J. P. Direct Measurements of the Optical Cross Sections and Refractive Indices of Individual Volatile and Hygroscopic Aerosol Particles. *J. Phys. Chem. A* **2015**, *119* (22), 5701–5713.

(9) Suzuki, H.; Matsuzaki, Y.; Muraoka, A.; Tachikawa, M. Raman Spectroscopy of Optically Levitated Supercooled Water Droplet. *J. Chem. Phys.* **2012**, *136*, 234508.

(10) Mael, L. E.; Peiker, G.; Busse, H. L.; Grassian, V. H. Temperature-Dependent Liquid Water Structure for Individual Micron-Sized, Supercooled Aqueous Droplets with Inclusions. *J. Phys. Chem. A* **2021**, *125*, 10742–10749.

(11) Davies, J. F.; Wilson, K. R. Raman Spectroscopy of Isotopic Water Diffusion in Ultraviscous, Glassy, and Gel States in Aerosol by Use of Optical Tweezers. *Anal. Chem.* **2016**, *88* (4), 2361–2366.

(12) Lienhard, D. M.; Huisman, A. J.; Bones, D. L.; Te, Y. F.; Luo, B. P.; Krieger, U. K.; Reid, J. P. Retrieving the Translational Diffusion Coefficient of Water from Experiments on Single Levitated Aerosol Droplets. *Phys. Chem. Chem. Phys.* **2014**, *16* (31), 16677–16683.

(13) Coddens, E. M.; Angle, K. J.; Grassian, V. H. Titration of Aerosol PH through Droplet Coalescence. *J. Phys. Chem. Lett.* **2019**, *10* (15), 4476–4483.

(14) Craig, R. L.; Nandy, L.; Axson, J. L.; Dutcher, C. S.; Ault, A. P. Spectroscopic Determination of Aerosol PH from Acid − Base Equilibria in Inorganic, Organic, and Mixed Systems. *J. Phys. Chem. A* **2017**, *121*, 5690–5699.

(15) Lee, A. K. Y.; Chan, C. K. Single Particle Raman Spectroscopy for Investigating Atmospheric Heterogeneous Reactions of Organic Aerosols. *Atmos. Environ.* **2007**, *41* (22), 4611–4621.

(16) Lee, A. K. Y.; Chan, C. K. Heterogeneous Reactions of Linoleic Acid and Linolenic Acid Particles with Ozone: Reaction Pathways and Changes in Particle Mass, Hygroscopicity, and Morphology. *J. Phys. Chem. A* **2007**, *111* (28), 6285–6295.

(17) Marshall, F. H.; Berkemeier, T.; Shiraiwa, M.; Nandy, L.; Ohm, P. B.; Dutcher, C. S.; Reid, J. P. Influence of Particle Viscosity on Mass Transfer and Heterogeneous Ozonolysis Kinetics in Aqueous-Sucrose-Maleic Acid Aerosol. *Phys. Chem. Chem. Phys.* **2018**, 17–20.

(18) Glantschnig, W. J.; Chen, S.-H. Light Scattering from Water Droplets in the Geometrical Optics Approximation. *Appl. Opt.* **1981**, *20* (14), 2499.

(19) Graßmann, A.; Peters, F. Size Measurement of Very Small Spherical Particles by Mie Scattering Imaging (MSI). *Part. Part. Syst. Charact.* **2004**, *21* (5), 379–389.

(20) Fong, C. S.; Black, N. D.; Kiefer, P. A.; Shaw, R. A. An Experiment on the Rayleigh Instability of Charged Liquid Drops. *Am. J. Phys.* **2007**, *75* (6), 499–503.

(21) Schlemmer, S.; Illemann, J.; Wellert, S.; Gerlich, D. Nondestructive High-Resolution and Absolute Mass Determination of Single Charged Particles in a Three-Dimensional Quadrupole Trap. *J. Appl. Phys.* **2001**, *90* (10), 5410–5418.

(22) Trevitt, A. J. *Ion Trap Studies of Single Microparticles: Optical Resonances and Mass Spectrometry*; University of Melbourne, School of Chemistry, 2006.

(23) Trevitt, A. J.; Wearne, P. J.; Bieske, E. J. Calibration of a Quadrupole Ion Trap for Particle Mass Spectrometry. *Int. J. Mass Spectrom.* **2007**, *262* (3), 241–246.

(24) Wuerker, R. F.; Shelton, H.; Langmuir, R. V. Electrodynamic Containment of Charged Particles. *J. Appl. Phys.* **1959**, *30* (3), 342–349.

(25) Seo, S.-C.; Hong, S.-K.; Boo, D.-W. Single Nanoparticle Ion Trap (SNIT): A Novel Tool

for Studying in-Situ Dynamics of Single Nanoparticles. *Bull. Korean Chem. Soc.* **2003**, *24* (5), 552–554.

(26) Ding, L.; Sudakov, M.; Brancia, F. L.; Giles, R.; Kumashiro, S. A Digital Ion Trap Mass Spectrometer Coupled with Atmospheric Pressure Ion Sources. *J. Mass Spectrom.* **2004**, *39* (5), 471–484.

(27) Philip, M. A.; Gelbard, F.; Arnold, S. An Absolute Method for Aerosol Particle Mass and Charge Measurement. *J. Colloid Interface Sci.* **1983**, *91* (2), 507–515.

(28) Davis, E. J. Electrodynamic Balance Stability Characteristics and Applications to the Study of Aerocolloidal Particles. *Langmuir* **1985**, *1* (3), 379–387.

(29) Peng, C.; Chan, M. N.; Chan, C. K. The Hygroscopic Properties of Dicarboxylic and Multifunctional Acids: Measurements and UNIFAC Predictions. *Environ. Sci. Technol.* **2001**, *35* (22), 4495–4501.

(30) Nadler, K. A. Application of a Mobile Electrodynamic Balance for Studying Water Diffusion in Single Charged Aerosol, 2018.

(31) Xu, Y. L.; Wang, L. Y.; Yu, M. G.; Wan, S. J.; Song, Z. P.; Wang, S. K. Study on the Characteristics of Gas Explosion Affected by Induction Charged Water Mist in Confined Space. *J. Loss Prev. Process Ind.* **2016**, *40*, 227–233.

(32) Pizág, B.; Nagy, B. V. Extrapolation of Saturated Diffraction Spikes in Photographs Containing Light Sources. *Period. Polytech. Mech. Eng.* **2020**, *64* (3), 233–239.

(33) Wilson, E. B.; Decius, J. C.; Cross, P. C. *Molecular Vibrations: The Theory of Infrared and Raman Vibrational Spectra*; Dover Publications: New York, NY, 1980.

(34) Lewis, I. R.; Edwards, H. *Handbook of Raman Spectroscopy: From the Research Laboratory to the Process Line*; Marcel Dekker: New York, NY, 2001.

(35) McHale, J. L. *Molecular Spectroscopy*; CRC Press: Boca Raton, FL, 2017.

(36) Brinck, T.; Murray, J. S.; Politzer, P. Polarizability and Volume. *J. Chem. Phys.* **1993**, *98* (5), 4305–4306.

(37) Ghanty, T. K.; Ghosh, S. K. Correlation between Hardness, Polarizability, and Size of Atoms, Molecules, and Clusters. *J. Phys. Chem.* **1993**, *97* (19), 4951–4953.

(38) Burke, J. T. IR Spectroscopy or Hooke’s Law at the Molecular Level-A Joint Freshman Physics-Chemistry Experience. *J. Chem. Educ.* **1997**, *74* (10), 1213.

(39) Clark, R. J. H.; Dines, T. J. Resonance Raman Spectroscopy, and Its Application to Inorganic Chemistry. New Analytical Methods (27). *Angew. Chemie Int. Ed. English* **1986**, *25* (2), 131–158.

(40) McQuarrie, D. A.; Simon, J. D. *Physical Chemistry: A Molecular Approach*; University science books Sausalito, CA, 1997; Vol. 1.

(41) Dai, D.-Q. Wavelets and Orthogonal Polynomials Based on Harmonic Oscillator Eigenstates. *J. Math. Phys.* **2000**, *41* (5), 3086–3103.

(42) Bersani, D.; Conti, C.; Matousek, P.; Pozzi, F.; Vandenabeele, P. Methodological Evolutions of Raman Spectroscopy in Art and Archaeology. *Anal. Methods* **2016**, *8* (48), 8395–8409.

(43) Widmann, J. F.; Aardahl, C. L.; Davis, E. J. Microparticle Raman Spectroscopy. *TrAC - Trends Anal. Chem.* **1998**, *17* (6), 339–345.

(44) Liang, Z.; Chu, Y.; Gen, M.; Chan, C. K. Single-Particle Raman Spectroscopy for Studying Physical and Chemical Processes of Atmospheric Particles. *Atmos. Chem. Phys.* **2022**, *22* (5), 3017–3044.

(45) Mie, G. Beiträge Zur Optik Trüber Medien, Speziell Kolloidaler Metallösungen. *Ann. Phys.* **1908**, *330* (3), 377–445.

(46) Bohren, C. F.; Huffman, D. R. *Absorption and Scattering of Light by Small Particles*; John Wiley & Sons, Inc.: New York, NY, 1998; Vol. 31.

(47) Davies, J. F.; Haddrell, A. E.; Reid, J. P. Time-Resolved Measurements of the Evaporation of Volatile Components from Single Aerosol Droplets. *Aerosol Sci. Technol.* **2012**, *46* (6), 666–677.

(48) Pope, F. D.; Tong, H. J.; Dennis-Smither, B. J.; Griffiths, P. T.; Clegg, S. L.; Reid, J. P.; Cox, R. A. Studies of Single Aerosol Particles Containing Malonic Acid, Glutaric Acid, and Their Mixtures with Sodium Chloride. II. Liquid-State Vapor Pressures of the Acids. *J. Phys. Chem. A* **2010**, *114* (37), 10156–10165.

CHAPTER 3: Kinetic Limitation of Water Diffusion in Aqueous Citric Acid Droplets

3.1: Introduction

The discovery of highly viscous and glassy atmospheric aerosols[1,2] has attracted attention due to the prospect for very slow kinetics governing chemical change in these systems.[3–5] The reduced translational mobility of molecules in high viscosity droplets reduces the rate of equilibration while aqueous droplets with low viscosities establish equilibrium with the surrounding environment rapidly. This reduced mobility leads to decreases in heterogeneous reaction rates,[6,7] impedes hygroscopic growth,[8–10] and enhances ice nucleation.[11,12] In order to quantify and model these phenomena accurately, an understanding of water diffusion within such aerosol particles is critical as water is often the most mobile component in a viscous aqueous solution. This work presents a method of measuring water diffusion spectroscopically using H_2O/D_2O isotopic exchange in single model organic aerosol using an electrodynamic balance (EDB).

The Stokes-Einstein relation describes the diffusivity of solutes as a function of viscosity. A number of experimental techniques, both in the field and the laboratory, have been developed[4,13–15] to measure the viscosity of individual aerosol particles. In particular, recent studies have examined the impact of chemical composition and oxidation state of a variety of organic compounds on viscosity spanning a dynamic range from 10^{-3} Pa·s to values above the glass transition of 10^{12} Pa·s.[16] Experimental techniques for measuring viscosity are important for understanding of how environmental factors impact the phase state and heterogeneous reaction rates of ambient aerosol. Aqueous sucrose droplets have been used as model systems for validating new techniques to measure viscosity of single aerosol, because they can undergo a change in viscosity of greater than 10 orders of magnitude between 0 – 100 % RH, allowing for the comparison of methods over a wide dynamic range.[9,15] Sea spray aerosols (SSAs) has been shown to contain a significant fraction of organic material, particularly in the smaller size range ($d < 1\mu m$).[17] Sucrose-water and CA-water droplets can serve as benchmark systems to study the impacts of oxidized organic solutes to the viscosity of sea spray aerosols at varying RH conditions. However, application of the Stokes-Einstein relation to aerosols using viscosity measurements alone has been shown to provide only a lower bound to the estimation of the diffusion coefficient because of the ability of water molecules to percolate through channels in viscous matrices.[16,18,19] Therefore, techniques for measuring water diffusion rates independent from using viscosity data and Stokes-Einstein relation are necessary to accurately predict heterogeneous reaction rates and cloud activation processes.

The development of methods to directly measure slow diffusion of water has been a challenge, and several complementary methods have been reported only in recent years. Zhu *et al.* quantified maltose diffusion using Raman microscopy and isotopic labeling by compressing a non-deuterated and deuterated drop of maltose between two glass slides, creating an interface between the droplets where maltose molecules are being exchanged from both sides.[20] The Raman C-D and C-H stretches near 2100 cm^{-1} and 2900 cm^{-1}, respectively, were used to observe the diffusion of the molecules across the interface as a function of temperature and relative humidity.[20] Price *et al.* extended the method of isotopic exchange to measure the diffusion coefficient for water in a sucrose-water disk by monitoring the substitution of D_2O vapor for H_2O in the solution with Raman microscopy.[21]

However, compared to studying water diffusion of atmospheric aerosols on a substrate, contactless single particle techniques are preferred, because the aerosol is free from impacts of surface perturbations at concentrations above the solubility limit. In addition, single particle measurements are preferred over ensemble-averaged experiments, because composition and local chemical environments vary from particle to particle. Optical tweezers are one technique for spectroscopic studies of single, spherical particles from 1-10 μm in diameter trapped at the center of a tightly focused laser beam by a balance of photon gradient forces that are insensitive to charge state.[22] Scattering from the focused laser is collected to provide high-resolution size measurements using cavity enhanced features of the light scattering such as morphology dependent resonances, as well as chemical identity from the Raman scattering or fluorescence.[23,24] The response of a single particle to changes in humidity or ambient gaseous composition provides measurements of chemical kinetics,[25,26] and hygroscopicity.[27] For example, Davies *et al.* combined the isotopic exchange technique with an aerosol optical tweezer for single-particle confinement[28] allowing for a reduction in the sample size to less than 6 μm radius, speeding up the experimental timescales from weeks to hours. Isotopic tracer experiments have been carried out at a constant relative humidity (RH) leading to a constant size and solute concentration. Using Fick's second law of diffusion, Davies *et al.* modeled the time-dependent intensities of the ν(O-D) and ν(O-H) Raman peaks to quantify the diffusion coefficient as a function of concentration or water activity.[28]

The electrodynamic balance (EDB) is a technique for single particles that offers similar advantages including contactless levitation. However, it is not limited by size or morphology, as the trapping potential depends solely on mass-to-charge (m/q) ratio. EDBs have been used extensively to measure physicochemical properties of single aerosol particles such as evaporation rates[29–32] and nucleation,[33–37] and provide complementary results to optical tweezers. For example, Zobrist *et al* used an EDB to conduct water diffusion measurements by creating a step change in the RH and observing the change in particle size using Mie resonance spectroscopy.[38] The result was interpreted using a theoretical framework based on principles of mass transport by dividing the particle into a discrete number of shells, within which water molecules translationally move to establish equilibrium. The flux of water molecules between shells, along with dynamic adjustment to the time-steps and shell thickness, was calculated to extract a concentration-dependent diffusion coefficient. Under high viscosity conditions the particle was assumed as a core-shell phase state as the surface established equilibrium rapidly while the core remained viscous, creating a non-linear radial concentration gradient. This led to the refractive index becoming a fit parameter along with the radius, decreasing the accuracy of the model at low RH. Despite differences in experimental setups, the isotope tracing model and mass transport model produce similar water diffusion coefficients in sucrose over a wide range of RH.[21,28,38]

The present work reports a technique that combines the Raman spectroscopic isotope tracing method previously applied on single aerosol in optical tweezers by Davies *et al.*[28] with an RH-controlled EDB to trap single charged aerosol droplets for measuring water diffusion. Aqueous sucrose and aqueous citric acid (CA) microdroplets are serially trapped and equilibrated at a specific RH, and then exposed to D_2O at the same RH. Raman spectra of the droplet are acquired as a function of time, in order to assess the progression of D_2O diffusing into the droplet. In the analysis of these measurements, it is assumed that the entire droplet is irradiated with the laser and the total content of water remains constant throughout an experiment so that a volume-averaged Fickian diffusion model can be used to describe the exponential growth of the ν(O-D) Raman peak.

In the case of sucrose, D_2O was observed to eventually replace all H_2O, as indicated by complete disappearance of the ν(O-H) asymmetric stretch peak in the Raman spectrum. At RH below 10% CA was not observed to completely exchange, indicating a kinetic limitation. In the following section, the experimental approach is described followed by presentation of the data for sucrose-water and CA-water.

3.2: Experimental Methods

Water diffusion in single, charged aqueous microdroplets was studied using a D_2O/H_2O isotope exchange method in the EDB. Schematics of the experimental setup and optical layout are shown in **Figure 3.1**. The geometry of EDB electrodes is based on the design of Schlemmer *et al.*[39] later characterized in detail by Trevitt *et al.*[40] In brief, the EDB is composed of two conical endcap electrodes separated by 5.3 mm with a 2.5 mm axial channel for laser optical access. Eight concentric rod electrodes replace the ring electrode in a traditional Paul trap, allowing for optical access over a wide range of angles. Each rod is electrically isolated, however an external DC levitation voltage is applied to the two rods directly below the trap center to counterbalance the gravitational force of the trapped microdroplet. The AC voltage is applied to the endcap electrodes only, at typical values V_p = 1500 V and f = 150 Hz. During an experiment the levitation voltage is adjusted using an automated LabView feedback control loop for maintaining the droplet in the trap center, while the AC frequency is maintained approximately constant.

The droplet generator is located above the balance, allowing droplets to be injected directly into the trapping area. An electronic shutter is located at the opening of the chamber that opens for the introduction of a new droplet. A piezoelectric droplet generator (Engineering Arts DE03) is

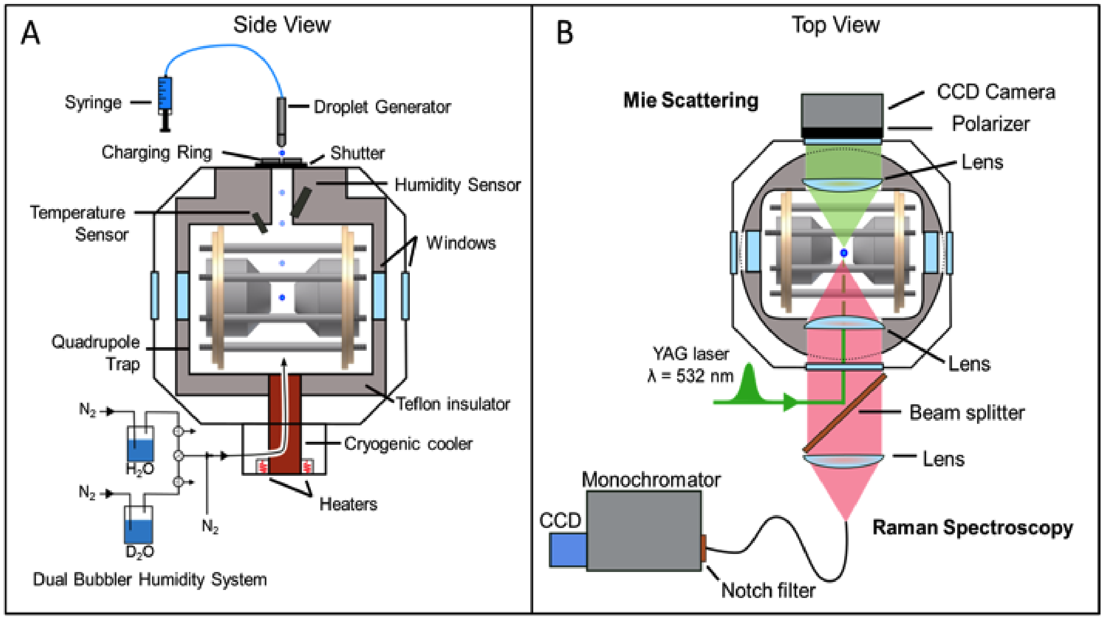

Figure 3.1: Schematic diagrams of EDB with spectrometer setup. (A) EDB chamber is equipped with a charged droplet generator and dual bubbler RH control system. (B) Optical layout for a trapped droplet irradiated by a 532 nm laser.

connected to an electronic syringe pump for precise control of the production of the aqueous droplets. Filtered aqueous sucrose or CA solutions are aspirated into the capillary of the droplet generator from which single droplets approximately 40 µm diameter are generated on demand using computer-controlled pulse generator to drive the piezoelectric element. A charging ring located above the shutter and electrically connected to the grounded piezoelectric tip inductively charges the droplets by causing ionic imbalance in the solution.

The RH in the environmental chamber is controlled with digital mass flow controllers (Alicat MC-500SCCM) by mixing dry N_2 with the humidified vapor headspace of a bubbler containing water. The temperature of EDB was maintained at the ambient laboratory temperature, approximately 20-23° C. The temperature is recorded using a temperature probe (Vaisala HMP60) with ±1° C accuracy. Two bubblers, one containing distilled H_2O and the other containing high purity D_2O (>99.8% D atom, Acros Organics), are arranged using 3-way valves as shown in **Figure 3.1A** so that air from one bubbler is selected to flow into the chamber while the other bubbler is exhausted. Experiments are carried out at constant RH by first trapping a single sucrose or CA droplet in H_2O RH and allowing sufficient time for equilibration. Then D_2O vapor at the same RH is introduced to the chamber, replacing the gas-phase H_2O in the balance and eventually diffusing into the H_2O droplet. During each experimental run, the H_2O humidified air is initially directed into the chamber for droplet equilibration while the D_2O bubbler is exhausted to fill intermediate tubing lines, minimizing changes in RH during the gas transition in the trap. The relative humidity and temperature are monitored using a humidity probe (Vaisala HMP60) with ±3% RH accuracy located approximately 25 mm downstream of the RH flow. For each water diffusion measurement the relative humidity is maintained constant to ±1%, or within the error of the probe. When the chamber atmosphere is switched to D_2O, the humidity probe measurement must be corrected for the difference in equilibrium vapor pressure of D_2O versus H_2O[41].

Two spectroscopic methods are used to characterize a trapped particle: Mie scattering for determining the particle size and Raman spectroscopy for chemical analysis. Shown in **Figure 3.1B** the trapped droplet is irradiated with a focused 80 kHz, 532 nm Nd:YAG laser beam (RPMC Wedge XF). The elastic Mie scattering is collimated using an *f/2* lens with a solid angle of 24.5° centered at 45° in the forward-scattering direction and imaged onto a monochromatic CCD camera. The morphology of the trapped droplet is determined by the Mie scattering pattern. Spherical droplets exhibit evenly spaced bands and crystalline or amorphous solid particles exhibit an irregular pattern.[33] **Figure 3.2** shows an example Mie image of a single droplet and the resulting angular intensity spectrum, previously demonstrated in the literature to follow closely with Mie theory.[24] The diameter of droplets in these experiments is significantly larger than the wavelength of light, allowing a geometric optics approximation to be applied. The intensity spectrum is processed using a fast Fourier Transform (FFT) to compute an average band spacing, $\Delta\theta$, (rad^{-1}). The band spacing is used in conjunction with the index of refraction, *n*, to calculate the particle radius, *r*, using equation (3.1):[42]

$$r = \frac{\lambda}{\Delta\theta}\left(\cos\left(\frac{\theta}{2}\right) + \frac{n\sin\left(\frac{\theta}{2}\right)}{\sqrt{1+n^2-2n\cos\left(\frac{\theta}{2}\right)}}\right)^{-1} \tag{3.1}$$

where λ is the laser wavelength (μm) and θ is the median scattering angle (rad).

Calculation of the index of refraction for the droplet as a function of varying RH requires parameterization of the mass fraction solute (MFS) and density (ρ). The dependence of MFS on water activity, a_w, has been well studied for sucrose solutions and the treatment by Norrish[43] has been shown to correlate with experimental measurements over the entire RH range:

$$a_w = x_w\, exp(k x_s^2) \tag{3.2}$$

where x_w and x_s are the mole fractions of water and solute, respectively, and k is an empirical constant equal to -6.47 for sucrose.[44] While other parameterizations have been proposed,[38,45] the Norrish parametrization was shown to be most appropriate for sucrose solutions over a wide range of RH.[16,28] The density of a sucrose-water mixture can be taken as the volume additivity of pure component densities (VAD), with the pure component density of water, $\rho_w = 1000\ \mathrm{kg \cdot m^{-3}}$, and sucrose,[44] $\rho_s = 1580.5\ \mathrm{kg \cdot m^{-3}}$ giving:

$$\frac{1}{\rho} = \frac{1-MFS}{\rho_w} + \frac{MFS}{\rho_s} \tag{3.3}$$

The refractive index of a sucrose solution varies with MFS and is parameterized using a linear fit with the refractive index for water, $n = 1.33$, at MFS(0) and $n = 1.558$ at MFS(1).[46] The calculated index of refraction of the sucrose droplet at a given RH is then used in equation (3.1) to calculate the droplet diameter. The uncertainty in droplet size (±10 nm) due to wavelength-dependent dispersion is negligible compared the experimental error (±500 nm) from the RH probe,[8] making it unnecessary to implement the highly accurate parameterization for sucrose solutions reported by Rosenbruch et al.[47] For CA, comprehensive parametrization of MFS with a_w and the refractive index of CA solution by Lienhard *et al.* was adopted.[48]

The evolving chemical composition of the trapped droplet from H_2O to D_2O is analyzed using the intensity of the stretches ν(O-D) and ν(O-H) centered near 2500 $\mathrm{cm^{-1}}$ and 3400 $\mathrm{cm^{-1}}$, respectively in the Raman spectrum. A representative Raman spectrum for a sucrose droplet is shown in **Figure 3.2**, and a representative spectrum for a CA droplet is shown in **Figure 3.3**. The integrated intensity of the O-H and O-D stretches features allows calculation of the fractional concentration of D_2O in the droplet over time. The Raman spectra are fit using a 7-term Gaussian expansion of the form:

$$Fit = \sum_{i=1}^{7} aexp\left(-\frac{(b-x)^2}{c^2}\right) \tag{3.4}$$

The back-scattered Raman signal is collected using *f/2* optics, transmitted through the 532 nm laser edge beam splitter, and focused into a fiber optic cable coupled into a spectrometer (Acton SpectraPro 275) with an open-electrode TE-cooled CCD detector (Horiba Syncerity). The spectrometer is equipped with a 600 g/mm grating with a 750 nm blaze for optimized quantum efficiency between 620 - 660 nm. The integration time for each spectrum is varied (30-120 seconds) to achieve adequate signal-to-noise ratio. The LabView control and data acquisition program records the Mie and Raman spectra at a designated interval along with trap settings and conditions.

The solution to Fick's second law of diffusion applied to a sphere is used to model the time-dependent dimensionless fractional concentration of the diffusing D_2O:[28,49]

$$\phi_{D_2O} = 1 - \left(\frac{6}{\pi^2}\right)\sum_{n=1}^{\infty}\frac{1}{n^2}exp\left(-\frac{n^2\pi^2 D_w t}{a^2}\right) \tag{3.5}$$

where a is the particle radius and D_w is the translational diffusion constant. A three-term expansion of equation (3.5) with a single adjustable parameter is used to calculate D_w for each of the experimental runs at a different RH. The upper limit for diffusion coefficients measured using this technique is calculated as ~5 x 10^{-13} m^2s^{-1}. The sources of the upper limit include the rapid diffusion in the droplet sizes at high RH, the acquisition time required for adequate spectral signal-to-noise, and the time delay associated with fully replacing the composition of the atmosphere in the trapping volume.[28]

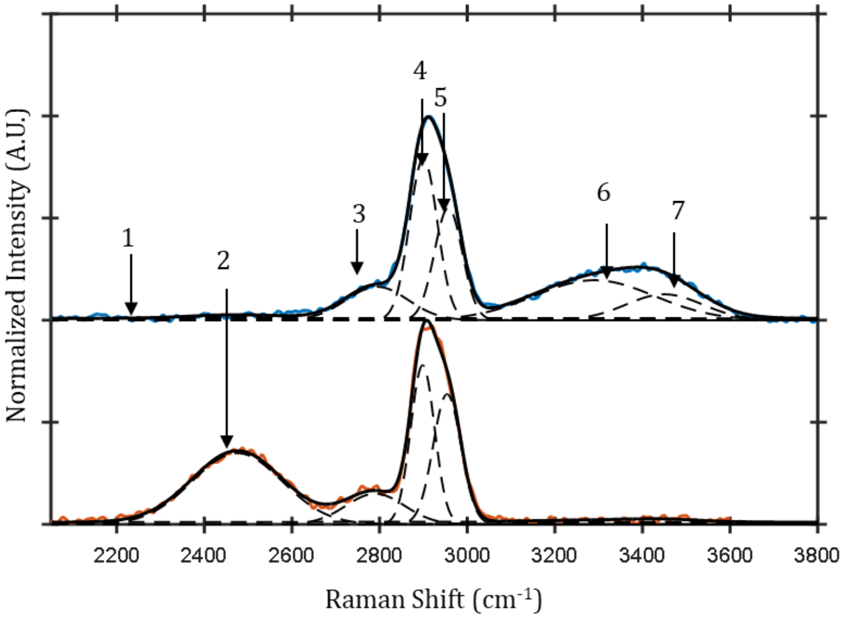

Figure 3.2: Raman spectra collected during an isotope exchange of a sucrose droplet carried out at 50% RH at early (top) and late (bottom) time points. The spectra are deconstructed into 7 Gaussians as described in the manuscript, which are shown here individually. The C-H stretches, peaks 4 and 5 peaking at 2930 cm^{-1}, are used for normalization.

Table 3.1: Gaussian fit parameters for each of the 7 Gaussians in a single sucrose droplet spectrum accompanying **Figure 3.2** where *a*, *b*, and *c* follow equation (3.4).

Upper	**Peak**	**a**	**b**	**c**
	1	0.010	2915	2000
	2	0.017	2475	150
	3	0.164	2794	100
	4	0.791	2900	45
	5	0.549	2957	45
	6	0.196	3290	194
	7	0.127	3450	123
Lower	**Peak**	**a**	**b**	**c**
	1	0.012	2915	2000
	2	0.349	2475	145
	3	0.150	2790	95
	4	0.779	2898	39
	5	0.637	2954	45
	6	0.009	3290	200
	7	0.010	3450	120

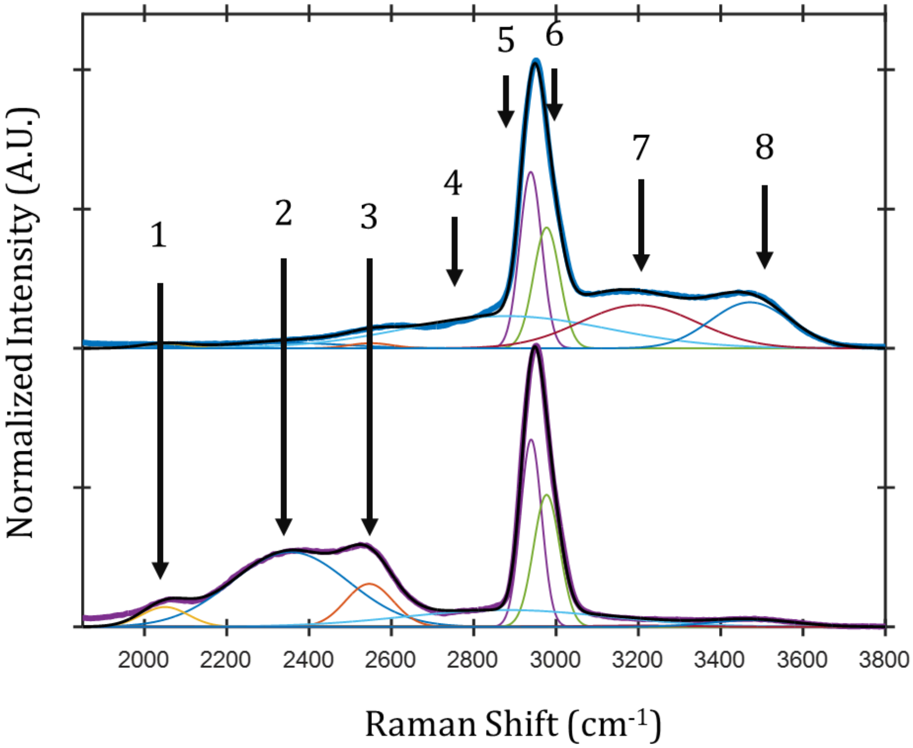

Figure 3.3: 8 Gaussians fit for CA droplets. Spectra for the early stage of exchange (top, blue line) and near the completion of exchange (bottom, purple line) conducted at 21% RH are shown. Black curves represent the overall Gaussian fitting as the sum of the 8 Gaussian functions with different colors. Normalization of the data was done using the C-H stretch feature peaking at 2950 cm^{-1}. Representative Gaussian fit parameters for these data are shown in Table S2.

Table 3.2: Gaussian fit parameters for **Figure 3.3**, two spectra of CA droplets showing pre/post H_2O/D_2O exchange. 8 sets of parameters are used.

Upper	**Peak**	**a**	**b**	**c**
	1	0.0194	2050	80
	2	0.0197	2350	210
	3	0.0163	2550	80
	4	0.1215	2880	350
	5	0.6362	2938	38
	6	0.4267	2977	45
	7	0.1537	3202	200
	8	0.1811	3473	198

Lower	**Peak**	**a**	**b**	**C**
	1	0.0753	2050	80
	2	0.2810	2354	206
	3	0.1742	2547	81
	4	0.0626	2880	350
	5	0.6702	2935	36
	6	0.4779	2977	45
	7	0.0000	3200	200
	8	0.0225	3480	140

3.3: Results and Discussion

The water diffusion coefficients measured for sucrose-water droplets at RH between 26-54% at room temperature are shown in **Figure 3.4**. The RH is reported with absolute error of the probe, ±3 %, and the error in the D_w measurement is estimated as 50%, calculated from an uncertainty of ±20% in the model fit, ±1 µm uncertainty in the size calculation, differences in self-diffusion between H_2O and D_2O (10-24%)[21], the fluctiation in RH (±1%) and temperature stabilization (± 1 °C) over the course of an experiment. The results are compared with parameterizations from literature reported by Zobrist *et al.*,[38] Price *et al.*,[21] and Davies *et al.*[28] Over the range where data was obtained, the results agree well with the Vignes-type parameterization that describes the variation of the water diffusion coefficient, D_w, with composition in a binary mixture:[50]

$$D_w = \left(D^0_{w,w}\right)^{x_w} \left(D^0_{w,s}\right)^{(1-x_w)} \tag{3.6}$$

where x_w is the mole fraction of water, $D^0_{w,w}$ is the translational diffusion coefficient in pure water (2×10^{-9} m^{2}s^{-1}), and $D^0_{w,s}$ is the self-diffusion coefficient of water in pure solute (1.9×10^{-27} m^{2}s^{-1}, reported by Davies *et al.*[28]). Excellent agreement was found between the present results using the EDB and previous reports with various techniques[28,51,52] showing the viability of this method for quantifying the translational diffusion coefficient over a range of water activities. However, the agreement deviates when approaching at the high RH limit. At 54% the timescale for diffusion is comparable to the turnover time for replacing the air in the chamber, allowing for isotopic exchange to occur rapidly in the droplet while exposed to an effectively lower D_2O concentration because the air is still a mixture of H_2O and D_2O. The resulting D_w at high RH, approximately 1×10^{-13} m^{2}s^{-1}, is lower than the Vignes-type trend followed by other published results and serves as an upper bound to the dynamic range of the diffusion coefficients that can be quantified using this experimental setup.

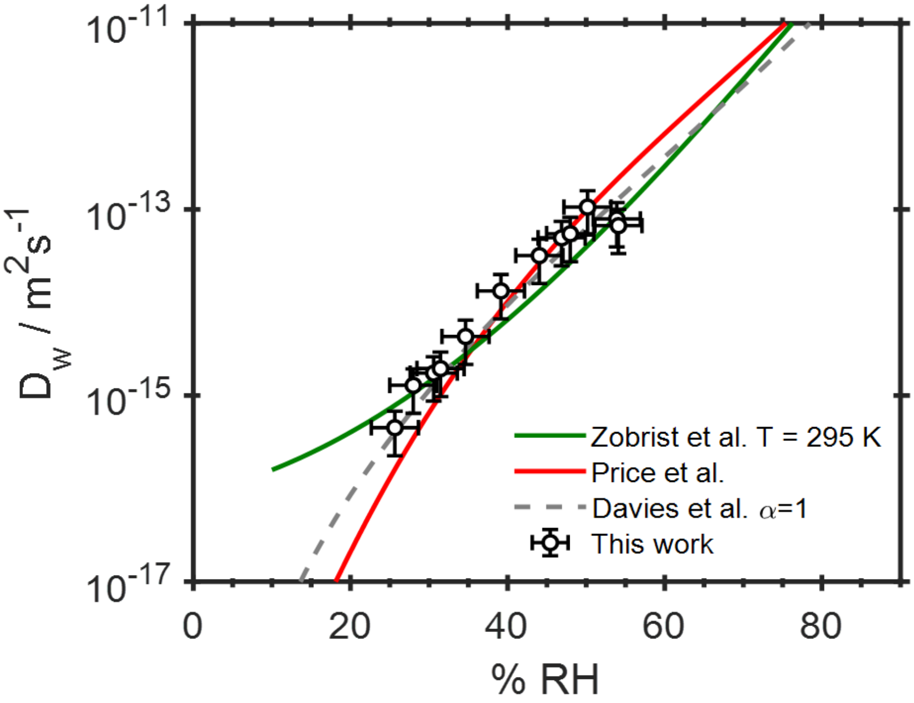

Figure 3.4: Calculated water diffusion coefficients in sucrose droplets at varying RH studied in this work compared with parameterizations provided by Zobrist *et al.*,[38] Price *et al.*[21] and Davies *et al.*[28]

The results in **Figure 3.4**. are consistent with measurements carried out using isotope exchange over 6 – 300 μm diameter samples which suggests there is not a significant impact of droplet size on the water diffusion coefficient in the 35 – 60 μm size range studied. The droplet diameters studied in this work were significantly larger than the <10 μm diameter droplets used by Zobrist *et al.*[38] and Davies *et al.*[28] and significantly smaller than the 200 – 300 μm diameter substrate-supported disks used by Price *et al.*[21] This suggests that the droplet size does not have a significant effect on the diffusion coefficient as a correlation between D_w and diameter across these different size ranges is not observed. D_w of sucrose solution below 25% RH is of great interest because prediction from two methods (isotope exchange and mass transport) diverges orders of magnitude. The large discrepancy is due to different assumptions used in two models. In the mass transport model, the radius of the droplet changes as it experiences sorption and desorption of water with the RH change. On the other hand, the isotope exchange model assumes a constant radius of the droplet held at fixed RH. Thus, the mass transport model involves a moving and nonlinear boundary condition while the isotope exchange model assumes a fixed linear boundary condition.[49,51] Measuring D_w at RH below 25% in the case of sucrose was beyond the scope of the current measurements due to the diffusion timescales.[53,54]

The present results can be compared with both charge-neutral particles in the case of the isotope-exchange measurements of Price *et al.*[21] and Davies *et al.*[28] and charged particles in the mass-transport measurements of Zobrist *et al.*[38] The comparison suggests that the surface charge density on the droplets in this work (<40 elementary charges/μm^2) do not significantly influence D_2O diffusion into droplets. If the charge state significantly impacted the diffusion of D_2O into the droplet the best agreement would be expected between the results conducted in EDBs, which is not the case. Instead, the best agreement was found with the optical tweezer measurements on neutral microdroplets using the isotope labeling technique. These results can be understood in the context of studies on the influence of charge on both ice nucleation and efflorescence. Homogeneous ice nucleation rates of pure water droplets were measured in a temperature-controlled EDB as a function of temperature and absolute charge and it was concluded that while temperature strongly influenced the nucleation rate, no correlation with the surface charge was observed over a range of ±200 charges/μm^2.[34,55] Charged droplets with 10x greater surface charge density compared to the droplets in the current work were examined and no effect of the charge on nucleation was found, supporting the conclusion that excess charges are not interfering with bulk processes such as diffusion within a droplet. Another recent study measured the dependence of the efflorescence relative humidity on the magnitude of the surface charge in sodium chloride microdroplets and found no correlation below 500 elementary charges/μm^2.[37] Molecular dynamics simulations showed that above this charge density threshold, the charges interact with dissolved ionic species to form stable critical cluster sizes necessary for overcoming the energetic nucleation barrier at higher RH compared to neutral droplets. In the present work, the sucrose droplets contain surface charge density significantly below the threshold suggested by Hermann *et al.*[37] to impact efflorescence behavior. Thus, the present work demonstrates an alternative way that can be used to study particles imcompatible with optical trapping techniques, e.g., amorphous (or glassy) aerosols or solid particles which have non-spherical morphology.

Water diffusion in citric acid solution droplets was measured over a lower RH range (7-25 %) compared to sucrose. The RH-dependent refractive index of a CA solution was parameterized using the MFS of CA and water to deduce droplet size.[48] The RH dependent D_w values of CA droplet are shown in **Figure 3.5**, revealing good agreement with the other isotope exchange measurements using optical tweezers[28] and a significant deviation from from D_w values measured

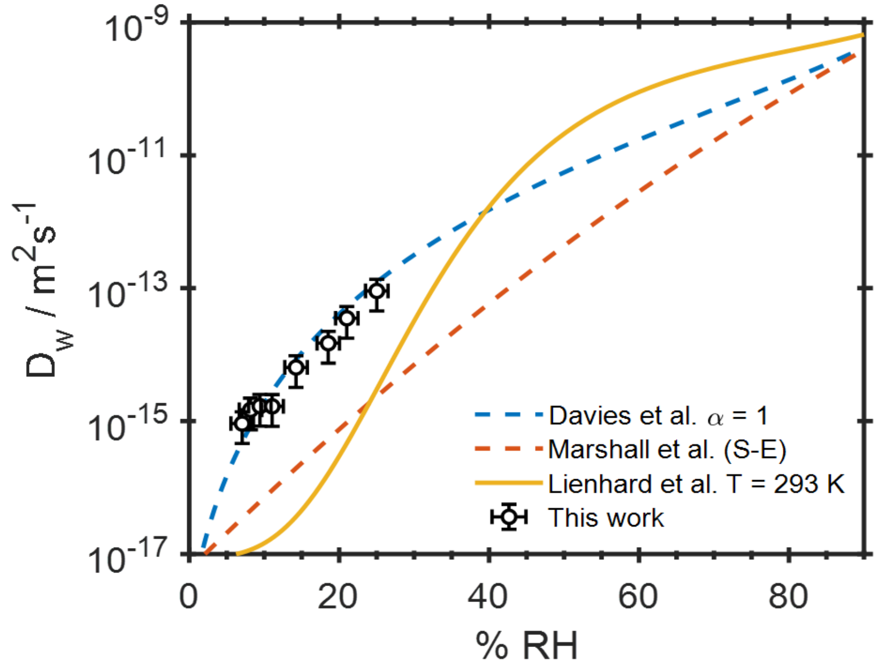

Figure 3.5: RH dependent D_w for CA droplets compared to other experiments. Isotopic exchange using optical tweezer (Davies *et al.*)[28], mass transfer (Lienhard *et al.*)[52], and S-E prediction from viscosity data (Marshall *et al.*)[53]

by mass-transfer[56] as well as the predictions of the the S-E equation.[57] Isotope-exchange derived D_w values of CA below 10% RH at room temperature are reported here for the first time, and it is found that in this regime, the intensity of Raman O-H band at 3400 cm^{-1} does not diminish to zero in the exchange process. This may arise from inhibited diffusion of water in CA droplet under very dry conditions. In addition, the results at RH lower than 15% reveal that the aqueous CA droplets do not undergo full isotope exchange, with all labile hydrogens replaced by deuterium, over a period up to 65 hours. This observation may be a result of the much larger size of the droplet compared to the study of Davies and Wilson.[28] Because equation (3.7) assumes complete H_2O/D_2O exchange, it is no longer valid for describing water diffusion at RH < 15%. To analyze incomplete H_2O/D_2O exchange for CA at lower RH's we introduce a modified solution to Fick's 2nd law, equation (3.7). The equation contains an additional parameter χ that represents the fractional exchange as a function of RH, and reveals the kinetic limitation of water diffusion. For instance, $\chi = 1$ means complete exchange of H_2O to D_2O and equation (3.7) is analogous to equation (3.5) while $\chi = 0.7$ indicates 70% of total H_2O in the droplet is exchanged to D_2O.

$$\phi_{D_2O} = \chi(1 - \left(\frac{6}{\pi^2}\right)\sum_{n=1}^{\infty}\frac{1}{n^2}exp\left(-\frac{n^2\pi^2 D_w t}{a^2}\right)) \tag{3.7}$$

Application of the two equations (3.5) and (3.7) to the isotope exchange data at low RH is illustrated in **Figure 3.6**, showing that equation (3.7) represents the physical phenomena significantly better than equation (3.5). **Figure 3.7** shows the strong observed dependence of χ on RH illustrating the incomplete H_2O/D_2O exchange at lower RH ($\chi < 1$) and full exchange of H_2O to D_2O at RH higher than 15% ($\chi \sim 1$). It is not surprising for CA droplets of this size to develop a radial concentration gradient under dry conditions. Consequently, the true values of D_w are expected to be smaller than the values calculated using equation (3.7) because the diffusion of D_2O

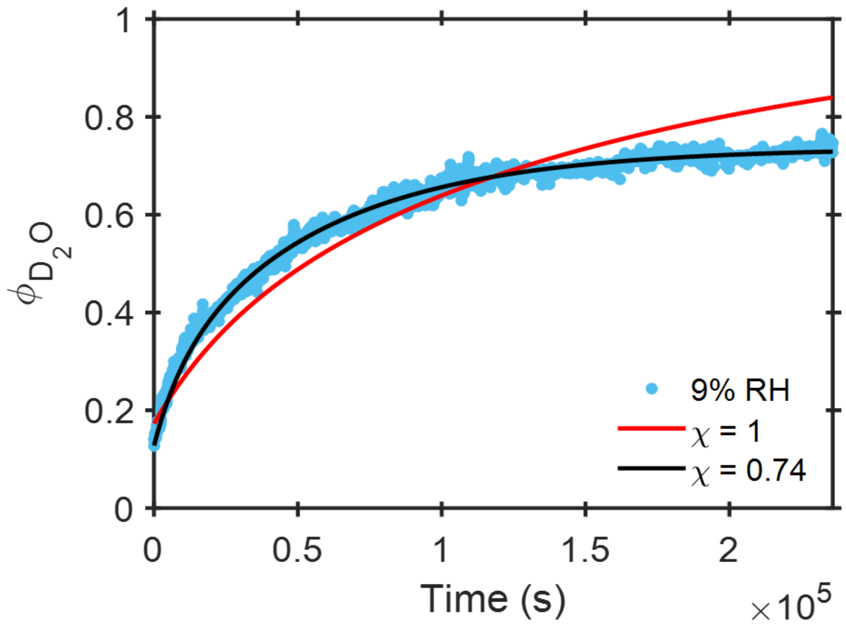

Figure 3.6: The result of using 1-parameter (equation 3.5, red) and 2-parameter (equation 3.7, black) fitting to ϕ_{D_2O} for CA droplet at 11% RH. Setting $\chi < 1$ represents the physical behavior better than assuming complete H_2O/D_2O exchange ($\chi = 1$).

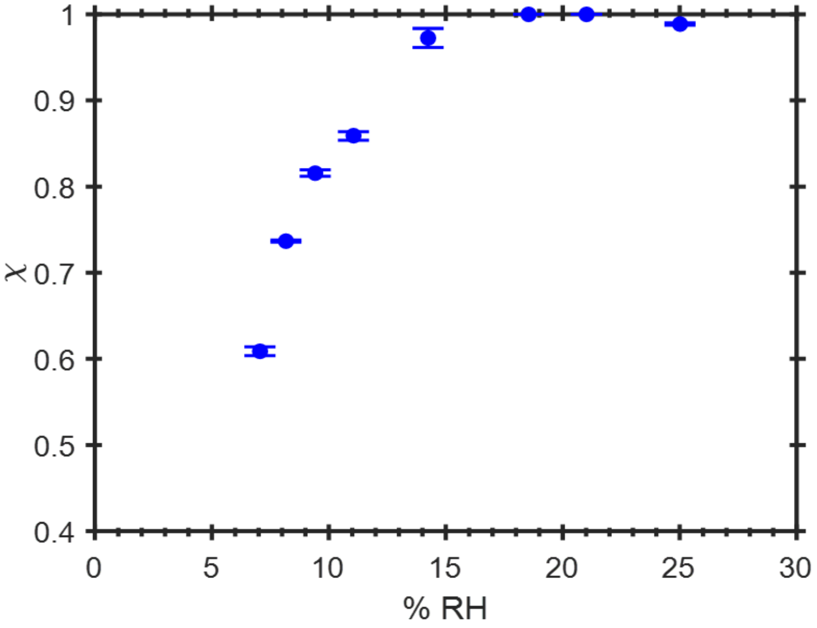

Figure 3.7: Kinetic limitations of water diffusion are evident at RH below 15% shown as nonunity ϕ_{D_2O} values given by equation (3.7). Error bars represent the 95% confidence interval of the fitting parameter χ.

into the droplet core is not complete. The Fickian diffusion model assumes a homogeneous mixture after sufficient equilibration time, which is not truly achieved here owing to the kinetic limitation, but it was chosen for analysis of D_w in the CA droplets as well owing to its simplicity and applicability to both sucrose and CA data. A kinetic multi-layer model[58] or Maxwell-Stefan diffusion model[59] may be used in future studies to describe the formation of concentration gradient within the droplet as these models explicitly consider the droplet as a series of spherical shells.

Similar kinetic limitations of diffusion have previously been observed for ambient organic aerosol, particularly in highly viscous or glassy state aerosol where formation of a significant radial concentration gradient in the droplet, inhibits reaching thermodynamic equilibrium.[1,60] The inhibited diffusion of water in CA droplets may be attributed to formation of molecular clusters in the supersaturated solution. It is worth comparing the results of H_2O/D_2O exchange at the lower RH bound for sucrose (26%) and CA (7%). The exchange was incomplete for CA over several days while sucrose showed full exchange ($\chi = 1$) even though the D_w value of CA (9.19×10^{-16} $m^2\ s^{-1}$) is notably higher than that of sucrose (4.52×10^{-16} $m^2\ s^{-1}$) at the stated conditions. In addition, the viscosities of the droplets show orders of magnitude difference (~10^{10} Pa·s for sucrose vs ~10^4 Pa·s for CA). Taking these observations into account, one can suppose that CA has a much higher propensity to form organized molecular structures with water than sucrose does within the highly saturated solution (MFS > 0.9). This is supported by studies that observed solute clustering in supersaturated CA solutions.[61–64] From a chemical perspective, citric acid is a tricarboxylic acid that will have much stronger interactions with water through the acidic hydrogens and the polar –COOH groups compared to sucrose. Similar kinetic inhibition for diffusion of reactive condensed-phase species have been reported for glassy aerosol at low RH[8,9,56] but our result explicitly shows the strong dependence of this phenomenon on RH. Aggregation of solute-water clusters in supersaturated droplets may lead to radial concentration gradients that promote formation of a core-shell morphology, preserving the unreacted core species with potential implications for surface-sensitive phenomena such as cloud condensation nucleation (CCN) and ice nucleation (IN) activities.[65] Mie scattering measurements remained consistent with liquid droplets even at these low RH, so the question that arises is how 'liquid' or 'solid' a particle needs to be to distinguish the particle phase by Mie scattering.[66,67]

3.4: Conclusions

The translational water diffusion coefficient was measured in aqueous sucrose and CA droplets as a model system for sea spray aerosol at humidities ranging from 26-54% RH for sucrose and 7-25% RH for CA at room temperature. Water diffusion has been quantified using H_2O/D_2O isotope tracing measured with Raman spectroscopy of a single charged droplet trapped in a humidity-controlled EDB. The measured water diffusion coefficients-molar concentration relationship follows an exponential dependence, described as a Vignes-type parameterization. The data were compared with previous studies of the CA-water system using the isotope exchange technique on neutral samples and a mass transport method on charged droplets. The comparison between our results and other Raman spectroscopy based methods shows good agreement of water diffusion coefficients across a wide range of sample sizes and volumes, suggesting the D_w values are not size-dependent. The agreement of this work using charged droplets in an EDB with neutral particles in an optical trap suggests that charge does not play a significant role under the conditions studies. Moreover, kinetic limitation of water diffusion observed from the CA droplets provides evidence of ultra-slow water diffusion which is predicted for glassy organic aerosols.

Acknowledgements

Chapter 3, in part, is a reprint of the material as it appears in Physical Chemistry Chemical Physics, 2019, Nadler, Katherine; Kim, Pyeongeun; Huang, Dao-Ling; Xiong, Wei; Continetti, Robert E. The dissertation author was the primary investigator and author of the work on citric acid in that manuscript and this chapter.

References

(1) Zobrist, B.; Marcolli, C.; Pedernera, D. A.; Koop, T. Do Atmospheric Aerosols Form Glasses? *Atmos. Chem. Phys.* **2008**, *8* (17), 5221–5244.

(2) Orellana, M. V; Matrai, P. A.; Leck, C.; Rauschenberg, C. D.; Lee, A. M.; Coz, E. Marine Microgels as a Source of Cloud Condensation Nuclei in the High Arctic. *Proc. Natl. Acad. Sci. U. S. A.* **2011**, *108* (33), 13612–13617.

(3) Virtanen, A.; Joutsensaari, J.; Koop, T.; Kannosto, J.; Yli-Pirila, P.; Leskinen, J.; Makela, J. M.; Holopainen, J. K.; Poschl, U.; Kulmala, M.; Worsnop, D. R.; Laaksonen, A. An Amorphous Solid State of Biogenic Secondary Organic Aerosol Particles. *Nature* **2010**, *467* (7317), 824–827.

(4) Jarvinen, E.; Ignatius, K.; Nichman, L.; Kristensen, T. B.; Fuchs, C.; Hoyle, C. R.; Hoppel, N.; Corbin, J. C.; Craven, J.; Duplissy, J.; Ehrhart, S.; El Haddad, I.; Frege, C.; Gordon, H.; Jokinen, T.; Kallinger, P.; Kirkby, J.; Kiselev, A.; Naumann, K. H.; Petaja, T.; Pinterich, T.; Prevot, A. S. H.; Saathoff, H.; Schiebel, T.; Sengupta, K.; Simon, M.; Slowik, J. G.; Trostl, J.; Virtanen, A.; Vochezer, P.; Vogt, S.; Wagner, A. C.; Wagner, R.; Williamson, C.; Winkler, P. M.; Yan, C.; Baltensperger, U.; Donahue, N. M.; Flagan, R. C.; Gallagher, M.; Hansel, A.; Kulmala, M.; Stratmann, F.; Worsnop, D. R.; Mohler, O.; Leisner, T.; Schnaiter, M. Observation of Viscosity Transition in Alpha-Pinene Secondary Organic Aerosol. *Atmos. Chem. Phys.* **2016**, *16* (7), 4423–4438.

(5) Shiraiwa, M.; Seinfeld, J. H. Equilibration Timescale of Atmospheric Secondary Organic Aerosol Partitioning. *Geophys. Res. Lett.* **2012**, *39* (24), L24801.

(6) Davies, J. F.; Wilson, K. R. Nanoscale Interfacial Gradients Formed by the Reactive Uptake of OH Radicals onto Viscous Aerosol Surfaces. *Chem. Sci.* **2015**, *6* (12), 7020–7027.

(7) Liu, P. F.; Li, Y. J.; Wang, Y.; Bateman, A. P.; Zhang, Y.; Gong, Z. H.; Bertram, A. K.;

Martin, S. T. Highly Viscous States Affect the Browning of Atmospheric Organic Particulate Matter. *Acs Cent. Sci.* **2018**, *4* (2), 207–215.

(8) Tong, H. J.; Reid, J. P.; Bones, D. L.; Luo, B. P.; Krieger, U. K. Measurements of the Timescales for the Mass Transfer of Water in Glassy Aerosol at Low Relative Humidity and Ambient Temperature. *Atmos. Chem. Phys.* **2011**, *11* (10), 4739–4754.

(9) Bones, D. L.; Reid, J. P.; Lienhard, D. M.; Krieger, U. K. Comparing the Mechanism of Water Condensation and Evaporation in Glassy Aerosol. *Proc. Natl. Acad. Sci.* **2012**, *109* (29), 11613–11618.

(10) Lu, J. W.; Rickards, A. M. J.; Walker, J. S.; Knox, K. J.; Miles, R. E. H.; Reid, J. P.; Signorell, R. Timescales of Water Transport in Viscous Aerosol: Measurements on Sub-Micron Particles and Dependence on Conditioning History. *Phys. Chem. Chem. Phys.* **2014**, *16* (21), 9819–9830.

(11) Lienhard, D. M.; Huisman, A. J.; Krieger, U. K.; Rudich, Y.; Marcolli, C.; Luo, B. P.; Bones, D. L.; Reid, J. P.; Lambe, A. T.; Canagaratna, M. R.; Davidovits, P.; Onasch, T. B.; Worsnop, D. R.; Steimer, S. S.; Koop, T.; Peter, T. Viscous Organic Aerosol Particles in the Upper Troposphere: Diffusivity-Controlled Water Uptake and Ice Nucleation? *Atmos. Chem. Phys.* **2015**, *15* (23), 13599–13613.

(12) Ignatius, K.; Kristensen, T. B.; Jarvinen, E.; Nichman, L.; Fuchs, C.; Gordon, H.; Herenz, P.; Hoyle, C. R.; Duplissy, J.; Garimella, S.; Dias, A.; Frege, C.; Hoppel, N.; Troestl, J.; Wagner, R.; Yan, C.; Amorim, A.; Baltensperger, U.; Curtius, J.; Donahue, N. M.; Gallagher, M. W.; Kirkby, J.; Kulmala, M.; Mohler, O.; Saathoff, H.; Schnaiter, M.; Tome, A.; Virtanen, A.; Worsnop, D.; Stratmann, F. Heterogeneous Ice Nucleation of Viscous Secondary Organic Aerosol Produced from Ozonolysis of Alpha-Pinene. *Atmos. Chem. Phys.* **2016**, *16* (10), 6495–6509.

(13) Grayson, J. W.; Song, M.; Sellier, M.; Bertram, A. K. Validation of the Poke-Flow Technique Combined with Simulations of Fluid Flow for Determining Viscosities in Samples with Small Volumes and High Viscosities. *Atmos. Meas. Tech.* **2015**, *8* (6), 2463–2472.

(14) Renbaum-Wolff, L.; Grayson, J. W.; Bertram, A. K. Technical Note: New Methodology for Measuring Viscosities in Small Volumes Characteristic of Environmental Chamber Particle Samples. *Atmos. Chem. Phys.* **2013**, *13* (2), 791–802.

(15) Song, Y. C.; Haddrell, A. E.; Bzdek, B. R.; Reid, J. P.; Barman, T.; Topping, D. O.; Percival, C.; Cai, C. Measurements and Predictions of Binary Component Aerosol Particle Viscosity. *J. Phys. Chem. A* **2016**, *120* (41), 8123–8137.

(16) Power, R. M.; Simpson, S. H.; Reid, J. P.; Hudson, A. J. The Transition from Liquid to Solid-like Behaviour in Ultrahigh Viscosity Aerosol Particles. *Chem. Sci.* **2013**, *4* (6), 2597–2604.

(17) O'Dowd, C. D.; Facchini, M. C.; Cavalli, F.; Ceburnis, D.; Mircea, M.; Decesari, S.; Fuzzi, S.; Young, J. Y.; Putaud, J. P. Biogenically Driven Organic Contribution to Marine

Aerosol. *Nature* **2004**, *431* (7009), 676–680.

(18) Kumar, S. K.; Szamel, G.; Douglas, J. F. Nature of the Breakdown in the Stokes-Einstein Relationship in a Hard Sphere Fluid. *J. Chem. Phys.* **2006**, *124* (21), 214501.

(19) Molinero, V.; Goddard, W. A. Microscopic Mechanism of Water Diffusion in Glucose Glasses. *Phys. Rev. Lett.* **2005**, *95* (4), 045701.

(20) Zhu, L.; Cai, T.; Huang, J.; Stringfellow, T. C.; Wall, M.; Yu, L. Water Self-Diffusion in Glassy and Liquid Maltose Measured by Raman Microscopy and NMR. *J. Phys. Chem. B* **2011**, *115* (19), 5849–5855.

(21) Price, H. C.; Murray, B. J.; Mattsson, J.; O'Sullivan, D.; Wilson, T. W.; Baustian, K. J.; Benning, L. G. Quantifying Water Diffusion in High-Viscosity and Glassy Aqueous Solutions Using a Raman Isotope Tracer Method. *Atmos. Chem. Phys.* **2014**, *14* (8), 3817–3830.

(22) Hopkins, R. J.; Mitchem, L.; Ward, A. D.; Reid, J. P. Control and Characterisation of a Single Aerosol Droplet in a Single-Beam Gradient-Force Optical Trap. *Phys. Chem. Chem. Phys.* **2004**, *6* (21), 4924–4927.

(23) Chylek, P.; Ramaswamy, V.; Ashkin, A.; Dziedzic, J. M. Simultaneous Determination of Refractive-Index and Size of Spherical Dielectric Particles from Light-Scattering Data. *Appl. Opt.* **1983**, *22* (15), 2302–2307.

(24) Ray, A. K.; Souyri, A.; Davis, E. J.; Allen, T. M. Precision of Light-Scattering Techniques for Measuring Optical-Parameters of Microspheres. *Appl. Opt.* **1991**, *30* (27), 3974–3983.

(25) Dennis-Smither, B. J.; Miles, R. E. H.; Reid, J. P. Oxidative Aging of Mixed Oleic Acid/Sodium Chloride Aerosol Particles. *J. Geophys. Res.* **2012**, *117*, D20204.

(26) Dennis-Smither, B. J.; Marshall, F. H.; Miles, R. E. H.; Preston, T. C.; Reid, J. P. Volatility and Oxidative Aging of Aqueous Maleic Acid Aerosol Droplets and the Dependence on Relative Humidity. *J. Phys. Chem. A* **2014**, *118* (30), 5680–5691.

(27) Cai, C.; Stewart, D. J.; Reid, J. P.; Zhang, Y. H.; Ohm, P.; Dutcher, C. S.; Clegg, S. L. Organic Component Vapor Pressures and Hygroscopicities of Aqueous Aerosol Measured by Optical Tweezers. *J. Phys. Chem. A* **2015**, *119* (4), 704–718.

(28) Davies, J. F.; Wilson, K. R. Raman Spectroscopy of Isotopic Water Diffusion in Ultraviscous, Glassy, and Gel States in Aerosol by Use of Optical Tweezers. *Anal. Chem.* **2016**, *88* (4), 2361–2366.

(29) Davies, J. F.; Haddrell, A. E.; Reid, J. P. Time-Resolved Measurements of the Evaporation of Volatile Components from Single Aerosol Droplets. *Aerosol Sci. Technol.* **2012**, *46* (6), 666–677.

(30) Davies, J. F.; Miles, R. E. H.; Haddrell, A. E.; Reid, J. P. Influence of Organic Films on

the Evaporation and Condensation of Water in Aerosol. *Proc. Natl. Acad. Sci. U. S. A.* **2013**, *110* (22), 8807–8812.

(31) Miles, R. E. H.; Davies, J. F.; Reid, J. P. The Influence of the Surface Composition of Mixed Monolayer Films on the Evaporation Coefficient of Water. *Phys. Chem. Chem. Phys.* **2016**, *18* (29), 19847–19858.

(32) Davies, J. F.; Miles, R. E. H.; Haddrell, A. E.; Reid, J. P. Temperature Dependence of the Vapor Pressure and Evaporation Coefficient of Supercooled Water. *J. Geophys. Res.* **2014**, *119* (18), 10931–10940.

(33) Vortisch, H.; Kramer, B.; Weidinger, I.; Woste, L.; Leisner, T.; Schwell, M.; Baumgartel, H.; Ruhl, E. Homogeneous Freezing Nucleation Rates and Crystallization Dynamics of Single Levitated Sulfuric Acid Solution Droplets. *Phys. Chem. Chem. Phys.* **2000**, *2* (7), 1407–1413.

(34) Kramer, B.; Hubner, O.; Vortisch, H.; Woste, L.; Leisner, T.; Schwell, M.; Ruhl, E.; Baumgartel, H. Homogeneous Nucleation Rates of Supercooled Water Measured in Single Levitated Microdroplets. *J. Chem. Phys.* **1999**, *111* (14), 6521–6527.

(35) Stockel, P.; Vortisch, H.; Leisner, T.; Baumgartel, H. Homogeneous Nucleation of Supercooled Liquid Water in Levitated Microdroplets. *J. Mol. Liq.* **2002**, *96–7*, 153–175.

(36) Tong, H. J.; Ouyang, B.; Nikolovski, N.; Lienhard, D. M.; Pope, F. D.; Kalberer, M. A New Electrodynamic Balance (EDB) Design for Low-Temperature Studies: Application to Immersion Freezing of Pollen Extract Bioaerosols. *Atmos. Meas. Tech.* **2015**, *8* (3), 1183–1195.

(37) Hermann, G.; Zhang, Y.; Wassermann, B.; Fischer, H.; Quennet, M.; Ruhl, E. Charge Effects on the Efflorescence in Single Levitated Droplets. *J. Phys. Chem. A* **2017**, *121* (36), 6790–6799.

(38) Zobrist, B.; Soonsin, V.; Luo, B. P.; Krieger, U. K.; Marcolli, C.; Peter, T.; Koop, T. Ultra-Slow Water Diffusion in Aqueous Sucrose Glasses. *Phys. Chem. Chem. Phys.* **2011**, *13* (8), 3514–3526.

(39) Schlemmer, S.; Illemann, J.; Wellert, S.; Gerlich, D. Nondestructive High-Resolution and Absolute Mass Determination of Single Charged Particles in a Three-Dimensional Quadrupole Trap. *J. Appl. Phys.* **2001**, *90* (10), 5410–5418.

(40) Trevitt, A. J.; Wearne, P. J.; Bieske, E. J. Calibration of a Quadrupole Ion Trap for Particle Mass Spectrometry. *Int. J. Mass Spectrom.* **2007**, *262* (3), 241–246.

(41) Salomon, M. *Thermodynamic Properties of Liquid* H_2O *and* D_2O *and Their Mixtures*; United States. National Aeronautics and Space Administration. “NASA Technical Note.” Print.: Washington, D.C., 1969.

(42) Glantschnig, W. J.; Chen, S. H. Light-Scattering From Water Droplets in the Geometrical-Optics Approximation. *Appl. Opt.* **1981**, *20* (14), 2499–2509.

(43) Norrish, R. S. An Equation for the Activity Coefficients and Equilibrium Relative Humidities of Water in Confectionery Syrups. *J. Food Sci. Technol.* **1966**, *1*, 25–39.

(44) Chirife, J.; Ferro Fontan, C.; Benmergui, E. A. The Prediction of Water Activity in Aqueous Solutions in Connection with Intermediate Moisture Foods IV. Aw Prediction in Aqueous Non Electrolyte Solutions. *J. Food Technol.* **1980**, *15*, 59–70.

(45) Starzak, M.; Peacock, S. D. Water Activity Coefficient in Aqueous Solutions of Sucrose. A Comprehensive Data Analysis. *Zuckerindustrie (Berlin)* **1997**, *122* (5), 380–387.

(46) Lide, D. R. *CRC Handbook of Chemistry and Physics. 79th Ed.*; CRC Press Inc.: Boca Raton, FL, 1998.

(47) K.-J. Rosenbruch, B. P. and H. R. Die Temperaturabhangigkeit Der Brechzahl von Wassrigen Saccharoselosungen. *PTB-Mitt.* **1975**, *85* (6), 458–465.

(48) Lienhard, D. M.; Bones, D. L.; Zuend, A.; Krieger, U. K.; Reid, J. P.; Peter, T. Measurements of Thermodynamic and Optical Properties of Selected Aqueous Organic and Organic-Inorganic Mixtures of Atmospheric Relevance. *J. Phys. Chem. A* **2012**, *116* (40), 9954–9968.

(49) Moridnejad, A.; Preston, T. C. Models of Isotopic Water Diffusion in Spherical Aerosol Particles. *J. Phys. Chem. A* **2016**, *120* (49), 9759–9766.

(50) Vignes, A. Diffusion in Binary Solutions - Variation of Diffusion Coefficient with Composition. *Ind. Eng. Chem. Fundam.* **1966**, *5* (2), 189–199.

(51) Zobrist, B.; Soonsin, V.; Luo, B. P.; Krieger, U. K.; Marcolli, C.; Peter, T.; Koop, T. Ultra-Slow Water Diffusion in Aqueous Sucrose Glasses. *Phys. Chem. Chem. Phys.* **2011**, *13* (8), 3514–3526.

(52) Price, H. C.; Mattsson, J.; Murray, B. J. Sucrose Diffusion in Aqueous Solution. *Phys. Chem. Chem. Phys.* **2016**, *18* (28), 19207–19216.

(53) Rickards, A. M. J.; Song, Y. C.; Miles, R. E. H.; Preston, T. C.; Reid, J. P. Variabilities and Uncertainties in Characterising Water Transport Kinetics in Glassy and Ultraviscous Aerosol. *Phys. Chem. Chem. Phys.* **2015**, *17* (15), 10059–10073.

(54) Preston, T. C.; Reid, J. P. Accurate and Efficient Determination of the Radius, Refractive Index, and Dispersion of Weakly Absorbing Spherical Particle Using Whispering Gallery Modes. *J. Opt. Soc. Am. B-Optical Phys.* **2013**, *30* (8), 2113–2122.

(55) Rzesanke, D.; Nadolny, J.; Duft, D.; Muller, R.; Kiselev, A.; Leisner, T. On the Role of Surface Charges for Homogeneous Freezing of Supercooled Water Microdroplets. *Phys. Chem. Chem. Phys.* **2012**, *14* (26), 9359–9363.

(56) Lienhard, D. M.; Huisman, A. J.; Bones, D. L.; Te, Y. F.; Luo, B. P.; Krieger, U. K.; Reid, J. P. Retrieving the Translational Diffusion Coefficient of Water from Experiments on

Single Levitated Aerosol Droplets. *Phys. Chem. Chem. Phys.* **2014**, *16* (31), 16677–16683.

(57) Marshall, F. H.; Miles, R. E. H.; Song, Y. C.; Ohm, P. B.; Power, R. M.; Reid, J. P.; Dutcher, C. S. Diffusion and Reactivity in Ultraviscous Aerosol and the Correlation with Particle Viscosity. *Chem. Sci.* **2016**, *7* (2), 1298–1308.

(58) Shiraiwa, M.; Pfrang, C.; Pöschl, U. Kinetic Multi-Layer Model of Aerosol Surface and Bulk Chemistry (KM-SUB): The Influence of Interfacial Transport and Bulk Diffusion on the Oxidation of Oleic Acid by Ozone. *Atmos. Chem. Phys.* **2010**, *10* (8), 3673–3691.

(59) Fowler, K.; Connolly, P. J.; Topping, D. O.; O'Meara, S. Maxwell-Stefan Diffusion: A Framework for Predicting Condensed Phase Diffusion and Phase Separation in Atmospheric Aerosol. *Atmos. Chem. Phys.* **2018**, *18* (3), 1629–1642.

(60) Virtanen, A.; Joutsensaari, J.; Koop, T.; Kannosto, J.; Yli-Pirilä, P.; Leskinen, J.; Mäkelä, J. M.; Holopainen, J. K.; Pöschl, U.; Kulmala, M.; Worsnop, D. R.; Laaksonen, A. An Amorphous Solid State of Biogenic Secondary Organic Aerosol Particles. *Nature* **2010**, *467* (7317), 824–827.

(61) Mullin, J. W.; Leci, C. L. Evidence of Molecular Cluster Formation in Supersaturated Solutions of Citric Acid. *Philos. Mag.* **1969**, *19* (161), 1075–1077.

(62) Ohgaki, K.; Makihara, Y.; Morishita, M.; Ueda, M.; Hirokawa, N. Solute Clusters in Aqueous Citric Acid Solutions. *Chem. Eng. Sci.* **1991**, *46* (12), 3283–3287.

(63) Ohgaki, K.; Hirokawa, N.; Ueda, M. Heterogeneity in Aqueous Solutions: Electron Microscopy of Citric Acid Solutions. *Chem. Eng. Sci.* **1992**, *47* (8), 1819–1823.

(64) Larson, M. A.; Garside, J. Solute Clustering in Supersaturated Solutions. *Chem. Eng. Sci.* **1986**, *41* (5), 1285–1289.

(65) Shiraiwa, M.; Li, Y.; Tsimpidi, A. P.; Karydis, V. A.; Berkemeier, T.; Pandis, S. N.; Lelieveld, J.; Koop, T.; Pöschl, U. Global Distribution of Particle Phase State in Atmospheric Secondary Organic Aerosols. *Nat. Commun.* **2017**, *8*, 1–7.

(66) Bohren, C. F.; Huffman, D. R. *Absorption and Scattering of Light by Small Particles*; John Wiley & Sons, Inc.: New York, NY, 1998; Vol. 31.

(67) Mätzler, C. MATLAB Functions for Mie Scattering and Absorption. *IAP Res Rep* **2002**, *2002–08*, opening-18.

CHAPTER 4: Evolution of Hydrogen Bond Interactions Within Aqueous Sucrose and Citric Acid Droplets

4.1: Introduction

Atmospheric aerosols are of great interest because of their significant impacts on the environment and human health by affecting climate through radiative forcing, providing reaction sites for heterogeneous chemistry, and causing respiratory and cardiovascular deseases.[1,2] Recent studies have shown viability of pathogenic bacteria and viruses in the aerosol form, including SARS-CoV-2 which is known to cause coronavirus disease 2019 (COVID-19).[3–5] Therefore, it is important to understand the unique physical and chemical properties of atmospheric aerosols that often differ from bulk properties of the same compounds, e.g., owing to the large surface to volume ratio and high supersaturation. Organic aerosols (OAs) can be emitted directly from the source (primary OAs) or produced by a series of oxidative reactions (secondary OAs). It has been discovered that OAs can exist as metastable liquid as well as amorphous solid (glassy) droplets.[6–8] This range of phenomena poses a significant difficulty for treating atmospheric aerosols in climate models because current models assume aerosols are in thermodynamically equilibrated liquid or solid states.[9] Moreover, recent studies have revealed phase separation and kinetic limitations for diffusion within highly supersaturated and glassy OAs, which are nonequilibrium phenomena mediated by intermolecular interactions including hydrogen bonding.[10,11] These results have substantial ramifications on the physical and chemical properties of atmospheric aerosols, such as water uptake, heterogeneous chemical reactions, ice nucleation, and long-range transport of toxic pollutants.[12–14] To provide further insights into these systems, the present study examines fundamental molecular interactions in supersaturated OAs, focusing on the hydrogen bonding network in these aerosol as a function of relative humidity.

Primary and secondary OAs can undergo oxidative reactions, forming less volatile and more hygroscopic oxygenated organic aerosols (OOAs).[15] To understand the unique properties of supersaturated OOAs, it is critical to characterize the hydrogen bond interactions within them. In supersaturated OOAs water acts as a bonding media between organic molecules and leads to significant intermolecular interactions through hydrogen bonds. Hydrogen bond interactions manifest themselves in macroscopic properties of OOAs such as phase state, viscosity, nucleation, and cloud condensation.[16] Although a water molecule has a simple structure, liquid water forms complex local structures, due to extensive hydrogen bond networks. Vibrational spectroscopy (FTIR or Raman) is a powerful experimental tool to unravel such intricate hydrogen bond interactions because of their sensitivity to O-H stretching vibrations. Studies on these topics have provided insights into the structure of water at ambient to extreme conditions,[17–19] effects of ions on the structure of water,[20–22] and hydrogen bond interactions in organic-water systems.[23]

Aqueous citric acid (CA) and aqueous sucrose droplets were chosen as model OOAs. They are common compounds in OOAs, and they both exhibit the ability to form glassy states under certain conditions.[14,24,25] In the form of an aqueous droplet, both CA-water and sucrose-water systems can exist in a supersaturated state at ambient temperature.[26] However, in detail, the hydrogen bond interactions in these two systems differ considerably because CA and sucrose have distinctive hydrophilic functional groups, i.e., CA is a tricarboxylic acid with one hydroxyl group and sucrose is a disaccharide containing 8 hydroxyl groups and three ether groups (**Figure 4.1**). In dilute aqueous solution, the difference of the solute effects on hydrogen bond interactions may be

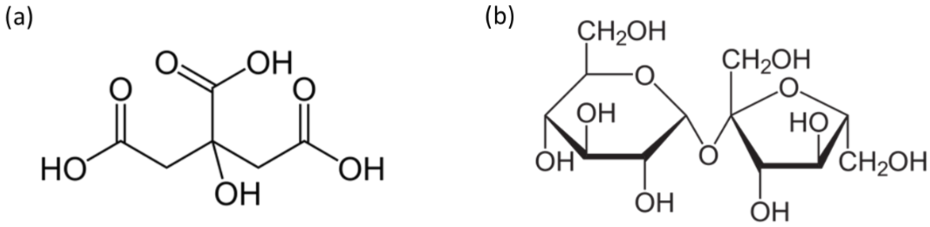

Figure 4.1: Molecular structure of citric acid (a) and sucrose (b).

minute as both solutes only disturb the local water-water interactions through solvation. The dissimilarity arises in high solute supersaturation as the fraction of solutes in the aqueous droplet become significant, and solute-solute interactions become increasingly important. Thus, it is expected that the different structures of the hydrophilic groups in these solutes can lead to differences in the hydrogen bond interactions in aqueous CA and aqueous sucrose droplets in highly supersaturated OOAs.

Contact-free levitation is a key condition in the investigations reported here because heterogeneous nucleation sites, such as surface contact, can trigger crystallization of metastable droplets. Aerosol optical tweezer (AOT) and electrodynamic balance (EDB) instruments are commonly used to confine single microdroplets in a contact-free manner.[27] AOT traps a single spherical droplet at the center of a tightly focused laser beam by balancing gravity with the photon gradient force. AOTs have been used in aerosol chemistry and physics including studies of chemical kinetics,[28] hygroscopicity,[29] optical properties,[26] and water diffusion.[30] EDBs are another widely-used technique in aerosol research, making use of a combination of AC and DC electric fields to confine single charged droplets.[31] The levitation ability of EDBs is not limited by size or morphology. Thus EDB can effectively perform studies involving phase transitions or nucleation.[32,33]

In spite of a number of theoretical investigations on understanding hydrogen bond structures in atmospheric aerosols, there has been a lack of laboratory studies.[16,34] The present work uses an environment-controlled EDB to trap single model OOAs (CA or sucrose) for study with *in situ*-Raman and Mie scattering spectroscopy. Integration of these techniques with the EDB allows measuring the spectroscopic signatures of hydrogen bonding in metastable liquid OOAs. Raman spectra of single droplets as a function of relative humidity (RH) were obtained. Mie scattering image analysis was used to probe the size and phase state of the droplet under study. The Raman spectral region of 3000 - 3800 cm^{-1} (O-H stretch band, ν(O-H)) upon evaporation was primarily analyzed by using Gaussian deconvolution as well as a 2D correlation method. The 2D correlation method provides a great advantage in this study because of the sensitivity to asynchronous intensity changes in different spectral regions, which are often overlooked by conventional spectrum analysis.[35,36] Thus, the 2D correlation method enables a detailed description of the evolution of the intermolecular hydrogen bond interactions in these systems. Combination of linear and 2D spectral analysis clearly shows the evidence of different hydrogen bond dynamics within CA and sucrose droplets. It was found that the persistence of local hydrogen bond interactions is determined by the functional groups of the solute, especially at high supersaturation. The results imply that carboxylic groups in CA lead to the sequential evolution of strong and weak hydrogen bond interactions as evaporation of a metastable CA droplet occurs. On the other hand, hydrogen bond interactions in a sucrose droplet display correlated network-like behavior.

4.2: Experimental Methods

4.2.1: Single Particle Confinement and *In-situ* Spectroscopic Techniques

The environment-controlled EDB with Mie and Raman spectroscopy setup has been previously described in detail.[11] Schematic layout of the EDB system is shown in **Figure 4.2.** In brief, a combination of AC and DC voltages from conical endcaps and 8 rod electrodes confines a single charged droplet at the null point of the trap. An inductive charging ring and a grounded piezoelectric tip charge the droplets. The principle and applications of EDB have been well

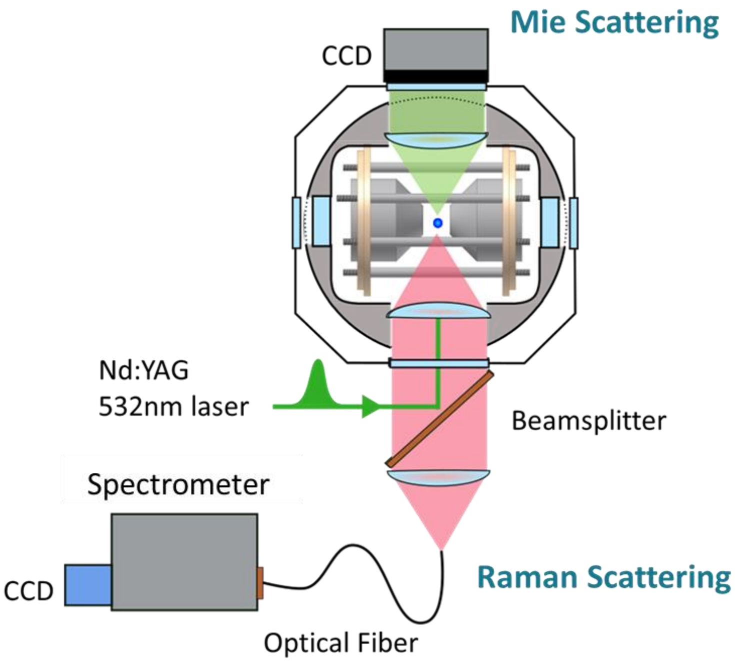

Figure 4.2: The electrodynamic balance (EDB) apparatus setup with Raman spectroscopy and Mie scattering imaging. A droplet is located at the center of the trap (blue dot). A 532 nm pulsed laser is focused on the droplet generating an elastic Mie scattering pattern (green shade) and inelastic Raman scattering signal (red shade).

established.[37,38] The trapped droplet was irradiated by a pulsed 532nm Nd:YAG laser beam (RPMC Wedge XF, 3.5 μs pulsewidth, 80kHz repetition rate) with ~25 mW average power. Back-scattered Raman signal with all polarizations was collected through a fiber optic coupled into a spectrometer (Acton SpectraPro 275, f/3.8) equipped with a 600 g/mm grating and an open-electrode TE-cooled CCD detector (Horiba Syncerity). The exposure time was 30-60 s, and two spectra at each RH were averaged to obtain high signal to noise ratio spectra for single droplets. The effective spectral resolution was ~6 cm^{-1}. Spectrometer calibration was done using four strong Raman peaks of solid naphthalene (764, 1382, 1577, 3056 cm^{-1}).[39] The forward scattered (45°) Mie scattering pattern was collected using a CCD camera with 16.3° solid angle. Typical diameters of the droplets determined by analysis of the Mie scattering patterns was 40-60 μm, with the analysis carried out as described in ref. 11 and earlier study.[40,41] Based on previous studies, the surface charge density of the droplet in this work (<40 elementary charges per μm^2) was assumed to have only negligible effects on the Raman spectra.[11,42,43]

Aqueous solutions were prepared by dissolving citric acid (99% purity, Macron Fine Chemicals) and sucrose (99.9% purity, Fisher) in deionized water. Typical initial concentrations of both solutions before injection into the trap was 1.5-2.0 M. Measurements were made over the RH range between 88% to 0.6% (±1.5%) as determined using a capacitive humidity sensor (Vaisala Humicap 180R). The relative humidity inside the trap was controlled by a bubbler system consisting of digital mass flow controllers (Alicat MC-500SCCM) coupled with dry and humid N_2. Both droplets are expected to have concentration inhomogeneity at lower RH region due to the slow diffusion rate of water (RH 11% and below for CA and 52% and below for sucrose). The inner concentration gradient of the droplets is modeled by using kinetic multi-layer model by Zobrist et al., and described in detail on Supporting Information **Figure S4.1**. Raman spectra collected at non-equilibrium conditions represent ensemble average of molecular vibrations of the droplets, not accountable for concentration gradient. All measurements were made at ambient temperature (19-21 °C). Over the entire RH range studied here, the Mie scattering images for both CA and sucrose droplets exhibited regular diffraction patterns, indicating that the droplets maintained spherically symmetric metastable liquid states without noticeable phase transition during these studies. Raman spectrum of neat water was obtained by using cuvette holder with optical fiber adapter (Thorlabs CVH100) located in the laser path past the EDB.

4.2.2: Raman Spectrum of Liquid Water: O-H Stretching Modes

The Raman spectrum of liquid water, especially the broad band of the O-H stretching region (ν(O-H); 2800 – 3800 cm^{-1}) is of great interest, and many studies have attempted to explain its unique spectral characteristics. [17,19,44,45] In the present study, this feature is examined using a conventional three-Gaussian peak deconvolution of the ν(O-H) band.[21,46,47] For analysis of liquid phase Raman spectra, Gaussians are commonly used because complex interactions between O-H oscillators lead to inhomogeneous broadening of the spectral lineshape.[48] **Figure 4.3** shows the Raman spectrum of bulk liquid water in the ν(O-H) region and its three-Gaussian fit. Following generally accepted peak assignments, the broad ν(O-H) band of liquid water consists of a strong hydrogen bond peak (~3250 cm^{-1}), a weak hydrogen bond peak (~3450 cm^{-1}), and a weakest hydrogen bond, or non-bonded O-H (~3650 cm^{-1}) peak.[21,49] As a general principle in the harmonic oscillator approximation for the O-H stretching oscillators, hydrogen bond interactions alter the force constants of the oscillators leading to the peak frequency shifts (stronger interactions lowers the force constant and frequency, and vice versa). In **Figure 4.3**, the first two peaks at ~3250 and ~3450 cm^{-1} have notably higher intensity than the non-bonded O-H peak (~3650 cm^{-1}). The overall

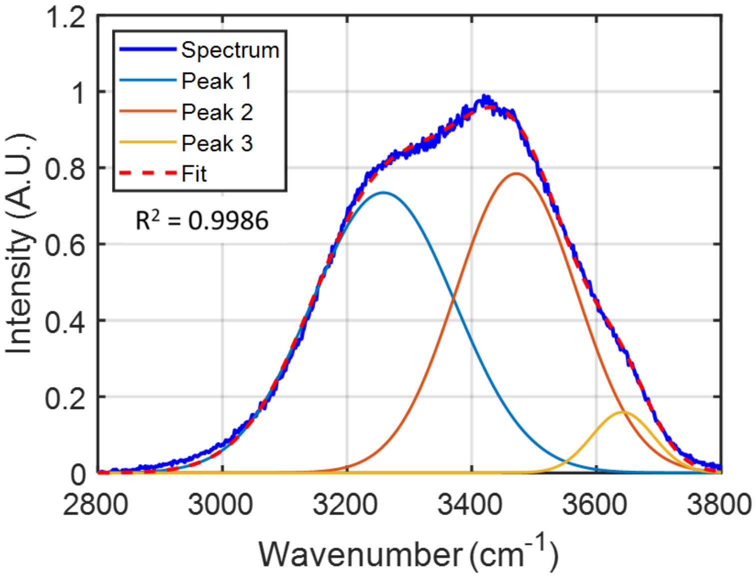

Figure 4.3: Raman spectrum of the O-H stretching band of neat liquid water at 20°C. Three Gaussian peaks are applied to represent different hydrogen bond interactions: peak 1 as strong, peak 2 as weak, and peak 3 as weakest (non-bonded O-H).

shape of the ν(O-H) band transforms in response to physical (temperature and pressure)[17,18,44,50,51] and chemical (concentration and character of solutes)[20–23,52] perturbations due to changes in the hydrogen bonding structure. In the present study the evolution of strong and weak hydrogen bond interactions represented by the peaks at ~3250 and ~3450 cm^{-1} of CA-water and sucrose-water systems is studied.

4.3.3: 2D-Correlation Analysis

The 2D correlation method for linear IR spectrum analysis was first introduced by Noda and has been widely used in various applications including analysis of the structure of water, protein structure and dynamics, and studies of catalytic mechanisms.[19,35,36,53] In 2D correlation analysis, spectral data are treated as matrices as described by equation 4.1,

$$\tilde{\boldsymbol{X}}(v) = \begin{bmatrix} \tilde{x}(v, t_1) \\ \tilde{x}(v, t_2) \\ \vdots \\ \tilde{x}(v, t_m) \end{bmatrix} \tag{4.1}$$

where v is a spectral variable (wavenumber), t_m is the external variable, and m is the number of spectra at given range of external perturbation (RH). $\tilde{x}$ is the dynamic spectrum defined by The difference between the raw and reference spectra is referred to as the dynamic spectrum $\tilde{x}(v, t)$,

$$\tilde{x}(v, t) = x(v, t) - \bar{x}(v) \tag{4.2}$$

where $\bar{x}(v)$ is the reference spectrum chosen in this study to be the spectrum at a chosen RH (67% for CA and 60% for sucrose). These RH points were chosen because the spectral intensities in the linear spectra exhibit more subtle changes at lower RH, making the 2D correlation method more useful in the analysis. Using a matrix notation for the dynamic spectrum of the system under study, the synchronous 2D correlation spectrum is obtained by:

$$\boldsymbol{\Phi}(v_1, v_2) = \frac{1}{m-1}\widetilde{\boldsymbol{X}}(v_1)^T\widetilde{\boldsymbol{X}}(v_2) \tag{4.3}$$

Following Noda, the asynchronous 2D correlation spectrum can be described as:

$$\boldsymbol{\psi}(v_1, v_2) = \frac{1}{m-1}\widetilde{\boldsymbol{X}}(v_1)^T\boldsymbol{N}\widetilde{\boldsymbol{X}}(v_2) \tag{4.4}$$

where $\boldsymbol{N}$ is the Hilbert-Noda transformation matrix that orthogonalizes the matrix of experimental data.[54] Equations 4.3 and 4.4 are generalizations of 2D correlation spectroscopy. In the results presented here, this method will be applied to understanding the evolution of the Raman spectra as RH decreases. All data analysis was carried out using Matlab (Mathworks, Naticks, USA).

4.3: Results and Discussion

In the following, first the Raman spectra of the aqueous CA and sucrose droplets as a function of RH will be presented, followed by examining the peak shifts observed as the droplets are dried and reach extreme levels of supersaturation. It should be noted that the intensity distribution of exciting laser within heterogeneous droplets is not homogeneous because different refractive indices in the outer and inner regions can cause the light focused in to particular region.[55,56] This effect should influence the spectral probe region as the droplets dry and from shell-core structures. In the dry particle case, the spectra spatially emphasize the molecular vibrations of outer shell than the inside core of droplets. The 2D correlation analysis of the spectral changes will then be presented.

4.3.1: Aqueous Citric Acid Droplets

A set of ten Raman spectra of the aqueous CA droplet versus decreasing RH (from 82% down to 1%) are shown in **Figure 4.4(a)**. All Mie scattering images obtained over the course of experiment showed regular fringe pattern (**Figure S4.2**), indicating that the droplet did not crystallize even at 1% RH, instead persisting as a spherically symmetric metastable liquid.[26] The wavenumber range of interest (2300 - 3800 cm^{-1}) consists of multiple narrow and wide peaks. **Figure 4.4(b)** shows one example of Gaussian deconvolution of a droplet Raman spectrum. Seven Gaussian components were used to represent different vibrational modes in the spectra. The ν(C-H) peak near 2950 cm^{-1} is minimally affected by RH, and thus it is used to normalize the spectral intensities over the measurements. As the droplet loses water content, the total number of O-H oscillators decreases accompanied by a reduction in the overall intensity of the ν(O-H) bands from 3000 - 3800 cm^{-1}. However, the intensity does not decrease at a uniform rate across the band because the aqueous CA droplet Raman signature contains several distinct O-H oscillators, including the carboxyl group (R-COOH), the hydroxyl group (R-OH), and the water solvent (HOH). These features evolve differently in the drying environment. To study evolution of the hydrogen bond interactions as a function of RH, it is necessary to deconvolute the Raman spectrum in Gaussian peaks assigned to the various O-H containing functional groups.

Compared to the Raman spectrum of water (**Figure 4.3**), spectrum of CA (**Figure 4.4(b)**) has unique features. First, the weak and broad shoulder at ~2600 cm^{-1} shows negligible intensity change over the evaporation of water. Given that this broad shoulder peak is not shown in the sucrose spectrum (**Figure 4.4(d)**), it can be considered as a unique interaction of carboxylic acid

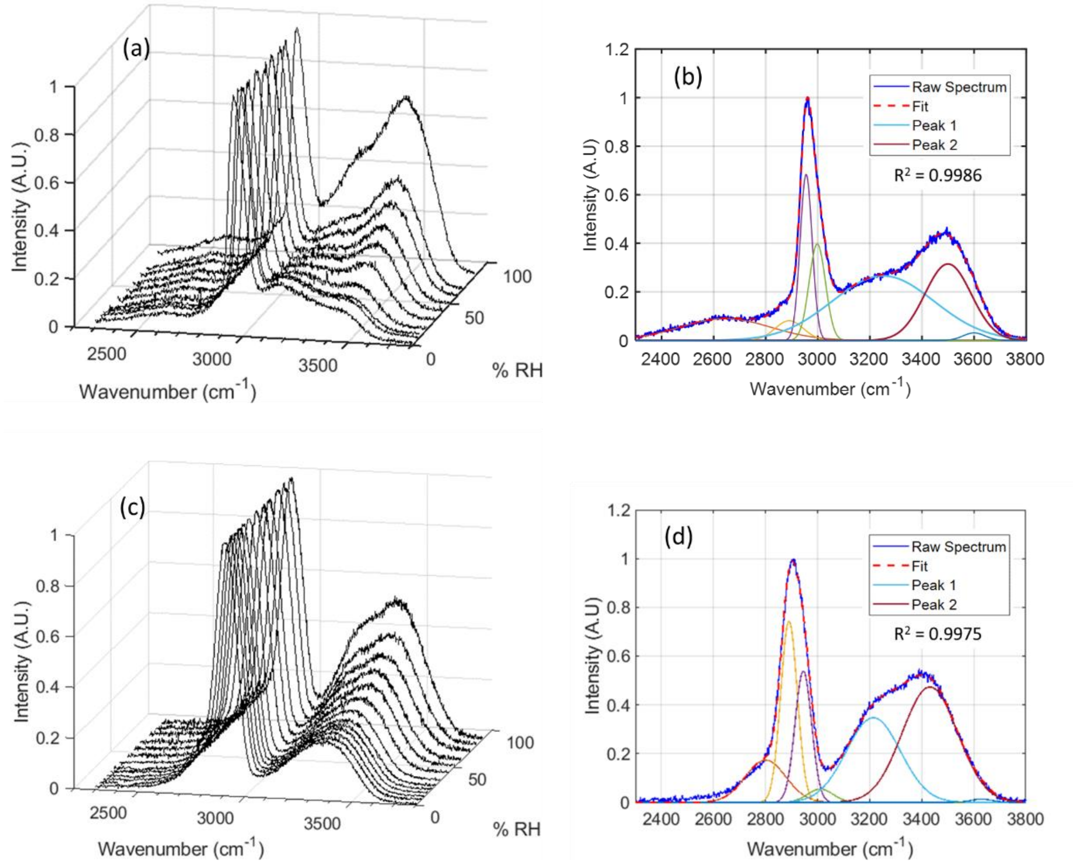

Figure 4.4: (a) Raman spectra of aqueous CA droplet versus RH. (b) Gaussian deconvolution of the Raman spectrum of the CA droplet at 67% RH. Peak assignments are as follows: ~2600 cm-1: ν(O-H) with strongest hydrogen bond, ~2950 cm-1: ~2880 cm^{-1}: combinational, ν(C-H), ~3250 cm-1 (peak 1): ν(O-H) with strong hydrogen bond, ~3500 cm-1(peak 2): ν(O-H) with weak hydrogen bond, and ~3600 cm-1: non-bonded ν(O-H). Frames (c) and (d) show Raman spectra of aqueous sucrose droplet and its Gaussian deconvolution. Peak assignments for sucrose droplet are: ~2800 cm-1: combinational, ~2950 cm-1: ν(C-H), ~3250 cm-1 (peak 1): ν(O-H) with strong hydrogen bond, ~3450 cm-1(peak 2): ν(O-H) with weak hydrogen bond, and ~3630 cm-1: non-bonded ν(O-H). Complete sets of fitting parameters are available in the Supporting Information **Table S4.2** and **S4.3**.

and water. Ab-initio study on hydrated acetic acid showed the strong hydrogen bond of water-bridged acetic acid dimer which leads to the vibrational wavenumber at ~2750 cm-1.[57] Thus, this broad shoulder peak can be assigned as strongest water-CA hydrogen bond interaction which is least affected by the evaporation of water. Similar strong hydrogen bond interactions were also observed recently in biomimetic self-assemblies by vibrational sum frequency generation spectroscopy.[58] Second, width of assigned peak 1 in CA spectrum is larger than the water or sucrose spectrum. According to vibrational spectroscopic studies on various carboxylic acids, small Raman peaks of the acidic O-H stretch lie in the 2800 – 3100 cm^{-1} range as weak shoulders on the strong C-H stretch peak (~2950 cm^{-1}).[59–61] Therefore, peak 1 contains acidic O-H character from CA along with the major contribution from water solvent.

The evolution of the hydrogen bond structures during evaporation of the CA droplet is evident in the overall shape change of the ν(O-H) band. Qualitatively, at the beginning of the measurement (82% RH) the weak hydrogen-bonding peak at ~3500 cm^{-1} (peak 2) is more intense than the strong hydrogen-bonding peak at ~3250 cm^{-1} (peak 1). In contrast, at the end of the measurement (1% RH), peak 1 is the dominant hydroxyl feature in the spectrum. This change can be explained by the interaction of CA and water molecule. Interactions of water molecules in the CA-water solution system can be classified into two broad classes: direct participation in the hydration of CA (first shell of solvent molecules) or only weakly (or not) engaged in the hydration of CA. Stronger hydrogen bond interaction is expected when the water molecules are in the first hydration shell of CA due to the stronger C=O···H-O interaction compared to water-water interactions by ~1 kcal/mol.[62,63] As strong hydrogen bond redshifts the vibrational frequency, one can assume a large contribution to peak 1 comes from water molecules in the first hydration shell and peak 2 has the character of water molecules outside of the hydration shell.

The different decreasing rates of the peaks 1 and 2's intensities upon dehumidifying supports this assignment. As the droplet evaporates, the increase in concentration of CA diminishes the probability of water-water interactions (peak 2) compared to direct water-CA interactions (peak 1), thus the overall intensity decrease is faster for peak 2. The decrease in intensity of peak 1, however, plateaus below 67% RH in spite of continuous evaporation of water. This behavior reinforces the hypothesis that peak 1 mainly originates from the water molecules in the first hydration shell. Given that the CA droplet maintained a spherically symmetric liquid state, as determined by Mie scattering, even under the driest conditions, it can be inferred that CA molecules must stay hydrated to a certain level. These observations are consistent with spectroscopic studies that have shown stronger hydrogen bonding in C=O···H-O interaction compared to H-O···H-O as determined by spectral red-shifts.[60,63,64]

4.3.2: Aqueous Sucrose Droplets

Raman measurements on aqueous sucrose droplets have also been made over the range from 88% down to 1% RH. Thirteen Raman spectra as a function of RH are shown in **Figure 4.4(c)**, exhibiting distinct spectral evolution compared to a CA droplet. At a glance, the intensities of all peaks decrease at similar rates as RH decreases. **Figure 4.4(d)** shows an example of the Gaussian deconvolution for sucrose. As seen in CA, the non-bonded ν(O-H) peak rapidly diminishes below 60% RH. The water-sucrose system contains hydroxyl groups (-OH), ether groups (-O-), as well as the water solvent (HOH). These different functional groups lead one to expect different structural evolution as supersaturation increases compared to the water-CA system. It is notable that the hydrogen bond interaction between sucrose-water (hydroxyl OH-water) is energetically closer to the water-water interaction than CA-water (acidic OH-water).[63,65,66] This means that in a sucrose droplet the formation of a strongly bound first hydration shell is not expected, and a randomized network-like liquid structure is expected to be maintained. Therefore, the overall intensity of the O-H band shows a commensurate decrease of both peaks upon evaporation, maintaining a balanced population ratio of strong to weak hydrogen bonds. Thus, the hydroxyl groups of sucrose and water molecules contribute almost equally to the Raman ν(O-H) spectral feature within the sucrose droplet. The striking dissimilarity of the spectral intensity changes between CA and sucrose droplets provides qualitative insight into the hydrogen bond interactions in these distinct solute systems.

4.3.3: Quantitative Analysis of Spectral Peak Shifts

In addition to the characteristic intensity changes of peak 1 and 2 of the CA and the sucrose droplets discussed earlier, the frequency shifts of the peaks provide further information on the hydrogen bond interactions. The strength of the intermolecular interactions of the O-H ensembles can be probed by examination of the blue- or red-shift of the peaks as a function of RH. The frequency shift of peak 1 and peak 2 of CA and sucrose droplets as a function of RH is shown in **Figure 4.5**. The unitless supersaturation ratio S is defined by $S = C/C_e$, where C is the solute concentration of the droplet and C_e is the molar concentration of the solution at the saturation point ($C_e(CA) = 3.08$ and $C_e(Sucrose) = 1.95$).[67,68] At each RH measurement, values of S and water mole fraction (x_w) has been calculated using the measured volume of the droplet (equilibrium RHs) and a kinetic model with existing parametrization from the literature.[14,69] Values of S increase from 1.2 to 2.6 for CA and 1.2 to 2.0 for sucrose as the droplets evaporate (data for RH versus S and x_w are available in **Table S4.1**). For the CA droplet, peak 1 shows a steady red-shift down to 10% RH. This frequency shift is consistent with increasingly strong hydrogen bond

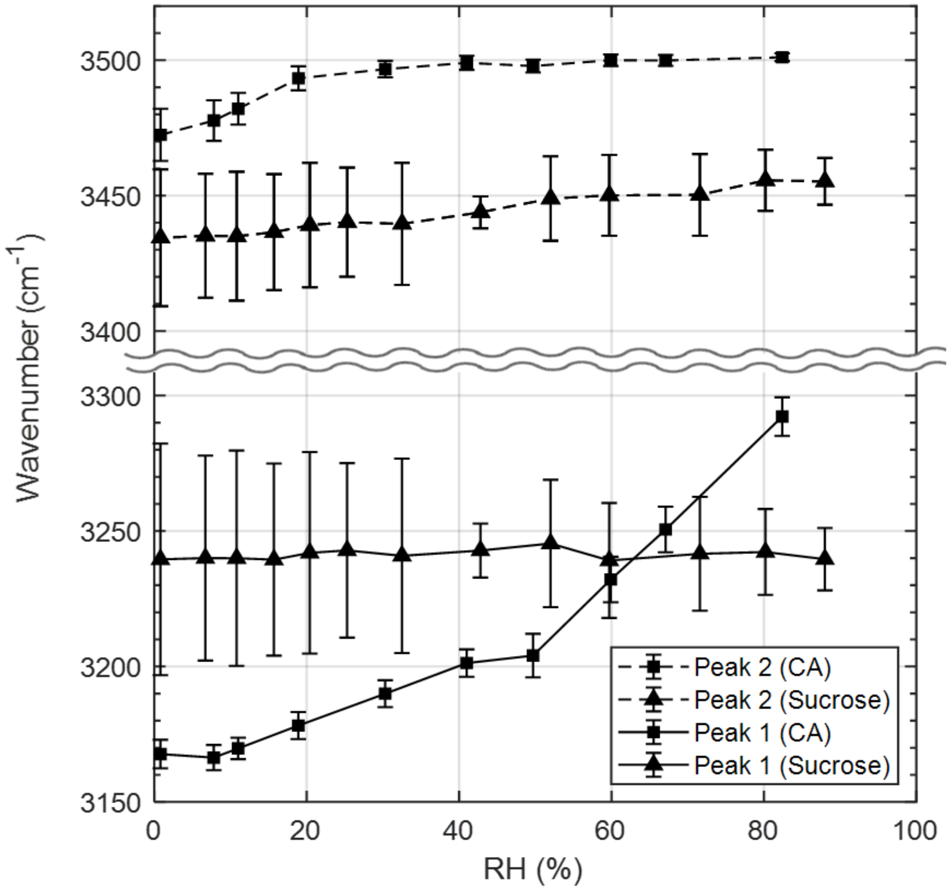

Figure 4.5: Frequency shifts of peak 1 and 2 for CA (squares) and sucrose (triangles) droplets versus RH. Lines are guides to the eyes. Error bars are expressed as 95% confidence intervals in the Gaussian fitting method.

interactions as the droplet evaporates and equilibrates to higher concentration. Below 10% RH, an abrupt diminution in the red-shift of peak 1 in this region is observed. The red-shift of peak 2 in CA exhibits a sudden change at high supersaturation (RH < 20%). This suggests that these different rates of frequency shift are related to the dependence of the distribution of hydrogen bonds in the water-CA system on the water content. The total frequency shift of peak 1 (120 cm^{-1}) is as large as the red-shift observed in the water to ice phase transition.[70] This comparison and the steady dependence of the red-shift support the assertion that C=O···H-O-H interactions in the hydration shell constitute the main contribution to peak 1. As the droplet evaporates, the CA molecules, including the hydration shell, gain more proximity and may form water-bridged (CA-water-CA) liquid structures. In addition, the local cyclic (COOH···HOOC) interaction of CA-CA can appear in such high solute concentration.[57] The strength of C=O···H-O hydrogen bond between cyclic CA-CA interaction is even stronger than that of COOH-water, and accompanied shift in the ν(O-H) frequency can be observed at the spectral region of peak 1 (3000~3200 cm^{-1}).[62] This increased probability for these strong interactions may lead to the substantial monotonic red-shift of peak 1 in CA droplets. Therefore, not only the increasing probability of CA-water contributes to the large red-shift of peak 1 but also the augmenting number of events in COOH···HOOC interactions play an important part as the evaporation of the droplet continues. These changes in overall hydrogen bond interactions and their spectral contribution can explain the peculiar read-shift (120 cm^{-1}) of peak 1.

On the other hand, the rapid red-shift of peak 2 below RH ~20% suggests that weaker hydrogen bond interactions are mainly affected at low RH, unlike peak 1 (strong interaction). These observations on peak shifts draws general molecular picture of hydrogen bond evolution in supersaturated CA-water system under continuous evaporation: CA molecules form water-bridged complex liquid structure early and the remaining water molecules start being incorporated with the structure. This de-coupling behavior of strong and weak interactions in CA droplet will be discussed in detail using 2D correlation analysis at later section.

In the case of sucrose droplet, the frequency shift of peak 1 is negligible considering the uncertainty of peak position determination using the Gaussian deconvolution. Unlike CA, the molecular structure of sucrose does not favor the formation of strongly bound water-bridged structures given the more weakly hydrogen-bonded hydroxyl groups that are involved. This is consistent with the absence of a pronounced red-shift of peak 1 in sucrose. For the weaker hydrogen bonds (peak 2), sucrose droplets exhibit a linear red-shift of about ~18 cm^{-1} over the evaporation. This red-shift may be caused by increased hydrogen bond interactions as the mobility of water molecules decrease. According to the calculation with the kinetic multi-layer model, sucrose droplet formed glassy outer shell and the rate of equilibration of the droplet dramatically decreases below 50% RH (**Figure S4.1**). Thus, frequency shift of peak 1 and 2 at this non-equilibrium RH region showed minimal variation considering large uncertainty (**Figure 4.5**). Overall, in sucrose droplets the strengthening of hydrogen bond interactions as shown by the red-shift of peak 2 (18 cm^{-1}) is minor compared to the red-shift of CA droplets (peak 1: 120 cm^{-1}, peak 2: 30 cm^{-1}).

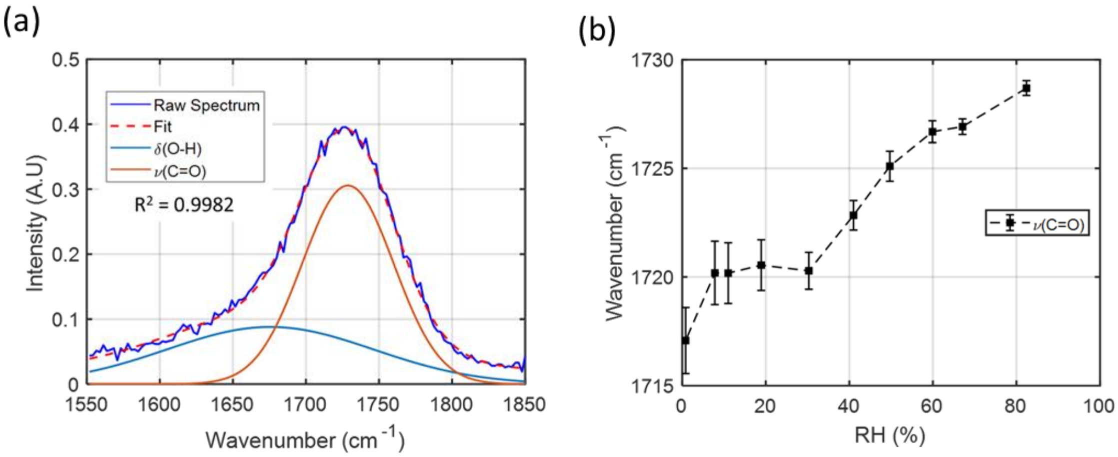

Figure 4.6: (a) Two-Gaussian fit of the 1550 – 1850 cm^{-1} region of the CA droplet at 82% RH. Here, the spectrum is deconvoluted with contributions from a broad water bending peak, δ(O-H), and a more strongly peaked carbonyl stretch, ν(C=O). (b) Upon the evaporation of the droplet, a red-shift of the ν(C=O) peak was observed. A full table of fitting parameters are given in Supporting Information **Table S4.4**.

In addition to the frequency shift of the ν(O-H) band, the evolution of the C=O stretch (~ 1730 cm^{-1}) and O-H bending (~1650 cm^{-1}) modes are demonstrated using a two-Gaussian analysis in **Figure 4.6**. Along with the decrease in RH, cyclic hydrogen bond interactions between carboxyl groups (COOH···HOOC) intensifies as the CA molecules gain more proximity as well as the CA-water-CA interaction. These growing interactions lead to the red-shift of ν(C=O) peak as shown in **Figure 4.6(b)**. The trend of red-shift of ν(C=O) peak is qualitatively similar to the peak 1 than peak 2 in **Figure 4.5**. This similarity strengthens the argument that the main contribution to peak 1 in CA droplets is the strong CA-water interaction within the first hydration shell.

3.3.4: 2D-Correlation (2DCOS) Analysis of Raman Spectra

2D correlation spectroscopy is a powerful analytical method especially for comparing multiple spectra with physical or chemical perturbations.[36] In the present study, dehydration through the reduction in the ambient RH is the perturbation for the system, and the 2D correlation Raman spectra (2DCOS) of aqueous CA and sucrose droplets provide insights into the nature of that perturbation independent of the linear spectra presented above. In what follows, the synchronous and asynchronous 2D correlation spectra for CA and sucrose aqueous droplets are presented.

In the 2D synchronous spectrum, simultaneous or coincidental changes of spectral intensities at ν_1 and ν_2 appear as diagonal autopeaks and cross peaks which are symmetric with respect to diagonal axis. When a certain region of the spectra exhibits greater intensity changes as a function of the perturbation, a strong diagonal autopeak appears in that region. Cross peaks emerge in off-diagonal positions when simultaneous spectral changes occur at two different frequencies. A significant cross peak provides evidence for the possibility of a coupled or related origin for the spectral variations at different frequencies. In the 2D asynchronous spectrum only off-diagonal and antisymmetric cross peaks appear. A significant asynchronous cross peak indicates that two dynamic changes in spectral intensities are occurring as a function of the perturbation, and that they vary out of phase with each other. The sign of an asynchronous cross peak is positive when the intensity change at ν_1 occurs before ν_2 as the perturbation progresses, and it is negative if the change at ν_1 occurs after ν_2 in the ordered progression of changing external perturbation.

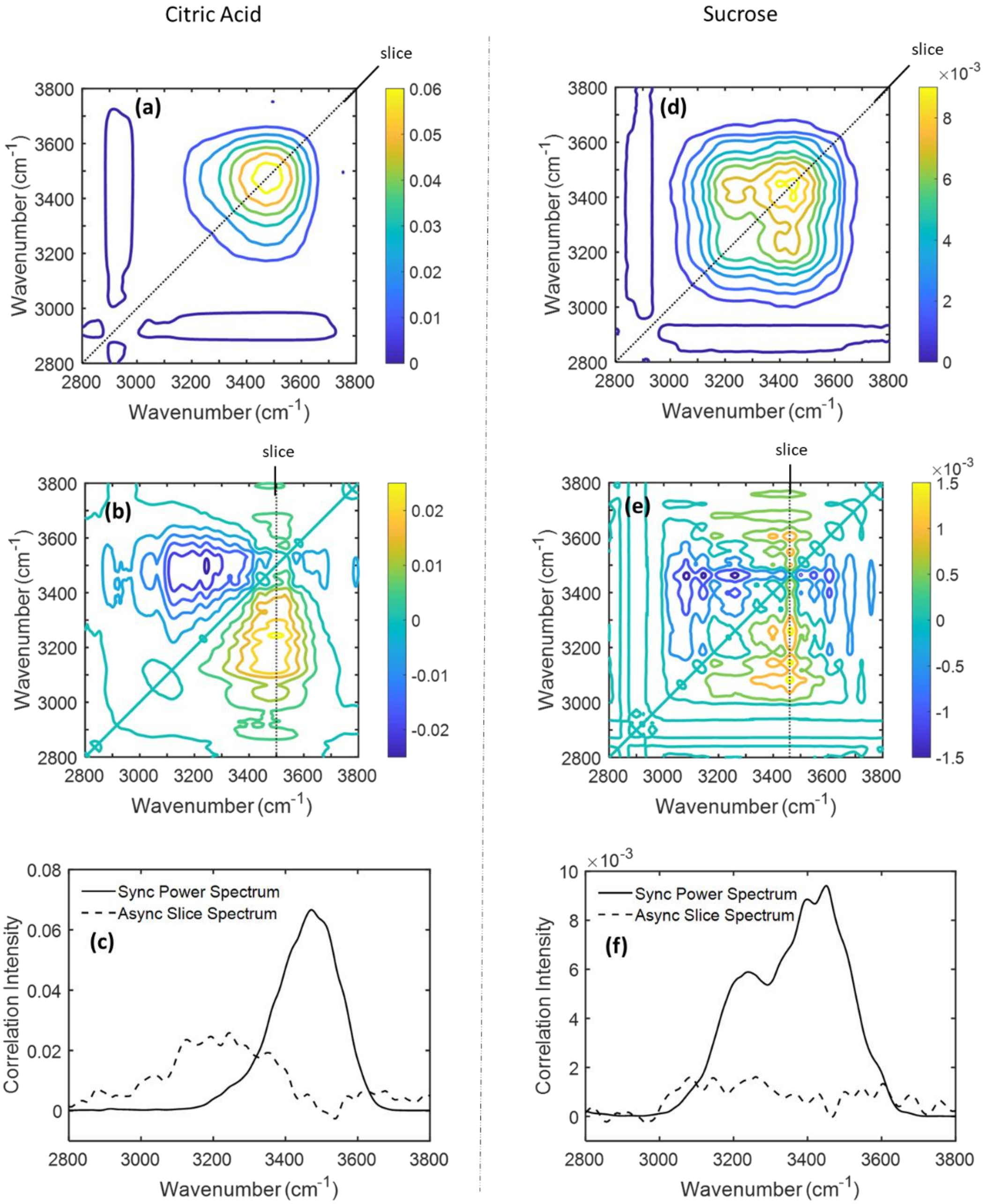

Figure 4.7: 2DCOS of CA and the sucrose droplets. On the left side of the frame, the synchronous spectrum (a), asynchronous spectrum (b), and slice spectra (c) are shown for a CA droplet. Synchronous spectrum (d), asynchronous spectrum (e), and slice spectra (f) for a sucrose droplet are placed on the right side. For synchronous spectra (a) and (d), all correlation intensity values are positive. In asynchronous spectra (b) and (e), yellow and blue lines represent positive and negative correlation intensities, respectively. Raw spectra were smoothed before 2D analysis until noise diminished.

Figure 4.7 shows the 2DCOS for CA (RH = 67 - 1%) and sucrose (RH = 60 - 1%) droplets. The frequencies (in wavenumbers) of the peaks observed in the synchronous and asynchronous spectra are given in **Table 1**. In the 2DCOS of the CA droplet, only a strong autopeak at (3475 cm^{-1}, 3475 cm^{-1}) is evident in the synchronous spectrum (**Figure 4.7(a)**). Except for the minor peak at ~2900 cm^{-1} (negligible correlation between O-H and C-H), there is no off-diagonal correlation peak. **Figure 4.7(c)** shows the power spectrum (diagonal slice) generated from the synchronous spectrum. From the power spectrum it can be inferred that most of the spectral intensity variance takes place near 3500 cm^{-1}. For the asynchronous spectrum (**Figure 4.7(b)**), strong asynchronicity near (3500 cm^{-1}, 3250 cm^{-1}) is observed and the corresponding slice spectrum is shown in **Figure 4.7(c)**. The presence of the asynchronous peak near (3500 cm^{-1}, 3250 cm^{-1}) informs that the intensity changes in the two frequency regions are out-of-phase, implying there are different kinds of interactions. The metastable CA-water system is not a simple two-component system otherwise asynchronous spectrum would not generate any peak. This asynchronicity and the absence of synchronous cross-peak in the CA droplet supports the hypothesis that there are different origins for the two peaks (~3250 cm^{-1} and ~3500 cm^{-1}) along with the frequency shifts discussed in the previous section. It should be noted that not every spectral feature of the two peaks are due to the strong interaction (CA-water and CA-CA in hydration shell) and weak interaction (water-water interaction outside hydration shell). The overlapping ν(C-H) peak and hydroxyl ν(O-H) from CA make minor contributions to the intensity of peak 1. To elucidate the intermolecular interactions in detail, information beyond the band positions of vibrational spectra is necessary.

2DCOS of the sucrose droplet shows distinct features compared to 2DCOS of CA droplets. The synchronous spectrum of the sucrose droplet (**Figure 4.7(d)**) features two overlapping autopeaks near 3235 cm^{-1} and 3450 cm^{-1} as well as a positive cross-peak at (3235 cm^{-1}, 3450 cm^{-}

^{1}). The position of this cross-peak corresponds with the initial assignment of strong and weak hydrogen bond interactions. The diagonal picture of the synchronous spectrum is explicitly shown in the power spectrum in **Figure 4.7(f)**. Unlike the case of CA droplet, the existence of a synchronous cross-peak indicates that the spectral intensity changes at 3235 cm^{-1} and 3450 cm^{-1} are correlated. Moreover, no significant spectral information can be obtained from the asynchronous spectra (**Figure 4.7(e)**). The slice spectrum at the highest correlation intensity (3460 cm^{-1}) shows small asynchronicity near 3100 cm^{-1} in **Figure 4.7(f)** but this band is indiscernible from the noise-like feature. The overall interpretations on the 2DCOS of the sucrose droplet further strengthens the supposition that the strong and weak hydrogen interactions in this system are correlated with each other and the ν(O-H) spectral features share the common origin (intertwined H-O···H-O interactions of sucrose-sucrose, sucrose-water, and water-water).

Up to this point, 2DCOS on the CA and the sucrose droplet has provided considerable information on the dynamic behavior of the Raman spectra. Peak assignment from the earlier section and the position of synchronous and asynchronous cross-peaks of each system manifest excellent agreement. This consistency may be the reinforcement for the theory: in CA droplets strong (CA-CA and CA-water) and weak (water-water) interactions are not associated, while in sucrose droplets both strong and weak interactions share the same origin. Even the simple observation that the synchronous and asynchronous spectra of both systems demonstrate contrasting patterns reveals that the different functional groups of the solute molecules govern the characters of hydrogen bond interactions, especially in the metastable liquid system.

The significant difference in the extent of strong and weak hydrogen bond interactions in CA versus sucrose can explain the peculiar behaviors of the corresponding droplets at their metastable states. First, it must be noted that the viscosity of sucrose droplets is 4 to 9 orders of magnitude higher than CA droplets in the range of RH = 10 – 50%.[71] According to the studies on the relationship between hydrogen bond and viscosity by Okada et al., the strength of hydrogen bond is not the main factor that affects viscosity.[47] Instead, our in-depth spectroscopic analysis on the CA and the sucrose droplet suggests that the large difference in the viscosity between two systems is due to the characteristic hydrogen bond structure of the solutions. As shown in the asynchronous spectrum of CA (**Figure** 4.**7(b)**), the strong hydrogen bond interactions within the hydration shell and the weak interactions change at different rates. For the sucrose droplet, it was argued that the evident correlation between strong and weak interaction may lead water and sucrose to be intertwined through hydrogen bond and form network-like liquid structure. This divergence in correlated intermolecular behavior may give rise to the orders of magnitudes lower viscosity of CA compared to the sucrose. NMR studies on the viscosity of organic acids in alcohol/water system supports this hypothesis by reporting the change in viscosity is due to the long-range interaction between non-adjacent molecular segments.[72] Strong long-range interactions mentioned in this study may correspond to the network-like liquid structure of the sucrose droplet. Viscosity of OAs is analyzed and predicted using O:C ratio or the types and the number of functional groups of organic molecules.[73,74] In addition to these methods, the results from this study suggest that investigating hydrogen bond dynamics can provide valuable insights to the viscosity of OAs, especially for the aqueous droplets.

Table 4.1: Peak positions (cm^{-1}) determined by 2DCOS analysis in the ν(O-H) vibrational band

Citric Acid		Sucrose	
Synchronous	Asynchronous	Synchronous	Asynchronous
3475	3500	3450	-
-	3250	3235	-

In addition, a previous study measuring diffusion coefficients of water (D_w) using H_2O/D_2O exchange from this laboratory presented evidence for significant diffusion inhibition of water in CA droplets at RH below 15%, while sucrose droplets showed slow but complete diffusion.[11] To account for incomplete exchange of H_2O to D_2O in CA droplets, a parameter χ ($0 < \chi < 1$) to represent the asymptotic isotope exchange fraction was adopted. For example, at 8% RH, the H_2O/D_2O exchange of the droplet was found to be ~82% complete ($\chi = 0.82$), and the measured D_w value was $2.45 \cdot 10^{-15}$ m^2 s^{-1}. In contrast, sucrose droplets showed complete H_2O/D_2O exchange at 26% RH, where measured value of D_w was nearly an order of magnitude lower ($4.52 \cdot 10^{-16}$ m^2 s^{-1}) than the case of incomplete diffusion in the CA droplet at RH 8%.[11] This distinctive behavior of limitation of water diffusion in metastable CA droplets was attributed to the strong hydrogen bond interactions leading to the formation of local water-bridged CA-water-CA oligomer liquid structures. The result of Raman 2D-COS of this study adds more evidence to the hypothesis that inhibition of diffusion is caused by strong hydrogen bond structures, and these metastable liquid structures lead to a significant internal barrier for diffusion of water within the droplet. The diffusion inhibition has been observed by others and our study sheds light on the fundamental cause of the phenomenon.[7,75]

It is counterintuitive that CA droplets with lower viscosity shows diffusion inhibition compared to the sucrose droplets with much higher viscosity. However, from the result of ν(O-H) frequency shift of the CA droplet, it is plausible that stronger hydrogen bond interaction may lead trapping and immobilization of water molecules around CA molecules. In other words, the primary reason for apparent incomplete H_2O/D_2O exchange of CA droplet below 15% RH described in previous paper is the thermodynamic limitation of water diffusion caused by strong hydrogen bonds. It is well known that the common form of CA crystal in ambient condition is monohydrated structure.[76] Similar to the hydrated crystal structure, highly supersaturated CA droplet may have water-bridged solute liquid structure, and this can be the cause of the diffusion inhibition of water.

4.4: Conclusions

In-situ Raman spectral observations on single aqueous CA and sucrose droplets in the ν(O-H) region over the RH range of 1 - 88 % exhibit changes in the hydrogen bond structures which are related to the differences in the functional groups of these solutes. Gaussian deconvolution of the Raman spectra allowed examination of the spectral reconstruction of the weak and strong hydrogen bond regions. The Raman spectra were analyzed using 2DCOS, showing the decoupling of strong and weak hydrogen bonds for CA droplet and correlation for sucrose droplets at a high level of solute supersaturation. The distinctive macroscopic properties of supersaturated OOAs such as viscosity and water diffusion can be governed by the liquid structures as demonstrated in the intensity ratio of strong and weak hydrogen bond peaks. Use of the environment controlled EDB system in this case allows access to extreme solute supersaturation states of model OOAs and their Raman spectroscopic analysis. These measurements have provided valuable insights into the evolution of hydrogen bond structures, and the molecular origin of nontrivial physical properties of metastable or glassy state OOAs. Further studies include spectral analysis of the temperature effect on these droplets, possibly providing more quantitative information on the energetics and dynamics of hydrogen bond interactions in OOAs.

4.5: Supplementary Information

In these experiments, the levitated single CA and sucrose droplets are not in equilibrium with the gas phase at low RH (11% and below for CA and 52% and below for sucrose). Since the equilibration time required for the droplets used in this experiment can be as large as a month, a kinetic multi-layer model of water diffusion described by Zobrist et al. (ETH model) is applied to the droplets to simulate internal concentration gradient.[14] According to the ETH model, droplets consist of concentric shells with water flow between each shell are dependent on the mole fraction of water (x_w) of adjacent shells. Following application of the ETH model by O'Meara et al., we treated the droplets as 40 concentric shells, and the outermost shell (shell #1) is assumed to rapidly establish equilibrium with the gas phase.[77] The contour plots in **Figure S4.1** below show the simulated response of the internal concentration gradient to step RH changes at the driest condition for CA (**S1(a)**) and sucrose droplets (**S1(b)** and **S1(c)**). For citric acid droplets, the concentration gradient profile showed characteristic relaxation behavior similar to other kinetic multi-layer modeling studies by Shiraiwa et al. and O'Meara et al.[78,79] However, the response of the inner concentration gradient of a sucrose droplet to step RH change became non-linear due to the formation of highly-viscous outer shell layer, greatly reducing the water diffusion rate and acting as a barrier to gas-droplet equilibration. Therefore, the timescale for establishing the gas-droplet equilibrium becomes much slower than the relaxation of the inner concentration gradient. **Figure S4.1(b)** and **(c)** describes the non-linear diffusion phenomena of the 'glassy shell with liquid core' droplet. In **Figure S4.1(b)**, the color bar scale is incapable of describing the droplet behavior due to the large concentration disparity of outer shell and inner core. The glassy shells have x_w value of less than 0.3 while the x_w of the liquid core stays near 0.6. The plot in **Figure S4.1(c)** excludes the outermost shells 1-4, so that the equilibrium process of the liquid fraction of the droplet can be shown. The inner core equilibrates after +40 hours but the concentration discrepancy between the core and shell is still present. This peculiar diffusion profile of sucrose droplets will further be investigated in later studies. Water mole fraction (x_w) and supersaturation ratio (S) of both droplets are calculated and given in **Table S4.1.** For sucrose, x_w and S values of the droplet at equilibrium RH ranges are derived from the measured droplet diameter, while values of non-equilibrium RH ranges are calculated using ETH model. For CA droplets, the density and refractive index parametrization by Lienhard et al. was used.[69]

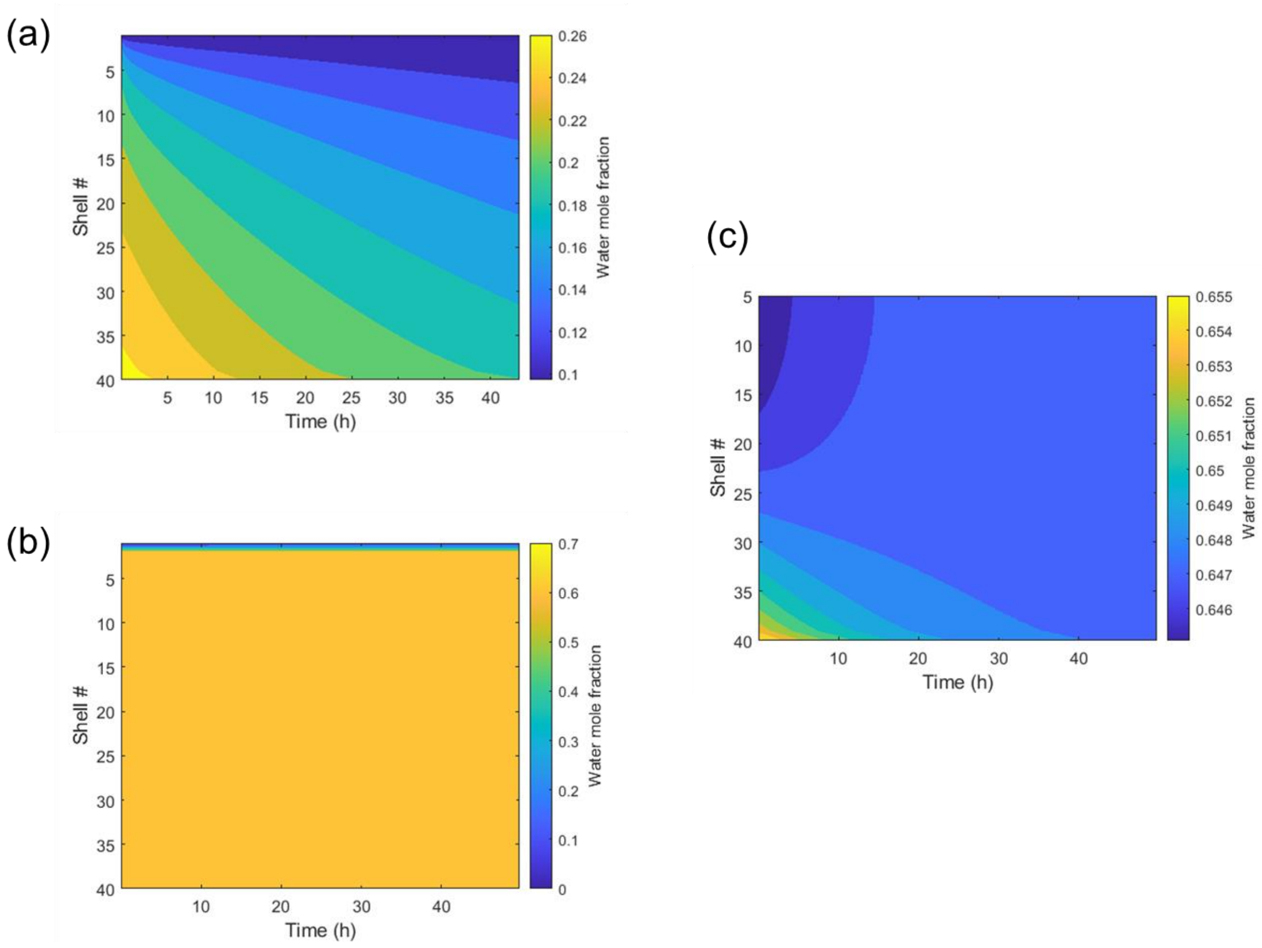

Figure S4.1: Radial concentration profile of the CA (a) and sucrose (b, c) droplets as a function of time. Note that y-axis of the plot is the shell number (#1: outermost shell and #40: innermost sphere). (a) Citric acid, step RH change from 8% to 1% at t = 0. (b) Sucrose, step RH change from 7% to 1% at t=0. (c) Sucrose, step RH change from 7% to 1% at t=0, excluding the outermost shells 1 - 4.

Table S4.1: Water mole fraction (x_w) and supersaturation ratio (S) of the droplets as a function of RH. Note that in the case of the sucrose droplet (b), the decrease of x_w becomes minimal below 25% RH.

(a) Citric acid

	Equilibrium							Non-equilibrium		
RH (%)	82	67	60	50	41	30	19	11	8	1
x_w	0.889	0.806	0.761	0.686	0.614	0.513	0.360	0.259	0.232	0.156
S	1.24	1.68	1.84	2.04	2.18	2.32	2.48	2.55	2.56	2.60

(b) Sucrose

	Equilibrium				
RH (%)	88	80	72	60	52
x_w	0.924	0.886	0.843	0.770	0.722
S	1.18	1.44	1.63	1.85	1.94

	Non-equilibrium							
RH (%)	43	33	25	20	16	11	7	1
x_w	0.690	0.670	0.649	0.646	0.645	0.644	0.643	0.643
S	1.99	2.02	2.05	2.05	2.05	2.05	2.06	2.06

Table S4.2: Gaussian fit parameters for each of the 7 Gaussians in a CA droplet at the full range of RH measurements.

$$Fit = \sum_{i=1}^{7} a_i e^{-\frac{(x-b_i)^2}{2c_i^2}}$$

	1			2			3			4		
RH	a	b	c	a	b	c	a	b	c	a	b	c
82	0.1088	2640.0	250	0.1050	2884.3	80	0.6570	2955.0	32	0.4117	2996.8	45
67	0.0896	2644.5	248	0.0812	2890.0	77	0.6843	2955.0	33	0.3973	2997.8	44
60	0.0835	2642.0	250	0.0683	2880.3	75	0.6728	2955.0	33	0.4052	2996.1	45
50	0.0786	2640.1	250	0.0648	2882.0	75	0.7441	2955.1	33	0.3918	2999.9	40
41	0.0742	2640.9	250	0.0595	2886.4	75	0.7462	2955.0	34	0.3781	3000.0	40
30	0.0732	2640.0	250	0.0590	2889.9	75	0.7638	2955.0	33	0.3715	3000.0	40
19	0.0750	2640.0	250	0.0571	2889.9	75	0.7403	2955.0	34	0.3509	3000.0	40
11	0.0835	2640.0	250	0.0712	2880.2	75	0.7486	2955.0	34	0.3794	2999.7	40
8	0.0803	2640.0	250	0.0671	2885.8	80	0.7515	2955.0	35	0.3861	3000.0	40
1	0.0767	2640.0	250	0.0599	2880.1	78	0.7612	2955.0	35	0.3589	3000.0	40

	5 (Peak 1)			6 (Peak 2)			7		
RH	a	b	c	a	b	c	a	b	c
82	0.4724	3292.3	258	0.4589	3501.1	131	0.0712	3600.0	60
67	0.2660	3250.6	277	0.3151	3499.9	126	0.0312	3600.0	60
60	0.2325	3231.4	278	0.2715	3499.7	126	0.0230	3600.0	60
50	0.2124	3204.0	280	0.2337	3497.9	125	0.0121	3600.0	60
41	0.2050	3201.4	280	0.1946	3499.2	124	0.0018	3600.0	60
30	0.2043	3190.0	276	0.1550	3496.7	121	0.0000	3600.0	60
19	0.2101	3178.8	269	0.1114	3493.5	122	0.0000	3600.0	60
11	0.2164	3169.8	228	0.1080	3482.1	140	0.0000	3600.0	60
8	0.2260	3166.3	232	0.1058	3477.6	137	0.0000	3600.0	60
1	0.2173	3167.6	234	0.0829	3472.2	132	0.0000	3600.0	60

Table S4.3: Gaussian fit parameters for each of the 7 Gaussians in a sucrose droplet at the full range of RH measurements.

	1			2			3			4		
RH	*a*	*b*	*c*	*a*	*b*	*c*	*a*	*b*	*c*	*a*	*b*	*c*
88	0.1732	2800.0	110	0.7424	2890.0	45	0.5381	2945.0	45	0.0542	3010.0	70
80	0.1815	2800.0	110	0.7332	2890.0	45	0.5432	2945.0	45	0.0537	3010.0	70
72	0.1942	2800.0	110	0.7373	2890.0	45	0.5453	2945.0	45	0.0558	3010.0	70
60	0.1990	2800.0	110	0.7211	2890.0	45	0.5452	2945.0	45	0.0608	3010.0	70
52	0.1843	2800.0	110	0.7271	2890.0	45	0.5435	2945.0	45	0.0619	3010.0	70
43	0.1878	2800.0	110	0.7312	2890.0	45	0.5489	2945.0	45	0.0580	3010.0	70
33	0.2011	2800.0	110	0.7277	2890.0	45	0.5511	2945.0	45	0.0609	3010.0	70
25	0.2109	2800.0	110	0.7293	2890.0	45	0.5375	2945.0	45	0.0614	3010.0	70
20	0.2074	2800.0	110	0.7229	2890.0	45	0.5405	2945.0	45	0.0619	3010.0	70
16	0.1830	2800.0	110	0.7369	2890.0	45	0.5462	2945.0	45	0.0596	3010.0	70
11	0.1848	2800.0	110	0.7303	2890.0	45	0.5460	2945.0	45	0.0621	3010.0	70
7	0.2117	2800.0	110	0.7161	2890.0	45	0.5438	2945.0	45	0.0619	3010.0	70
1	0.2111	2800.0	110	0.7241	2890.0	45	0.5561	2945.0	45	0.0582	3010.0	70

	5 (Peak 1)			6 (Peak 2)			7		
RH	*a*	*b*	*c*	*a*	*b*	*c*	*a*	*b*	*c*
88	0.3471	3214.3	147	0.4732	3431.3	150	0.0130	3630.0	60
80	0.2665	3212.9	144	0.3803	3427.2	150	0.0044	3630.0	60
72	0.2262	3215.9	145	0.3244	3424.8	150	0.0006	3630.0	60
60	0.2045	3214.7	150	0.2990	3425.0	150	0.0000	3630.0	60
52	0.1879	3222.2	150	0.2650	3425.6	144	0.0000	3630.0	60
43	0.1653	3218.9	150	0.2442	3419.6	144	0.0000	3630.0	60
33	0.1523	3219.3	150	0.2270	3416.9	146	0.0000	3630.0	60
25	0.1472	3219.9	150	0.2126	3416.7	144	0.0000	3630.0	60
20	0.1407	3217.9	150	0.2088	3414.9	144	0.0000	3630.0	60
16	0.1378	3216.0	150	0.2097	3412.3	144	0.0000	3630.0	60
11	0.1341	3216.8	150	0.2057	3411.2	144	0.0000	3630.0	60
7	0.1315	3218.1	150	0.1983	3411.3	144	0.0000	3630.0	60
1	0.1249	3212.0	150	0.2034	3406.9	146	0.0000	3630.0	60

Table S4.4: Gaussian fit parameters for water bending peak and carbonyl stretch peak of the CA droplet

	δ(O-H)			ν(C=O)		
RH	*a*	*b*	*c*	*a*	*b*	*c*
82.4	0.0880	1675.5	100	0.3058	1728.7	44
67.1	0.0635	1672.8	100	0.2916	1726.9	47
59.9	0.0620	1672.4	100	0.2956	1726.7	49
49.7	0.0527	1663.7	100	0.2952	1725.1	53
41.0	0.0536	1668.5	100	0.2669	1722.8	53
30.3	0.0393	1654.1	100	0.2716	1720.3	58
18.9	0.0465	1662.8	100	0.2399	1720.5	59
11.0	0.0383	1626.7	100	0.2575	1720.2	65
7.8	0.0382	1636.1	100	0.2578	1720.2	63
0.8	0.0236	1598.4	100	0.2493	1717.1	67

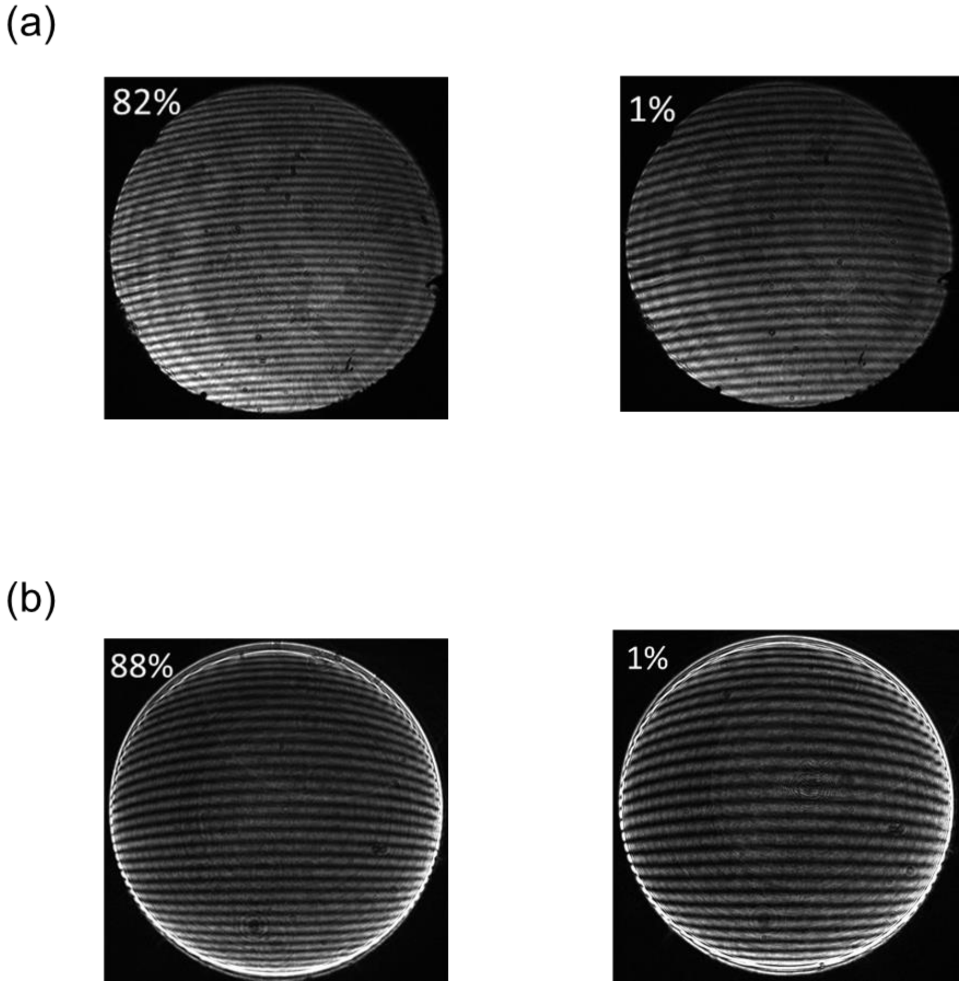

Figure S4.2: Mie scattering images of the droplets at the highest and the lowest RH over the course of the experiment (optical modification for the camera lens system was made between CA and sucrose measurement). (a) Citric Acid, droplet diameter: 51.6 µm (82% RH), 40.0 µm (1% RH). (b) Sucrose, droplet diameter: 59.3 µm (88% RH), 48.0 µm (1% RH).

Acknowledgements

Chapter 4, in full, is a reprint of the material as it appears in Journal of Physical Chemistry B, 2020, Kim, Pyeongeun; Xiong, Wei; Continetti, Robert E. The dissertation author was the primary investigator and author of this paper.

References

(1) Seinfeld, J. H.; Pandis, S. N. *Atmospheric Chemistry and Physics: From Air Pollution to Climate Change*; John Wiley & Sons, 2016.

(2) Shiraiwa, M.; Ueda, K.; Pozzer, A.; Lammel, G.; Kampf, C. J.; Fushimi, A.; Enami, S.; Arangio, A. M.; Fröhlich-Nowoisky, J.; Fujitani, Y.; Furuyama, A.; Lakey, P. S. J.; Lelieveld, J.; Lucas, K.; Morino, Y.; Pöschl, U.; Takahama, S.; Takami, A.; Tong, H.; Weber, B.; Yoshino, A.; Sato, K. Aerosol Health Effects from Molecular to Global Scales. *Environ. Sci. Technol.* **2017**, *51* (23), 13545–13567.

(3) Knibbs, L. D.; Johnson, G. R.; Kidd, T. J.; Cheney, J.; Grimwood, K.; Kattenbelt, J. A.; O'Rourke, P. K.; Ramsay, K. A.; Sly, P. D.; Wainwright, C. E.; Wood, M. E.; Morawska, L.; Bell, S. C. Viability of Pseudomonas Aeruginosa in Cough Aerosols Generated by Persons with Cystic Fibrosis. *Thorax* **2014**, *69* (8), 740–745.

(4) van Doremalen, N.; Bushmaker, T.; Morris, D. H.; Holbrook, M. G.; Gamble, A.; Williamson, B. N.; Tamin, A.; Harcourt, J. L.; Thornburg, N. J.; Gerber, S. I.; Lloyd-Smith, J. O.; de Wit, E.; Munster, V. J. Aerosol and Surface Stability of SARS-CoV-2 as Compared with SARS-CoV-1. *N. Engl. J. Med.* **2020**, *382* (16), 1564–1567.

(5) Prather, K. A.; Wang, C. C.; Schooley, R. T. Reducing Transmission of SARS-CoV-2. *Science* **2020**, *368* (6498), 1422–1424.

(6) Rood, M. J.; Shaw, M. A.; Larson, T. V.; Covert, D. S. Ubiquitous Nature of Ambient Metastable Aerosol. *Nature* **1989**, *337*, 537–539.

(7) Zobrist, B.; Marcolli, C.; Pedernera, D. A.; Koop, T. Do Atmospheric Aerosols Form Glasses? *Atmos. Chem. Phys.* **2008**, *8* (17), 5221–5244.

(8) Shiraiwa, M.; Li, Y.; Tsimpidi, A. P.; Karydis, V. A.; Berkemeier, T.; Pandis, S. N.; Lelieveld, J.; Koop, T.; Pöschl, U. Global Distribution of Particle Phase State in Atmospheric Secondary Organic Aerosols. *Nat. Commun.* **2017**, *8*, 1–7.

(9) Pankow, J. F. An Absorption Model of the Gas/Aerosol Partitioning Involved in the Formation of Secondary Organic Aerosol. *Atmos. Environ.* **1994**, *28*, 189–193.

(10) Freedman, M. A. Phase Separation in Organic Aerosol. *Chem. Soc. Rev.* **2017**, *46* (24), 7694–7705.

(11) Nadler, K. A.; Kim, P.; Huang, D. L.; Xiong, W.; Continetti, R. E. Water Diffusion Measurements of Single Charged Aerosols Using H2O/D2O Isotope Exchange and Raman Spectroscopy in an Electrodynamic Balance. *Phys. Chem. Chem. Phys.* **2019**, *21* (27), 15062–15071.

(12) Davies, J. F.; Wilson, K. R. Nanoscale Interfacial Gradients Formed by the Reactive Uptake of OH Radicals onto Viscous Aerosol Surfaces. *Chem. Sci.* **2015**, *6* (12), 7020–7027.

(13) Bones, D. L.; Reid, J. P.; Lienhard, D. M.; Krieger, U. K. Comparing the Mechanism of Water Condensation and Evaporation in Glassy Aerosol. *Proc. Natl. Acad. Sci.* **2012**, *109* (29), 11613–11618.

(14) Zobrist, B.; Soonsin, V.; Luo, B. P.; Krieger, U. K.; Marcolli, C.; Peter, T.; Koop, T. Ultra-Slow Water Diffusion in Aqueous Sucrose Glasses. *Phys. Chem. Chem. Phys.* **2011**, *13* (8), 3514–3526.

(15) Jimenez, J. L.; Canagaratna, M. R.; Donahue, N. M.; Prevot, A. S. H.; Zhang, Q.; Kroll, J. H.; DeCarlo, P. F.; Allan, J. D.; Coe, H.; Ng, N. L.; Aiken, A. C.; Docherty, K. S.; Ulbrich, I. M.; Grieshop, A. P.; Robinson, A. L.; Duplissy, J.; Smith, J. D.; Wilson, K. R.; Lanz, V. A.; Hueglin, C.; Sun, Y. L.; Tian, J.; Laaksonen, A.; Raatikainen, T.; Rautiainen, J.; Vaattovaara, P.; Ehn, M.; Kulmala, M.; Tomlinson, J. M.; Collins, D. R.; Cubison, M. J.; Dunlea, E. J.; Huffman, J. A.; Onasch, T. B.; Alfarra, M. R.; Williams, P. I.; Bower, K.; Kondo, Y.; Schneider, J.; Drewnick, F.; Borrmann, S.; Weimer, S.; Demerjian, K.; Salcedo, D.; Cottrell, L.; Griffin, R.; Takami, A.; Miyoshi, T.; Hatakeyama, S.; Shimono, A.; Sun, J. Y.; Zhang, Y. M.; Dzepina, K.; Kimmel, J. R.; Sueper, D.; Jayne, J. T.; Herndon, S. C.; Trimborn, A. M.; Williams, L. R.; Wood, E. C.; Middlebrook, A. M.; Kolb, C. E.; Baltensperger, U.; Worsnop, D. R. Evolution of Organic Aerosols in the Atmosphere. *Science* **2009**, *326* (5959), 1525–1529.

(16) Zhao, J.; Khalizov, A.; Zhang, R.; McGraw, R. Hydrogen-Bonding Interaction in Molecular Complexes and Clusters of Aerosol Nucleation Precursors. *J. Phys. Chem. A* **2009**, *113* (4), 680–689.

(17) Walrafen, G. E. Raman Spectral Studies of Water Structure. *J. Chem. Phys.* **1964**, *40* (11), 3249–3256.

(18) Goy, C.; Potenza, M. A. C.; Dedera, S.; Tomut, M.; Guillerm, E.; Kalinin, A.; Voss, K. O.; Schottelius, A.; Petridis, N.; Prosvetov, A.; Tejeda, G.; Fernández, J. M.; Trautmann, C.; Caupin, F.; Glasmacher, U.; Grisenti, R. E. Shrinking of Rapidly Evaporating Water Microdroplets Reveals Their Extreme Supercooling. *Phys. Rev. Lett.* **2018**, *120* (1), 2–7.

(19) Segtnan, V. H.; Šašić, Š.; Isaksson, T.; Ozaki, Y. Studies on the Structure of Water Using Two-Dimensional near-Infrared Correlation Spectroscopy and Principal Component Analysis. *Anal. Chem.* **2001**, *73* (13), 3153–3161.

(20) Vollmar, P. M. Ionic Interactions in Aqueous Solution: A Raman Spectral Study. *J. Chem. Phys.* **1963**, *39* (9), 2236–2248.

(21) Liu, D.; Ma, G.; Levering, L. M.; Allen, H. C. Vibrational Spectroscopy of Aqueous Sodium Halide Solutions and Air−Liquid Interfaces: Observation of Increased Interfacial Depth. *J. Phys. Chem. B* **2004**, *108* (7), 2252–2260.

(22) Ahmed, M.; Namboodiri, V.; Singh, A. K.; Mondal, J. A.; Sarkar, S. K. How Ions Affect the Structure of Water: A Combined Raman Spectroscopy and Multivariate Curve Resolution Study. *J. Phys. Chem. B* **2013**, *117* (51), 16479–16485.

(23) Dolenko, T. A.; Burikov, S. A.; Dolenko, S. A.; Efitorov, A. O.; Plastinin, I. V.; Yuzhakov, V. I.; Patsaeva, S. V. Raman Spectroscopy of Water-Ethanol Solutions: The Estimation of Hydrogen Bonding Energy and the Appearance of Clathrate-like Structures in Solutions. *J. Phys. Chem. A* **2015**, *119* (44), 10806–10815.

(24) Bogdan, A.; Molina, M. J.; Tenhu, H.; Loerting, T. Multiple Glass Transitions and Freezing Events of Aqueous Citric Acid. *J. Phys. Chem. A* **2015**, *119* (19), 4515–4523.

(25) Dette, H. P.; Koop, T. Glass Formation Processes in Mixed Inorganic/Organic Aerosol Particles. *J. Phys. Chem. A* **2015**, *119* (19), 4552–4561.

(26) Lienhard, D. M.; Bones, D. L.; Zuend, A.; Krieger, U. K.; Reid, J. P.; Peter, T. Measurements of Thermodynamic and Optical Properties of Selected Aqueous Organic and Organic-Inorganic Mixtures of Atmospheric Relevance. *J. Phys. Chem. A* **2012**, *116* (40), 9954–9968.

(27) Ashkin, A. Acceleration and Trapping of Particles by Radiation Pressure. *Phys. Rev. Lett.* **1970**, *24* (4), 156–159.

(28) Dennis-Smither, B. J.; Marshall, F. H.; Miles, R. E. H.; Preston, T. C.; Reid, J. P. Volatility and Oxidative Aging of Aqueous Maleic Acid Aerosol Droplets and the Dependence on Relative Humidity. *J. Phys. Chem. A* **2014**, *118* (30), 5680–5691.

(29) Cai, C.; Stewart, D. J.; Reid, J. P.; Zhang, Y. H.; Ohm, P.; Dutcher, C. S.; Clegg, S. L. Organic Component Vapor Pressures and Hygroscopicities of Aqueous Aerosol Measured by Optical Tweezers. *J. Phys. Chem. A* **2015**, *119* (4), 704–718.

(30) Davies, J. F.; Wilson, K. R. Raman Spectroscopy of Isotopic Water Diffusion in Ultraviscous, Glassy, and Gel States in Aerosol by Use of Optical Tweezers. *Anal. Chem.* **2016**, *88* (4), 2361–2366.

(31) Davis, E. J. A History of Single Aerosol Particle Levitation. *Aerosol Sci. Technol.* **1997**, *26* (3), 212–254.

(32) Tong, H. J.; Ouyang, B.; Nikolovski, N.; Lienhard, D. M.; Pope, F. D.; Kalberer, M. A New Electrodynamic Balance (EDB) Design for Low-Temperature Studies: Application to Immersion Freezing of Pollen Extract Bioaerosols. *Atmos. Meas. Tech.* **2015**, *8* (3), 1183–1195.

(33) Miles, R. E. H.; Davies, J. F.; Reid, J. P. The Influence of the Surface Composition of Mixed Monolayer Films on the Evaporation Coefficient of Water. *Phys. Chem. Chem. Phys.* **2016**, *18* (29), 19847–19858.

(34) Darvas, M.; Picaud, S.; Jedlovszky, P. Molecular Dynamics Simulations of the Water Adsorption around Malonic Acid Aerosol Models. *Phys. Chem. Chem. Phys.* **2013**, *15* (26), 10942–10951.

(35) Noda, I. Generalized Two-Dimensional Correlation Method Applicable to Infrared, Raman, and Other Types of Spectroscopy. *Appl. Spectrosc.* **1993**, *47* (9), 1329–1336.

(36) Noda, I. Advances in Two-Dimensional Correlation Spectroscopy (2DCOS). *Front. Adv. Mol. Spectrosc.* **2017**, *54* (July 2000), 47–75.

(37) Paul, W. Electromagnetic Traps for Charged and Neutral Particles (Nobel Lecture). *Rev. Mod. Phys.* **1990**, *29* (7), 739–748.

(38) Trevitt, A. J.; Wearne, P. J.; Bieske, E. J. Calibration of a Quadrupole Ion Trap for Particle Mass Spectrometry. *Int. J. Mass Spectrom.* **2007**, *262* (3), 241–246.

(39) Shinohara, H.; Yamakita, Y.; Ohno, K. Raman Spectra of Polycyclic Aromatic Hydrocarbons. Comparison of Calculated Raman Intensity Distributions with Observed Spectra for Naphthalene, Anthracene, Pyrene, and Perylene. *J. Mol. Struct.* **1998**, *442* (1–3), 221–234.

(40) Glantschnig, W. J.; Chen, S.-H. Light Scattering from Water Droplets in the Geometrical Optics Approximation. *Appl. Opt.* **1981**, *20* (14), 2499.

(41) Graßmann, A.; Peters, F. Size Measurement of Very Small Spherical Particles by Mie Scattering Imaging (MSI). *Part. Part. Syst. Charact.* **2004**, *21* (5), 379–389.

(42) Rzesanke, D.; Nadolny, J.; Duft, D.; Muller, R.; Kiselev, A.; Leisner, T. On the Role of Surface Charges for Homogeneous Freezing of Supercooled Water Microdroplets. *Phys. Chem. Chem. Phys.* **2012**, *14* (26), 9359–9363.

(43) Hermann, G.; Zhang, Y.; Wassermann, B.; Fischer, H.; Quennet, M.; Ruhl, E. Charge Effects on the Efflorescence in Single Levitated Droplets. *J. Phys. Chem. A* **2017**, *121* (36), 6790–6799.

(44) Hu, Q.; Zhao, H.; Ouyang, S. Understanding Water Structure from Raman Spectra of Isotopic Substitution H2O/D2O up to 573 K. *Phys. Chem. Chem. Phys.* **2017**, *19* (32), 21540–21547.

(45) Smith, J. D.; Cappa, C. D.; Wilson, K. R.; Cohen, R. C.; Geissler, P. L.; Saykally, R. J. Unified Description of Temperature-Dependent Hydrogen-Bond Rearrangements in Liquid Water. *Proc. Natl. Acad. Sci.* **2005**, *102* (40), 14171–14174.

(46) Kojima, S. Anomalous Behaviour of the O-H Stretching Vibrational Mode in the Liquid-Glass Transition of Glycerol. *J. Mol. Struct.* **1993**, *294* (C), 193–195.

(47) Okada, T.; Komatsu, K.; Kawamoto, T.; Yamanaka, T.; Kagi, H. Pressure Response of Raman Spectra of Water and Its Implication to the Change in Hydrogen Bond Interaction. *Spectrochim. Acta - Part A Mol. Biomol. Spectrosc.* **2005**, *61* (10), 2423–2427.

(48) Palombo, F.; Paolantoni, M.; Sassi, P.; Morresi, A.; Cataliotti, R. S. Spectroscopic Studies of the “Free” OH Stretching Bands in Liquid Alcohols. *J. Mol. Liq.* **2006**, *125* (2–3), 139–146.

(49) Pershin, S. M.; Bunkin, A. F.; Lukyanchenko, V. A.; Nigmatullin, R. R. Detection of the OH Band Fine Structure in Liquid Water by Means of New Treatment Procedure Based on the Statistics of the Fractional Moments. *Laser Phys. Lett.* **2007**, *4* (11), 809–813.

(50) Ikushima, Y.; Hatakeda, K.; Saito, N.; Arai, M. An in Situ Raman Spectroscopy Study of Subcritical and Supercritical Water: The Peculiarity of Hydrogen Bonding near the Critical Point. *J. Chem. Phys.* **1998**, *108* (14), 5855–5860.

(51) Carey, D. M. Measurement of the Raman Spectrum of Liquid Water. *J. Chem. Phys.* **1998**, *108* (7), 2669–2675.

(52) Burikov, S.; Dolenko, T.; Patsaeva, S.; Starokurov, Y.; Yuzhakov, V. Raman and IR Spectroscopy Research on Hydrogen Bonding in Water-Ethanol Systems. *Mol. Phys.* **2010**, *108* (18), 2427–2436.

(53) Jung, Y. M.; Czarnik-Matusewicz, B.; Kim, S. Bin. Characterization of Concentration-Dependent Infrared Spectral Variations of Urea Aqueous Solutions by Principal Component Analysis and Two-Dimensional Correlation Spectroscopy. *J. Phys. Chem. B* **2004**, *108* (34), 13008–13014.

(54) Noda, I. Determination of Two-Dimensional Correlation Spectra Using the Hilbert Transform. *Appl. Spectrosc.* **2000**, *54* (7), 994–998.

(55) Bohren, C. F.; Huffman, D. R. *Absorption and Scattering of Light by Small Particles*; John Wiley & Sons, Inc.: New York, NY, 1998; Vol. 31.

(56) Bastelberger, S.; Krieger, U. K.; Luo, B. P.; Peter, T. Time Evolution of Steep Diffusion Fronts in Highly Viscous Aerosol Particles Measured with Mie Resonance Spectroscopy. *J. Chem. Phys.* **2018**, *149* (24).

(57) Chocholoušová, J.; Vacek, J.; Hobza, P. Acetic Acid Dimer in the Gas Phase, Nonpolar Solvent, Microhydrated Environment, and Dilute and Concentrated Acetic Acid: Ab Initio Quantum Chemical and Molecular Dynamics Simulations. *J. Phys. Chem. A* **2003**, *107*

(17), 3086–3092.

(58) Wang, H.; Chen, W.; Wagner, J. C.; Xiong, W. Local Ordering of Lattice Self-Assembled SDS@2β-CD Materials and Adsorbed Water Revealed by Vibrational Sum Frequency Generation Microscope. *J. Phys. Chem. B* **2019**, *123* (29), 6212–6221.

(59) Nakabayashi, T.; Kosugi, K.; Nishi, N. Liquid Structure of Acetic Acid Studied by Raman Spectroscopy and Ab Initio Molecular Orbital Calculations. *J. Phys. Chem. A* **1999**, *103* (43), 8595–8603.

(60) Tonannavar, J.; Chavan, Y. B.; Yenagi, J. A Study of Hydrogen Bonded Vibrational Spectra of (R)-(+)-Methylsuccinic Acid, as Aided by DFT Dimer Analysis. *Spectrochim. Acta - Part A Mol. Biomol. Spectrosc.* **2016**, *160*, 19–25.

(61) Ng, J. B.; Shurvell, H. F. Application of Factor Analysis and Band Contour Resolution Techniques to the Raman Spectra of Acetic Acid in Aqueous Solution. *J. Phys. Chem.* **1987**, *91* (2), 496–500.

(62) Bhattacharjee, R.; Jain, Y. S.; Bist, H. D. Laser Raman and Infrared Spectra of Tartaric Acid Crystals. *J. Raman Spectrosc.* **1989**, *20* (February 1989), 91–97.

(63) Desiraju, G. R. Hydrogen Bridges in Crystal Engineering: Interactions without Borders. *Acc. Chem. Res.* **2002**, *35* (7), 565–573.

(64) Ebisuzaki, Y.; Angel, S. M. Raman Study of Hydrogen Bonding in α and Β-oxalic Acid Dihydrate. *J. Raman Spectrosc.* **1981**, *11* (4), 306–311.

(65) Nishikawa, K.; Iijima, T. Small-Angle X-Ray Scattering Study of Fluctuations in Ethanol and Water Mixtures. *J. Phys. Chem.* **1993**, *97* (41), 10824–10828.

(66) Mohaček-Grošev, V.; Grdadolnik, J.; Stare, J.; Hadži, D. Identification of Hydrogen Bond Modes in Polarized Raman Spectra of Single Crystals of α-Oxalic Acid Dihydrate. *J. Raman Spectrosc.* **2009**, *40* (11), 1605–1614.

(67) Peng, C.; Chan, M. N.; Chan, C. K. The Hygroscopic Properties of Dicarboxylic and Multifunctional Acids: Measurements and UNIFAC Predictions. *Environ. Sci. Technol.* **2001**, *35* (22), 4495–4501.

(68) Yalkowsky, S. H.; He, Y.; Jain, P. *Handbook of Aqueous Solubility Data*, 2nd ed.; CRC Press Inc., 2010.

(69) Lienhard, D. M.; Huisman, A. J.; Bones, D. L.; Te, Y. F.; Luo, B. P.; Krieger, U. K.; Reid, J. P. Retrieving the Translational Diffusion Coefficient of Water from Experiments on Single Levitated Aerosol Droplets. *Phys. Chem. Chem. Phys.* **2014**, *16* (31), 16677–16683.

(70) Xue, X.; He, Z. Z.; Liu, J. Detection of Water-Ice Phase Transition Based on Raman Spectrum. *J. Raman Spectrosc.* **2013**, *44* (7), 1045–1048.

(71) Song, Y. C.; Haddrell, A. E.; Bzdek, B. R.; Reid, J. P.; Bannan, T.; Topping, D. O.; Percival, C.; Cai, C. Measurements and Predictions of Binary Component Aerosol Particle Viscosity. *J. Phys. Chem. A* **2016**, *120* (41), 8123–8137.

(72) Miyamoto, T.; Cantow, H.-J. A Nuclear Magnetic Resonance Study on the Conformation and Molecular Interaction of Polyelectrolyte Model Compound in Alcohol/Water Mixtures. *Die Makromol. Chemie* **1973**, *169* (1), 211–218.

(73) Marsh, A.; Rovelli, G.; Song, Y. C.; Pereira, K. L.; Willoughby, R. E.; Bzdek, B. R.; Hamilton, J. F.; Orr-Ewing, A. J.; Topping, D. O.; Reid, J. P. Accurate Representations of the Physicochemical Properties of Atmospheric Aerosols: When Are Laboratory Measurements of Value? *Faraday Discuss.* **2017**, *200*, 639–661.

(74) Rothfuss, N. E.; Marsh, A.; Rovelli, G.; Petters, M. D.; Reid, J. P. Condensation Kinetics of Water on Amorphous Aerosol Particles. *J. Phys. Chem. Lett.* **2018**, *9* (13), 3708–3713.

(75) Tong, H. J.; Reid, J. P.; Bones, D. L.; Luo, B. P.; Krieger, U. K. Measurements of the Timescales for the Mass Transfer of Water in Glassy Aerosol at Low Relative Humidity and Ambient Temperature. *Atmos. Chem. Phys.* **2011**, *11* (10), 4739–4754.

(76) Caillet, A.; Rivoire, A.; Galvan, J. M.; Puel, F.; Fevotte, G. Crystallization of Monohydrate Citric Acid. 1. In Situ Monitoring through the Joint Use of Raman Spectroscopy and Image Analysis. *Cryst. Growth Des.* **2007**, *7* (10), 2080–2087.

(77) O'Meara, S.; Topping, D. O.; McFiggans, G. The Rate of Equilibration of Viscous Aerosol Particles. *Atmos. Chem. Phys.* **2016**, *16* (8), 5299–5313.

(78) Shiraiwa, M.; Pfrang, C.; Koop, T.; Pöschl, U. Kinetic Multi-Layer Model of Gas-Particle Interactions in Aerosols and Clouds (KM-GAP): Linking Condensation, Evaporation and Chemical Reactions of Organics, Oxidants and Water. *Atmos. Chem. Phys.* **2012**, *12* (5), 2777–2794.

(79) O'Meara, S.; Topping, D. O.; Zaveri, R. A.; McFiggans, G. An Efficient Approach for Treating Composition-Dependent Diffusion within Organic Particles. *Atmos. Chem. Phys.* **2017**, *17* (17), 10477–10494.

CHAPTER 5: Accelerated Keto-Enol Tautomerization Kinetics of Malonic Acid in Aqueous Droplets

5.1: Introduction

Organic aerosol (OA) particles constitute a major fraction (20 – 90%) of the submicron particulate mass in the troposphere, and their impact on climate and human health has been recognized for several decades.[1–3] When OA is directly emitted from a source, it is known as primary OA (POA). On the other hand, secondary OA (SOA) can be formed through the oxidation of volatile organic compounds (VOCs) from various biogenic and anthropogenic sources. ‘Aging’ of POA and SOA occurs through reaction with hydroxyl radicals (OH) or other oxidants present in the atmosphere. Various efforts, from field observations to global atmospheric modeling, have been made to study the reactions in OA and its impact.[4–6] However, aged OA contains a myriad of chemical compounds and this complexity adds significant uncertainty for understanding the physicochemical properties of OA.[7–10] In this regard, it is of particular interest that organic reactions in the droplet phase have been reported to be accelerated compared to the reaction rate in bulk solutions.[11–14] Suggested reasons for this acceleration of reaction rates include partial solvation, entropy effects, concentration effects, and/or fast diffusion.[15] In spite of recent efforts, much remains to be learned about accelerated chemical kinetics in droplets. In this work we will examine this effect in the keto-enol tautomerization of malonic acid as studied by hydrogen/deuterium (H/D) isotopic exchange.

Malonic acid (propanedioic acid, $CH_2(COOH)_2$, MA) is the second acid in the series of aliphatic dicarboxylic acids, after oxalic acid, and it is widely found in atmospheric OA over oceans and urban areas.[16] One characteristic reaction of MA is keto-enol tautomerization (**Scheme 5.1**). In dilute aqueous solution states, the keto form of MA dominates over the enol form as the equilibrium constant (K_{eq}) for this reaction has been estimated to be ~10^{-4}.[17] However, a near-edge X-ray fine structure spectroscopy study of deliquesced MA particles by Ghorai *et al.* showed evidence for a large shift of K_{eq} up to ~2.2 at 90% relative humidity (RH).[18] This observation was supported by the theoretical study of Yamabe *et al.* that suggested possible reaction pathways for keto-enol tautomerization of MA with lower activation energy.[19] They found that a system of six water molecules acts as a catalytic proton relay by forming a hydrogen-bond network with the MA molecule.[19] Although the keto-enol tautomerization of MA in droplets has been studied in terms of keto-enol equilibrium and activation energy,[18,19] no measurements of the chemical kinetics have been reported. Thus, the motivation of this work is to study the reaction kinetics of keto-enol tautomerization of MA and determine how the environmental conditions such as RH and droplet size affect the reaction rates.

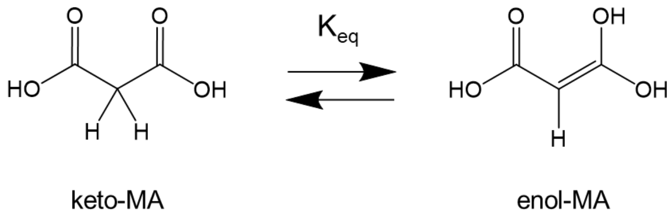

Scheme 5.1: Keto-enol tautomerization of malonic acid (MA).

To investigate the reaction kinetics of MA in aqueous droplets, an environment-controlled electrodynamic balance (EDB) equipped with Mie scattering imaging (MSI) and a Raman spectrometer has been used. The EDB enables contactless levitation of a single charged droplet at chosen relative humidity (RH) conditions while MSI and Raman spectroscopy provide information about the size, phase, and chemical composition, as well as molecular interactions. One of the frequently used methods for studying reactions in droplets is electrospray ionization mass spectrometry (ESI-MS). Accelerated reactions of various organics in droplets using ESI-MS technique have been reported.[13,20] However, recent study by Rovelli *et al.* asserted limitations of ESI-MS in quantitatively determining acceleration factors in droplets.[21] The limitations include competition of droplet versus gas phase chemistry and differences in ionization efficiency of analytes.[21] Unlike ESI-MS, the EDB coupled with MSI and Raman spectroscopy allows in-situ investigation of reaction kinetics in a single droplet of constant concentration, in a non-destructive way. Although the EDB setup of this study is incapable of identifying each species involved in the reactions, applying a kinetic model derived from the keto-enol tautomerization mechanism of MA enabled quantitative analysis of reaction rates in levitated MA droplets.

Reaction kinetics of keto-enol tautomerization of MA in aqueous solution can be monitored by using H/D isotopic exchange.[22] In the presence of D_2O as a solvent, H atoms in the carboxylic acid functional groups of MA are rapidly exchanged to deuterium.[22] On the other hand, the α hydrogen atoms attached to the center carbon of MA undergo slower isotopic exchange compared to the acidic hydrogens. This exchange of α hydrogen is mediated by the keto-enol tautomerization mechanism as shown in **Scheme 5.2**. During enolization, an α hydrogen of keto-MA is eliminated, resulting in a carbon-carbon double bond. When keto-MA is formed from enol-MA, addition of deuterium to the α carbon takes place in a deuterated environment. Eventually, the α hydrogens of

MA are completely exchanged to deuterium through the 4-step mechanism involving 5 MA species (keto_H_2, enol_H, keto_HD, enol_D, keto_D_2) shown in **Scheme 5.2**.

In this study, the environment controlled EDB coupled with MSI and Raman spectroscopy was used to investigate the reaction kinetics of keto-enol tautomerization of MA in aqueous droplets of 28 – 91 µm diameter at RH conditions ranging from 90% to 30%. Hydrogen-deuterium isotopic exchange at the α carbon of MA provided a spectroscopic measure of the reaction progress, as the change of C-H stretch (ν(C-H), ~2950 cm^{-1}) and C-D stretch (ν(C-D), ~2200 cm^{-1}) peaks can be readily analyzed. At 90% RH, an explicit step-by-step mechanism was applied to the data to obtain the enolization rate (k_1) of MA. We discovered the enolization was accelerated by up to 10-fold in MA droplets at 90% RH compared to the literature value from a bulk solution study.[22] At lower RH, viscosity increases and diffusion becomes a dominant contribution to the overall rate, and the detailed mechanism is no longer relevant. To account for this in a simplified quantitative analysis of the RH and size effect on the tautomerization rates, a pseudo-first order approximation was applied. Pseudo-first order approximations are widely used in a range of chemical kinetics studies such as adsorption of dye molecules, hydrolysis of fluorescein diacetate, and dehydration of secondary alcohols.[23–25] Using this approximation, it was observed that the lower RH conditions and larger droplet size reduce the tautomerization rate of MA. The size effect becomes more evident for droplets at lower RH conditions. In the following section the experimental method will be presented in detail.

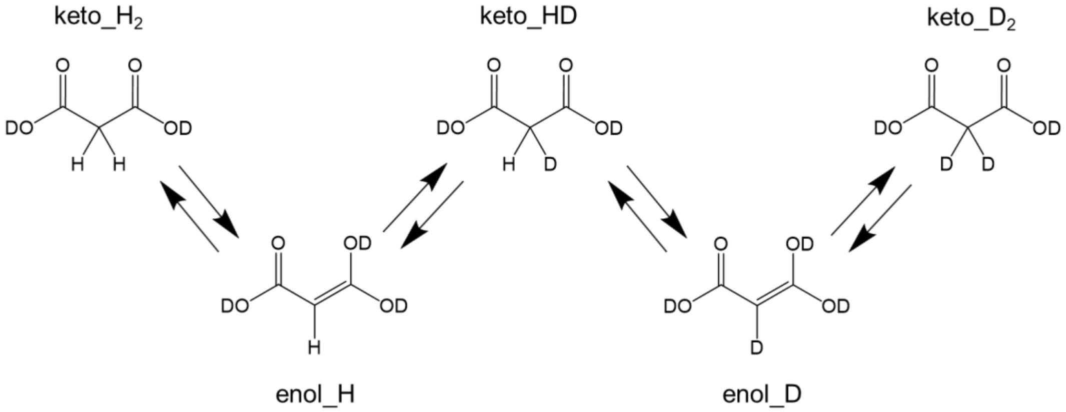

Scheme 5.2: Propagation of hydrogen-deuterium exchange (C-H to C-D) of MA through keto-enol tautomerization.

5.2: Experimental Methods

Details of the environment-controlled EDB coupled with Mie and Raman spectroscopy have been described in previous work from this laboratory.[26,27] The reagents, Malonic acid (99%, Aldrich) and D_2O (99.9% D, Cambridge Isotope Laboratories) were used as purchased without further purification. MA was dissolved in HPLC-grade water (max. 1 ppm residue after evaporation, Fisher Chemical) with concentrations of 3 molal and 6 molal. 3 molal solutions generate relatively smaller size droplets compared to 6 molal solutions, because the size of the droplet is determined by the amount of solute present in each droplet at a given RH condition. The MA solutions were loaded into a piezoelectric droplet generator (Engineering Arts DE03) using a motorized syringe. The MA solution was then introduced as a burst of 30 droplets into the environmental chamber equilibrated at the desired RH of D_2O. The RH inside the chamber was controlled by a constant flow of dry and humid N_2 gas into the chamber, with the humidity controlled by bubbling N_2 through a D_2O bubbler held at room temperature. The flow rates of the gases were controlled by digital mass flow controllers (Alicat MC-500SCCM) with a total flow rate of 120 sccm (cm^3/min). The burst of droplets was generated by a user-selected waveform that drives the piezoelectric element to induce tip vibration and eject the loaded solution. Droplet charging was controlled using the grounded metallic tip of the droplet generator in a circuit with an inductive charging ring to induce an imbalance of charge as the droplets were generated, yielding charged droplets (<40 elementary charges per μm^2).[26] A radio frequency (RF) sine wave generated from a frequency synthesizer (Agilent 33210A) was amplified by a set of amplifiers (Krohn-Hite 7602M wideband amplifier and Matsusada AMS 1.5kV high voltage amplifier) and directed to two conical-shaped endcap electrodes of the trap located at the center of the chamber. The combination of RF voltage from the endcap electrodes and a DC potential (Stanford Research Systems PS350) applied to two rod electrodes at the bottom of the trap were adjusted until a single droplet was confined and stabilized at the null point of the alternating electric field.[28] Typical trapping conditions for MA droplets were 90 - 180Hz, 1.5kV (rms) AC and 200 - 400V DC depending on droplet size (mass).

The schematic layout of MSI and Raman spectroscopy setup is shown in **Figure 5.1**. The levitated MA droplet was illuminated by a vertically polarized pulsed 532nm Nd:YAG laser (RMPC Wedge XF, 500 – 700ps pulse width, 1 – 40kHz repetition rate) with 25-50mW average power. The perpendicular-polarized Mie scattering pattern was collected in the 45° forward direction with respect to the laser path using a charge-coupled device (CCD) camera equipped with a polarizer. Collected Mie scattering images were processed using a MATLAB script to obtain the diameter of MA droplets in the geometrical optics approximation.[29,30] The refractive index of MA droplets at all RH conditions were calculated using parameters adopted from the

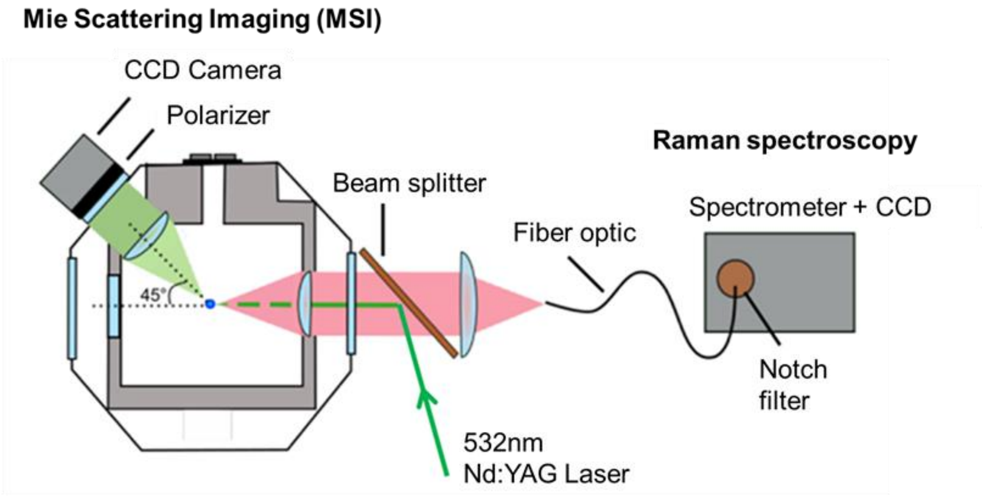

Figure 5.1: Schematic diagram of the EDB with MSI and Raman spectroscopy. A single MA droplet trapped inside the chamber is being illuminated by a pulsed 532nm laser. The MSI pattern (green shade) is captured from the camera located at the 45° forward direction of scattering whereas backscattered Raman signal (red shade) is collected through the fiber optic coupled with spectrometer and CCD detector.

study by Cai *et al* (**Figure S5.5** in the Supplementary Information (SI)).[31] The droplet size calculated using MSI ranged between 28 – 91 µm in diameter (±0.5 µm error due to the uncertainty of RH). The Mie scattering images of MA droplets showed regular fringes of diffraction patterns under all RH conditions (**Figure S5.2**), indicating that no phase-transitions occurred under the conditions of these measurements.

The Stokes-shifted Raman signal of all polarization was collected using a fiber optic located in the backscattering direction (180°) of the laser path into the chamber. The fiber optic introduced the Raman signal into the spectrometer (Acton SpectraPro 275, f/3.8) equipped with a 600 g/mm grating. The spectral image obtained by the thermoelectric-cooled CCD detector (Horiba Syncerity) was converted into the Raman spectra presented here. Raman measurements were made after stable levitation of the droplet in the EDB was achieved. Typical time difference between introduction of the droplet into the chamber and measurement of the first Raman spectrum (t = 0 s) was ~2 minutes. The integration time varied between 30 and 120 seconds depending on the size of the droplets. Generally, smaller droplets needed longer exposure for better signal to noise ratio (S/N).

Measurements were made at D_2O RH conditions of 90%, 70%, 50%, and 30% (±1.5%) and ambient temperature (19–21 °C). The temperature and RH of the chamber was determined using a capacitive sensor (Vaisala Humicap 180R). The humidity data measured by the sensor were converted according to the difference in equilibrium vapor pressure of D_2O versus H_2O.[32]

Analysis of the spectra was supported by density-functional theory calculations of the Raman signals using Gaussian 09 software. The level of theory used to calculate the Raman shift and Raman activities for the optimized structures of MA molecules with every conformation in Scheme 2 was B3LYP/6-311++g(d,p). All other data processing was carried out using MATLAB.

5.3: Results and Discussion

In the following section, dynamic Raman spectra of an MA droplet in the 1500 – 4000 cm^{-1} spectral region will be presented. The dynamic spectra will be used to describe reaction kinetics of keto-enol tautomerization of MA by observing evolution of the ν(C-H) and ν(C-D) peaks as changes in these peaks are caused by H/D exchange during the tautomerization. The effect of size and RH on the H/D exchange and tautomerization rates will then be presented.

5.3.1: C-H/C-D Exchange of Malonic Acid

Time-resolved Raman spectra of MA droplets levitated in the EDB and equilibrated under the desired D_2O-RH conditions evolve in a manner consistent with C-H/C-D exchange kinetics. The rate of exchange was found to be affected by the RH in the EDB chamber and size of the droplet, and the time-resolved Raman spectra allow a quantitative analysis of the kinetics of isotopic exchange. **Figure 5.2** shows dynamic spectra of a MA droplet (57 µm diameter) undergoing C-H/C-D exchange at 50% RH. The decrease in intensity of the ν(C-H) peak at ~2935 cm^{-1} and the rise of ν(C-D) peaks at ~2166 and ~2223 cm^{-1} indicate the equilibrium of MA droplet shifts from keto_H_2 ⇌ enol_H to keto_D_2 ⇌ enol_D over the timescale of 1 – 2 hours. The RH and size dependencies of the rate of isotopic exchange will be discussed in later section.

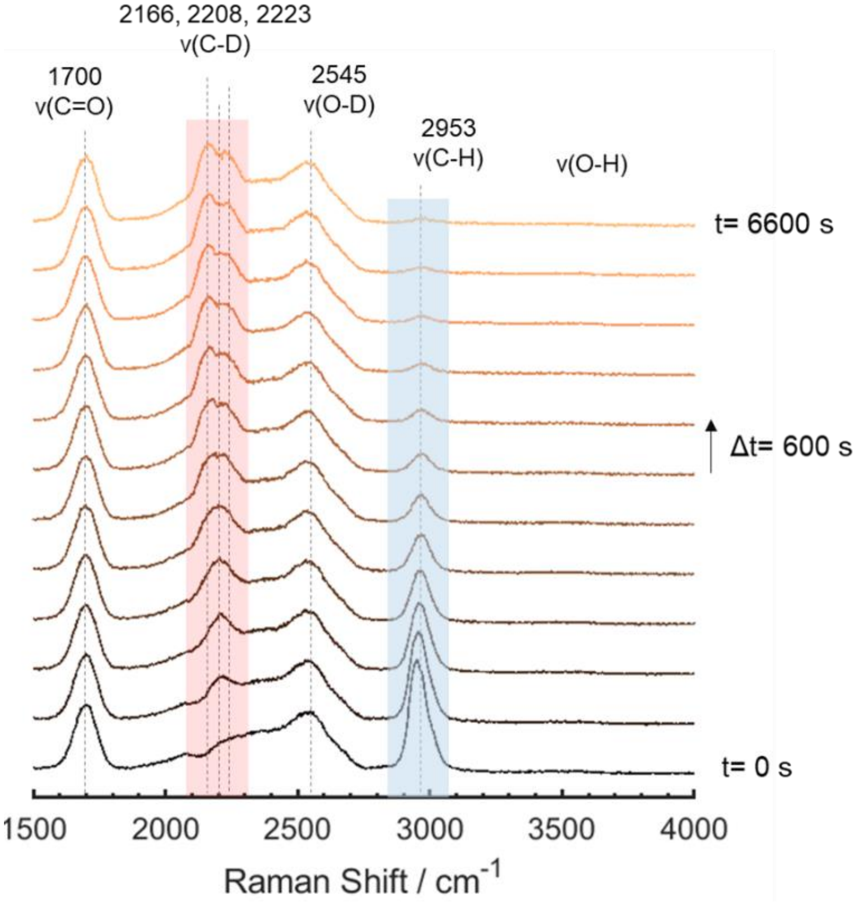

Figure 5.2: Dynamic Raman spectra of a MA droplet of 57.3 μm diameter undergoing H/D exchange at 50% RH. Timestep between each spectrum is 10 minutes (600 seconds). The rise of intensity of the ν(C-D) peaks (2166, 2208, 2223 cm^{-1}) is highlighted with a red shade while the intensity decrease of the ν(C-H) peak (2950 cm^{-1}) is emphasized with a blue shade. All spectra are normalized to the intensity of ν(C=O) peak (1700 cm^{-1}).

In the dynamic Raman spectra recorded as a function of time in **Figure 5.2**, some spectroscopic features reveal valuable details of the C-H/C-D exchange process. First, it is worth noting that at the beginning of the experiment (t = 0 s), there was already no observable ν(O-H) band present at 3000 – 3800 cm^{-1} region. Conversely, the ν(O-D) band at 2000 – 2700 cm^{-1} exists from t = 0 s and the band does not show major intensity changes over the course of the experiment. The Raman ν(O-H) band would have two intensity contributions – from water (H-O-H) and the carboxylic acid functional groups (-COOH) from MA. Therefore, the analysis of the ν(O-H) and ν(O-D) bands supports our assumption that the MA droplets establish rapid equilibrium with the D_2O-environment upon the initial droplet generation and levitation, and -COOH/-COOD isotopic exchange is much more rapid than C-H/C-D exchange. Second, the splitting of the ν(C-D) peak is observed as the exchange continues. The ν(C-D) peak near 2208 cm^{-1} emerges at the beginning (t = 600 – 1800 s) of the exchange and eventually splits in to two peaks at near 2166 and 2223 cm^{-1} towards the end point of the exchange (t = 3600 – 6600 s). This splitting of the ν(C-D) peak can be explained by evaluating vibrational frequencies of molecules involved in the exchange process, in particular, for the C-D stretch vibrations of the keto_HD, keto_D_2, and enol_D molecules. **Table 5.1** lists the calculated frequencies and Raman activities for the C-H and C-D stretch vibrations. During the course of isotopic exchange, the equilibrium shifts from keto_H_2 ⇌ enol_H to keto_D_2 ⇌ enol_D with keto_HD as an intermediate. From **Table 5.1**, it can be noticed that the ν(C-D) frequency of keto_HD (2268 cm^{-1}) lies between those of keto_D_2 (sym. 2236 and asym. 2315 cm^{-1}) and enol_D (2387 cm^{-1}). Accordingly, assessing the calculated vibrational frequencies listed in **Table 5.1**, three ν(C-D) peaks (2166, 2208, 2223 cm^{-1}) found in **Figure 5.2** can be assigned as keto_D_2, keto_HD, and enol_D of MA, respectively. The symmetric and asymmetric ν(C-D) frequencies are not distinguishable in these spectra possibly due to the smaller Raman intensity of the asymmetric ν(C-D) compared to the symmetric ν(C-D) and the overlap between other ν(C-D) peaks.[33] Lastly, the intensity of the ν(C=O) peak at 1700 cm^{-1} does not noticeably change during the progression of isotopic exchange. Thus, the dynamic spectra of **Figure 5.2.** are normalized using the Raman intensity of ν(C=O) peak. This near-steady intensity of the ν(C=O) peak indicates the keto:enol ratio of MA stays constant during the isotopic exchange of a MA droplet. The intensity of the ν(C=O) peak would fluctuate if the keto:enol ratio changed over time as keto-MA contains two carbonyl groups (C=O) while enol-MA has one C=O.[18]

Table 5.1: Calculated values of Raman shift and Raman activity of ν(C-D) and ν(C-H)

Species	ν(C-D)		ν(C-H)	
	Raman Shift (cm^{-1})	Raman Activity ($Å^4$/amu)	Raman Shift (cm^{-1})	Raman Activity ($Å^4$/amu)
keto_H_2	-	-	3123 (asym) 3073 (sym)	48 (asym) 106 (sym)
Enol_H	-	-	3232	61
Keto_HD	2268	42	3107	71
Enol_D	2387	26	-	-
Keto_D_2	2315 (asym) 2236 (sym)	25 (asym) 52 (sym)	-	-

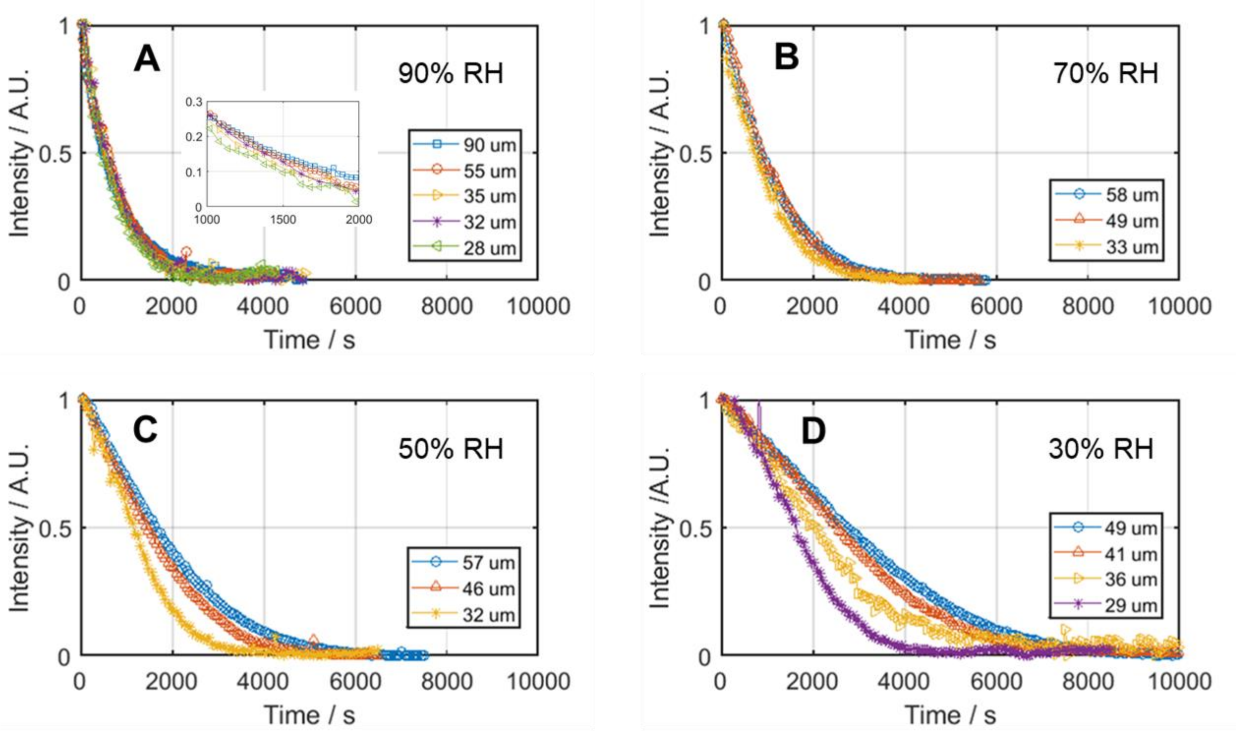

Figure 5.3: Integrated Raman intensity of ν(C-H) peak of MA droplets (28 – 91 µm diameter) as a function of time at 90% (A), 70% (B), 50% (C), and 30% RH (D). The inset of (A) is a magnified plot at 1000 – 2000 s timeframe to show the difference in intensities of various-sized droplets. Size dependency of isotopic exchange rates is more pronounced in lower RH conditions.

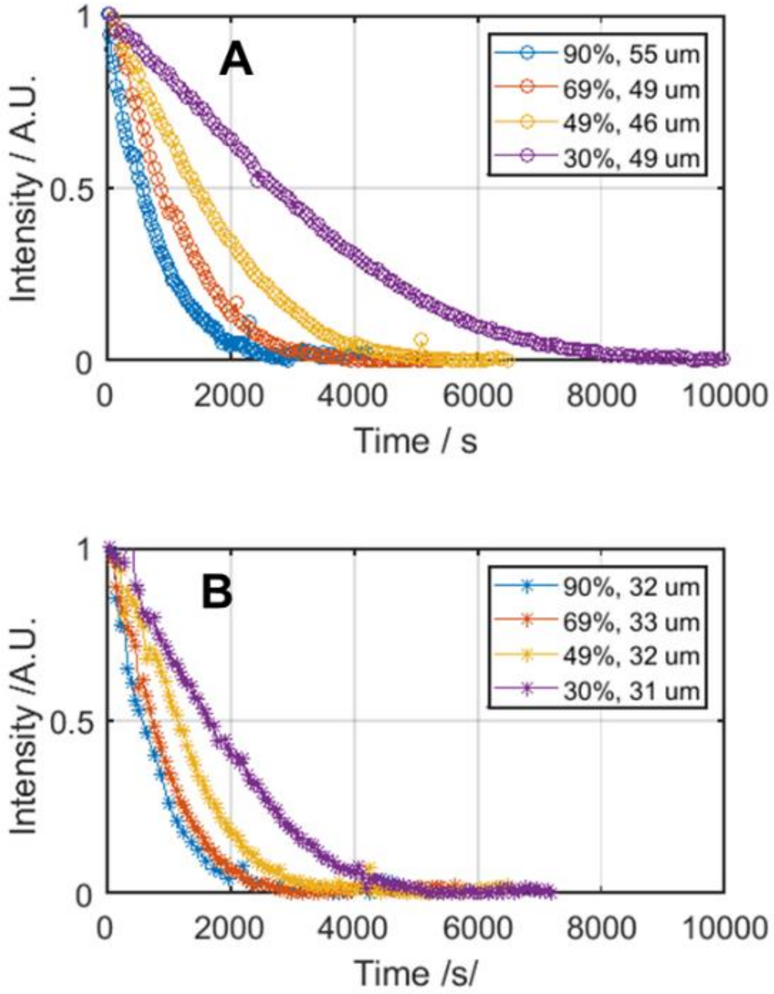

Figure 5.4: Integrated Raman intensity decrease of ν(C-H) peak over time for two different size ranges of MA droplets, 46 – 55 µm diameter (A) and 31-33 µm diameter (B). Smaller droplets show a faster overall rate of isotopic exchange than larger droplets. Additionally, there is larger influence of RH conditions on the larger droplets compared to smaller droplets.

5.3.2: Size and RH Dependency

The rate of C-H/C-D exchange is affected by both RH and size of the droplet. **Figure 5.3** shows the ν(C-H) Raman intensity versus time at 90%, 70%, 50%, 30% RH for various sizes of the MA droplets (28 – 91 µm diameter). It has been observed that the size of MA droplet plays a more important role in isotopic exchange rates at lower RH conditions. **Figure 5.3A** shows that at 90% RH, droplet size has a minimal effect on the exchange kinetics. As the condition gets drier (**Figure 5.3B, C, and D**), a general trend is observed that the exchange rates are relatively slower for larger MA droplets. The impact of RH on the exchange kinetics can be clearly noticed in **Figure 5.4**. **Figure 5.4A** shows the data for droplets in the size range of 45 – 55 µm diameter while **Figure 5.4B** shows the data for droplets of 31 – 33 µm diameter. For both size groups of MA droplets, it is observed that the rate of isotopic exchange is faster for droplets at higher RH.

5.3.3: Application of Pseudo-First Order Approximation

For quantitative analysis of the isotopic exchange kinetics of MA droplets of various sizes and under varying RH conditions, a pseudo-first order approximation method is applied for the ν(C-H) Raman intensity versus time data. In this study, the premise for this approximation is that the entire system of isotopic exchange (**Scheme 6.2**) can be simplified to the reaction that only involves C-H and C-D functional groups. This simplified exchange reaction is schematically illustrated in **Scheme 6.3**. The hydrogen atom that is covalently bonded to the α carbon of MA undergoes the reversible isotopic exchange reaction with a D_2O molecule, thus producing C-D and HOD. The rate coefficients for the forward (C-H to C-D) and reverse (C-D to C-H) are noted as k_f and k_r, respectively. In addition, HOD/D_2O exchange at the droplet surface is considered as the droplet is in dynamic equilibrium with the vapor phase of D_2O with a set RH condition. The

HOD/D_2O exchange coefficient is given as k_{ex}, thus the overall gas-droplet exchange rate at the surface is related to surface to volume ratio (S/V) and k_{ex}.

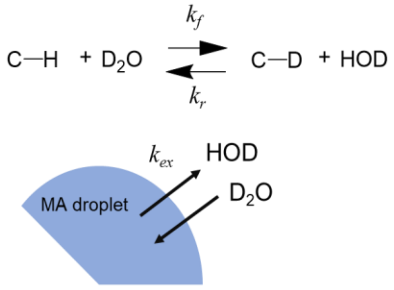

Scenario 1 (High RH) : $k_{obs} = k_f[D_2O]$

Scenario 2 (Low RH): $k_{obs} = k_f[D_2O] - k_r[HOD]$

Scheme 5.3: Description of forward (k_f) and reverse (k_r) reaction of isotopic exchange as well as gas-droplet exchange interaction (k_{ex}) at the surface. Two scenarios for the pseudo-first order approximation can be considered depending on the rate of the reverse exchange reaction determined by k_r[HOD].

In this simplified picture of H/D exchange of MA, there are two possible scenarios for higher RH conditions and lower RH conditions. At higher RH conditions where diffusion rate and gas-droplet exchange are fast, reverse H/D exchange can be ignored due to the rapid extinction of HOD in the droplet. Therefore, in scenario A, observed rate coefficient (k_{obs}) is only dependent on the forward (k_f) H to D exchange (Scheme 3). In this case where $[HOD]$ is negligible, the pseudo-first order rate of disappearance of ν(C-H) Raman intensity over time can be interpreted by defining k_{obs} from the experimental data. **Figure 5.5** shows examples of the application of the pseudo-first order approximation to the experimental data for droplets at 90% RH and 50% RH. In **Figure 5.5**, the data were fit with the following equation,

$$I_{obs}(t) = I_0 e^{-k_{obs}t} \tag{5.1}$$

where $I_{obs}(t)$ is the integrated intensity of ν(C-H) peak intensity, I_0 is the initial integrated intensity of ν(C-H) peak, k_{obs} (observable rate coefficient) is the fitting parameter, and t is time in seconds.

For a 35 µm droplet at 90% RH (**Figure 5.5A**), $I_{obs}(t)$ displays excellent agreement with the experimental data, suggesting the isotopic exchange kinetics under these conditions can be suitably approximated to the first order reaction. At 50% RH (**Figure 5.5B**), however, there exists a deviation of first-order exponential $I_{obs}(t)$ from experiment, where the earlier stage of the data (≤ 1500 s) shows a linear decrease in intensity rather than exponential decay. To understand this divergence from the pseudo-first order approximation in the data, a second scenario where $[HOD]$ cannot be ignored must be considered. As seen in Scheme 3, C-D and HOD can undergo reverse exchange reaction and $[HOD]$ is highly dependent on S/V of the droplet, k_{ex}, and overall diffusion rate in the droplet. Therefore, the value of k_{obs} is the result of competing of forward and backward H/D exchange reactions as well as the gas-droplet exchange at the surface. These perturbations are not the only source of deviation of the fit from the pseudo-first order (**Figure 5.5B**)—the size and RH dependency of k_{obs} can also be explained in terms of k_r and k_{ex}. Applications of the pseudo first-order approximation to MA droplets at all experimental conditions are shown in the SI in **Figure S5.3**.

The observable rate coefficients (k_{obs}) are obtained under the various experimental conditions and are listed in **Table 5.2**. It should be noted that applications of the pseudo first-order approximation diverge more from the experimental data for lower RH and bigger droplets. Therefore, this discrepancy reflects the effect of k_r and k_{ex}. However, the pseudo-first order approximation with its fitting parameter k_{obs} provides a quantitative measure for overall C-H/C-

D exchange rate and enables further analysis of kinetics for varying experimental conditions. The values of k_{obs} under the full experimental conditions are presented in **Figure 5.6**. It is apparent from the **Figure 5.6** that the isotopic exchange rate is slower at relatively lower RH conditions. This deceleration of the kinetics at lower RH is due to the increasing viscosity which leads to the slow diffusion of the molecules in the droplet following exchange at the gas-droplet interface.[34,35] Higher viscosity at lower RH results in a slower diffusion rate and exchange rate (k_{ex}), leading to the accumulation of HOD, which eventually promotes reverse reaction (k_r) of Scheme 3 and lowers k_{obs}. Along with the effect of RH on k_{obs}, a larger droplet size also leads to slower isotopic exchange kinetics. Bigger droplets have lower surface to volume (S/V) ratios, limiting surface HOD-D_2O exchange for the increased HOD production that is proportional to the volume of the droplet. In addition, in bigger droplets, it takes longer for HOD molecules to diffuse to the surface for the HOD-D_2O exchange. Therefore, larger droplet sizes lower the value of k_{ex}, eventually causing slower isotopic exchange (lower k_{obs}) for conditions of RH 70% and below. Surprisingly, the size of the droplet has only minor impact on the isotopic exchange kinetics at 90% RH condition. Along with the fact that at 90% RH the experimental data for ν(C-H) intensity decrease over time showing a near first-order exponential decay, it can be argued that the diffusion rate of HOD and the gas-droplet interaction are fast enough to ignore the reverse reaction of Scheme 3. In other words, C-H/C-D exchange kinetics of MA droplets at 90% RH can be successfully approximated to the first-order reaction with a slight size effect.

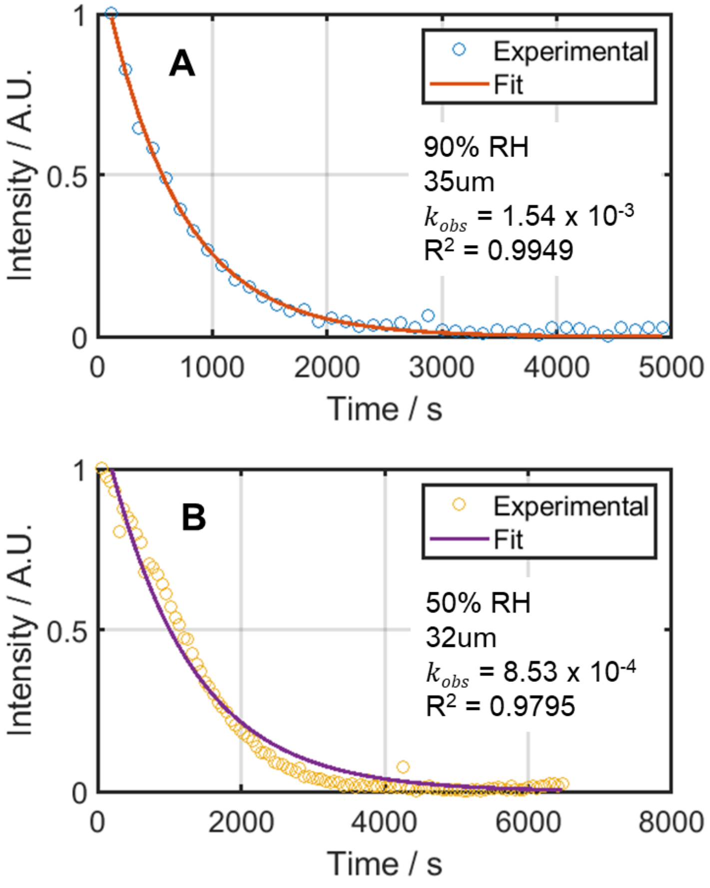

Figure 5.5: Result of least-squares fit of pseudo-first order approximation (eq. 5.1) to the experimental data of ν(C-H) intensity over time for 35µm diameter droplet at 90% RH (A) and 32µm diameter droplet at 50% RH (B). Open circles represent experimental data and solid line curves are pseudo-first order fit. The MA droplet at 90% RH (A) show better agreement of the data to the pseudo first-order approximation compared to the droplet at 50% RH (B).

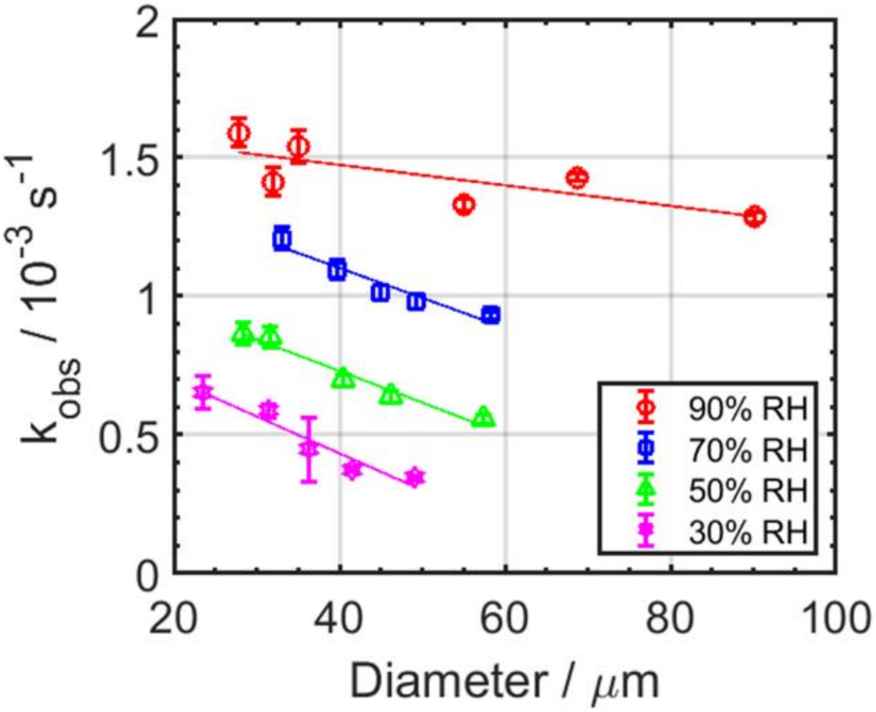

Figure 5.6. Values of observable rate coefficient (k_{obs}) for all MA droplets plotted with droplet diameter and RH condition. Error bars represent 95% confidence interval of the fit (eq. 1 to the ν(C-H) intensity).

Table 5.2: Values of k_{obs} derived from pseudo-first order approximation for all MA droplets.

RH (%)	d (μm)	$k_{obs}/10^{-3}$ (s^{-1})	RH (%)	d (μm)	$k_{obs}/10^{-3}$ (s^{-1})
90	90.5	1.29 ± 0.02	50	57.3	0.56 ± 0.02
	68.8	1.43 ± 0.02		46.2	0.64 ± 0.02
	55.0	1.33 ± 0.02		40.4	0.70 ± 0.02
	35.1	1.54 ± 0.06		31.7	0.85 ± 0.04
	32.0	1.54 ± 0.06		28.4	0.86 ± 0.04
	27.8	1.59 ± 0.05	30	49.1	0.34 ± 0.01
70	58.2	0.93 ± 0.01		41.5	0.38 ± 0.01
	49.3	0.98 ± 0.03		36.3	0.45 ± 0.1
	45.0	1.02 ± 0.03		31.4	0.59 ± 0.02
	39.7	1.10 ± 0.03		23.5	0.65 ± 0.06
	33.0	1.21 ± 0.04			

5.3.4: Rate of Enolization Estimated by Kinetic Model

As discussed in the previous section, the isotopic exchange kinetics of MA droplets at 90% RH are the least size-dependent under the experimental conditions in this study, thus the reverse reaction involving HOD can be ignored due to fast diffusion and gas-droplet exchange. This assumption for MA droplets at 90% RH allows a step-by-step description of the isotopic exchange process as given in Scheme 4. It should be noted that Scheme 4 is a step-by-step representation of Scheme 2, with reactions involving HOD neglected under the assumption that as an intermediate in the deuterated environment it will not accumulate appreciably. Rate coefficients for keto to enol (enolization) and enol to keto (ketonization) are indicated as k_1 and k_2, respectively. k_1' and k_2' are the corresponding rate coefficients with the secondary kinetic isotope effect (KIE). The value for KIE=1.3 has been adopted from the ^{1}H NMR study of malonic acid isotopic exchange by Hansen *et al*.[22] To establish a mathematical model and to derive kinetic parameters from the data using the model, a minimum number of unknown variables is necessary. The X-ray absorption fine structure study of deliquesced MA particles by Ghorai *et al.* determined the value of the equilibrium constant (K) for keto-enol tautomerization of MA droplet to be 2.2 ± 0.4 at 90% RH,[18] and we have used that value to minimize the unknown variables in the step-by-step model.

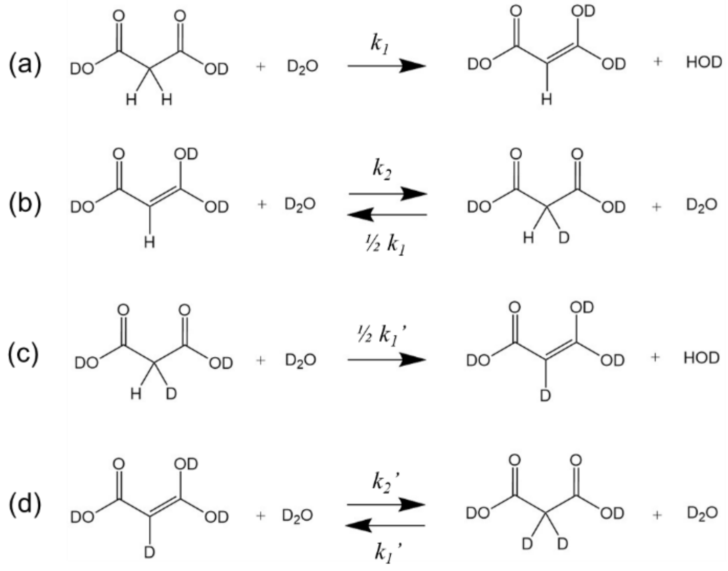

$k_1' = k_1/KIE$ $\quad$ $KIE = 1.3$ $\quad$ $K = k_1/k_2 = 2.2$

$k_2' = k_2/KIE$

Scheme 5.4: Step-by-step kinetic model derived from C-H/C-D exchange mechanism of MA. k_1 and k_2 are rate coefficient for enolization and ketonization, respectively.

A series of ordinary differential equations (ODEs) describing the step-by-step kinetic model given in Scheme 4 can be simply represented in matrix notation (**SI Note 1**). This mathematical modeling is a standard method for quantitative analysis of H/D isotopic exchange reactions.[20] Solving this series of ODEs with the aid of the relationships of kinetic parameters discussed above (Scheme 4) yields the concentration of each compound as a function of time, as shown for the five species in **Figure 5.7**. It is noticeable from **Figure 5.7** that concentrations of initial compounds (keto_H_2 and enol_H) decrease over time and those of deuterated compounds (keto_D_2 and enol_D) rise while the concentration of intermediate keto_HD increases at first then decays, as expected for an intermediate in a multistep reaction sequence. This evolution of each specie from solving model ODEs can explain the splitting of ν(C-D) peak shown in **Figure 5.2**.

The dynamic series of spectra in **Figure 5.2** show that the ν(C-D) peak initially emerges near 2208 cm-1, then splits into two peaks around 2166 and 2223 cm^{-1}. Referring to the DFT calculations (**Table 5.1**), the Raman shift of the intermediate keto_HD (2268 cm^{-1}) lies between keto_D$_2$ (2236 cm^{-1}, symmetric) and enol_D (2387 cm^{-1}). Therefore, it can be suggested that initial increase of ν(C-D) peak at ~2208 cm^{-1} is caused by formation of intermediate keto_HD and the splitting of ν(C-D) peak is due to the conversion of keto_HD into of fully deuterated species (keto_D$_2$ and enol_D).

The solutions of the system of ODEs can be combined to simulate the experimental data given in **Figure 5.3A**. To represent the ν(C-H) intensity decrease, the solutions of $keto\_H_2(t)$, $enol\_H(t)$, and $keto\_HD(t)$ need to be summed with appropriate coefficients. Although the number of C-H oscillators for each element is 2, 1, and 1, respectively, this does not consider the Raman intensities for these oscillators. Accordingly, the calculated Raman activity coefficient for every ν(C-H) and ν(C-D) vibration has been used to simulate the data with the maximum fidelity (**Table 5.3**). The equations for ν(C-H) and ν(C-D) intensity are given as,

$$I_{CH}(t) = (48 + 106)\ keto\_H_2(t) + 61\ enol\_H(t) + 71\ keto\_HD(t) \tag{5.2}$$

$$I_{CD}(t) = (25 + 52)\ keto\_D_2(t) + 26\ enol\_D(t) + 42\ keto\_HD(t) \tag{5.3}$$

where $I_{CH}(t)$ and $I_{CD}(t)$ represent Raman intensity of (C-H) and ν(C-D) peak, respectively, and the integer factors are the relative Raman activities. The values of Raman activity coefficient for all the species are given in **Table 5.1**. Since the right side of equation 5.2 contains solutions of ODEs set up using step-by-step model (**Scheme 5.4** and **SI Note 1**), $I_{CH}(t)$ is a function of time with an unknown parameter, k_1. Therefore, equation 5.2 can be used to fit the simulated Raman intensity ($I_{CH}(t)$) to the time evolution of ν(C-H) peak to estimate the value of enolization rate coefficient k_1. Then, using the obtained value of k_1 from the fit of equation 5.2, $I_{CD}(t)$ is constructed from the solutions of ODEs to verify that equation 5.3 shows adequate agreement with the data of ν(C-D) intensity increase. The comparison of the simulated $I_{CH}(t)$ and $I_{CD}(t)$ with the experiment is shown in **Figure 5.7B**. Verification for the full range of droplet sizes is available in Supplementary Information (**Figure S5.1**). For MA droplets at RH 90% condition excellent agreement was found between the experimental data and the simulated intensity functions created using the step-by-step model. The values of $[D_2O]k_1$ are listed in **Table 5.4**. The value of $[D_2O]$ is assumed to be same for every droplet at 90% RH because at the given experimental conditions, RH is the only factor that determines the water content in MA droplets. Similar to the pseudo-first order approximation analysis, small dependency on size is observed, as the difference of the value of k_1 is about 22% for the biggest (90.5 µm) and smallest (27.8µm) MA droplets (**Table 5.4**). This minor size effect may originate from the elongated diffusion time of HOD to reach the surface for HOD-D_2O exchange in larger droplets as discussed in the previous section.

While there is no previous study on keto-enol tautomerization kinetics of MA in aqueous droplets, Hansen *et al*. reported the enolization rate coefficient ($[D_2O]k_1$) of MA to be 1.066 x 10^{-3} in 1M D_2SO_4 solution.[22] Comparing this value of $[D_2O]k_1$ with the data from this study, our result shows a 10-fold increase in the enolization rate coefficient. It should be noted that the bulk measurement was performed at a MA concentration of 0.25 M while the concentration of MA in a droplet at 90% RH is 3.35 M, thus the comparison is not a direct one.[31] This dramatic acceleration is more striking considering MA droplets only consist of MA and D_2O, without any acidic compound added to facilitate enolization. The pH of 1M D_2SO_4 solution is close to 0, and the pH of MA droplet at 90% RH is expected to be ~ 1 according to Raman spectroscopic study by Chang *et al*.[36] C-H/C-D exchange can be catalyzed by the presence of acid, base, and/or water.[20] It is safe to say that the pH is not responsible for acceleration of enolization rate in MA droplet, because the droplets in this study have higher pH than 1M D_2SO_4. Yamabe *et al.* suggested that the activation energy of keto-enol tautomerization of MA can be significantly lowered by a hydrogen bonded water-MA network.[19] According to their calculation, the transition state was most stabilized when a single MA molecule is surrounded by 6 water molecules as they form a proton-relay network.[19] Water-catalyzed reaction paths provide another explanation on why isotopic exchange rates are slower at lower RH conditions (**Figure 5.6**). The water to solute ratio (WSR) of MA droplets at given RH conditions can be modeled using the modified-UNIFAC (Universal quasichemical Functional group Activity Coefficients) parametrization (**Figure S5.4**).[37,38] 90%, 70%, 50%, 30% RH conditions correspond to the WSR of 10:1, 3:1, 1.5:1, 0.7:1 for MA droplets. The catalytic proton-relay facilitated by the hydrogen bond network (WSR of 6) would thus be more favorable for MA droplets at 90% RH than the drier conditions. Less solute-water interaction is available in droplets at lower RH, leading to slower keto-enol tautomerization rates.

The hydrogen bond network of organic aerosol (OA) is highly affected by the RH, since the WSR and solute-water interaction change with respect to the functional groups of solutes.[27] It should be noted that isotopic exchange kinetics in MA droplets is a complex system difficult to completely unravel because it is intertwined with numerous factors to consider such as reaction, diffusion, and gas-surface interaction. However, our result in **Table 5.3** shows that the keto-enol tautomerization rate is significantly accelerated (10-fold) in the droplet phase compared to bulk solution, facilitated by the catalytic role of the hydrogen-bonded water-solute network on the enolization reaction of MA. In addition, the value of the estimated enolization coefficient (k_1) versus size of the droplet (**Table 5.3**) shows a similar trend as discussed earlier (**Figure 5.6**) in that the reaction rates are faster for smaller droplets. Although the size dependency of tautomerization reaction rates in MA droplets are primarily due to the diffusion effect, the acceleration of reactions at gas-droplet interface may contribute to the overall reaction kinetics.[39] However, surface behavior of MA is outside the scope of this paper and requires further investigation with surface-sensitive techniques such as sum-frequency generation (SFG) spectroscopy.[40–43]

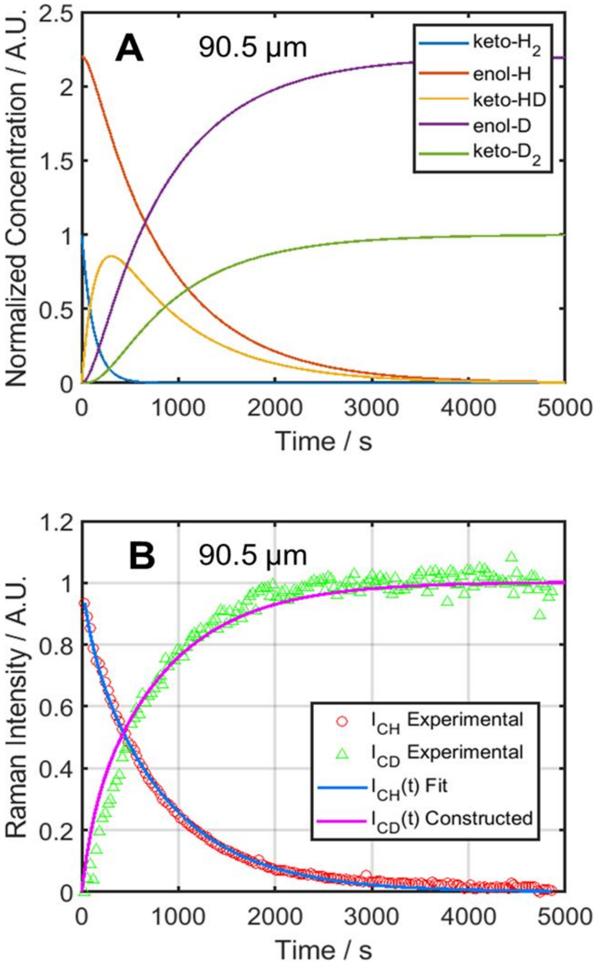

Figure 5.7: Comparison of MA tautomerization kinetics between the simulation and experiment. (A) Normalized concentration of all the species in MA droplet (90.5 μm diameter) as a function of time from a solution of the ODEs describing the step-by-step kinetic model (SI Note 1) during isotopic exchange at 90% RH. (B) Application of the kinetic model to the experimental data. Solid blue line shows the least-squares fit of equation 5.2 to the experimental data. The solid magenta line represents equation 5.3 constructed using the value of k_1 derived from the fitting of equation 5.2. Similar plots for MA droplets of all sizes at 90% RH are available in **Figure S5.1**.

Table 5.3: Estimated enolization rate coefficients ($[D_2O]k_1$) of MA in aqueous droplets at 90% RH. The value of $[D_2O]k_1$ from the bulk solution study is 1.066 x 10^{-3} s^{-1}.[22] Errors of $[D_2O]k_1$ originate from the error of keto-enol equilibrium constant (K) which value was assumed to be 2.2 ± 0.4.[18]

RH (%)	d (μm)	$[D_2O]k_1/10^{-3}$ (s^{-1})
90	90.5	8.2 ± 1.1
	68.8	8.5 ± 1.1
	55.0	8.2 ± 1.1
	35.1	10.2 ± 1.4
	32.0	8.5 ± 1.2
	27.8	10.2 ± 1.4

There are important implications of the results of this study. First, accelerated keto-enol tautomerization kinetics of MA may promote unexpected chemical reactions in atmospheric OA particles. Usually, enols of simple aliphatic compounds have a short lifetime compared with their keto tautomers.[44] However, for MA, the previous experimental[18] and theoretical[19] studies imply that the enol form of MA may exist in larger fractions in aqueous droplets compared to dilute bulk solutions. Furthermore, the work of Lim *et al*. has shown aqueous chemistry in SOA formation including aldol condensation, sulfur esters formation, and oligomerization of hydrated glyoxal enols.[45] Another theoretical study by Lei *et al*. showed atmospherically relevant reactions of ethenol with OH radical, with glycolaldehyde is predicted to be the main product.[46] According to these observations, our results strongly suggest that it may be possible that MA in the atmospheric OA particles can undergo unpredicted chemical reactions with other organic compounds and form low-volatility SOA products in the presence of highly reactive species such as OH radical. Furthermore, the rate of reactions involving MA can be faster than the general assumption for OA aging. This unpredictability of MA reaction kinetics can have considerable impact on aging of OA because MA is found in significant concentrations in aerosols.[16,47]

Also, the enhanced enolization and unexpected chemical reactions of MA in aqueous droplets can hinder the accurate description of physicochemical properties of OA by thermodynamic models. For the complex system represented by OA, the AIOMFAC (Aerosol Inorganic-Organic Mixtures Functional groups Activity Coefficients) thermodynamic model has been widely used to predict activity coefficients of each compound in OA system.[48] Models based on AIOMFAC need information about the number of organic functional groups present to calculate interactions between functional groups and inorganic ions, then predict physicochemical properties such as gas-particle partitioning and hygroscopic properties of OA.[48,49] However, the fact that MA can exist in dynamic equilibrium of keto form (2 -COOH and 2 C-H groups) and enol form (1 -COOH, 1 C-H, and 2 -OH groups) adds uncertainty to the precise prediction of physicochemical properties of MA-containing OA. Field observation studies by Kawamura *et al.* have shown that MA is the second most abundant dicarboxylic acid in marine aerosols.[16] In addition, the variability of functional groups due to keto-enol tautomerization of MA can affect the overall hydrogen bond network in OA. The impact of hydrophilic functional groups (-OH and -COOH) on the hydrogen bond network of OA has been reported in our previous work.[27] Changes in the hydrogen bond network of MA-water system due to the contribution from different functional groups may affect the macroscopic physicochemical properties of OA particles, i.e., viscosity, water diffusion, and hygroscopic properties.

5.4: Conclusions

The reaction kinetics of keto-enol tautomerization of aqueous MA droplets were studied using in-situ Raman spectroscopy and hydrogen-deuterium isotopic exchange. The dynamic Raman spectra revealed the decay of the ν(C-H) peak and rise of the ν(C-D) peak as isotopic exchange took place at the α carbon of MA. A step-by-step model of keto-enol tautomerization and isotopic exchange of MA was used to simulate the decrease of the ν(C-H) peak ($I_{CH}(t)$) and to derive the enolization rate coefficient (k_1) of MA at 90% RH. The result showed a 10-fold increase of k_1 compared to the bulk measurements[22] in the smallest droplets, with a factor 8 in larger droplets. In addition, a pseudo-first order approximation was adopted to perform quantitative analysis of size- and RH-dependence of keto-enol tautomerization of MA. Our results are consistent with slower reaction rates in drier conditions owing to the slower diffusion rate of water and gas-droplet exchange that led to accumulation of HOD in the droplet, eventually promoting the reverse isotopic exchange (D→H). The size of the droplets was found to be another factor that governed the rate of tautomerization as the gas-droplet exchange rate depends on surface to volume ratio. To the best of our knowledge, accelerated keto-enol tautomerization rates of MA in aerosol has not been previously reported, and we note that these Raman spectroscopic measurements provide non-destructive measurements of enhanced reaction kinetics where gas phase reactions can be neglected. Since MA is an atmospherically relevant molecule, the findings from this work have potentially broad impacts on the current understanding of aqueous OA particles, with many aspects of the unique chemistry requiring further investigation.

5.5: Supplementary Information

The isotopic exchange mechanism given in **Scheme 5.5** consists of coupled reactions with 5 species of MA (keto_H_2, enol_H, keto_HD, enol_D, and keto_D_2). This series of reactions can be described as a system of ordinary differential equations (ODEs) in matrix notation,

$$\frac{d}{dt}\begin{pmatrix} keto\_H_2(t) \\ enol\_H(t) \\ keto\_HD(t) \\ enol\_D(t) \\ keto\_D_2(t) \end{pmatrix} = [D_2O]\begin{pmatrix} -k_1 & & & & \\ k_1 & -k_2 & {}^1\!/_2\, k_1 & & \\ & k_2 & -{}^1\!/_2\,(k_1' + k_1) & & \\ & & {}^1\!/_2\, k_1' & -k_2' & k_1' \\ & & & k_2' & -k_1' \end{pmatrix}\begin{pmatrix} keto\_H_2(t) \\ enol\_H(t) \\ keto\_HD(t) \\ enol\_D(t) \\ keto\_D_2(t) \end{pmatrix}$$

where the left side of the equation is time derivatives of the concentrations of all species in MA droplets. Definitions for kinetic parameters were given in **Scheme 5.5**. Right side contains a product of kinetic parameters for the reactions and concentrations of five species. This set of ODEs were solved using dsolve function of MATLAB.

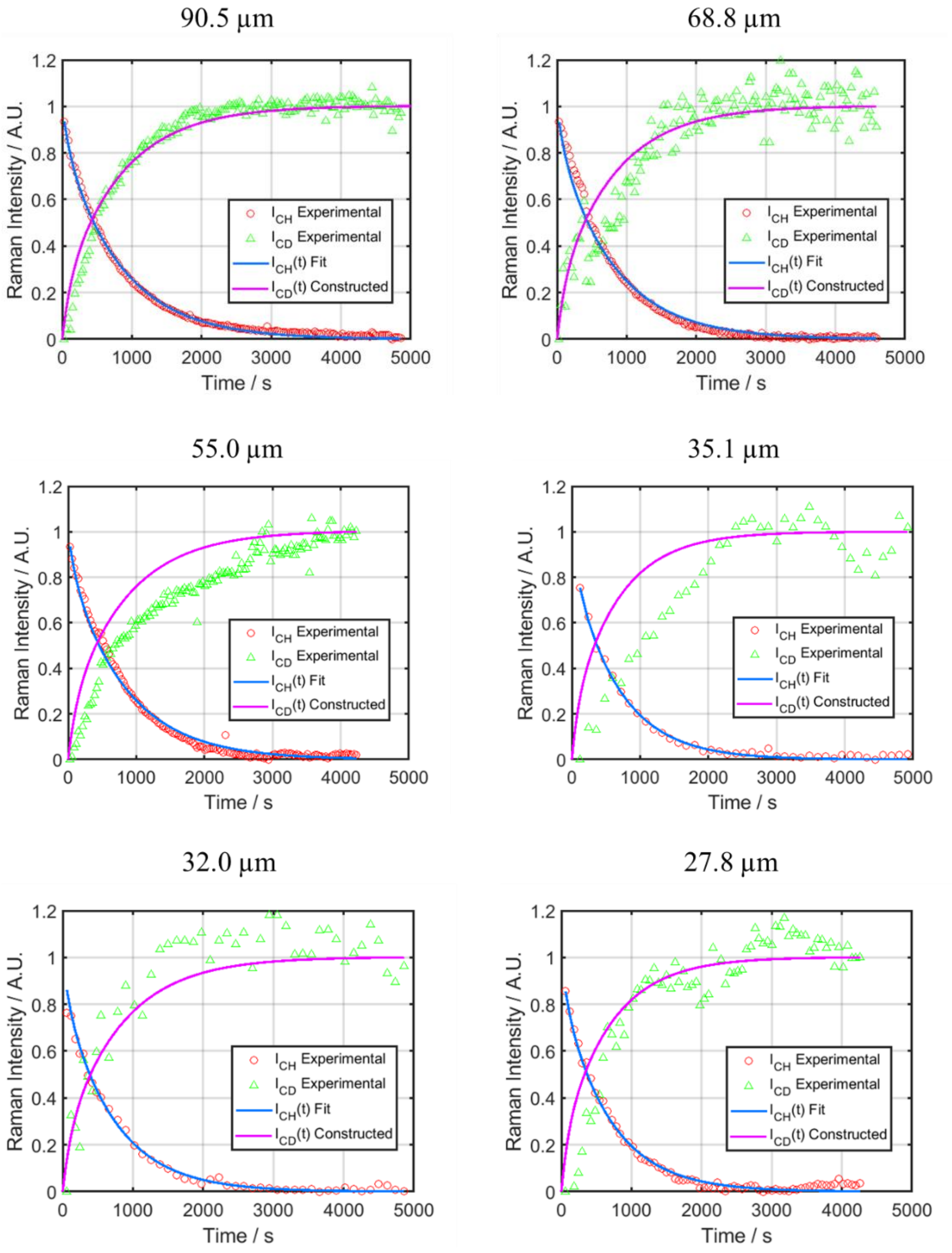

Figure S5.1: Overlays of simulated $I_{CH}(t)$ and $I_{CD}(t)$ curves with normalized Raman intensity of ν(C-H) and ν(C-D) peaks of MA droplets at 90% RH. First, $I_{CH}(t)$ (solid blue line) was fitted to the decay of ν(C-H) intensity (red circle) to estimate the enolization rate constant (k_1). Using the value of k_1 obtained from the fit, the $I_{CD}(t)$ curve (solid magenta line) was constructed and overlayed with the rise of ν(C-D) intensity (green triangle). Droplets of 55.0 and 35.1 µm diameter show relatively poor agreement of $I_{CD}(t)$ curve and ν(C-D) intensity due to the slight increase of RH during the progress of H/D exchange during the experiment at 55.0 µm, and the fluctuation of RH in the 35.1 µm experiment. Unlike the ν(C-H) peak, the ν(C-D) peaks overlap with ν(O-D) band and the change in ν(O-D) intensity can affect the measurement of ν(C-D) intensity.

Figure S5.2: Mie scattering images of all MA droplets at RH conditions of (A) 90%, (B) 70%, (C) 50%, and (D) 30%. All given images are paired with the calculated diameter of the droplet from the geometrical optics approximation of Mie scattering.[29] It can be noticed that larger droplets show smaller spacing of the scattering pattern and vice versa. The error for the diameter of droplets is ±0.5 μm due to the uncertainty of refractive indices of droplets calculated using the measured RH from the RH probe, which has an accuracy of ±1.5%.

A) 90% RH

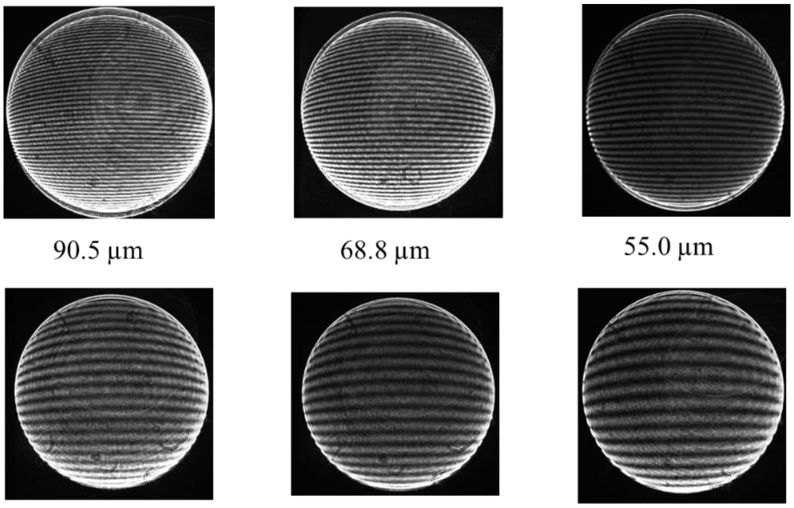

90.5 μm

68.8 μm

55.0 μm

35.1 μm

32.0 μm

27.8 μm

B) 70% RH

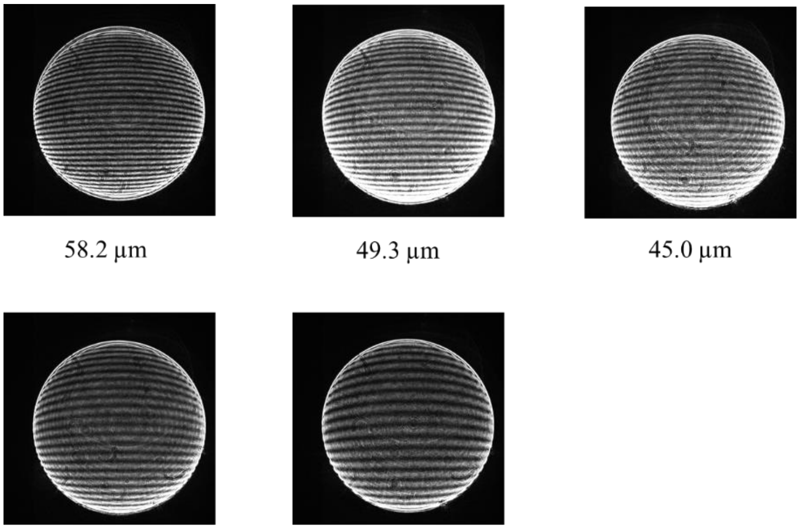

58.2 μm

49.3 μm

45.0 μm

39.7 μm

33.0 μm

Figure S5.2 (Continued)

C) 50% RH

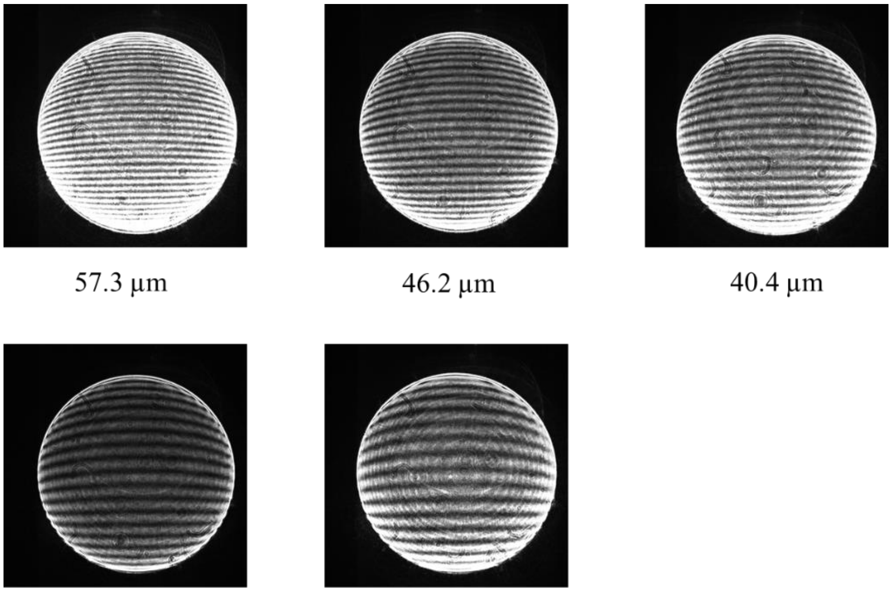

57.3 µm

46.2 µm

40.4 µm

31.7 µm

28.4 µm

D) 30% RH

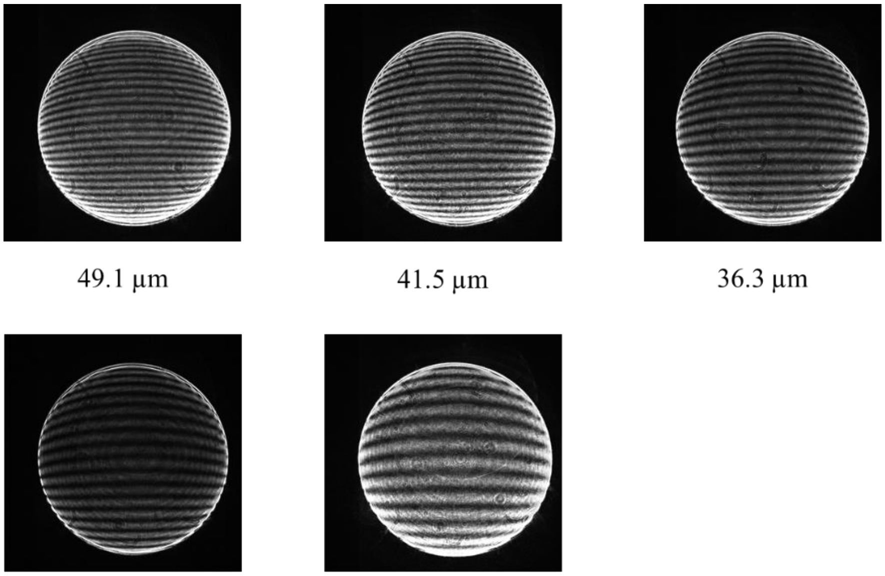

49.1 µm

41.5 µm

36.3 µm

31.4 µm

23.5 µm

Figure S5.3: Decay of ν(C-H) intensity over time in MA droplets (red circles) overlayed with first-order fit (solid blue curve). Each droplet is indicated by its diameter. (**A**) At 90% RH experimental data shows excellent agreement with first-order fit. (**B, C, D**) The deviation between data and first-order fit is higher in lower RH conditions and for bigger droplets due to slower diffusion rates. However, pseudo-first order approximation provides observable rate constants (k_{obs}) for quantitative investigation of size- and RH-dependent keto-enol tautomerization kinetics of MA droplets. Values of k_{obs} are listed in **Table 5.2**.

A) 90% RH

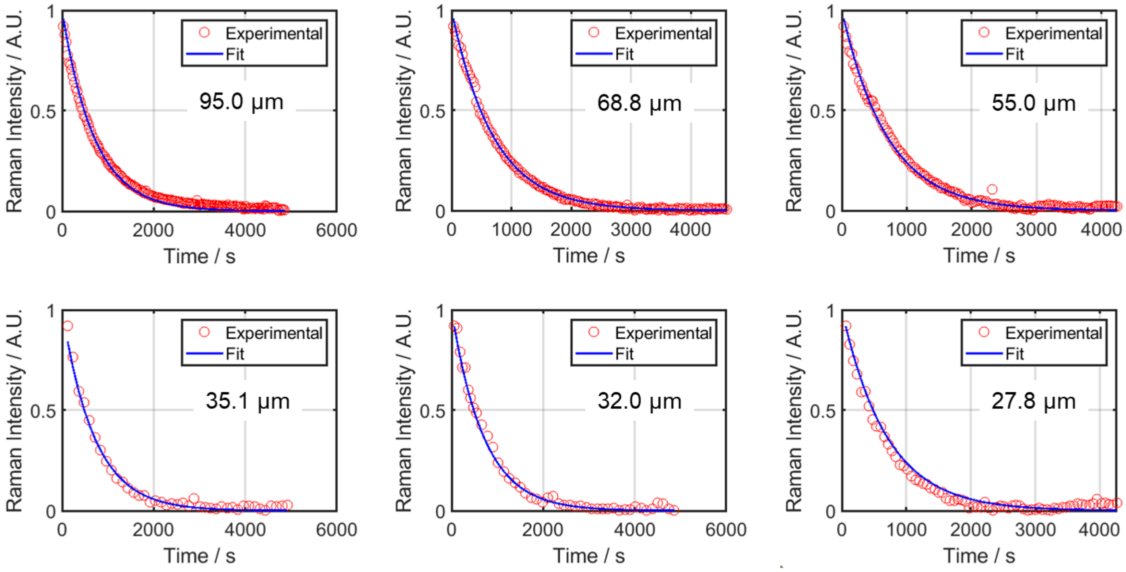

B) 70% RH

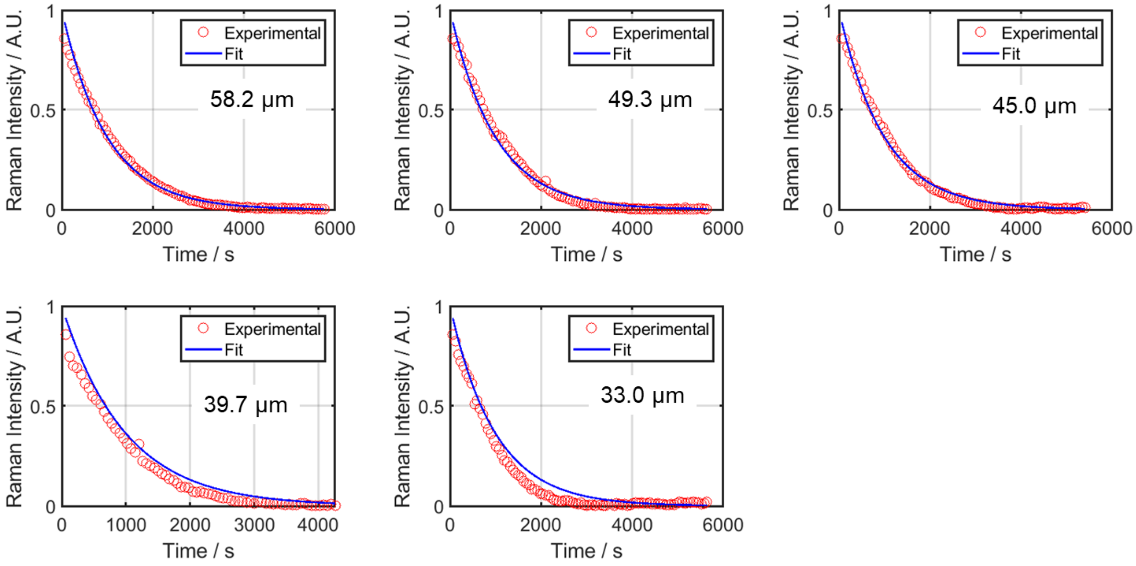

Figure S5.3 (Continued)

C) 50% RH

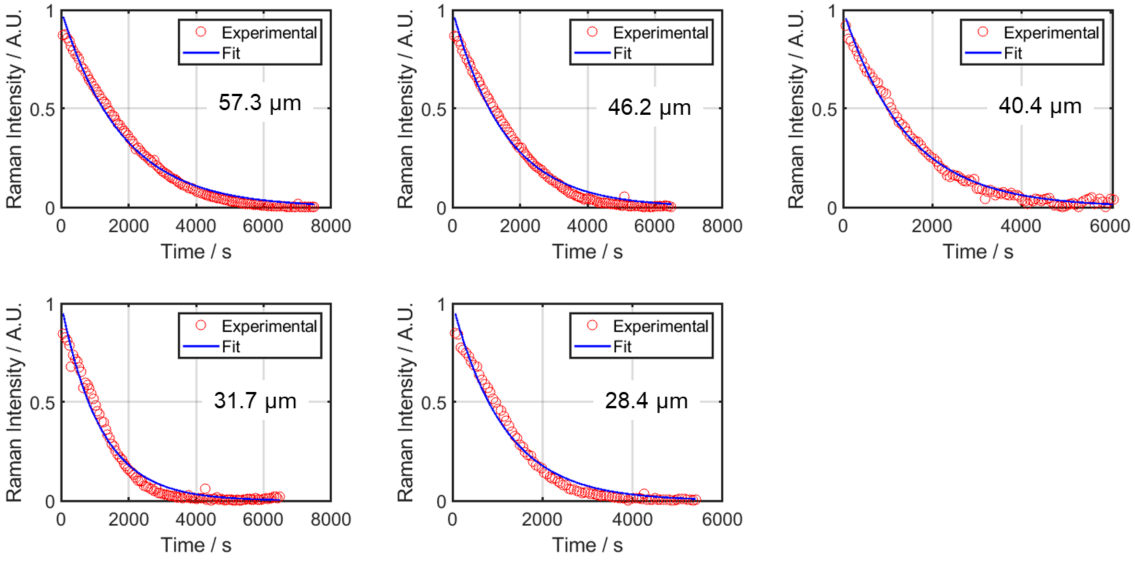

D) 30% RH

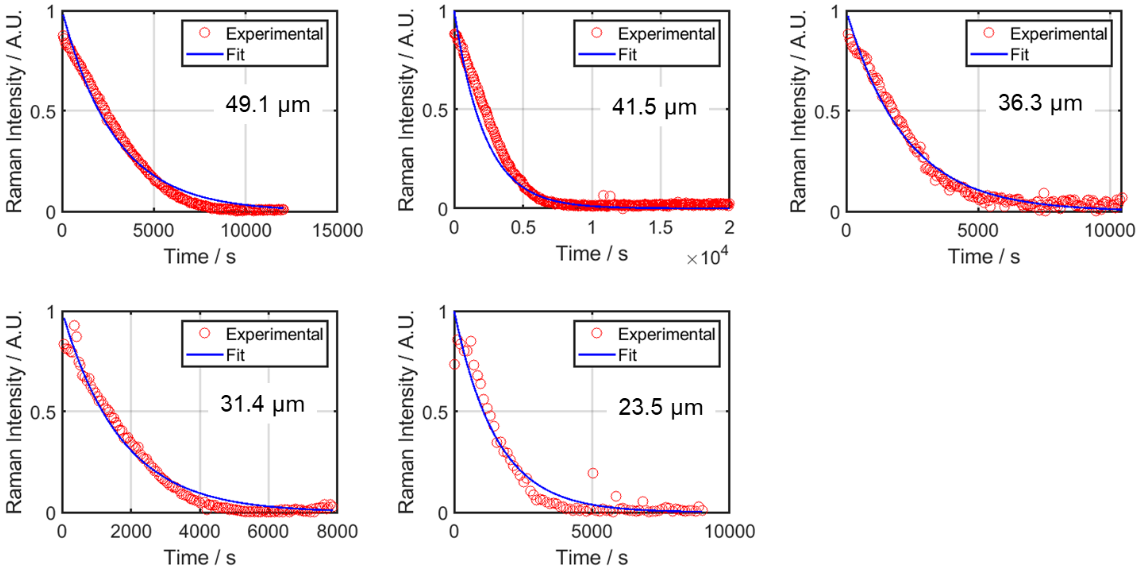

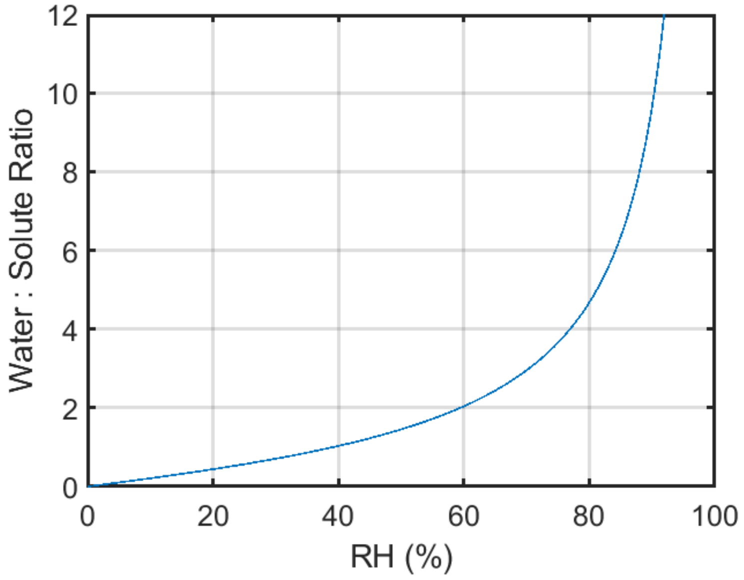

Figure S5.4: Plot of water to solute ratio (WSR) versus RH derived using modified UNIFAC parametrization.[49] MA droplets at 90, 70, 50, 30% RH conditions correspond to the WSR value of 8:1, 3:1, 1.5:1, 0.7:1 respectively.

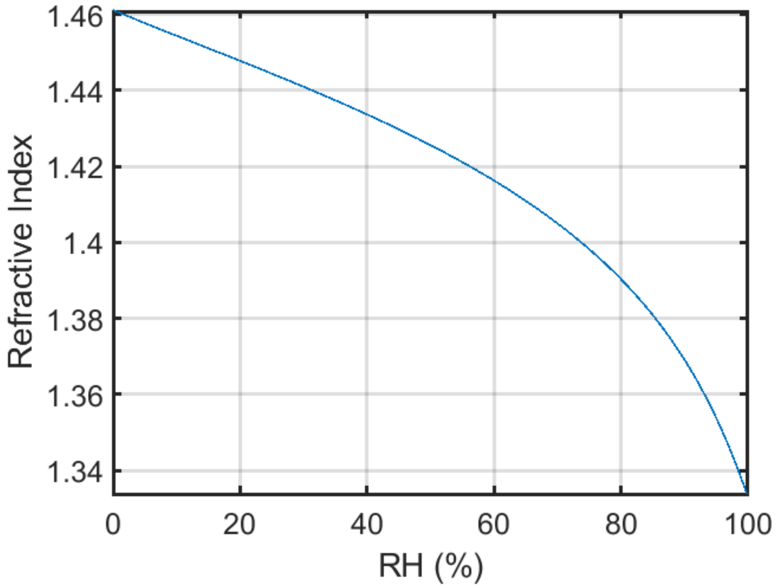

Figure S5.5: Calculated refractive index of MA droplets as a function of RH. The density treatment by Reid and coworkers[31] was employed to estimate refractive index of MA droplets using third order polynomial fit. Measured values of RH were used to estimate refractive indices of MA droplets at given RH conditions which are essential for size measurements of droplets.

Acknowledgements

Chapter 5, in full, is a reprint of the material as it appears in ACS Earth and Space Chemistry, 2021, Kim, Pyeongeun; Continetti, Robert E. The dissertation author was the primary investigator and author of this paper.

References

(1) McCormick, R. A.; Ludwig, J. H. Climate Modification by Atmospheric Aerosols. *Science* **1967**, *156* (3780), 1358 LP – 1359.

(2) Field, C. B.; Barros, V. R. *Climate Change 2014–Impacts, Adaptation and Vulnerability: Regional Aspects*; Cambridge University Press, 2014.

(3) Mauderly, J. L.; Chow, J. C. Health Effects of Organic Aerosols. *Inhal. Toxicol.* **2008**, *20* (3), 257–288.

(4) Li, Y.; Shiraiwa, M. Timescales of Secondary Organic Aerosols to Reach Equilibrium at Various Temperatures and Relative Humidities. *Atmos. Chem. Phys.* **2019**, *19* (9), 5959–5971.

(5) Shiraiwa, M.; Seinfeld, J. H. Equilibration Timescale of Atmospheric Secondary Organic Aerosol Partitioning. *Geophys. Res. Lett.* **2012**, *39* (24), L24801.

(6) Chan, M. N.; Zhang, H.; Goldstein, A. H.; Wilson, K. R. Role of Water and Phase in the Heterogeneous Oxidation of Solid and Aqueous Succinic Acid Aerosol by Hydroxyl Radicals. *J. Phys. Chem. C* **2014**, *118* (50), 28978–28992.

(7) Gentner, D. R.; Jathar, S. H.; Gordon, T. D.; Bahreini, R.; Day, D. A.; El Haddad, I.; Hayes, P. L.; Pieber, S. M.; Platt, S. M.; De Gouw, J.; Goldstein, A. H.; Harley, R. A.; Jimenez, J. L.; Prévôt, A. S. H.; Robinson, A. L. Review of Urban Secondary Organic Aerosol Formation from Gasoline and Diesel Motor Vehicle Emissions. *Environ. Sci. Technol.* **2017**, *51* (3), 1074–1093.

(8) Volkamer, R.; Jimenez, J. L.; San Martini, F.; Dzepina, K.; Zhang, Q.; Salcedo, D.; Molina, L. T.; Worsnop, D. R.; Molina, M. J. Secondary Organic Aerosol Formation from Anthropogenic Air Pollution: Rapid and Higher than Expected. *Geophys. Res. Lett.* **2006**, *33* (17), 7–10.

(9) Shrivastava, M.; Cappa, C. D.; Fan, J.; Goldstein, A. H.; Guenther, A. B.; Jimenez, J. L.; Kuang, C.; Laskin, A.; Martin, S. T.; Ng, N. L.; Petaja, T.; Pierce, J. R.; Rasch, P. J.; Roldin, P.; Seinfeld, J. H.; Shilling, J.; Smith, J. N.; Thornton, J. A.; Volkamer, R.; Wang, J.; Worsnop, D. R.; Zaveri, R. A.; Zelenyuk, A.; Zhang, Q. Recent Advances in Understanding Secondary Organic Aerosol: Implications for Global Climate Forcing. *Rev. Geophys.* **2017**, *55* (2), 509–559.

(10) Liu, M. J.; Wiegel, A. A.; Wilson, K. R.; Houle, F. A. Aerosol Fragmentation Driven by Coupling of Acid-Base and Free-Radical Chemistry in the Heterogeneous Oxidation of Aqueous Citric Acid by OH Radicals. *J. Phys. Chem. A* **2017**, *121* (31), 5856–5870.

(11) Banerjee, S.; Gnanamani, E.; Yan, X.; Zare, R. N. Can All Bulk-Phase Reactions Be Accelerated in Microdroplets? *Analyst* **2017**, *142* (9), 1399–1402.

(12) Crawford, E. A.; Esen, C.; Volmer, D. A. Real Time Monitoring of Containerless Microreactions in Acoustically Levitated Droplets via Ambient Ionization Mass Spectrometry. *Anal. Chem.* **2016**, *88* (17), 8396–8403.

(13) Yan, X.; Bain, R. M.; Cooks, R. G. Organic Reactions in Microdroplets: Reaction Acceleration Revealed by Mass Spectrometry. *Angew. Chemie - Int. Ed.* **2016**, *55* (42), 12960–12972.

(14) Li, Y.; Liu, Y.; Gao, H.; Helmy, R.; Wuelfing, W. P.; Welch, C. J.; Cooks, R. G. Accelerated Forced Degradation of Pharmaceuticals in Levitated Microdroplet Reactors. *Chem. - A Eur. J.* **2018**, *24* (29), 7349–7353.

(15) Wei, Z.; Li, Y.; Cooks, R. G.; Yan, X. Accelerated Reaction Kinetics in Microdroplets: Overview and Recent Developments. *Annu. Rev. Phys. Chem.* **2020**, *71*, 31–51.

(16) Kawamura, K.; Usukura, K. Distributions of Low Molecular Weight Dicarboxylic Acids in the North Pacific Aerosol Samples. *J. Oceanogr.* **1993**, *49* (3), 271–283.

(17) Leopold, K. R.; Haim, A. Equilibrium, Kinetics, and Mechanism of the Malonic Acid–Iodine Reaction. *Int. J. Chem. Kinet.* **1977**, *9* (1), 83–95.

(18) Ghorai, S.; Laskin, A.; Tivanski, A. V. Spectroscopic Evidence of Keto Enol Tautomerism in Deliquesced Malonic Acid Particles. *J. Phys. Chem. A* **2011**, *115* (17), 4373–4380.

(19) Yamabe, S.; Tsuchida, N.; Miyajima, K. Reaction Paths of Keto-Enol Tautomerization of β-Diketones. *J. Phys. Chem. A* **2004**, *108* (14), 2750–2757.

(20) Jansson, E. T.; Lai, Y. H.; Santiago, J. G.; Zare, R. N. Rapid Hydrogen-Deuterium Exchange in Liquid Droplets. *J. Am. Chem. Soc.* **2017**, *139* (20), 6851–6854.

(21) Rovelli, G.; Jacobs, M. I.; Willis, M. D.; Rapf, R. J.; Prophet, A. M.; Wilson, K. R. A Critical Analysis of Electrospray Techniques for the Determination of Accelerated Rates and Mechanisms of Chemical Reactions in Droplets. *Chem. Sci.* **2020**, *11* (48), 13026–

13043.

(22) Hansen, E. W.; Ruoff, P. Estimation of Malonic Acid and Methylmalonic Acid Enolization Rate Constants by an Isotopic-Exchange Reaction Using 1H NMR Spectroscopy. *J. Phys. Chem.* **1988**, *92* (9), 2641–2645.

(23) Lee, C. R.; Kim, H. S.; Jang, I. H.; Im, J. H.; Park, N. G. Pseudo First-Order Adsorption Kinetics of N719 Dye on TiO2 Surface. *ACS Appl. Mater. Interfaces* **2011**, *3* (6), 1953–1957.

(24) Anzo, K.; Harada, M.; Okada, T. Enhanced Kinetics of Pseudo First-Order Hydrolysis in Liquid Phase Coexistent with Ice. *J. Phys. Chem. A* **2013**, *117* (41), 10619–10625.

(25) Bockisch, C.; Lorance, E. D.; Hartnett, H. E.; Shock, E. L.; Gould, I. R. Kinetics and Mechanisms of Dehydration of Secondary Alcohols under Hydrothermal Conditions. *ACS Earth Sp. Chem.* **2018**, *2* (8), 821–832.

(26) Nadler, K. A.; Kim, P.; Huang, D. L.; Xiong, W.; Continetti, R. E. Water Diffusion Measurements of Single Charged Aerosols Using H_2O/D_2O Isotope Exchange and Raman Spectroscopy in an Electrodynamic Balance. *Phys. Chem. Chem. Phys.* **2019**, *21* (27), 15062–15071.

(27) Kim, P.; Xiong, W.; Continetti, R. E. Evolution of Hydrogen-Bond Interactions within Single Levitated Metastable Aerosols Studied by in Situ Raman Spectroscopy. *J. Phys. Chem. B* **2020**, *124* (42), 9385–9395.

(28) Trevitt, A. J.; Wearne, P. J.; Bieske, E. J. Calibration of a Quadrupole Ion Trap for Particle Mass Spectrometry. *Int. J. Mass Spectrom.* **2007**, *262* (3), 241–246.

(29) Glantschnig, W. J.; Chen, S.-H. Light Scattering from Water Droplets in the Geometrical Optics Approximation. *Appl. Opt.* **1981**, *20* (14), 2499.

(30) Graßmann, A.; Peters, F. Size Measurement of Very Small Spherical Particles by Mie Scattering Imaging (MSI). *Part. Part. Syst. Charact.* **2004**, *21* (5), 379–389.

(31) Cai, C.; Miles, R. E. H.; Cotterell, M. I.; Marsh, A.; Rovelli, G.; Rickards, A. M. J.; Zhang, Y. H.; Reid, J. P. Comparison of Methods for Predicting the Compositional Dependence of the Density and Refractive Index of Organic-Aqueous Aerosols. *J. Phys. Chem. A* **2016**, *120* (33), 6604–6617.

(32) Salomon, M. *Thermodynamic Properties of Liquid H_2O and D_2O and Their Mixtures*; United States. National Aeronautics and Space Administration. “NASA Technical Note.” Print.: Washington, D.C., 1969.

(33) Bykov, S. V.; Myshakina, N. S.; Asher, S. A. Dependence of Glycine CH2 Stretching Frequencies on Conformation, Ionization State, and Hydrogen Bonding. *J. Phys. Chem. B* **2008**, *112* (18), 5803–5812.

(34) Zhou, S.; Shiraiwa, M.; McWhinney, R. D.; Pöschl, U.; Abbatt, J. P. D. Kinetic Limitations in Gas-Particle Reactions Arising from Slow Diffusion in Secondary Organic Aerosol. *Faraday Discuss.* **2013**, *165*, 391–406.

(35) Slade, J. H.; Knopf, D. A. Multiphase OH Oxidation Kinetics of Organic Aerosol: The Role of Particle Phase State and Relative Humidity. *Geophys. Res. Lett.* **2014**, *41* (14), 5297–5306.

(36) Chang, P.; Chen, Z.; Zhang, Y.; Liu, Y. Direct Measurement of Aerosol PH in Individual Malonic Acid and Citric Acid Droplets under Different Relative Humidity Conditions via Raman Spectroscopy. *Chemosphere* **2020**, *241*, 124960.

(37) Seinfeld, J. H.; Pandis, S. N. *Atmospheric Chemistry and Physics: From Air Pollution to Climate Change*; John Wiley & Sons, 2016.

(38) Peng, C.; Chan, C. K.; Chow, A. H. L. Hygroscopic Study of Glucose, Citric Acid, and Sorbitol Using an Electrodynamic Balance: Comparison with UNIFAC Predictions. *Aerosol Sci. Technol.* **2001**, *35* (3), 753–758.

(39) Wilson, K. R.; Prophet, A. M.; Rovelli, G.; Willis, M. D.; Rapf, R. J.; Jacobs, M. I. A Kinetic Description of How Interfaces Accelerate Reactions in Micro-Compartments. *Chem. Sci.* **2020**, *11* (32), 8533–8545.

(40) Hua, W.; Chen, X.; Allen, H. C. Phase-Sensitive Sum Frequency Revealing Accommodation of Bicarbonate Ions, and Charge Separation of Sodium and Carbonate Ions within the Air/Water Interface. *J. Phys. Chem. A* **2011**, *115* (23), 6233–6238.

(41) Blower, P. G.; Shamay, E.; Kringle, L.; Ota, S. T.; Richmond, G. L. Surface Behavior of Malonic Acid Adsorption at the Air/Water Interface. *J. Phys. Chem. A* **2013**, *117* (12), 2529–2542.

(42) Liu, D.; Ma, G.; Levering, L. M.; Allen, H. C. Vibrational Spectroscopy of Aqueous Sodium Halide Solutions and Air−Liquid Interfaces: Observation of Increased Interfacial Depth. *J. Phys. Chem. B* **2004**, *108* (7), 2252–2260.

(43) Shrestha, M.; Luo, M.; Li, Y.; Xiang, B.; Xiong, W.; Grassian, V. H. Let There Be Light: Stability of Palmitic Acid Monolayers at the Air/Salt Water Interface in the Presence and Absence of Simulated Solar Light and a Photosensitizer. *Chem. Sci.* **2018**, *9* (26), 5716–5723.

(44) J. R. Keeffe, A. J. Kresge, and N. P. S. Generation of Simple Enols by Photooxidation. Keto-Enol Equilibrium Constants of Some Aliphatic Systems in Aqueous Solution. *J. Am. Chem. Soc.* **1988**, *110*, 1993–1995.

(45) Lim, Y. B.; Tan, Y.; Perri, M. J.; Seitzinger, S. P.; Turpin, B. J. Aqueous Chemistry and Its Role in Secondary Organic Aerosol (SOA) Formation. *Atmos. Chem. Phys.* **2010**, *10* (21), 10521–10539.

(46) Lei, X.; Wang, W.; Cai, J.; Wang, C.; Liu, F.; Wang, W. Atmospheric Chemistry of Enols: Vinyl Alcohol + OH + O 2 Reaction Revisited. *J. Phys. Chem. A* **2019**, *123* (14), 3205–3213.

(47) Narukawa, M.; Kawamura, K.; Li, S. M.; Bottenheim, J. W. Dicarboxylic Acids in the Arctic Aerosols and Snowpacks Collected during ALERT 2000. *Atmos. Environ.* **2002**, *36* (15–16), 2491–2499.

(48) Zuend, A.; Marcolli, C.; Booth, A. M.; Lienhard, D. M.; Soonsin, V.; Krieger, U. K.; Topping, D. O.; McFiggans, G.; Peter, T.; Seinfeld, J. H. New and Extended Parameterization of the Thermodynamic Model AIOMFAC: Calculation of Activity Coefficients for Organic-Inorganic Mixtures Containing Carboxyl, Hydroxyl, Carbonyl, Ether, Ester, Alkenyl, Alkyl, and Aromatic Functional Groups. *Atmos. Chem. Phys.* **2011**, *11* (17), 9155–9206.

(49) Peng, C.; Chan, M. N.; Chan, C. K. The Hygroscopic Properties of Dicarboxylic and Multifunctional Acids: Measurements and UNIFAC Predictions. *Environ. Sci. Technol.* **2001**, *35* (22), 4495–4501.

CHAPTER 6: Photo-Induced Reactions of Nitrate in Aqueous Droplets Through a Triplet-Triplet Energy Transfer Mechanism

6.1: Introduction

Aerosols are ubiquitous in nature, and greatly impact the Earth's climate and human health.[1–4] In the atmosphere, aerosols can undergo various chemical reactions including heterogeneous reactions, photochemical reactions by irradiation of ultraviolet (UV) light, and accelerated reactions of organic molecules.[5–9] In particular, photochemical reactions of aqueous NO_3^- are of great interest because the reactions produce highly reactive species such as NO_2, HONO, and hydroxyl radical (·OH).[10] NO_3^- is a ubiquitous compound found in surface waters and atmospheric aerosols.[11] Since it is known that the photolysis of NO_3^- can play a role modulating the concentration of volatile organic compounds and affect the formation of secondary organic aerosols (SOAs), understanding the pathways and rates of photochemical reactions is an essential step for gaining a quantitative understanding of the chemical evolution of atmospheric aerosols containing NO_3^-.[12–15]

The UV-absorption spectrum of aqueous NO_3^- contains a very weak $n \rightarrow \pi^*$ band centered near 302 nm and a strong $\pi \rightarrow \pi^*$ band at 200 nm.[16] The $n \rightarrow \pi^*$ transition of NO_3^- is forbidden by symmetry, however the influence of solvent molecules breaks the symmetry, lifting the dipole-forbidden character of the transition and leading to a weak absorption in the 280 – 330 nm range.[17,18] The solar UV spectrum overlaps with the energy of the $n \rightarrow \pi^*$ transition of nitrate, and the direct photolysis of aqueous NO_3^- in this wavelength range leads to two main dissociation pathways.[16]

$$NO_3^- \xrightarrow{h\nu} NO_2^- + O\,(^3P) \qquad \Phi = 1.1 * 10^{-3} \tag{6.1}$$

$$NO_3^- \xrightarrow{h\nu\ H^+} NO_2 + \cdot OH \qquad \Phi = 9.2 * 10^{-3} \tag{6.2}$$

In acidic conditions, the nitrite anion (NO_2^-) can readily react with H^+ and produce gaseous HONO.[19]

$$NO_2^- + H_3O^+ \rightarrow H_2O + HONO \tag{6.3}$$

HONO is a major precursor of ·OH radicals that play a key role as one of the most important oxidants in the atmosphere.[13] However, field studies have reported unexpectedly high emissions of HONO during the day,[20,21] and it has been suggested that UV-photolysis of NO_3^- is potentially an important unaccounted source for daytime HONO production.[22]

Recent studies have revealed that dissolved organic matter can act as a photosensitizer and enhance nitrate photolysis.[23–25] Wang *et al.* showed an increased quantum yield of NO_2^- from photolysis of NO_3^- in the presence of UV-absorbing vanillic acid.[23] Gen *et al.* used iron-organic complexes to measure increased HONO production rates.[24] The photosensitizing effect of marine chromophoric dissolved organic matter (m-CDOM) was compared with other organic photosensitizers (humic acid and 4-benzoylbenzoic acid) by Mora-Garcia *et al.*[25] These studies suggested that the presence of photosensitizers increases the production rates of HONO, however, the exact mechanisms of photosensitized reactions of nitrate leading to the enhanced production of HONO remain unclear. These studies made use of a Xe lamp with a broadband output between

290 – 350 nm as a source of UV radiation, simultaneously promoting photosensitized reactions and direct photolysis of nitrate.[23–25] This makes it difficult to isolate and quantify the effect of photosensitizers as the rate of the depletion of NO_3^- has contributions from both direct photolysis and photosensitized reactions of NO_3^-. Therefore, there is a great demand for an investigation that separates the photosensitized reaction of NO_3^- from direct photolysis to provide a better understanding of the factors governing HONO and NO_2 production in organic-laden aqueous aerosols.

To effectively simulate photo-induced reactions in atmospheric aerosols, an environment-controlled electrodynamic balance (EDB) was utilized for the levitation of single aqueous microdroplets.[26,27] Sample solutions for droplet generation were made with water, sodium nitrate ($NaNO_3$), citric acid (CA), and SA, and the pH of the droplets was adjusted by using a citric acid/sodium citrate buffer. Sulfanilic acid (SA) was chosen as a model light-absorbing organic molecule, and the 266 nm output from a Nd:YAG laser was used as a source of photoexcitation. SA has a strong UV-absorption band at 230 – 280 nm,[28] thus it is effectively excited by the 266 nm laser irradiation ($\varepsilon > 200$ M^{-1} cm^{-1}). Photolysis of NO_3^- by 266 nm is improbable owing to the low molar extinction coefficient ($\varepsilon = 1.5$ M^{-1} cm^{-1}) at this wavelength.[12]

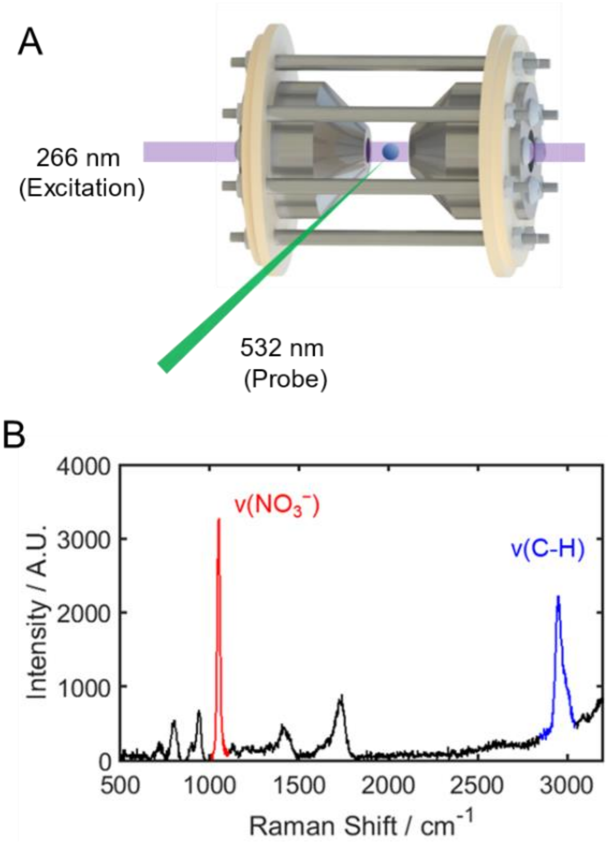

Figure 6.1: Determination of nitrate concentration in levitated droplets. (A) Schematic of the EDB with a levitated aqueous microdroplet. In these experiments, an aqueous droplet with ~80 µm diameter is trapped between the two endcap electrodes of the EDB. A 266 nm beam (purple) is passed through the holes of the endcap electrodes. The beam waist of the 266 nm laser and size of the droplet are exaggerated for visibility. A 532 nm (green) probe beam is focused on the droplet with a direction perpendicular to the 266 nm beam. (B) Raman spectrum of the droplet generated from an aqueous solution of CA, SA and $NaNO_3$. The $\nu_s(NO_3^-)$ peak at 1050 cm^{-1} and ν(C-H) peak of SA at 2950 cm^{-1} are colored red and blue, respectively.

6.2: Experimental Methods

Figure 6.1A shows a simplified schematic of the EDB and a levitated microdroplet. The 266 nm irradiation photoexcites the SA in the droplet, while the 532 nm laser produces the Raman spectrum and allows for Mie scattering imaging (MSI) analysis. Real-time molal concentrations (m) of NO_3^- ($[NO_3^-]$) of the levitated microdroplets were measured by quantifying the intensities of characteristic Raman peaks of NO_3^- symmetric stretch ($\nu_s(NO_3^-)$) relative to the C-H stretch (ν(C-H)) in CA (**Figure 6.1B**).

Droplets were generated and introduced into the EDB using piezoelectric droplet generator (Engineering Arts DE03) with a motorized syringe. The droplet generator was loaded with aqueous solutions containing HPLC grade water (Fisher Chemical), 2.4 molal (m) citric acid (>99.0%, Fisher Chemical), 2.0 m sodium nitrate (>99.0%, Alfa Aesar), and 0 - 75 x 10^{-3} m sulfanilic acid (>99.0%, Tokyo Chemical Industry Co.). Sodium citrate (>99.0%, Fisher Chemical) was added to solutions to adjust the pH of the solution/droplet, which will be discussed later. Droplet charging was necessary for the electrodynamic trapping and was achieved by the grounded metallic tip of the droplet generator in a circuit with an inductive charging ring (-600 V).

The levitation of single droplets was accomplished by an environment=controlled EDB coupled with laser spectroscopy setup. The schematic layout of the instrument used in this study is shown in **Figure 6.2**. Principles of particle levitation by EDBs have well been established in the literature.[29,30] In short, a charged single droplet was trapped at the null point of the alternating quadrupole electric field generated by two conical-shaped endcap electrodes. Gravitational force exerted on the droplet was compensated by a DC potential applied to two rod electrodes at the bottom of the EDB. Typical trapping conditions for this experiment were 1.5 kV and 60-120 Hz for the AC quadrupole electric field and +400-800 V DC for gravitational compensation.

The levitated droplet was illuminated by 4th and 2nd harmonic output beams (266 and 532 nm) from the pulsed Nd:YAG laser with a vertical polarization (RMPC Wedge XF, 80kHz repetition rate). Laser power for 266 and 532 nm irradiation was 0.1 mw and 40 mw, respectively. Both 266 nm and 532 nm beams were generated simultaneously, then separated by a harmonic beamsplitter (Thorlabs HBSY134). After the separation, both beams are redirected perpendicularly to the center of the EDB where a droplet is levitated. 266 nm beam was used to induce photochemical reactions for the levitated droplet. A motorized filter flip (Thorlabs MFF101) equipped with a 532 nm laser line filter was served as an on-and-off switch for 266 nm beam. On the other hand, the 532 nm beam was utilized as a probe for MSI and Raman spectroscopy.

The relative humidity (RH) of the EDB were controlled by an automated bubbler system with solenoid valves and mass flow controllers (Alicat MC-500SCCM). Humid and dry N_2 gas were mixed to maintain the chamber at 80% RH (flow rate 120 sccm). The temperature was maintained at ambient temperature (20-21 °C). The temperature and RH were recorded using a capacitance probe (Vaisala HMP110) with ±1 °C and ±1.5% accuracy, respectively. The RH was maintained at 80% during all experiments, and the fluctuation of RH was no greater than ±1%.

Images of Mie scattering pattern were collected by a camera (Allied Vision Mako GigE) equipped with a polarizer in the 45° forward direction with respect to the laser path. Collected Mie scattering images were processed with a MATLAB script to estimate the diameter of levitated droplets from the spacing between the pattern **(Figure 6.3)**.[31] The geometrical approximation of

Mie theory was used to simplify the calculation of droplet size determination. The range of droplet diameters studied was 70 to 100 μm (**Figure 6.4**).

The chemical evolution of the droplets was analyzed by Raman spectroscopy. Backscattered Stokes-shifted Raman signal of all polarization was focused into a fiber optic cable coupled into a f/4.1 spectrometer (Horiba iHR-320) with a TE-cooled CCD detector (Horiba SynapsePro, 2048x512 pixels). The integration time for each spectrum was 30 seconds, then two spectra were averaged for a better signal-to-noise (S/N) ratio. Assuming only nitrate would undergo photosensitized reactions upon 266 nm irradiation, intensity ratios between the $\nu(NO_3^-)$ peak at 1050 cm^{-1} and ν(C-H) peak at 2950 cm^{-1} were used to measure the concentration of nitrate in droplets. The calibration curve was made by Raman spectra of droplets with known nitrate concentration (**Figure 6.5**). Due to the relatively lower concentration of sulfanilic acid in droplets compared to citric acid or sodium nitrate, its Raman spectral feature was unnoticeable.

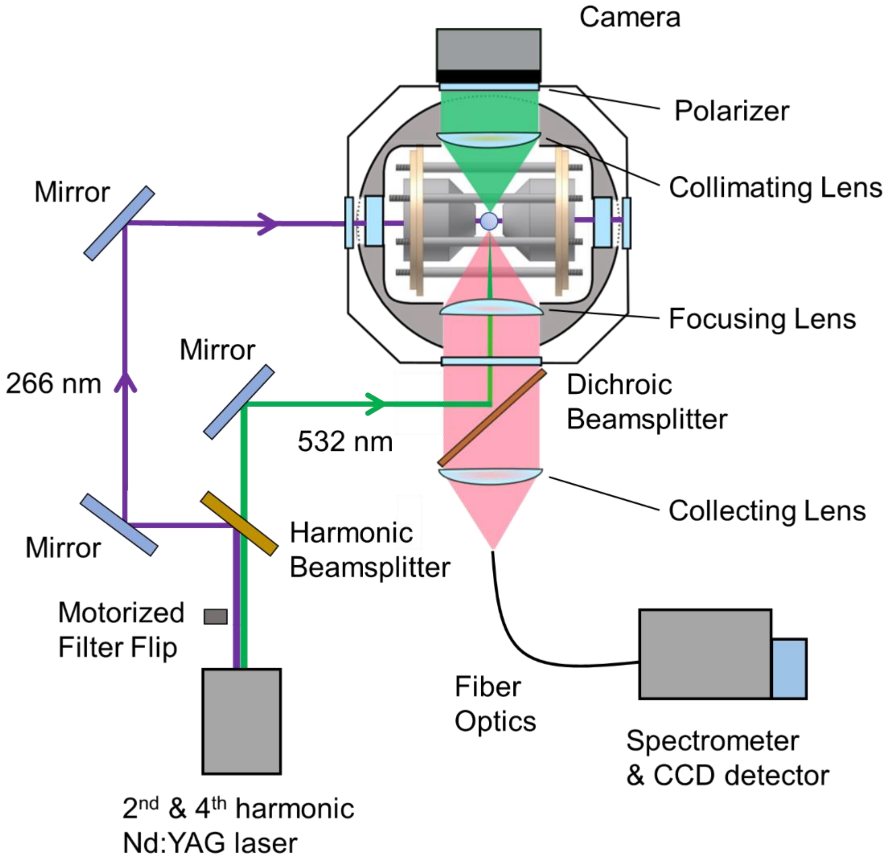

Figure 6.2: Schematic diagram of the EDB with dual-beam spectroscopy setup.

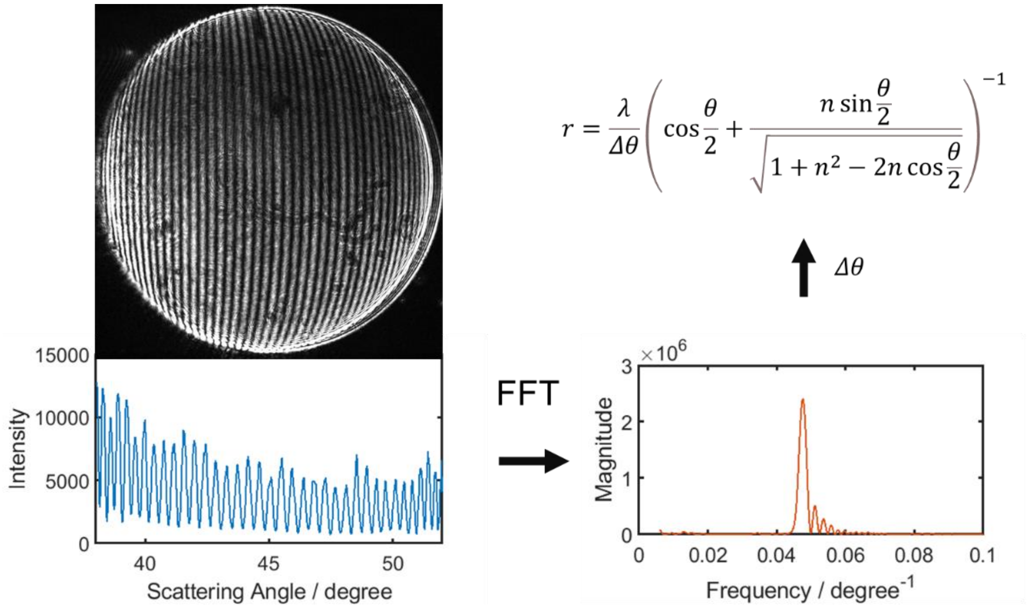

$$r = \frac{\lambda}{\Delta\theta}\left(\cos\frac{\theta}{2} + \frac{n\sin\frac{\theta}{2}}{\sqrt{1+n^2-2n\cos\frac{\theta}{2}}}\right)^{-1}$$

Figure 6.3: Illustration of the Mie scattering imaging (MSI) process. Scattering image collected from the CCD camera is expressed into an intensity spectrum by summing the 2D intensity values vertically. The fast Fourier transform (FFT) converts the intensity spectrum into a frequency domain, then the pattern frequency ($\Delta\theta$, unit: degree^{-1}). Is obtained. Then the equation for geometrical optics approximation of Mie theory is used to determine the size of the droplet.[31] In the equation, r is the droplet radius, θ is the image collection solid angle (16.3 degree), λ is wavelength of incoming light (532 nm), and n is the refractive index of the droplet. $n \sim 1.38$ is approximated by comparing refractive index values of aqueous CA and aqueous $NaNO_3$ solutions.[32,33]

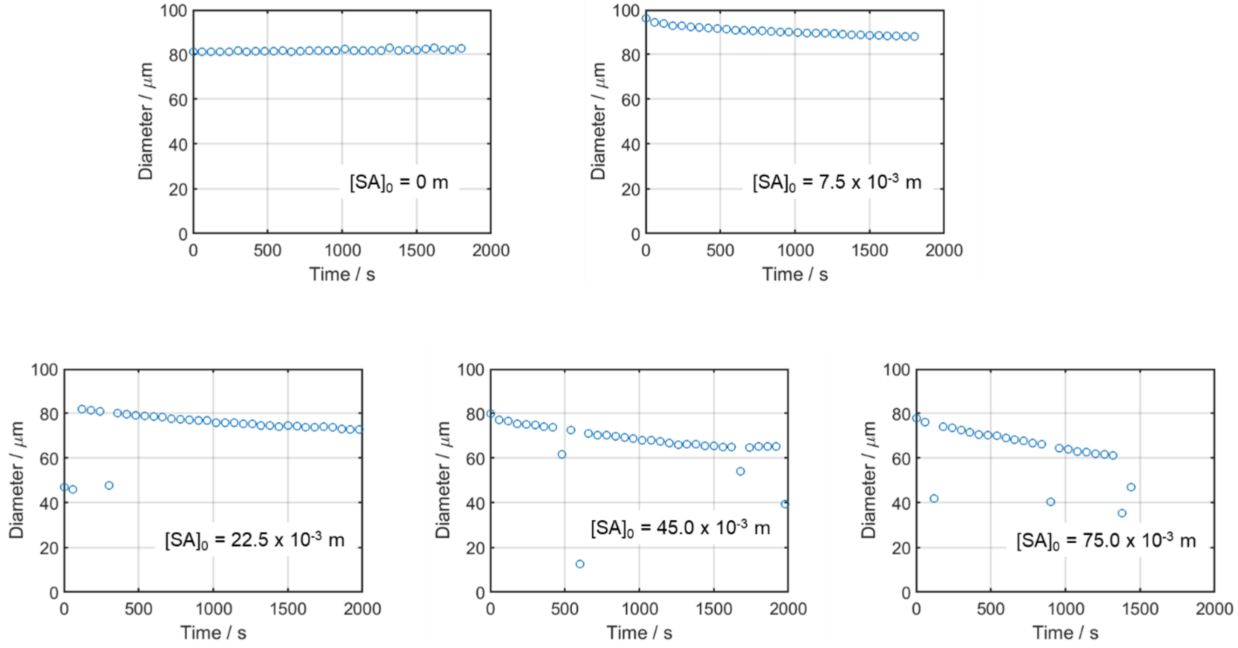

Figure 6.4: Diameters of the droplet versus 266 nm irradiation time at varying [SA]$_0$.

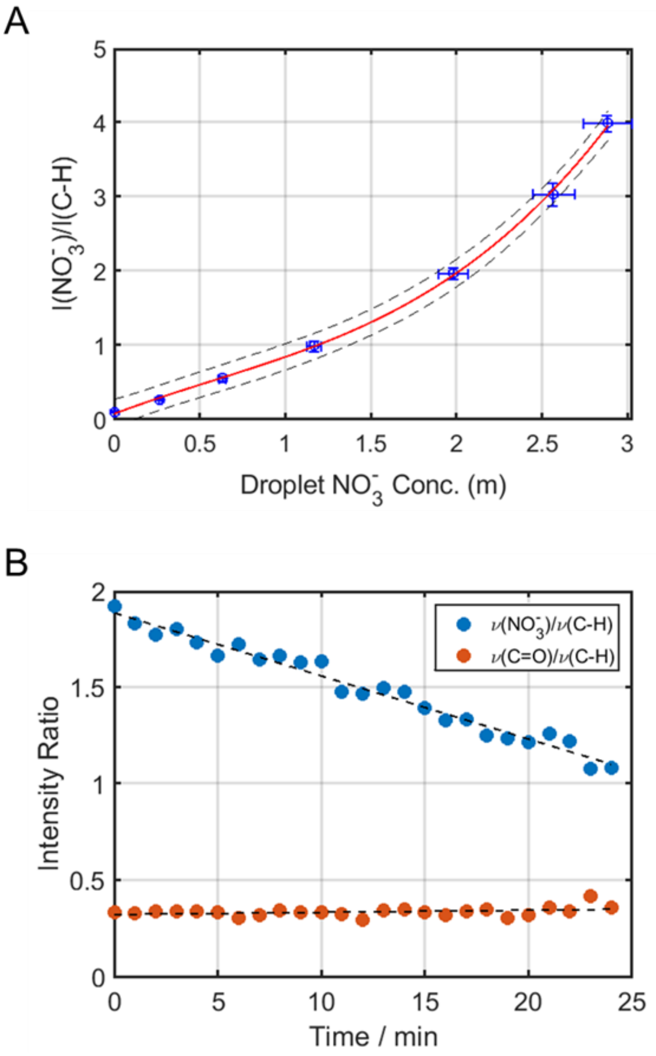

Figure 6.5: Relationship between intensity ratio and concentration. (A) Calibration curve for the correlation between [NO_3^-] and intensity ratio ($\nu_s(NO_3^-)$ to ν(C-H)). [NO_3^-] values of the levitated droplets at 80% RH were determined from calculation of starting conditions using AIOMFAC model.[34,35] The calibration curve is a third-order polynomial equation with a = 0.1416, b= -0.2430, c= 0.8673, and d = 0.0755. (B) Comparison of intensity ratios of $\nu_s(NO_3^-)$ to ν(C-H) (blue circles) and ν(C=O) to ν(C-H) (orange circles) as the depletion of NO_3^- from the droplet continues. Initial concentration of SA was 75.0 x 10^{-3} m. Note that ν(C=O) to ν(C-H) intensity ratio stayed nearly constant over the 266 nm irradiation, showing that CA is not affected by 266 nm laser.

6.3: Results and Discussion

As the levitated microdroplets with pH ~ 0.5 were irradiated by 266 nm, a decrease in [NO_3^-] in the presence of SA was observed over ~30-minute reaction timeframes. Observations were limited to ~30 minutes of UV irradiation, as individual droplets became unstable and eventually were ejected from the EDB. A possible reason for this limitation is discussed below. **Figure 6.6A** shows the depletion of [NO_3^-] as a function of irradiation time with varying initial concentrations of SA ($[SA]_0$). The loss of NO_3^- is due to the reduction of NO_3^- into HONO (g) and NO_2 (g) which are volatile and can escape from the droplet.[25,36] The effect of SA with 266 nm irradiation as a reaction initiator for reduction of NO_3^- is apparent as higher $[SA]_0$ leads to faster depletion of NO_3^-. **Figure 6.6B** shows the linear relationship observed between $[SA]_0$ and the rate of NO_3^- depletion. The depletion rate of NO_3^- was minimal (6.06×10^{-6} s^{-1}) for the droplet with $[SA]_0 = 0$ m, hence the results here indicate that without SA, the 266 nm irradiation does not induce noticeable depletion of NO_3^-. Measurements of [NO_3^-] with and without UV irradiation further proves that both UV and SA are needed for reactions of NO_3^- (**Figure 6.7**). It is worth noting that even under the acidic conditions used the evaporation of nitric acid (HNO_3) was negligible during the ~30 minutes of reaction time (**Figure 6.8**). Given the fact that the depletion rates of NO_3^- are linearly related to $[SA]_0$ and the rates remain stable over the course of measurements, it is clear that photo-induced nitrate depletion is due to the presence of SA.

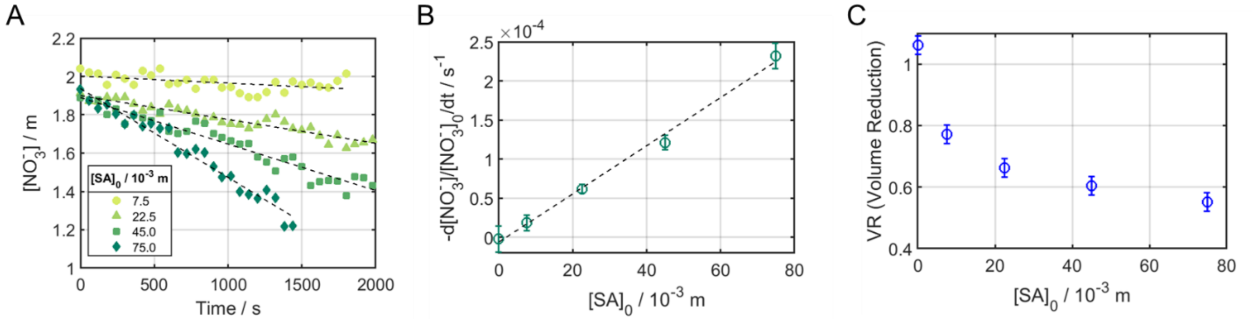

Figure 6.6: Photo-induced depletion of NO_3^- from the levitated aqueous microdroplets. (A) Measured $[NO_3^-]$ as a function of time with varying $[SA]_0$ in the range up to 75.0 x 10^{-3} m. Dashed black lines represent linear fits to the data. Data with $[SA]_0 = 0$ showed no NO_3^- depletion and not pictured here for clarity, instead provided in SI (**Figure S2**). (B) Relative rates (s^{-1}) of NO_3^- depletion versus initial [SA]. Error bars represent 95% confidence intervals of the linear fit. (C) Volume reduction (VR) of the droplets versus initial [SA] conditions. Error bars represent uncertainties from approximated refractive index of the droplets.

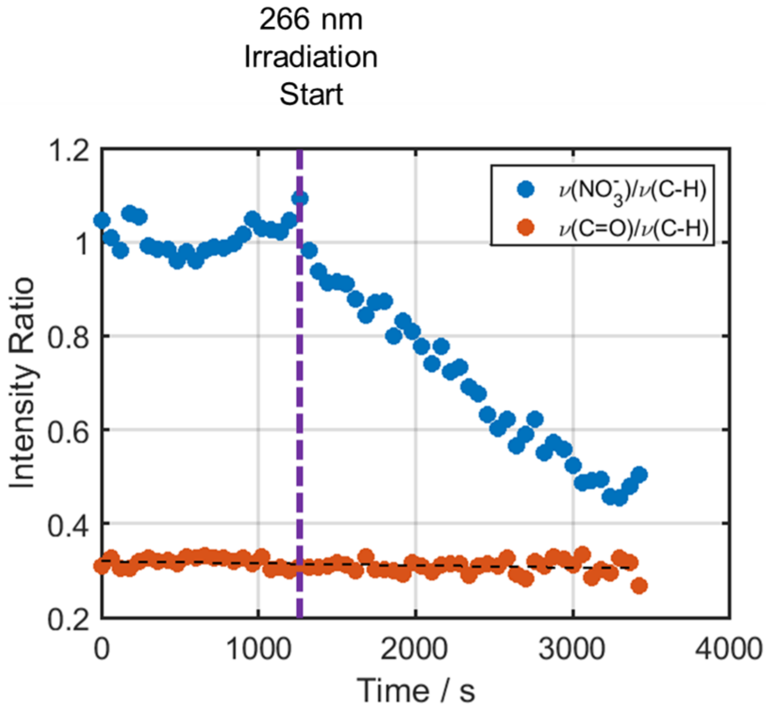

Figure 6.7: Raman intensity ratios of $\nu_s(NO_3^-)/\nu(C\text{-}H)$ and $\nu(C=O)/\nu(C\text{-}H)$ versus time when 266 nm irradiation was started at t = 1260 s.

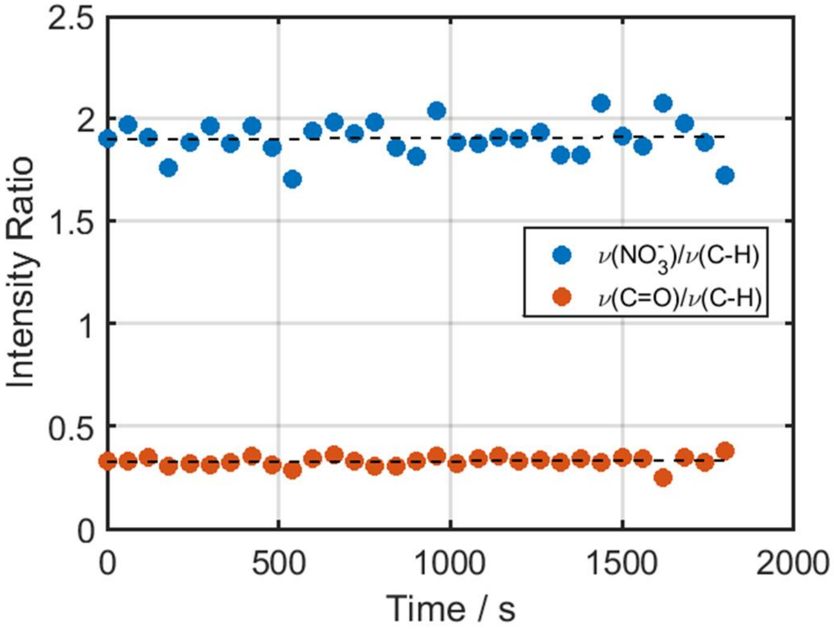

Figure 6.8: Raman intensity ratios of the droplet with 0 m SA for 30 minutes. The pH of the droplet is about 0.5, and no noticeable depletion of NO_3^- is observed. Therefore, evaporation rate of HNO3 from the droplet is negligible for timeframe of ~30 minutes.

The observed rates of NO_3^- depletion by SA and 266 nm irradiation are unexpectedly fast. For the droplet with [SA] = 75.0 x 10^{-3} m, ~40% of the nitrate was depleted after 23 minutes of 266 nm irradiation (**Figure 6.6A**) and the rate of depletion was 2.3 x 10^{-4} s^{-1}. Comparing this value of nitrate depletion rate with the highest enhanced rate (1.70 x 10^{-5} s^{-1}) from the study by Gen *et al.*,[24] the depletion rate from our measurement is more than an order of magnitude higher. This striking enhancement of nitrate depletion rate by UV-excited SA clearly demonstrates the effectiveness of SA as a photocatalyst for reduction of NO_3^-. A control experiment was conducted with hydrogen peroxide (H_2O_2) instead of SA, thus producing ·OH in the droplet. The result showed no significant decrease of [NO_3^-] during the 266 nm irradiation with H_2O_2 (**Figure 6.9**). This observation rules out the possibility of NO_3^- depletion by ·OH that is typically produced in photosensitized reactions.[25,37,38] Additionally, the rate of NO_3^- depletion in droplets with varying [NO_3^-] and fixed $[SA]_0$ was also measured, and slower depletion rate for higher and [NO_3^-] was observed (**Figure 6.10**). This trend may arise from the hygroscopic effect of $NaNO_3$, as more NO_3^- leads to larger water content in droplets and further diluting $[SA]_0$. These thorough examinations further confirm that the reduction of NO_3^- (equation 6.1 and 6.2) can proceed without the photolysis of NO_3^- but indirectly and efficiently by the UV-excitation of SA.

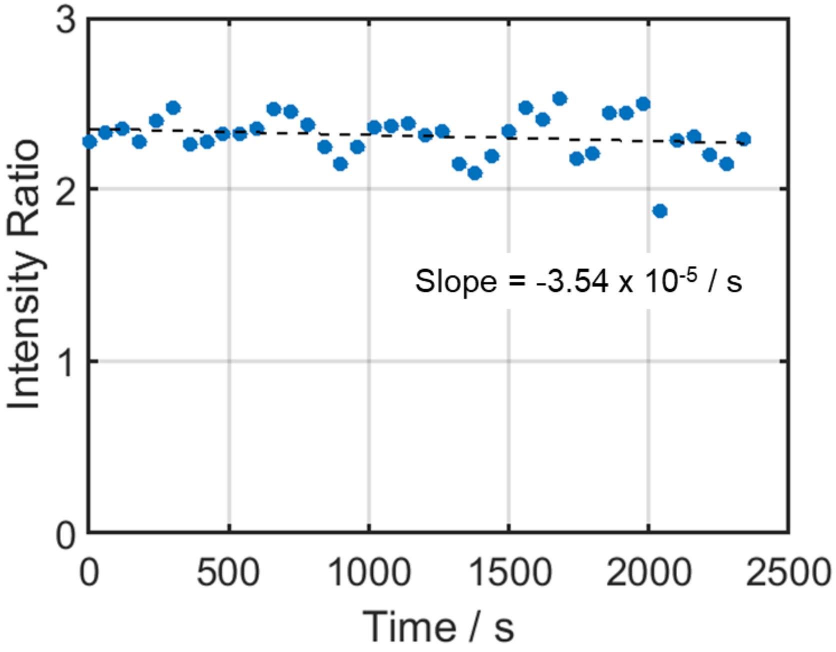

Figure 6.9: Raman intensity ratios of $\nu_s(NO_3^-)/\nu(C\text{-}H)$ versus time when H_2O_2 is added instead of SA. Concentration of H_2O_2 in the droplet is estimated to be ~ 1 M.

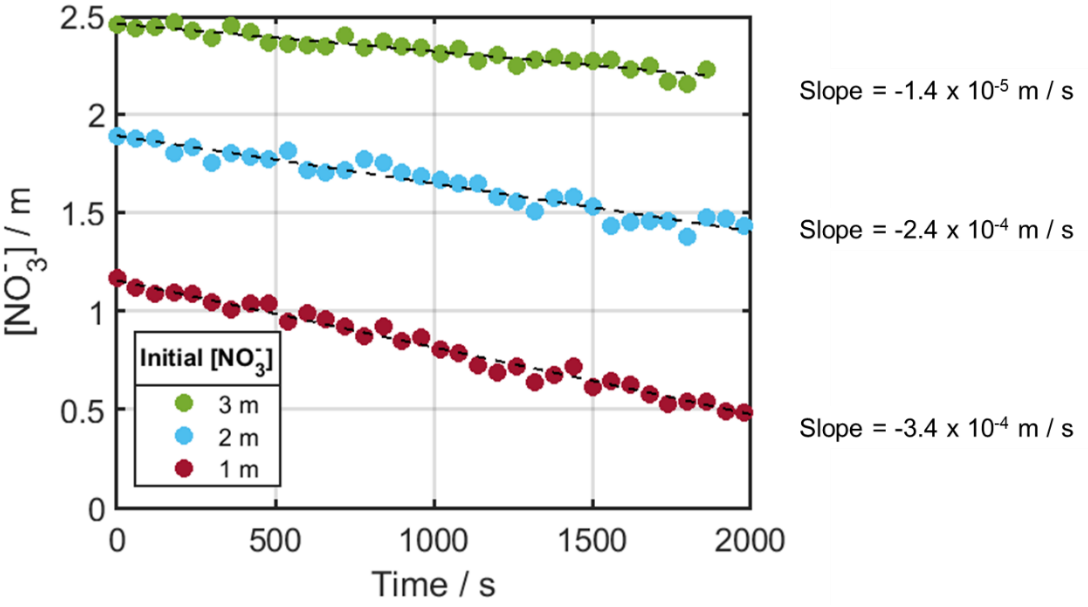

Figure 6.10: Depletion of NO_3^- from the droplets over time when $[NO_3^-]_0$ is varied from 1 m to 3 m, and $[SA]_0$ is kept constant at 22.5 x 10^{-3} m.

In addition to the depletion of NO_3^-, the volume of the droplets with SA decreased during 266 nm irradiation as shown in **Figure 6.6C**. The droplets with higher [SA] showed a higher volume reduction (VR) which is defined as follows,

$$VR = \frac{V_f}{V_i} \tag{6.4}$$

where V_i is the volume of the droplet at the start (t = 0) of 266 nm irradiation and V_f is the volume of the droplet measured at the end of the run. It is clear that the volume reduction of the droplets is caused by the photochemical reactions triggered by the excited-state SA, as NO_3^- molecules can transform into volatile compounds such as NO_2 and HONO gas. Equation 6.1 is a possible pathway for nitrate reduction and the produced NO_2 (g) can escape from the droplet surface. Given that the droplets are in highly acidic conditions due to CA (pH ~0.5), the NO_2^- produced from equation 6.2 can readily form HONO (g) (equation 6.3) and escape the droplets as well.[25] Depletion of NO_3^- from the droplet is accompanied by the evaporation of water because of the hygroscopic effect of NO_3^-.[39] Therefore, the droplets with 266 nm irradiation show VR (**Figure 6.6C**) as well as a decrease in droplet mass.Stable trapping condition of a single droplet in the EDB is dependent on the mass-to-charge ratio (m/q).[30] This can be the reason for the upper bound (~30 minutes) limit of the droplet trapping time with 266 nm irradiation as the loss of NO_3^- and water driving the reduction in droplet volume exceeds the limit in m/q value required for stable trapping condition.

Observations of enhanced NO_3^- depletion from UV-excited SA (**Figure 6.6**) lead to an important question: what is the underlying mechanism of the photocatalytic effect of SA? We suggest a triplet-triplet energy transfer (TTET) mechanism between SA and NO_3^- which is supported by the absorption-emission analysis and excitation energy calculation. **Figure 6.11** shows the absorption-emission spectra of SA (pH = 0.82) along with an absorption spectrum of

NO_3^-. The absorption spectrum of SA (first singlet-excitation, ($S_0 \rightarrow S_1$) was seen at 240 – 270 nm, and the emission was observed in the 300 -450 nm range. It is noticeable that there is a significant energy gap between absorption and emission of SA. Comparing the energy with respect to the λ_{max} for absorption (263 nm) and emission (344 nm) yields an energy difference of 1.11 eV. Therefore, it is plausible that the observed emission of SA (**Figure 6.11**) from 266 nm excitation is phosphorescence, *i.e.*, the photoexcited singlet-excited state (S_1) undergoes radiationless intersystem crossing (ISC) to the triplet-excited state (T_1) that then phosphoresces byrelaxation to singlet-ground state ($T_1 \rightarrow S_0$).[40] This argument is supported by the CIS excitation energy calculation, where it was shown that the energy differences between SA (S_1) and SA (T_1) is ~1.0 eV (**Table 6.1**) which is close to the observation from the experiment. Note that both the zwitterionic (net charge 0) and protonated (net charge +1) forms of SA were included in the excitation energy calculation because these two forms of SA coexist in the acidic condition of the experiment.

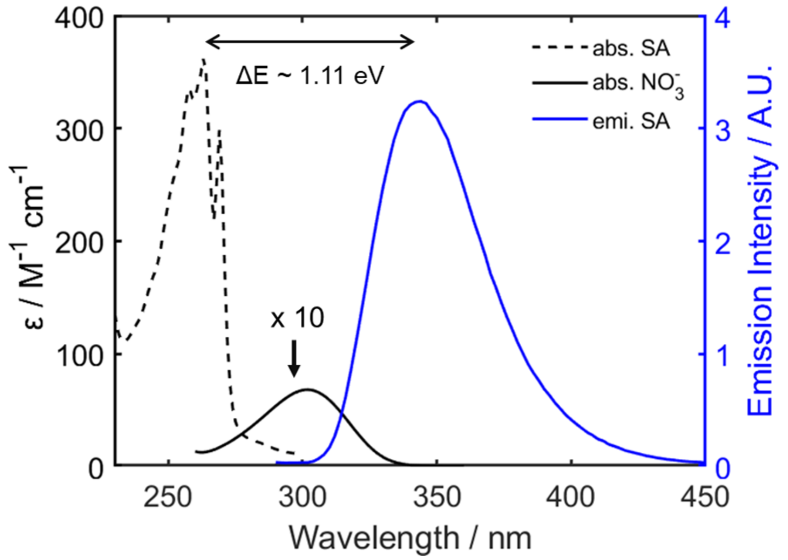

Figure 6.11: Absorption-emission spectra of SA and NO_3^-. Left y-axis represents the molar extinction coefficient (ε, units: M^{-1} cm^{-1}) of SA and NO_3^-. The $S_0 \rightarrow S_1$ absorption band of SA is located at 230 – 280 nm range (dashed black line). ε of NO_3^- is magnified by 10 times (solid black line) because of its relatively small value compared to SA. y-axis on the right side shows emission intensity in arbitrary units. The emission band from SA is observed at 300 – 450 nm (solid blue line). The difference between absorption and emission energy is about 1.11 eV.

Table 6.1: Excitation Energies with Respect to the Ground State of the Nitrate Anion and Sulfanilic Acid in the Gas Phase[a]

	ΔE (S_1) / eV	ΔE (T_1) / eV
NO_3^- (this study)	4.66	4.23
NO_3^- (ref. 36)	4.08	3.88
SA (zwitterion)	5.44	4.44
SA^+ (protonated)	5.64	4.66

[a] Ref. 36 used EOM-CCSD/aug-cc-pVQZ level for the calculation of NO_3^- excitation energy. For this study, the energy levels are calculated at the CIS level which requires lower computation power than EOM-CCSD/aug-cc-pVQZ. 6-31G basis set was used for NO_3^-, and p and d functions were added to the basis set of SA (6-31G(p,d)) for sulfur and hydrogens.

The excitation energy of NO_3^-, however, shows about 0.4 eV difference between S_1 and T_1 states (**Table 6.1**). Calculated energy values by Svoboda *et al.* are listed in **Table 6.1** as well for comparison.[41] Given that the SA (T_1) (zwitterion: 4.44 eV protonated: 4.66 eV) and NO_3^- (T_1) (4.23 eV) have comparable excitation energy values, TTET can occur between them. This energy transfer mechanism is often referred to as photosensitization, and it is believed to contribute significantly to the overall redox chemistry of the Earth's atmosphere.[38] The graphical description of the photosensitization process between SA and NO_3^- leading to the depletion of NO_3^- in the droplet is shown in **Figure 6.12**. First, SA (S_0) is excited to S_1 state by absorbing 266 nm radiation, followed by ISC from SA (S_1) to SA (T_1). Then, TTET takes place between SA (T_1) and NO_3^- (S_0), resulting in SA (S_0) and NO_3^- (T_1) according to the rule of spin conservation. Finally, NO_3^- (T_1) molecules are reduced to NO_2 (g) and HONO (g) (equation 6.1 and 6.2) with those products then evaporating from the droplet. Meanwhile SA (S_0) can again absorb a 266 nm photon, serving as a photocatalyst for these reactions. In addition, there is a possibility of proton (H^+) transfer from SA to NO_3^- during the energy transfer process, as observed in other cases of photosensitization.[42]

It is interesting that the NO_3^- (T_1) has been a subject of various theoretical studies, and it was suggested that the triplet-excited state can contribute to the photolysis of NO_3^-.[17,41,43] Svoboda et al. argued that the dissociation (reduction) of NO_3^- is more likely from the T_1 state than the S_1 state, so singlet to triplet absorption of NO_3^- can be important.[41] However, singlet-triplet absorption of NO_3^- has not been observed experimentally, due to the dipole-forbidden and spin-forbidden nature of this transition.[17,18] Here, our result from **Figure 6.6** and the proposed TTET mechanism shown in **Figure 6.12** can provide an important piece of the puzzle to understanding the efficient reduction of triplet-excited NO_3^-. To be specific, dissociation of NO_3^- from T_1 state can occur through TTET rather than singlet-triplet absorption ($S_0 \rightarrow T_1$).

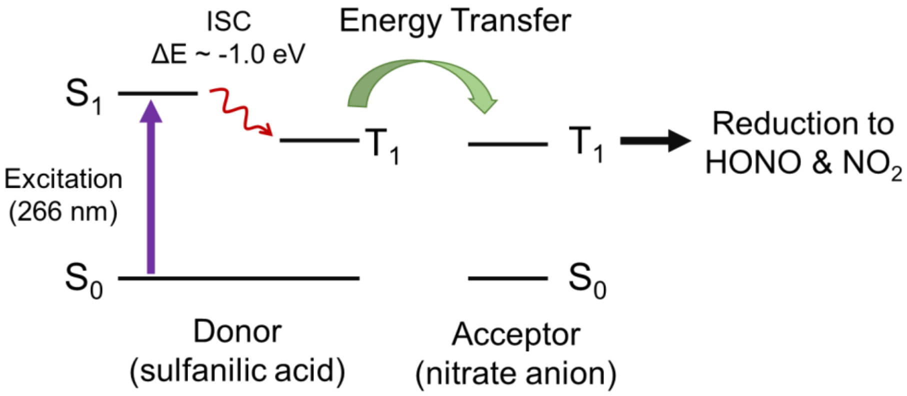

Figure 6.12: Energy level diagram for triplet-triplet energy transfer (TTET) between SA and NO_3^-.

To further support the TTET mechanism for enhanced reactions of NO_3^-, the depletion rate and absorption-emission spectra of SA at different pH conditions were measured. **Figure 6.13A** shows that the depletion of NO_3^- is faster for less-acidic (higher pH) droplets. This pH-dependence of NO_3^- depletion rate can be related to the absorption and emission character of SA. In **Figure 6.13B**, it is clear that the absorption cross section and emission intensity of SA rise as the pH of the solution increases from 0.56 to 1.31. It can be inferred that in less acidic conditions higher population of SA (T_1) molecules are available for energy transfer to NO_3^- (S_0) molecules, thus increasing the rate of NO_3^- depletion. In addition, triplet excitation energy of zwitterionic SA is closer to the triplet excitation energy of NO_3^- than that of protonated SA by ~0.23 eV (**Table 6.1**). For this reason, it is reasonable that the probability of TTET can be higher for the zwitterionic SA than protonated SA. In less acidic conditions, the population ratio between zwitterionic and protonated SA will increase, *i.e.*, SA molecules in the droplet are less protonated in overall. Therefore, higher pH can promote more TTET between SA and NO_3^- which leads to the higher depletion rate of NO_3^- (**Figure 6.13A**).

In the results of this study, the photolysis reactions (equation 6.1 and 6.2) of NO_3^- are shown to be triggered by SA (T_1) without the photolysis of NO_3^- by UV. It is striking that the rapid depletion of NO_3^- can occur without excitation of NO_3^- by actinic UV wavelengths. In previous studies, one of the proposed mechanism for enhanced reactions of NO_3^- is the production of solvated electrons (e_s^-) from the UV-irradiated photosensitizers (equation 6.5, *Ph*: photosensitizer) followed by the reaction between NO_3^- and e_s^- (equation 6.6).[23]

$$Ph + h\nu \rightarrow Ph^* \rightarrow Ph^+ + e_s^- \tag{6.5}$$

$$NO_3{}^- + e_s{}^- \rightarrow NO_3{}^{2-} \tag{6.6}$$

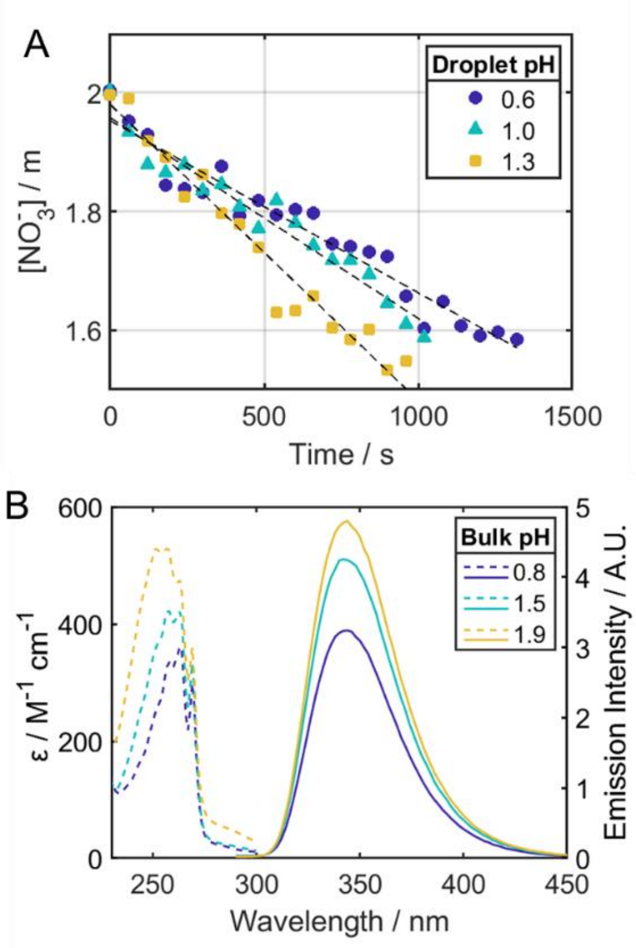

Figure 6.13: pH-dependence of NO_3^- depletion rate and absorption-emission properties of SA. (A) $[NO_3^-]$ versus time at different pH conditions of the droplets and fixed SA content ([SA] = 45.0 x 10^{-3} m). (B) Absorption (dashed lines) and emission (solid lines) spectra of SA in bulk aqueous solutions with varying pH.

However, the production of NO_3^{2-} radical from the one-electron reduction of NO_3^- is thermodynamically unfavored (E° ≈ −1.1 V vs NHE) and the collision between two negatively charged particles may not be a frequent event in aqueous solutions due to the strong Coulombic repulsion.[44] In comparison, this reaction is less favorable than the reduction of water by e_s^- given in equation 6.7 (E° = -0.83 V vs NHE).[45]

$$H_2O \quad + \quad e_s^- \quad \rightarrow \quad \frac{1}{2}H_2 \quad + \quad OH^- \tag{6.7}$$

Therefore, in this study, we suggest the TTET mechanism as a more plausible explanation for the depletion of NO_3^- in the presence of organic photosensitizers. Enhanced production of HONO by the energy transfer mechanism can potentially contribute to the missing budget of daytime HONO production.

6.4: Conclusions

In conclusion, in-situ spectroscopic analysis of single levitated droplets with 266 nm laser irradiation revealed the depletion of NO_3^- caused by energy transfer from excited-state SA to ground-state NO_3^-. The rate of NO_3^- depletion and volume reduction were directly dependent on the initial concentration of SA, suggesting the photocatalytic role of SA for reduction of NO_3^-. It is expected that the main products for the reactions are NO_2 and HONO gas, and they can be readily evaporated from the droplet surface which leads to the observed decrease in droplet size. Absorption-emission spectra of SA NO_3^- and SA with excitation energy calculations suggest that TTET can occur between the two species. Moreover, the absorption and emission character of SA with varying pH conditions are correlated with the depletion rate of NO_3^-, consistent with a larger population of SA (T_1) leading to faster NO_3^- depletion. The experimental results reported in this work provide an original view to how photochemical reactions of aqueous NO_3^- can be enhanced by TTET from light-absorbing organic molecules and,[23–25] more broadly, on promoting optically forbidden transitions in a molecule by a complementary molecular photocatalyst.

Acknowledgements

Chapter 6, in full, has been in preparation for publication of the material as it may appear in Journal of Physical Chemistry Letters, 2022, Kim, Pyeongeun; Boothby, Christian; Grassian, Vicki H.; Continetti, Robert E. The dissertation author was the primary investigator and author of this paper.

References

(1) McCormick, R. A.; Ludwig, J. H. Climate Modification by Atmospheric Aerosols. *Science* **1967**, *156* (3780), 1358 LP – 1359.

(2) Field, C. B.; Barros, V. R. *Climate Change 2014–Impacts, Adaptation and Vulnerability: Regional Aspects*; Cambridge University Press, 2014.

(3) Mauderly, J. L.; Chow, J. C. Health Effects of Organic Aerosols. *Inhal. Toxicol.* **2008**, *20* (3), 257–288.

(4) Wang, C. C.; Prather, K. A.; Sznitman, J.; Jimenez, J. L.; Lakdawala, S. S.; Tufekci, Z.; Marr, L. C. Airborne Transmission of Respiratory Viruses. *Science* **2021**, *373* (6558).

(5) Grassian, V. H. Heterogeneous Uptake and Reaction of Nitrogen Oxides and Volatile Organic Compounds on the Surface of Atmospheric Particles Including Oxides, Carbonates, Soot and Mineral Dust: Implications for the Chemical Balance of the Troposphere. *Int. Rev. Phys. Chem.* **2001**, *20* (3), 467–548.

(6) Shrivastava, M.; Lou, S.; Zelenyuk, A.; Easter, R. C.; Corley, R. A.; Thrall, B. D.; Rasch, P. J.; Fast, J. D.; Simonich, S. L. M.; Shen, H.; Tao, S. Global Long-Range Transport and Lung Cancer Risk from Polycyclic Aromatic Hydrocarbons Shielded by Coatings of Organic Aerosol. *Proc. Natl. Acad. Sci. U. S. A.* **2017**, *114* (6), 1246–1251.

(7) Zeng, M.; Wilson, K. R. Efficient Coupling of Reaction Pathways of Criegee Intermediates and Free Radicals in the Heterogeneous Ozonolysis of Alkenes. *J. Phys. Chem. Lett.* **2020**, *11* (16), 6580–6585.

(8) Dalton, A. B.; Nizkorodov, S. A. Photochemical Degradation of 4-Nitrocatechol and 2,4-Dinitrophenol in a Sugar-Glass Secondary Organic Aerosol Surrogate. *Environ. Sci. Technol.* **2021**, *55* (21), 14586–14594.

(9) Kim, P.; Continetti, R. E. Accelerated Keto-Enol Tautomerization Kinetics of Malonic Acid in Aqueous Droplets. *ACS Earth Sp. Chem.* **2021**, *5* (9), 2212–2222.

(10) Zafiriou, O. C.; True, M. B. Nitrate Photolysis in Seawater by Sunlight. *Mar. Chem.* **1979**, *8* (1), 33–42.

(11) Li, J.; Gao, W.; Cao, L.; Xiao, Y.; Zhang, Y.; Zhao, S.; Liu, Z.; Liu, Z.; Tang, G.; Ji, D.; Hu, B.; Song, T.; He, L.; Hu, M.; Wang, Y. Significant Changes in Autumn and Winter Aerosol Composition and Sources in Beijing from 2012 to 2018: Effects of Clean Air Actions. *Environ. Pollut.* **2021**, *268*, 115855.

(12) Mack, J.; Bolton, J. R. Photochemistry of Nitrite and Nitrate in Aqueous Solution: A Review. *J. Photochem. Photobiol. A Chem.* **1999**, *128* (1–3), 1–13.

(13) Comes, F. J. Recycling in the Earth's Atmosphere: The OH Radical—Its Importance for the Chemistry of the Atmosphere and the Determination of Its Concentration. *Angew. Chemie Int. Ed. English* **1994**, *33* (18), 1816–1826.

(14) Arakaki, T.; Miyake, T.; Hirakawa, T.; Sakugawa, H. PH Dependent Photoformation of Hydroxyl Radical and Absorbance of Aqueous-Phase N(III) (HNO2 and NO2-). *Environ. Sci. Technol.* **1999**, *33* (15), 2561–2565.

(15) Han, C.; Yang, W.; Wu, Q.; Yang, H.; Xue, X. Heterogeneous Photochemical Conversion of NO2 to HONO on the Humic Acid Surface under Simulated Sunlight. *Environ. Sci. Technol.* **2016**, *50* (10), 5017–5023.

(16) Goldstein, S.; Rabani, J. Mechanism of Nitrite Formation by Nitrate Photolysis in Aqueous Solutions: The Role of Peroxynitrite, Nitrogen Dioxide, and Hydroxyl Radical. *J. Am. Chem. Soc.* **2007**, *129* (34), 10597–10601.

(17) Svoboda, O.; Kubelová, L.; Slavíček, P. Enabling Forbidden Processes: Quantum and Solvation Enhancement of Nitrate Anion UV Absorption. *J. Phys. Chem. A* **2013**, *117* (48), 12868–12877.

(18) Marcotte, G.; Marchand, P.; Pronovost, S.; Ayotte, P.; Laffon, C.; Parent, P. Surface-Enhanced Nitrate Photolysis on Ice. *J. Phys. Chem. A* **2015**, *119* (10), 1996–2005.

(19) Scharko, N. K.; Berke, A. E.; Raff, J. D. Release of Nitrous Acid and Nitrogen Dioxide from Nitrate Photolysis in Acidic Aqueous Solutions. *Environ. Sci. Technol.* **2014**, *48* (20), 11991–12001.

(20) Couzo, E.; Lefer, B.; Stutz, J.; Yarwood, G.; Karamchandani, P.; Henderson, B.; Vizuete, W. Impacts of Heterogeneous HONO Formation on Radical Sources and Ozone Chemistry in Houston, Texas. *Atmos. Environ.* **2014**, *112*, 344–355.

(21) Lee, J. D.; Whalley, L. K.; Heard, D. E.; Stone, D.; Dunmore, R. E.; Hamilton, J. F.; Young, D. E.; Allan, J. D.; Laufs, S.; Kleffmann, J. Detailed Budget Analysis of HONO in Central London Reveals a Missing Daytime Source. *Atmos. Chem. Phys.* **2016**, *16* (5), 2747–2764.

(22) Ye, C.; Zhang, N.; Gao, H.; Zhou, X. Photolysis of Particulate Nitrate as a Source of

HONO and NOx. *Environ. Sci. Technol.* **2017**, *51* (12), 6849–6856.

(23) Wang, Y.; Huang, D. D.; Huang, W.; Liu, B.; Chen, Q.; Huang, R.; Gen, M.; Mabato, B. R. G.; Chan, C. K.; Li, X.; Hao, T.; Tan, Y.; Hoi, K. I.; Mok, K. M.; Li, Y. J. Enhanced Nitrite Production from the Aqueous Photolysis of Nitrate in the Presence of Vanillic Acid and Implications for the Roles of Light-Absorbing Organics. *Environ. Sci. Technol.* **2021**, *55* (23), 15694–15704.

(24) Gen, M.; Zhang, R.; Chan, C. K. Nitrite/Nitrous Acid Generation from the Reaction of Nitrate and Fe(II) Promoted by Photolysis of Iron-Organic Complexes. *Environ. Sci. Technol.* **2021**, *55* (23), 15715–15723.

(25) Mora Garcia, S. L.; Pandit, S.; Navea, J. G.; Grassian, V. H. Nitrous Acid (HONO) Formation from the Irradiation of Aqueous Nitrate Solutions in the Presence of Marine Chromophoric Dissolved Organic Matter: Comparison to Other Organic Photosensitizers. *ACS Earth Sp. Chem.* **2021**, *5* (11), 3056–3064.

(26) Nadler, K. A.; Kim, P.; Huang, D. L.; Xiong, W.; Continetti, R. E. Water Diffusion Measurements of Single Charged Aerosols Using H_2O/D_2O Isotope Exchange and Raman Spectroscopy in an Electrodynamic Balance. *Phys. Chem. Chem. Phys.* **2019**, *21* (27), 15062–15071.

(27) Kim, P.; Xiong, W.; Continetti, R. E. Evolution of Hydrogen-Bond Interactions within Single Levitated Metastable Aerosols Studied by in Situ Raman Spectroscopy. *J. Phys. Chem. B* **2020**, *124* (42), 9385–9395.

(28) Yang, X.; Zhang, Y.; Wang, L.; Cao, L.; Li, K.; Hursthouse, A. Preparation of a Thermally Modified Diatomite and a Removal Mechanism for 1-Naphthol from Solution. *Water (Switzerland)* **2017**, *9* (9), 1–15.

(29) Paul, W. Electromagnetic Traps for Charged and Neutral Particles (Nobel Lecture). *Rev. Mod. Phys.* **1990**, *29* (7), 739–748.

(30) Trevitt, A. J.; Wearne, P. J.; Bieske, E. J. Calibration of a Quadrupole Ion Trap for Particle Mass Spectrometry. *Int. J. Mass Spectrom.* **2007**, *262* (3), 241–246.

(31) Glantschnig, W. J.; Chen, S.-H. Light Scattering from Water Droplets in the Geometrical Optics Approximation. *Appl. Opt.* **1981**, *20* (14), 2499.

(32) Lienhard, D. M.; Bones, D. L.; Zuend, A.; Krieger, U. K.; Reid, J. P.; Peter, T. Measurements of Thermodynamic and Optical Properties of Selected Aqueous Organic and Organic-Inorganic Mixtures of Atmospheric Relevance. *J. Phys. Chem. A* **2012**, *116* (40), 9954–9968.

(33) Ally, M. R.; Zaltaeh, A.; Linkous, R. L.; Klatt, L. N. Densities and Refractive Indexes of Aqueous (Li, K, Na) NO_3 Mixtures. *J. Chem. Eng. Data* **1991**, *36* (2), 209–213.

(34) Zuend, A.; Marcolli, C.; Booth, A. M.; Lienhard, D. M.; Soonsin, V.; Krieger, U. K.;

Topping, D. O.; McFiggans, G.; Peter, T.; Seinfeld, J. H. New and Extended Parameterization of the Thermodynamic Model AIOMFAC: Calculation of Activity Coefficients for Organic-Inorganic Mixtures Containing Carboxyl, Hydroxyl, Carbonyl, Ether, Ester, Alkenyl, Alkyl, and Aromatic Functional Groups. *Atmos. Chem. Phys.* **2011**, *11* (17), 9155–9206.

(35) Gervasi, N. R.; Topping, D. O.; Zuend, A. A Predictive Group-Contribution Model for the Viscosity of Aqueous Organic Aerosol. *Atmos. Chem. Phys.* **2020**, *20* (5), 2987–3008.

(36) Pandit, S.; Mora Garcia, S. L.; Grassian, V. H. HONO Production from Gypsum Surfaces Following Exposure to NO_2 and HNO_3: Roles of Relative Humidity and Light Source. *Environ. Sci. Technol.* **2021**, *55* (14), 9761–9772.

(37) Goldstein, S.; Aschengrau, D.; Diamant, Y.; Rabani, J. Photolysis of Aqueous H_2O_2: Quantum Yield and Applications for Polychromatic UV Actinometry in Photoreactors. *Environ. Sci. Technol.* **2007**, *41* (21), 7486–7490.

(38) Martins-Costa, M. T. C.; Anglada, J. M.; Francisco, J. S.; Ruiz-López, M. F. Photosensitization Mechanisms at the Air-Water Interface of Aqueous Aerosols. *Chem. Sci.* **2022**, *13* (9), 2624–2631.

(39) Jing, B.; Wang, Z.; Tan, F.; Guo, Y.; Tong, S.; Wang, W.; Zhang, Y.; Ge, M. Hygroscopic Behavior of Atmospheric Aerosols Containing Nitrate Salts and Water-Soluble Organic Acids. *Atmos. Chem. Phys.* **2018**, *18* (7), 5115–5127.

(40) Lysenko, G. M.; Kislyak, G. M. On Photoluminescence Reabsorption in Organic Phosphors. *J. Appl. Spectrosc.* **1967**, *7* (3), 272–275.

(41) Svoboda, O.; Slavíček, P. Is Nitrate Anion Photodissociation Mediated by Singlet-Triplet Absorption? *J. Phys. Chem. Lett.* **2014**, *5* (11), 1958–1962.

(42) Baptista, M. S.; Cadet, J.; Di Mascio, P.; Ghogare, A. A.; Greer, A.; Hamblin, M. R.; Lorente, C.; Nunez, S. C.; Ribeiro, M. S.; Thomas, A. H. Type I and Type II Photosensitized Oxidation Reactions: Guidelines and Mechanistic Pathways. *Photochem. Photobiol.* **2017**, *93* (4), 912–919.

(43) Peterson, K. A.; Li, Y.; Francisco, J. S.; Zou, P.; Webster, C. E.; Pérez, L. M.; Hall, M. B.; North, S. W. The Role of Triplet States in the Long Wavelength Absorption Region of Bromine Nitrate. *J. Chem. Phys.* **2003**, *119* (15), 7864–7870.

(44) Cook, A. R.; Dimitrijevic, N.; Dreyfus, B. W.; Meisel, D.; Curtiss, L. A.; Camaioni, D. M. Reducing Radicals in Nitrate Solutions. The NO_3^{2-} System Revisited. *J. Phys. Chem. A* **2001**, *105* (14), 3658–3666.

(45) Lide, D. R. *CRC Handbook of Chemistry and Physics. 79th Ed.*; CRC Press Inc.: Boca Raton, FL, 1998.